CONTACTLESS, HIGH RESOLUTION CHARACTERIZATION OF CURRENT AND VOLTAGE WAVEFORMS WITHIN HIGH POWER COMMUNICATION AMPLIFIERS

This dissertation is submitted to the Cardiff University

in candidature for the degree of

Doctor of Philosophy

By

Ali Mahdi Lafta Al-Ziayree

Centre for High Frequency Engineering

Cardiff School of Engineering

Cardiff University

United Kingdom

March 2018

To my parents and my family.

DECLARATION

This work has not been submitted in substance for any other degree or award at this or any other university or place of learning, nor is being submitted concurrently in candidature for any degree or other award.

Signed ……..…… (candidate) Date ……..……

STATEMENT 1

This thesis is being submitted in partial fulfillment of the requirements for the degree of PhD.

Signed ……..…… (candidate) Date ……..……

STATEMENT 2

This thesis is the result of my own independent work/investigation, except where otherwise stated, and the thesis has not been edited by a third party beyond what is permitted by Cardiff University's Policy on the Use of Third Party Editors by Research Degree Students. Other sources are acknowledged by explicit references. The views expressed are my own.

Signed ……..……..…… (candidate) Date ……..……

STATEMENT 3

I hereby give consent for my thesis, if accepted, to be available online in the University's Open Access repository and for inter-library loan, and for the title and summary to be made available to outside organisations.

Signed ……..…..….. (candidate) Date ……

ABSTRACT

Characterisation of high-power communications-based amplifiers (PAs) has generated many thousands of research papers and much of this work assumes the transistors at the heart of these (PAs) to be a 'large' holistic entity. Given that high-power communications-based transistors are made up of multiple, parallel transistors on a single substrate, it is this intermediate scale range, within the periphery of the device, but much larger than the geometrical scale of the epitaxy and the lithography, that requires deeper investigation. Raman-based thermography may add a dimension of spatially varying heat dissipation but 'lifting the bonnet' of the transistor and making internal contactless measurements of current and voltage is the only way to fully account for the myriads of parasitic effects that have been observed by countless researchers. To date, however, very little research has been conducted on quantifying the individual spatial voltages within the transistor in order to fully characterise it. Miniaturised contactless current and voltage probes are theorised, designed, characterised and optimised in this thesis to deliver a robust and reliable means of transistor characterisation at these internal spatial dimensions. The contactless voltage probe presented in this work has a spatial resolution four times finer than the previously reported voltage probe, with a useful bandwidth up to 7 GHz and a controllable passive gain up to 20 dB at the desired operating frequency. The pinnacle of this thesis delivers a novel shielded contactless current probe, capable of high-resolution scanning, culminating in a 'quasi-calibrated' measurement of the distributed currents within a multi-finger LDMOS transistor operating at high power and high frequency. The spatial resolution of this shielded contactless current probe is 62.5 µm with 22.7 dB average rejection ratio to the electric field, and it has a broad bandwidth up to 9 GHz. To date, this type of contactless current measurement has not been reported elsewhere.

ACKNOWLEDGEMENTS

I would like to thank my parents and my wife for their unlimited support and encouragement over the past four years.

I would like to express my sincere appreciation to my country Iraq for giving me the opportunity to complete this work.

I wish to express my great gratitude thanks to my supervisor Doctor Richard Perks for his understanding, guidance, constructive advice and priceless supervision. His expertise and experience are very valuable and essential to completion of this work.

I am also very grateful to Professor Steve Cripps for his overall support and dedication into the project and my professional development.

A special thanks to the wonderful staff of the School of Engineering in the University of Cardiff of their kindness and support.

PUBLICATIONS

1. “A novel microwave non-contact current probe with high spatial resolution” 2016 IEEE MTT-S International Microwave Symposium (IMS).
2. “Integrated simulation and high resolution E & H field probing for multi-finger GaN HFET device scaling and optimisation” Proceedings of the 40th Workshop on Compound Semiconductor Devices and Integrated Circuits, (WOCSDICE 2016) Aveiro, Portugal.
3. “A 25 μm Spatial Resolution Broadband Microwave Voltage Probe” 2016 International Conference for Students on Applied Engineering (ICSAE).

CONTENTS

LIST OF ABBREVIATIONS

a	Radius of the current loop
A	Area
A_{dp}	Crosse sectional area.
$A_{\ell p}$	Cylindrical area.
AM	Amplitude Modulation.
AWG	American Wire Gauge.
B	Magnetic flux density.
BALUN	BALanced to UNbalanced convertor.
BNC	Bayonet Neill–Concelman.
BS	Base Stations.
c	Speed of light.
C	Loop circumference
C_{Amp}	Amplifier input capacitor.
C_c	Coupling Capacitor.
C_{gs}	Capacitance between gate and source.
CMOS	Complementary Metal Oxide Semiconductor.
CMRR	Common Mode Rejection Ratio.
d	Diameter of the bond wire
D	Largest antenna dimension
D	Electric flux density.
D	Distance between bond wires.
d_p	Diameter of the enamelled wire.
D_p	Diameter of the loop antenna.
DUT	Device Under Test.
E	Electric field intensity.
EFRR	Electric Field Rejection Ratio.
EM	Electro Magnetic.
EMC	Electro Magnetic Compatibility.
EMCA	European Computer Manufacturers Association
EMF	Electro Magnetic Field.
EO	Electro-Optic.
EOM	Electro-Optic Modulator.
f	Frequency.
f_c	Cut off frequency.
FET	Field Effect Transistor.
g	Gap width.
GaN	Gallium Nitride.
GPIB	General Purpose Interface Bus.
GSG	Ground Signal Ground.
h	Probe height above the DUT.
H	Magnetic field intensity.
HPLD	High Power Laser Diode.
I	Instantaneous current.
IC	Integrated Circuit.
I_d	Displacement current.
ID	Inner Diameter.
I_o	Current peak value.
I_e	Electric current.
IEC	International Electrotechnical Commission.

I_m	Magnetic current.
ICT	Information and Communication Technology.
J_e	Electric current density,
J_m	Magnetic current density.
K	Probe constant.
L	Transmission line length.
L_{Cox}	Coaxial cable inductance.
LDMOS	Laterally Diffused Metal Oxide Semiconductor.
L_m	Coupling inductance.
LNA	Low Noise Amplifier.
LTCC	Low Temperature Co-fired Ceramics.
LabVIEW	Laboratory Virtual Instrument Engineering Workbench.
MA	Measurement Action.
MCMD	Measurement Control and Data Management.
MIs	Measurement Instruments.
MMIC	Microwave/Millimetre-wave Monolithic Integrated Circuit.
MO	Magneto-Optic.
MOM	Magneto-Optic Modulator.
MOSFET	Metal-Oxide Semiconductor Field-Effect Transistor.
MZ	Mach-Zehnder.
n	Number of infinitesimal partition.
NF	Noise Figure.
OD	Outer Diameter.
PA	Power Amplifier.
PCB	Printed Circuit Board.
P_{de}	Power density around the electric dipole
P_{dm}	Power density around the Magnetic dipole.
PHEMT	Pseudomorphic High Electron Mobility Transistor.
PM	Phase Modulation.
PSD	Position Signal Differences.
PSDT	Position Signal Differences Technique.
r	Distance between probe and the source of radiation.
R	Spatial resolution.
RF	Radio Frequency.
RS232	Recommended Standard 232.
R_v	Spatial resolution in terms of probe output voltage.
R_{wg}	Spatial resolution in terms of track / gap width.
s	Loop width.
SF	Scale Factor
SMA	Sub Miniature version A.
t	Time.
t	Thickness.
TCP/IP	Transmission Control Protocol/Internet Protocol.
V	Voltage.
V_c	Coupling voltage.
V_i	Induced voltage.
V_g	Gate voltage.
VNA	Vector Network Analyser.
V_o	Peak source voltage.
V_{OE}	Loop voltage in response to the magnetic field.
V_{OH}	Loop voltage in response to the magnetic field.

VSWR	Voltage Standing Wave Ratio.
w	Track width.
W_i	Wire number.
XC_c	Impedance of the coupling capacitor.
XC_{cox}	Impedance of the coaxial cable capacitor.
XC_{gs}	Impedance of the gate source capacitor.
XLcox	Impedance of the coaxial cable inductor.
Z_{Amp}	Amplifier input impedance.
Z_c	Circuit impedance.
Z_{Cox}	Coaxial cable impedance.
Z_G	Source impedance.
Z_L	Load impedance.
Zo	Characteristic impedance of free space.
ZPT	Zero Protrusion Technique
Z_T	Transmission line impedance.
Z_w	Wave impedance.
Z_{we}	Wave impedance of the electric source.
Z_{wm}	Wave impedance of the magnetic source.
$\delta\ell p$	Increment to the protrusion length.
δ_{rm}	Maximum distance increment.
ℓ	Length.
ℓ_p	Length of the probe tip.
β	Wave number.
ε	Permittivity.
ε_r	Relative permittivity.
μ	Permeability.
ρ_e	Electric volume charge density.
ρ_m	Magnetic volume charge density.
ω	Angular frequency.
λ	Wavelength.

1 INTRODUCTION

Nowadays, it is hard to imagine human life without wireless communication facilities. The features offered by telecommunications networks have caused widespread demand for broadband mobile services everywhere. Subscribers to mobile networks represent more than 50% of the global population and the forecast of developments in this field shows no evidence of slowing down [1]. These mobile networks offer the required radio links between smart phones through wireless transmitters and receivers via widely distributed base stations (BS).

The tremendous success of the mobile networks requires more BS to be included in the network to offer wide expansion in the coverage area and/or to overcome fading and interferences problems. However, the impact of this success and growth is impeded by the need to consume more energy by BSs, which is leading to an increased contribution to the global carbon footprint and rising network energy costs.

The philosophy underpinning the 'Green Communications' revolution are the kind of environmentally friendly technologies that aim to reduce the harmful environmental effects of expanding ICT use. The emergence of the term Green Communications has come about as a result of research into the consequences of the emission of carbon dioxide on the climate. These effects are known as the phenomenon of global warming, greenhouse phenomenon or Thermal Greenhouse.

To reduce the ecological and economic implications of the greenhouse effects, the overall energy efficiency of the mobile communication systems need to be improved with a major focus on the BS which consumes around 57% of the total power [2]. A significant amount

of this energy, around 50% - 80%, is consumed at the transmitter part of the base station and more specifically by the microwave power amplifiers (PA) stage [3].

High power microwave transistors like the laterally diffused metal oxide semiconductor (LDMOS) field effect transistors are broadly used in the BS power amplification stage due to their low fabricating cost. While for the BSs that work at a high frequency, the gallium nitride (GaN) high electron mobility transistors are predominant. For both types, enhancing the efficiency and the linearity of these PAs is a key factor towards achieving realistic wireless green communication systems.

Power dissipation by semiconductors: 'the self-heating phenomena' have negative consequences on the performance and the reliability of high power microwave transistors [4], [5]. Some of these effects can be marginally reduced by either using proper external matching circuits and/or using active cooling. Although the later solution can enhance the quality and reliability of the device, it further adds to the carbon footprint attributed to the overall system.

High power microwave transistors are usually constructed from a chain of parallel cell transistors encapsulated in the same package and share the same external leads. Internal characterization and optimization of these devices represent a real challenge for the microwave power transistors designers. This is due to the lack of suitable tools and probes to perform voltage and current measurements inside the microwave power transistors without loading or altering the performance of the device under test (DUT). The move away from Si based PAs which require active cooling towards GaN based PAs that do not require active cooling represents the single most effective step towards green communications.

1.1 Structure of the High-Power Microwave Transistors

Fabricating a high power microwave transistor is not an easy task [6] and there are many factors that must be considered to achieve this target. One of them is the correct width of the transistor gate which needs to meet two opposing requirements. For high-frequency applications, the gate width should be very thin, while in contrast, the wider the gate is, more power can be delivered by the transistor.

One solution to overcome this problem is to replicate many low power high-frequency transistor fingers to scale up the power and forming transistor cell. Cells are connected in parallel to gain the desired power rating at the desired operating frequency. These cell

transistors share the same substrate and their combined structure is referred to as a die. Transistor dies forming the basic unit within a microwave power transistor.

In many high-power transistors, there is often more than one die which share the same external leads (drain, source and gate), see Figure 1-1. The gate and drain pads on the die are connected to the respective gate and drain leads via an array of bond wires. Internal matching capacitors are connected to the input and output sides of the die to achieve the desired input/output impedances.

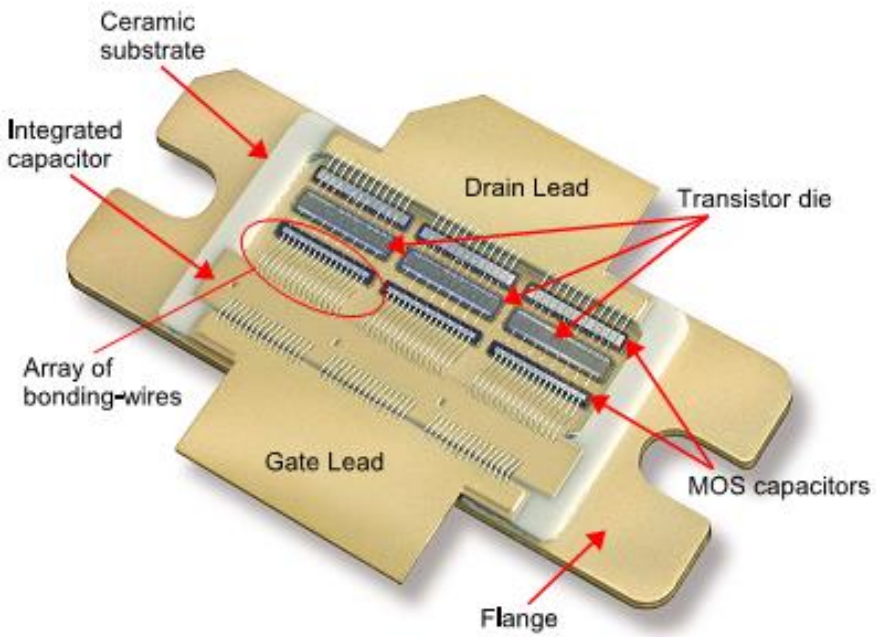

Figure 1-1 Structure of the LDMOS microwave power transistor [7].

1.2 Measurements within Microwave Power Transistor

Unfortunately scaling up the power, by using multiple transistors cells, is a nonlinear process and the total power is not proportional to the total sum of the width of the gate. Practically, this might occur due to the non-even heat distribution and the mutual coupling between adjacent parts, fingers and bond wires [8]. This nonlinear behaviour leads to more power dissipated as heat and causes a greater efficiency degradation.

To overcome these problems, it is essential first to know the voltages and more importantly, the currents that pass through individual parts inside the microwave power transistor. This must be performed under normal operating conditions to find out how the load is divided between dies and then between individual cell transistors.

One way to quantify the amount of power dissipated in each die is to capture their thermal images in order to identify how the load is shared among them depending on their temperatures. This method has two advantages over the Ground Signal Ground[1] (GSG) probing, it is nonintrusive, and it doesn't need any galvanic contacts with DUT. These features are very important in high-frequency measurements where the presence of foreign objects (such as probes, etc.) might alter the measurement. However, thermometry is a consequential measurement rather than direct as it is quantifying not just the joule heating due to the current but perturbed by factors such as heatsink efficiency, geometry, location in the die (central as opposed to periphery) and specifically for GaN, the thermal conductivity of the GaN-Substrate and nucleation layer.

1.3 Motivation

Measuring the localized voltages and currents within microwave power transistors are very important to improve their efficiency and linearity. The designer of these devices needs suitable probing tools to perform these localized measurements.

Miniaturized voltage and current probes represent an alternative method to locally quantify the intensities of both the electrical and the magnetic field, radiated from the dies and the bond wires within microwave power transistors. Variation in these localized intensities is proportional to those in the voltages and currents respectively.

This type of measurement is known as the near field measurement or the contactless voltage and current measurement because no galvanic contact is made.

1.4 Thesis Objectives

The ultimate objective of this thesis is to deliver a means of quantifying currents and voltages at specific locations within a semiconductor device. Significant progress has been made by numerous research organisations in quantifying current and voltage for a device as a holistic entity.

In order to fully de-embed the factors that give rise to the vast array of parasitic and non-linear phenomena such as the memory effect, AM-PM distortion, efficiency, etc., this holistic perspective requires much more introspective detail.

[1] The measurement with GSG probing is performed by creating a low impedance metallic contact with DUT and therefor it can simply alter the impedance of the bond wire.

1.5 Thesis Outline

This thesis largely focuses on the design and development of contactless voltage and current probes intended for diagnostic and characterization of communications-based microwave power transistors under normal operating conditions.

Chapter One: **Introduction.** Chapter one introduces the problem of high power dissipation inside microwave power devices and brings into focus the motivation for this research.

Chapter Two: Electromagnetic Fields measurement at Microwave Frequency. Chapter two reviews the theoretical principles of contactless electromagnetic field probes and sources of electromagnetic radiation including their types and their important properties and limits. The focus here is on the monopole and the loop antenna where their characteristics are studied in both directions as a source and as a receiver. None of the information described in this chapter is new but it offers the essential background needed for designing and implementing contactless voltage and current probes. The chapter ends with a review of the most important papers on contactless voltage and current probes.

Chapter Three: Measurement Setup and Fabrication Requirements. Chapter three presents the generic setup for the contactless voltage and current measurements and describes the main parts and tools used in it; together with the connections and communication between them. Also, it highlights the environments and the nature of the targeted devices inside microwave power transistors. A brief description is provided in this chapter for the bond wires and the structure of the die to gain an adequate understanding of the interaction that occurs between these parts and the probe within the measurement process. The details of a range of tests that are needed to verify the characteristics of the newly fabricated miniaturized probes are illustrated. These tests are firstly applied to 'scaled-up' contactless probes fabricated from standard coaxial cables and their results are considered as a reference.

Chapter Four: Voltage Probe Realization and Testing. Chapter four address the impacts of the geometrical aspects of contactless voltage probes on their spatial resolution and sensitivity. At the beginning, large scale monopole antennas, fabricated from the open end standard coaxial cables, are used to study these impacts and to establish general design criteria. These criteria are then applied to the design and realization of the miniaturized contactless voltage probes. Different methods of enhancing the spatial resolution and the sensitivity of these voltage probes are explored and discussed in this

chapter in detail with highlights of their advantages and disadvantages. This chapter is then finalised with multiple tests to verify the important specifications of the newly fabricated miniaturized voltage probes. The novelties in this chapter can be summarized in three points: firstly, this miniaturized voltage probe has high spatial resolution of at least 25 µm, secondly, it has a controllable passive gain of around 20 dB and thirdly, a useful operating bandwidth of about 7 GHz.

Chapter Five: Current Probe Realization and Testing. Chapter five starts with the same procedure given in chapter four to identify the relationship between the geometry of the loop antenna and their spatial resolution and sensitivity. The design criteria are then applied to the design and fabrication of a miniaturized contactless current probe with high spatial resolution capabilities. Chapter five describes a novel technique to enhance the current probe's rejection of the unwanted electric field pick-up. The fidelity of this novel miniaturized current probe is then examined by applying three other tests: the electric field rejection with average rejection of around 22.7 dB, the standing wave test and the test of the inverted umbrella current distribution across the width of a microstrip line. The novel structure of the miniaturized current probe allows it to move freely and thus perform a direct current measurement inside operating microwave power transistors. The other novelties recorded in this chapter are: a spatial resolution of around 62 µm and useful operating bandwidth of 9 GHz.

Chapter Six: Novel Measurements of Current within a Microwave Transistor. Chapter six focuses on a new method of characterizing microwave power transistors by using the miniaturized contactless current probes to perform multiple current measurements within these devices. Real time direct current quantification is of great importance for the designer of these devices because they need to know how the currents are distributed among the internal structure, like the parallel dies and their associated bond wires. This type of information will help designers to improve and modify their designs and thus enhancing their overall efficiency. A 130 W LDMOS power transistor (consisting of three multi-finger dies) is used as the DUT which is then scanned with the miniaturized current probe seven times along its length. These multiple scans show that the identical dies are carrying different amount of currents and those sides dies are passing more current than the central one. This is the first direct confirmation of such a variation.

Chapter Seven: Conclusions and Future Work. Chapter seven summarizes the conclusions and the important outcome from this work and suggest further ideas and modifications for the future work.

2 ELECTROMAGNETIC FIELDS MEASUREMENTS AT MICROWAVE FREQUENCY

2.1 Introduction.

This chapter presents the theoretical concepts necessary to gain an adequate understanding of how the contactless measurements of voltages and currents are achieved at microwave frequency. Also, it establishes the essential background required for designing and implementing a range of non-contact electromagnetic probes. Three main topics are covered here: the different types of electromagnetic sources and their characteristics, voltage and current probes and their transfer functions and noise and signals and how to separate them.

2.2 Electromagnetic Fields.

Theoretical determination of the voltage and current at any arbitrary point in the space requires the calculation of the phase and magnitude of electric and magnetic fields respectively. These fields are governed by a set of four differential equations called Maxwell equations. Maxwell equations form the foundation of the classic electromagnetic fields theory. It is considered to be valid over the whole range of the frequency spectrum and applicable to ultimately any geometry and boundary conditions. In a homogeneous medium, any solution for the symmetric, time-harmonic electric and magnetic fields must satisfy these equations [9].

$$\nabla \times \mathbf{E} = -\mathbf{J_m} - j\omega\mu\mathbf{H} = -\mathbf{J_m} - j\omega\mathbf{B} \tag{2-1}$$

$$\nabla \times \mathbf{H} = \mathbf{J_e} + \mathrm{j}\omega\varepsilon\mathbf{E} = \mathbf{J_e} + \mathrm{j}\omega\mathbf{D} \tag{2-2}$$

$$\nabla \cdot \mathbf{E} = \frac{\rho_e}{\varepsilon} \quad or \quad \nabla \cdot \mathbf{D} = \rho_e \tag{2-3}$$

$$\nabla \cdot \mathbf{H} = \frac{\rho_m}{\mu} \quad or \quad \nabla \cdot \mathbf{B} = \rho_m \tag{2-4}$$

Where, **E** - electric field intensity, **H** - magnetic field intensity, **D** - electric flux density, **B** - magnetic flux density, $\mathbf{J_e}$ - electric current density, $\mathbf{J_m}$ -magnetic current density, ρ_e - electric volume charge density, ρ_m - magnetic volume charge density, ω - angular frequency, μ- permeability, ε- permittivity.

These equations switch to a simpler form for regions of no sources, $\mathbf{J_e} = \mathbf{J_m} = \boldsymbol{\rho_e} = \boldsymbol{\rho_m} = \mathbf{0}$. Practically $\mathbf{J_e}$ may represent either actual or equivalent electric current sources, while $\mathbf{J_m}$ may not actually exist and it may only represent other equivalent sources.

The first equation is known as Faraday's law that relates the electric field to the time-varying magnetic field that induces it. The second one is an extension of Ampere's law and demonstrates how an electric current and /or time-varying electric field can produce a magnetic field. Gauss' law for the electric field in (2-3) relates an electric field to its originating electric charges. Gauss' law for magnetism states that magnetic monopoles do not exist. However, it had been written as in (2-4) to reflect the theoretical hypothetical symmetry required to express the equivalent magnetic current source of radiation. Substituting $\mathbf{J_m}$ and $\boldsymbol{\rho_m}$ with zeros in the above set of equations will bring back the time-harmonic form of Maxwell's equations [10].

2.3 Radiation of the Electromagnetic Fields.

Electromagnetic radiation can be either caused by a time-varying electric current or accelerated electric charges [11]. Usually, individual sources that radiate electromagnetic (EM) fields are known as antennas. For example, the dipole antenna is an electric source of radiation while the loop antenna is considered as a magnetic source of radiation. In both cases, the E and H fields are radiated. The difference is related to which type of field is dominant in the near region around the antenna. In this region and the flowing regions away from the antenna, the currents are equal to zero ($\mathbf{J_e} = \mathbf{J_m} = \boldsymbol{\rho_e} = \boldsymbol{\rho_m} = \mathbf{0}$). Figure 2-1 illustrates how the EM fields propagate around and near to a dipole antenna.

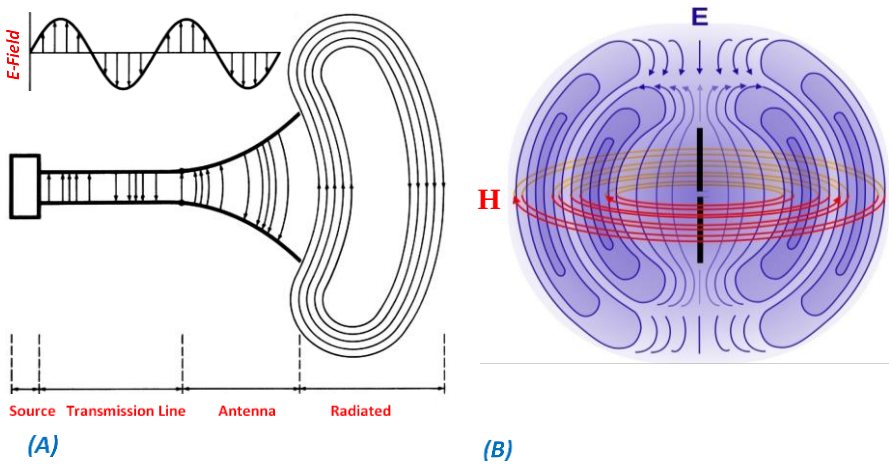

Figure 2-1 (A) Fields propagated to the dipole antenna [12]. (B) Fields around the dipole antenna [13].

The fact that Maxwell's equations are linear (thus the superposition is applicable), allow us to systematically represent the electromagnetic fields radiated for any arbitrary current distribution by simply dividing it into infinitesimal elements (dipoles). Integrating the field components of each dipole reproduce the total fields [14]. The role governing this type of solution is the assumption of uniform current distribution along these dipoles. This cannot be assumed true until the dipole's largest dimension is chosen to be extremely small with respect to the field wavelength. These infinitesimal dipoles have spherical wave radiation [15] and thus they are best described in terms of spherical coordinates (r, θ, φ) [16].

2.3.1 Regions of Electromagnetic Field Radiation.

Before proceeding to state the mathematical description of the electromagnetic waves radiating from a certain source, it is important to designate the regions surrounding it and

the boundary limits for these regions. The space surrounding a source is usually classified as either near field or far field regions [17]. Many texts also identify two subdivisions within the near field regions, which are the reactive near field and the radiative near-field, see Figure 2-2. Boarders between these regions are not unique and many definitions of their limits have been reported [12], [18]–[20]. Some of them are expressed in terms of the wavelength λ only while others are adapting the largest dimension of the source D and λ [12], [18].

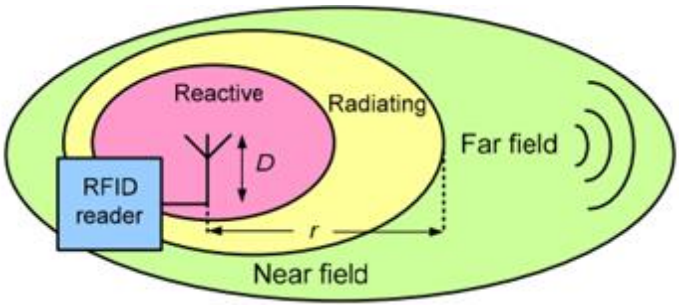

Figure 2-2 Regions of Electromagnetic Field Radiation [17].

2.3.1.1 Reactive Near-Field Region.

It is also called The Very Near-Field Region [18], [19], [21]. The reactive nature of the fields here is dominating [22] and the intensity rapidly changes with distance from the source. It is immediately surrounding the source and starts from its surface [12]. While for the outer limit, many definitions had been reported, some of them are listed below:

- If D is large comparable to λ, according to [12] $r < 0.62\sqrt{D^3/\lambda}$ and according to [19] $r < D^2/8\lambda$.
- If $D < \lambda/10$ and , according to [22]–[24] $r < \lambda/2\pi$ and according to [20] $r < 0.1\lambda/2\pi$.

2.3.1.2 Radiative Near Field (Fresnel) Region.

It is also called the Transition Region [23]. In this region, the source emitted its initial radiation of electromagnetic waves and the field description depends on the distance from the surface of the source [12]. The existence of this region depends on the size of the source, if D is very small in comparison to λ then this region may not exist [12], [24]. Otherwise the boundary of this region starts where the reactive near field region ends and ends at [12], [18], [22] $r < 2D^2/\lambda$. Alternatively, [20] provides this definition $r < 0.8\lambda/2\pi$.

2.3.1.3 Far Field (Fraunhofer) Region.

In this region, the electromagnet field radiates outwards and the waves usually travel toward infinity which represents the outer limit for this region. The field description becomes independent of the distance from the surface of the source [12], [18], [22] and can be approximated to a spherical wavefront. This region surrounding the reactive and the radiative region and its inner bounding limit (for the case of D is large comparable to λ) starts at $r > 2D^2/\lambda$ and for the case of $D < \lambda/10$, it might start from $r > \lambda/2\pi$. While according to [20] it starts at $r > 0.8\lambda/2\pi$.

2.3.2 Radiation of Infinitesimally Small Electric Source.

The Hertzian dipole is defined to be an infinitesimally small current element of current I and extremely short length ℓ, where $\ell \ll \lambda$. Although such a dipole antenna is not realistic, it is wildly used as a building block in the analysis of large and/or complex real antennas [11]. Field observation distance must be large compered to this infinitesimally small dipole length. Under these conditions, it is assumed that its current distribution is uniform (approximately constant magnitude and phase through the dipole) [15]. For an electric source of radiation carrying a current $I = I_o e^{j\omega t}$, where $I_e = I_o$, located at the origin of the coordinate system, the electromagnetic fields observed at any arbitrary point $P_{(r,\theta,\varphi)}$ (see Figure 2-3), is given by the following set of equations [12]:

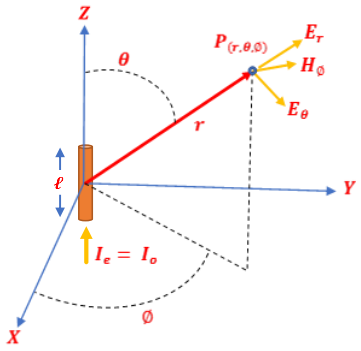

Figure 2-3 Electric and magnetic fields around an infinitesimally small electric dipole.

$$\mathbf{H_{\phi_e}} = j\frac{\beta I_e \ell \sin\theta}{4\pi}\left[\frac{1}{r} + \frac{1}{j\beta r^2}\right] e^{j(\omega t - \beta r)} \tag{2-5}$$

$$\mathbf{E_{r_e}} = Z_o \frac{I_e \ell \cos\theta}{2\pi}\left[\frac{1}{r^2} + \frac{1}{j\beta r^3}\right] e^{j(\omega t - \beta r)} \tag{2-6}$$

$$\mathbf{E_{\theta_e}} = jZ_o \frac{\beta I_e \ell \sin\theta}{4\pi}\left[\frac{1}{r} + \frac{1}{j\beta r^2} - \frac{1}{\beta^2 r^3}\right] e^{j(\omega t - \beta r)} \tag{2-7}$$

$$\mathbf{E_{\phi_e}} = \mathbf{H_{r_e}} = \mathbf{H_{\theta_e}} = 0 \tag{2-8}$$

$$Z_o = \frac{\beta}{\omega\varepsilon} = \sqrt{\frac{\mu}{\varepsilon}} = 377\Omega \tag{2-9}$$

$$\beta = \frac{2\pi}{\lambda} = \frac{\omega}{c} \tag{2-10}$$

Where, β is the wave number, Z_o is the characteristic impedance of free space, ω is the angular frequency and c is the speed of light.

The power density around the electric dipole is

$$P_{d_e} = Z_o \frac{\pi \ell^2 {I_o}^2}{3\lambda^2}\left[1 - j\frac{1}{\beta^3 r^3}\right] \tag{2-11}$$

And the electric dipole radiation resistance is

$$R_{r_e} = Z_o \frac{2\pi\ell^2}{3\lambda^2} \tag{2-12}$$

2.3.3 Radiation of an Infinitesimally Small Magnetic Source.

Analogous to the infinitesimally small electric dipole is the magnetic dipole. It is a very small current loop of radius a located in the xy plane carrying current $I = I_o e^{j\omega t}$ and it is assumed that its circumference $2\pi a \ll \lambda$ so that the current distribution is uniform (approximately constant magnitude and phase through the small loop) [15]. In addition, the observation distance must be large compered to its circumference. This small current loop, shown in Figure 2-4, is placed with its equivalent magnetic dipole moment $I_m \ell$ and furthermore, by adapting the duality of electromagnetic theory, the electromagnetic fields observed at any arbitrary point $P_{(r,\theta,\varphi)}$ can be given by the following set of equations [12]:

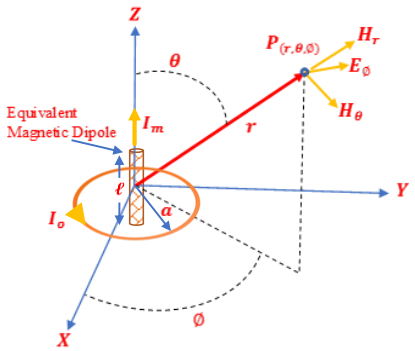

Figure 2-4 Electric and magnetic fields components around infinitesimal magnetic dipole.

$$\mathbf{E_{\phi_m}} = -j\frac{\beta I_m \ell \sin\theta}{4\pi}\left[\frac{1}{r}+\frac{1}{j\beta r^2}\right]e^{j(\omega t-\beta r)} \tag{2-13}$$

$$\mathbf{H_{r_m}} = \frac{I_m \ell \cos\theta}{2\pi Z_o}\left[\frac{1}{r^2}+\frac{1}{j\beta r^3}\right]e^{j(\omega t-\beta r)} \tag{2-14}$$

$$\mathbf{H_{\theta_m}} = j\frac{\beta I_m \ell \sin\theta}{4\pi Z_o}\left[\frac{1}{r}+\frac{1}{j\beta r^2}-\frac{1}{\beta^2 r^3}\right]e^{j(\omega t-\beta r)} \tag{2-15}$$

$$\mathbf{H_{\phi_m}} = \mathbf{E_{r_m}} = \mathbf{E_{\theta_m}} = 0 \tag{2-16}$$

The relation between the equivalent magnetic current I_m and the actual loop current I_o is given by [12] $I_m \ell = jA\omega\mu I_o$.

Where $A = \pi a^2$, (the area of the small loop). In terms of the actual loop current, the above set of equations become

$$\mathbf{E_{\phi_m}} = Z_o\frac{\beta^2 a^2 I_o \sin\theta}{4}\left[\frac{1}{r}+\frac{1}{j\beta r^2}\right]e^{j(\omega t-\beta r)} \tag{2-17}$$

$$\mathbf{H_{r_m}} = j\frac{\beta a^2 I_o \cos\theta}{2}\left[\frac{1}{r^2}+\frac{1}{j\beta r^3}\right]e^{j(\omega t-\beta r)} \tag{2-18}$$

$$\mathbf{H_{\theta_m}} = -\frac{\beta^2 a^2 I_o \sin\theta}{4}\left[\frac{1}{r}+\frac{1}{j\beta r^2}-\frac{1}{\beta^2 r^3}\right]e^{j(\omega t-\beta r)} \tag{2-19}$$

$$\mathbf{H_{\phi_m}} = \mathbf{E_{r_m}} = \mathbf{E_{\theta_m}} = 0 \tag{2-20}$$

where power density around the magnetic dipole is given by

$$P_{d_m} = Z_o\frac{\pi\beta^4 a^4 {I_o}^2}{12}\left[1+j\frac{1}{\beta^3 r^3}\right] \tag{2-21}$$

and the loop radiation resistance is

$$R_{r_m} = Z_o\frac{\pi\beta^4 a^4}{6} \tag{2-22}$$

2.3.4 Radian Distance and Radian Sphere.

The electric and magnetic fields presented by (2-5),(2-6),(2-7) and (2-17),(2-18),(2-19) are valid at any point around the infinitesimally small source except on its surface[12]. The values of these fields might be either real, or imaginary depending on how far from the source they are observed. The terms inside the brackets in any of these equations can have identical absolute values at a specific distance from the source known as the radial distance:

$$r = \frac{\lambda}{2\pi}, \qquad \beta r = 1 \tag{2-23}$$

Within a sphere of radius equal to the radial distance, the reactive part is greater than the radiative part, while outside the sphere it is the opposite. Moving radially away from the sphere either inward or outward makes the power density either primarily imaginary or primarily real respectively, see Figure 2-5.

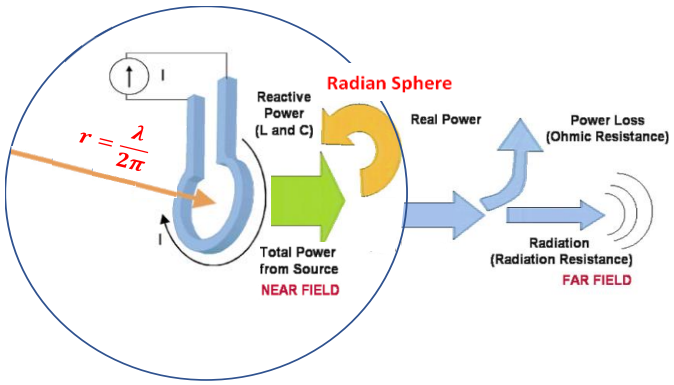

Figure 2-5 Power flow through the near and the far regions [25].

2.3.5 Comparison of Electric and Magnetic Radiation Source.

In order to attain a deeper understanding of electromagnetic fields in this context, we will compare those coming out from an electric source to those of a magnetic source at the near field region. Moving far away from the complicated transitional area between the far field and the near field regions [26], the previous fields equations could be rewritten in an approximated and simplified form [12], [26] if the following condition is satisfied:

If $\beta r \ll 1$, i.e. the very near field region, then the term $1/r^3$ (in (2-5) it is the $1/r^2$ term) become dominant compared to the remaining terms in the brackets.

- For the infinitesimally small electric source, the electric and magnetic fields are presented by [12], [26]:

$$\mathbf{H_{\phi_e}} \cong \frac{I_o \ell}{4\pi r^2} \sin\theta \, e^{j(\omega t)} \qquad \propto \frac{1}{r^2} \tag{2-24}$$

$$\mathbf{E_{r_e}} \cong -jZ_o \frac{I_o \ell \lambda}{4\pi^2 r^3} \cos\theta \, e^{j(\omega t)} \qquad \propto \frac{1}{\omega r^3} \tag{2-25}$$

$$\mathbf{E_{\theta_e}} \cong -jZ_o \frac{I_o \ell \lambda}{8\pi^2 r^3} \sin\theta \, e^{j(\omega t)} \qquad \propto \frac{1}{\omega r^3} \tag{2-26}$$

$$\mathbf{E_{\phi_e}} = \mathbf{H_{r_e}} = \mathbf{H_{\theta_e}} = 0 \tag{2-27}$$

the power density around the electric dipole is

$$P_{d_e} \cong -jZ_o \frac{\ell^2 {I_o}^2 \lambda}{24\pi^2 r^3} \qquad \propto \frac{1}{\omega r^3} \qquad (2\text{-}28)$$

and wave impedance is

$$Z_{w_e} = \frac{\mathbf{E_{\theta_e}}}{\mathbf{H_{\phi_e}}} = -jZ_o \frac{\lambda}{2\pi r} \qquad \propto \frac{1}{\omega r} \qquad (2\text{-}29)$$

- For the infinitesimally small magnetic source, the electric and magnetic fields are presented by:

$$\mathbf{E_{\phi_m}} \cong -jZ_o \frac{\pi a^2 I_o}{2\lambda r^2} sin\,\theta\, e^{j(\omega t)} \qquad \propto \frac{\omega}{r^2} \qquad (2\text{-}30)$$

$$\mathbf{H_{r_m}} \cong \frac{a^2 I_o}{2r^3} \cos\theta\, e^{j(\omega t)} \qquad \propto \frac{1}{r^3} \qquad (2\text{-}31)$$

$$\mathbf{H_{\theta_m}} \cong -\frac{a^2 I_o}{4r^3} sin\,\theta\, e^{j(\omega t)} \qquad \propto \frac{1}{r^3} \qquad (2\text{-}32)$$

$$\mathbf{H_{\phi_m}} = \mathbf{E_{r_m}} = \mathbf{E_{\theta_m}} = 0 \qquad (2\text{-}33)$$

the power density around the magnetic dipole is

$$P_{d_m} \cong jZ_o \frac{\pi^2 a^4 {I_o}^2}{6\lambda r^3} \qquad \propto \frac{\omega}{r^3} \qquad (2\text{-}34)$$

and wave impedance is

$$Z_{w_m} = \frac{\mathbf{E_{\theta_m}}}{\mathbf{H_{\phi_m}}} = jZ_o \frac{2\pi r}{\lambda} \qquad \propto \omega r \qquad (2\text{-}35)$$

Electric and magnetic sources in the very near field region are surrounded by the **E** and **H** fields. The individual components of them ($\mathbf{E_{\theta_e}}$, $\mathbf{E_{r_e}}$ and $\mathbf{H_{\theta_m}}$, $\mathbf{H_{r_m}}$) are in phase and strongly dependent on the distance, inversely proportional to r^3 while $\mathbf{H_{\phi_e}}$ and $\mathbf{E_{\phi_m}}$ are inversely proportional to r^2. Field components in the radial direction $\mathbf{E_{r_e}}$ and $\mathbf{H_{r_m}}$ are in the axis of the dipole and they are equal to zero in the plane crossing the middle of the dipole. The magnetic field for both types of source is not a function of frequency.

The electric field around electric source is inversely proportional with frequency while around the magnetic source it is proportional with frequency. Wave impedances, shown in Figure 2-6, have imaginary values only and it is dependent on the source that created it[26].

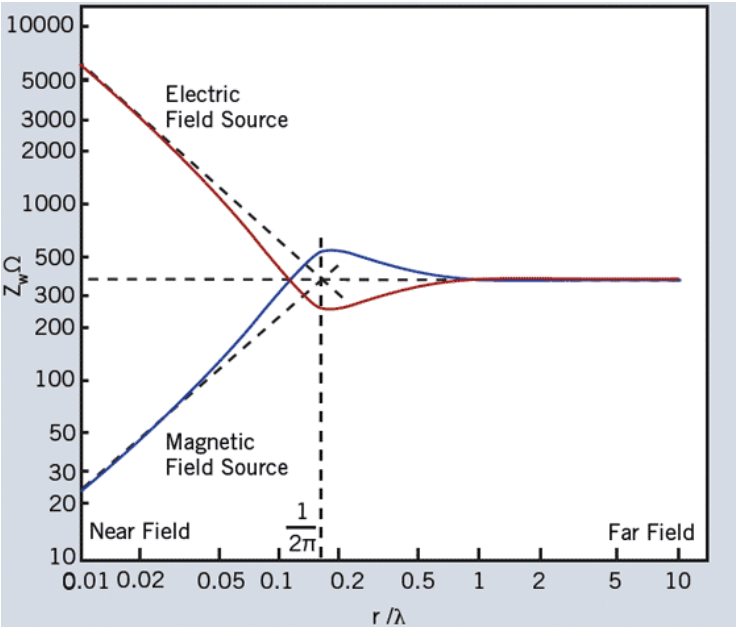

Figure 2-6 Electric and magnetic sources wave impedance in near and far zones [27].

These values go high, with a capacitive nature, as the distance to the electric source decreases. Conversely, they go low, with an inductive nature, as the distance to the magnetic source decreases. Increasing the frequency leads to a decrease in the wave impedance and the power density around the electric source. The opposite being true around the magnetic source. Energy in the very near field region is reactively stored and is strongly dependant on the distance from the source. Table 2-1 summarises, in brief, the dependency of the field components, wave impedance and power density on the frequency and the distance from the source in the near field region.

Table 2-1 Near Zone Electromagnetic fields around electric and magnetic sources.

	Electric Dipole	**Magnetic Dipole**
$\mathbf{E_\theta}$	$\propto 1/\omega r^3$	0
$\mathbf{E_\phi}$	0	$\propto \omega/r^2$
$\mathbf{E_r}$	$\propto 1/\omega r^3$	0
$\mathbf{H_\theta}$	0	$\propto 1/r^3$
$\mathbf{H_\phi}$	$\propto 1/r^2$	0
$\mathbf{H_r}$	0	$\propto 1/r^3$
P_d	$\propto 1/\omega r^3$	$\propto \omega/r^3$
Z_w	$\propto 1/\omega r$	$\propto \omega r$

Contactless measurement of currents and voltages are performed usually in the near field region especially when there are many sources of radiation located very close to each

other as will be seen in chapter four and five. Under such circumstances, where the total length of any of these sources (which is equal to $\ell \times n$, where n is number of infinitesimal partition) become larger than r, the values of $\mathbf{E}_{r_e}$ and $\mathbf{H}_{r_m}$ approach zero (due to $cos\,\theta$ in (2-25) and (2-31) when θ approaches 90 degrees) and substituting 1 instead of $sin\,\theta$ in the remaining set of equations. Figure 2-7 graphically summarises the previous comparison and illustrates the actual field components around the electric and the magnetic source of electromagnetic energy (sub notations of the electric and magnetic fields around the loop are exchanged in this figure due to the vertical orientation of the loop).

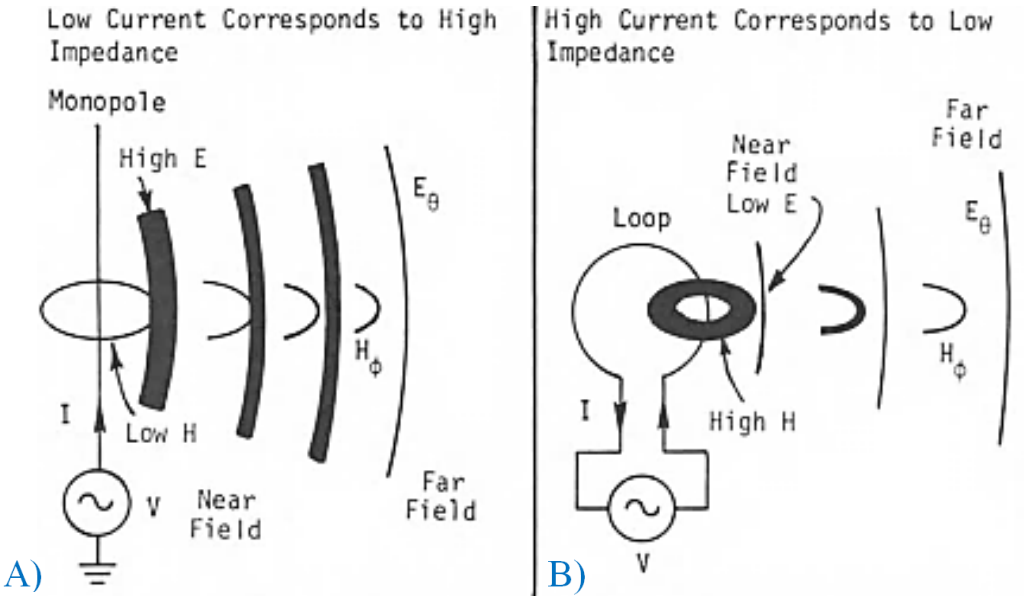

Figure 2-7 Electric and magnetic fields components around (A) The monopole. (B) The loop antenna in the near and far zones [28].

2.4 Practical, "Real-Life", Sources of Radiation.

Through the previous sections, a single piece of wire has been used to represent an infinitesimally small ideal source of electromagnetic energy. If the ends of a straight piece of wire are open circuit, then it is defined as an electric dipole while if the ends of a loop wire are closed circuit then it is considered as a magnetic dipole. In both cases, the value of the wave impedance in the near field region is changing until it reaches the transition region equal to that of the intrinsic impedance of the free space (see Figure 2-6). In many practical circuits, sources are neither purely open wires nor perfect loops, they are circuit configurations in between having source and/or load impedances [26], see Figure 2-8.

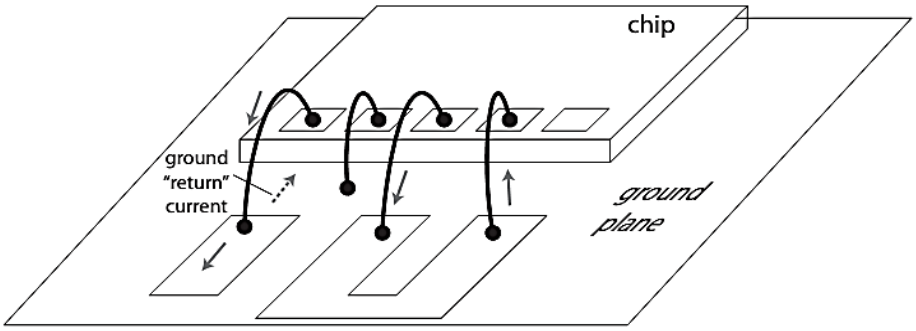

Figure 2-8 Practical circuit example, a chip has source and/or load impedances [29].

Real circuit configurations usually consist of a source combined with its internal impedance Z_G, a load Z_L impedance and galvanic connections between them (wires), see Figure 2-9 (A). The sum of these impedance represents the total circuit impedance Z_C.

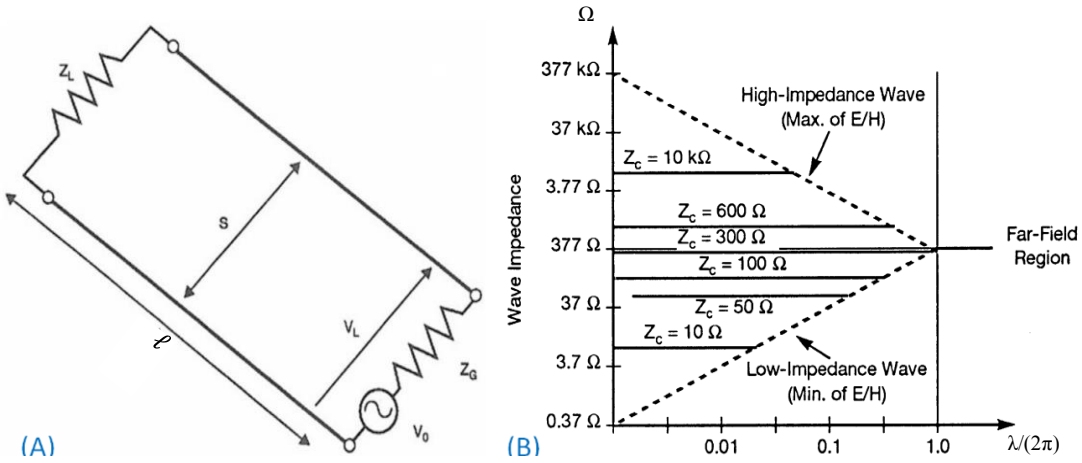

Figure 2-9 (A)Real circuit configuration [26]. (B) Wave impedance vs. circuit impedance in the near field region [26].

The area occupied by this circuit is $\ell \times s$ and its total circuit impedance $Z_C = Z_G + Z_L$. Figure 2-9 (B) illustrates the strong dependency of Z_w on Z_C in the near field region (see also 2.3.5). Z_w is controlled by Z_C and is in between a perfect magnetic dipole creating low Z_w and a pure electric dipole that produces high Z_w.

As a result, this circuit area ($\ell \times s$) can be described either by the loop equations or considered as two single wires with a phase shift equal to $2\pi s/\lambda$ between them and use modified loop equations [26]. For the case where Z_C & $Z_w \geq Z_o$, a modified equation, suggested by [26], for the electric field only (assuming the electric field is dominant and $V_o = I_o Z_o$), is given by

$$\mathbf{E} \cong \frac{\ell s V_o}{4\pi r^3} e^{j(\omega t)} \qquad (2\text{-}36)$$

In matched (majority of cases) and short circuit termination of microwave circuits, the values of Z_C & Z_w are usually $< Z_o$. Therefore; the mathematical expressions for the electric and magnetic fields are those given by (2-30) & (2-32) after replacing the ideal loop area with the actual circuit area ($\ell \times s$) thus resulting in its final form:

$$\mathbf{E} \cong -j\, Z_o \frac{\omega \ell s I_o}{4\pi c r^2} e^{j(\omega t)} \tag{2-37}$$

$$\mathbf{H} \cong -\frac{\ell s I_o}{4\pi r^3} e^{j(\omega t)} \tag{2-38}$$

Where $\boldsymbol{c}$ is light speed in free space.

2.5 Sensing Electromagnetic Fields.

The antenna is the device that captures the radiated electromagnetic fields and converts them to voltages and currents. The simplest and oldest form of antennas are those constructed from wires (see Figure 2-10).

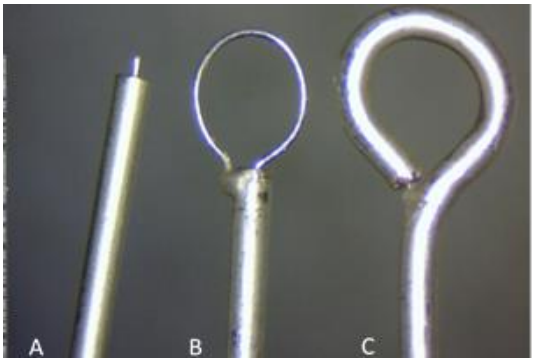

Figure 2-10 (A) Monopole. (B) Unshielded loop. (C) Shielded loop.

The shape and size of wire antennas are important in defining its ability to sense and capture certain electromagnetic field components. The antenna can, depending on its shape, receive either one component of the electromagnetic field (electric field or magnetic field) or receive both components. For example, monopole and dipole antennas are dealing with electric field component only and a shielded loop antenna does the same but with the magnetic field component. While an unshielded loop antenna responds to both components; in general, antennas are frequency selective devices. This selectivity mainly depends on their size [30] or more specifically on the ratio between its largest dimension and the wavelength of the electromagnetic wave (λ). In many antennas, this ratio is a multiple of 0.5λ and thus current passing through the antenna varies along its length, see Figure 2-11.

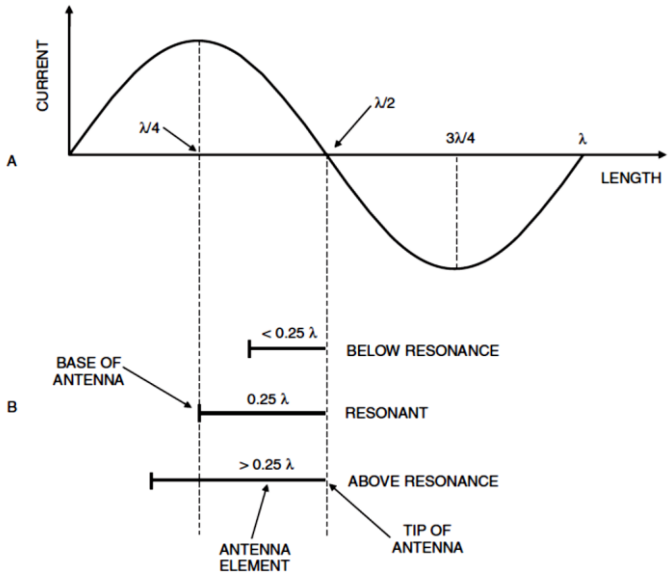

Figure 2-11 (A) Current distribution along the length of a conductor. (B) Current distribution on various length antenna elements [31].

When the overall size becomes an issue in some applications, like cell phones for example, this ratio can drop beyond 0.1λ and this category of antenna called a small antenna [16], [32]. For this case, the current distribution is assumed to be uniform [12], [19], [21]. The main disadvantage of this arrangement is a corresponding reduction in the gain of the antenna. Other applications for small antennas, especially the monopole antennas and the shielded loop antennas, are the electromagnetic probes. To design and implement a very high-resolution electric or magnetic field probe, this ratio might be reduced to the range of 0.0003λ (as will be seen in chapter four). Current variation along this very small antenna can be considered to be constant [16], [33]. A supplementary advantage of this ratio reduction is that this antenna can be treated as lumped elements and thus circuit theory can be applied [16]. Also, the complexity of solving functions of four variables (x,y,z and t), given by the electromagnetic theory can be confidently avoided [34].

2.6 Probe Coupling to the Electromagnetic Sources.

Coupling is the mechanism in which the electromagnetic signals transfer through from the source to the destination. Generally, the coupling can be either direct or indirect. By direct, we mean the direct metallic connection between source and destination. This sort of coupling is adopted in direct voltage and current measurements. The indirect coupling is also divided into two categories, radiative coupling and the reactive coupling. Radiative coupling is seen in the far field region and it is the fundamental application of antennas.

Reactive coupling is usually found around and between adjacent devices and it could be either capacitive, inductive or both, see Figure 2-12.

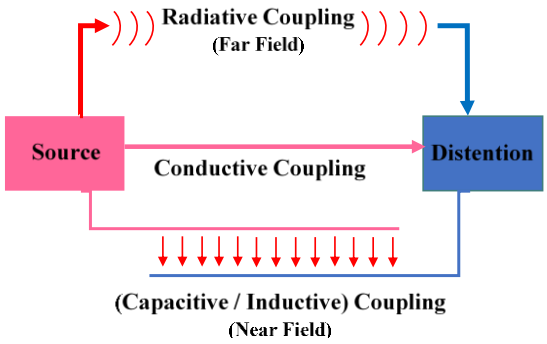

Figure 2-12 Electromagnetic energy Coupling Mechanisms.

Both radiative and conductive coupling mechanisms are well known in many measurements applications and thus, they are out of the scope of this work. In fact, the aim here is to introduce the advantages and disadvantages of using the reactive coupling mechanism as an alternative to voltage and current measurement techniques.

2.7 Reactive Coupling Mechanisms.

In contactless measurements, it is essential to locate the measurement probe very close to the DUT (source) to ensure adequate sensing of its voltage and/or current (see chapter four and five). From the details presented in section 2.3.5, the electromagnetic fields in the very near field region are entirely reactive, which means that any probe located there is almost not exposed to any radiated field. Instead of that, the probe sensing process in this environment is strongly biased on the reactive coupling mechanism. Selecting which type of reactive coupling the probe is capable of responding to depends entirely on its physical characteristics.

2.7.1 Capacitively Coupled Probe.

The probe and the source of electromagnetic energy are called capacitively coupled if the probe can recognize and capture the electric field only. Open end coaxial cables have been used widely as voltage probes due to their ability to only respond to the electric field component [15]. A small part of the outer shield is removed to allow the inner conductor to function as a miniaturized monopole antenna. Usually the length ℓ_p of this part is $\ll \lambda$ and thus the rules of circuit theory can be applied to model the transfer function of this type of probe. The level of coupling between this part of the inner conductor and the source of the field depends on the rate of change of the electric field and the capacitance

between them. From Gauss law (2-3), lines of the electric fields are perpendicular to / from the outer surface of the conductor [35]. However, at any point away from the conductor surface, these lines take the shape of the path between their starting and ending points, see Figure 2-13. Therefore, part of the longitudinal surface-area and the cross-section area of the inner conductor are exposed to the electric fields lines around the source in its near field zone. Summation of these areas A represent the active area of the capacitor C_c coupling the probe and the source.

$$A = \pi d_p \ell_p + \pi(\frac{d_p}{2})^2 \tag{2-39}$$

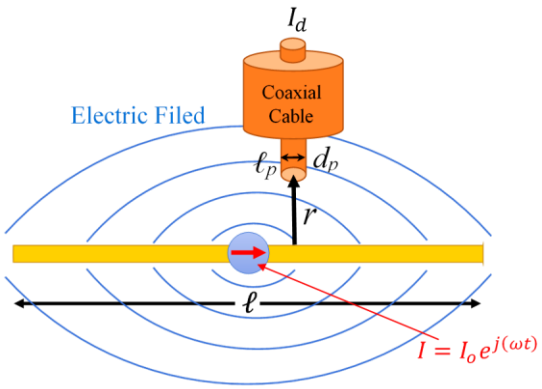

Figure 2-13 Capacitively Coupled Probe.

Thus coupling capacitor is [35]

$$C_c = \varepsilon \frac{A}{r} \tag{2-40}$$

Where, d_p is the diameter of the probe tip (inner conductor of the coaxial cable), ℓ_p is length of the tip and r is distance between the probe and the source.

According to the extension of Ampere's law, in (2-2), those electric flux lines which are crossing the tip of the probe in its active area initiate a displacement current [35] given by,

$$I_d = \frac{\partial \boldsymbol{D}}{\partial t} A = \varepsilon A \frac{\partial \boldsymbol{E}}{\partial t} \tag{2-41}$$

From (2-37) & (2-40), equation (2-41) can be rewritten as

$$I_d = Z_o C_c \frac{\omega^2 \ell s I_o}{4\pi c r} e^{j(\omega t)} = \frac{V_c}{\frac{1}{j\omega C_c}} \tag{2-42}$$

According to (2-42), a capacitively coupled probe can be represented in terms of circuit elements by either a virtual voltage source V_c in series with the coupling capacitor C_c between probe tip and the source or as a virtual current source I_d , see Figure 2-14.

Where V_c is given by

$$V_c = -jZ_o \frac{\omega \ell s I_o}{4\pi c r} e^{j(\omega t)} \tag{2-43}$$

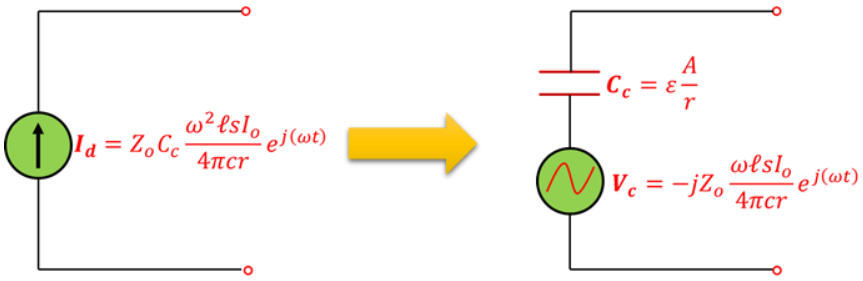

Figure 2-14 The equivalent circuit of the capacitively coupled probe.

2.7.2 Inductively Coupled Probe.

The probe and the source of electromagnetic energy are called inductively coupled if the probe can recognize and capture the magnetic field only. The loop antenna is one of the oldest and simplest forms of this type of probe and it has been wildly used in many applications of current measurement. In such applications, the loop circumference C is chosen to be very small ($C \ll \lambda$) to enhance probe resolution, see chapter five, and thus, the rules of circuit theory can also be applied to model the transfer function of this loop probe. Unlike the open coaxial probe, which has symmetrical geometry, the loop probe response is a function of its orientation with respect to the magnetic field lines crossing it [36] see Figure 2-15.

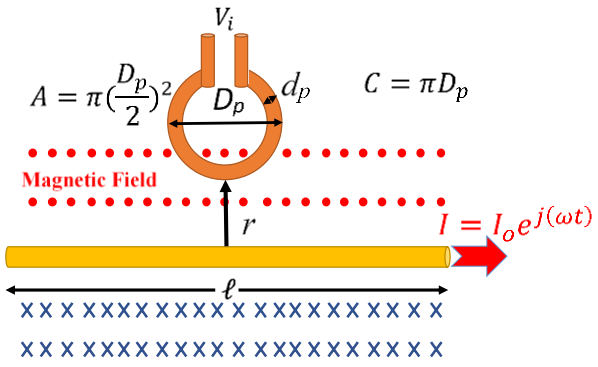

Figure 2-15 Inductively Coupled Probe.

The level of inductive coupling between the loop and the source of the field mainly depends on the rate of change of the magnetic field and the mutual inductance L_m between them. According to Faraday's law in (2-1), magnetic flux lines crossing the plane containing the loop, induces a voltage at its ends [35]

$$V_i = \frac{\partial \mathbf{B}}{\partial t} \cdot \mathbf{A} = \mu \mathbf{A} \cdot \frac{\partial \mathbf{H}}{\partial t} = \mu |\mathbf{A}| \left| \frac{\partial \mathbf{H}}{\partial t} \right| \cos\theta \tag{2-44}$$

Where, $|\mathbf{A}| = A = \pi (D_p/2)^2$ is the area of the loop and θ is the angle between **A** and **B**.

The induced voltage can be expressed in terms of the mutual inductance given by [35]

$$V_i = -\frac{\partial I}{\partial t} L_m \tag{2-45}$$

From (2-38) and (2-45), equation (2-44) can be rewritten as

$$V_i = -j\omega\mu A \frac{\ell s I_o}{4\pi r^3} e^{j(\omega t)} \cos\theta = -j\omega L_m I \tag{2-46}$$

According to (2-46), an inductively coupled probe can be represented in terms of circuit elements by either a virtual current source I in parallel with the coupling inductance L_m between probe and the source or as a virtual voltage source V_i , see Figure 2-16.

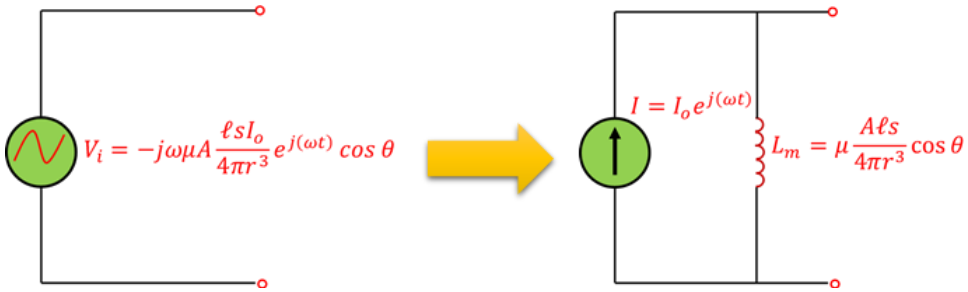

Figure 2-16 The equivalent circuit of the inductively coupled probe.

Where, $I = I_o e^{j(\omega t)}$ is the instantaneous source current and L_m is the mutual inductance that behaves as a high pass network [29] expressed in terms of source and probe dimensions [37]

$$L_m = \mu \frac{A\ell s}{4\pi r^3} \cos\theta \tag{2-47}$$

In principle, the loop probe is just a piece of wire and it is exposed to the electrical flux lines as well, therefore an additional induced voltage is introduced [31], [38]

$$V_i = \frac{2\pi A}{\lambda} \mathbf{E} \cos\theta' \tag{2-48}$$

Where, $2\pi A/\lambda$ represent the effective length of the loop, and $\theta'$is the angle between the electric field lines and the plane of the loop [31], [38].

The presence of the factor $\cos\theta'$ here indicates the dependence of this induced voltage on the orientation of the loop, which is a direct result of its asymmetry. Usually, with a small loop ($C \ll \lambda$) this induced voltage is typically small compared to that induced by the magnetic fields. Thus for many applications, such as antenna magnetic field pattern determination, unshielded loops might provide acceptable results [39].

However, this is not the case for voltage and current measurements. The generation of two induced voltages in the loop simply means it is sensing both voltage and current at the same time with a variable ratio between them depending on the orientation of the loop. Theoretically, if both the loop and the source have perfect symmetry around their axis, then at $\theta = 0$ the loop responds to the magnetic field only and at $\theta' = 0$ the loop responds to the electric field only (where $\theta' = 90 - \theta$). However, in practice neither the loop or the source can easily have such a perfect geometrical symmetry, especially when dimensions go down to the range of a millimetre or even a fraction of a millimetre. The practical outcome of this is a misleading measurement and suggests the need to eliminate this induced voltage due to the electric field or at least significantly attenuate it. By supressing this electric field element, the loop antenna can be used as a viable current probe, retaining its mathematical description and maintaining the validity of the equivalent circuit. The following sections present different methods of e-field suppression.

2.8 Signals and Noise in Contactless Measurement.

For the purposes of this work, the term noise applies to any signal other than the measurement target (be that voltage or current). Obviously, other sources of noise exist e.g. 1/f, thermal, background, etc. However; these are common to all measurement techniques and is beyond the scope of this work. According to this definition, even the source under test itself can produce noise, like the case of current measurement with a bare loop, see section 2.9.2. Of course, the general case is when the noise comes from other sources located close to the source under test. An example of this, is the case of bond wires inside microwave power transistors; where the separation distance between them is in the range of tens of micrometres. Reducing the impact of noise can be ensured by one of two techniques, either by using a barrier to prevent it from reaching to the probe

or by cancelling (or at least significantly attenuating) their effects after it has been captured by the probe.

2.9 Noise Inhibition Techniques.

Undesired electromagnetic fields can be enforced to change their path away from the probe, either by coupling them to the barrier or by repulsion. The first type is widely used in a variety of communication and electronic systems, where the barrier is a real physical material located between the source of noise and the probe. Usually, it is called the shield but to differentiate it from the second type, this work shall refer to it as a "Real Physical Shield". The second type of barrier doesn't have a real physical material between the source of noise and the probe and thus we may call it a "Virtual Shield". Both of them offer a vital safeguard to the probe when the necessary conditions are satisfied.

2.9.1 Real Physical Shield.

As the name suggest, it is an object or barrier, of specific size and shape, inserted between the source and the probe. Materials used for this type of shielding can be categorized into two groups depending on their characteristics. Materials with high permeability, such as ferrite, are commonly used for magnetic shielding only, where it can redirect the magnetic fields to another path. The main limitations of this group of materials are their humble frequency response and the difficulty associated with their miniaturisation. On the other hand, materials that have high conductivity are overwhelmingly used as electromagnetic shields: such as gold, silver, copper and aluminium. It is very rare to find a communication system without a metallic shield. Metallic shielding has three main advantages. It can efficiently work at high frequency, their shielding action can either individually control the electric field or control both fields (electric and magnetic), and finally their ability to be shaped in a miniaturized size. These three features are extremely valuable when designing and implementing contactless current and voltage probes at microwave frequencies. The metallic shield is essential at two different areas within the construction of these probes. The first one, which is common for all probes, is the shield used to protect the output signal of the probe while it is propagating to the sensing instrument. Coaxial cables are the preferred transmission line for this purpose, see Figure 2-13. The second part is needed to solve the problem of magnetic probe field discrimination, see section 2.7.2. Surrounding the bare loop with grounded metallic tube efficiently prevents this interference. If the surrounding tube fully covers the loop without

an opening or a gap then it is electromagnetic shielding (blocking both the electric and magnetic fields), see Figure 2-17 (B). While if the shield is not completely enclosing the loop then the electric field is shielded only [31], see Figure 2-17 (C).

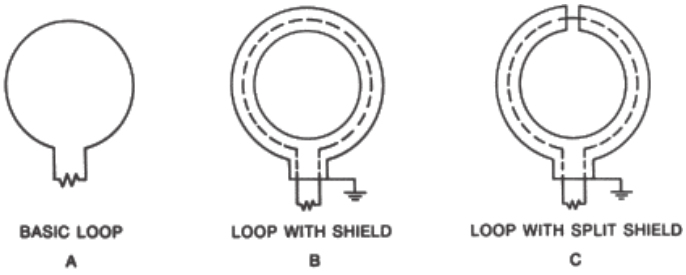

Figure 2-17 (A) Unshielded loop. (B) Shielded loop. (C) Shielded loop with a gap. [31].

2.9.2 Virtual Shield.

The barrier in this context are the field lines themselves rather than any physical object. Unwanted fields are prevented from stimulating the probe by means of a similar type of field (electric or magnetic) emanating from the source under test and because of that it is called a virtual shield. This type of shield can be found in special but important environments such as the bond wires inside microwave power transistors. Inside these transistors, there are many bond wires (sources) carrying currents in the same direction and they are located very close to each other. A repulsion action occurs between field lines (electric and magnetic) surrounding adjacent bond wires (sources), see Figure 2-18. If the dimensions of the probe tip are in a comparable range to those of the bond wires and if it is located close to a specific bond wire, then it will only respond to the voltage or the current of that bond wire. This type of shield is a key factor in defining the contactless probe resolution, see chapter four.

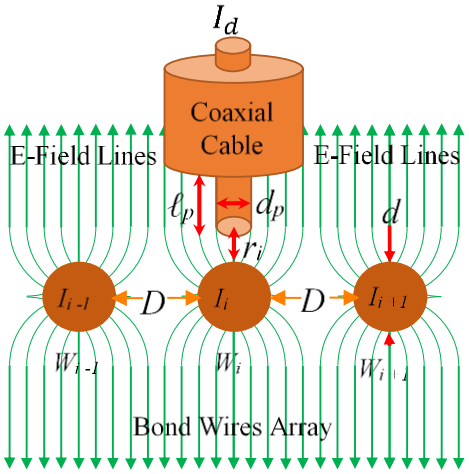

Figure 2-18 Virtual shields around probe tip.

2.10 Near Field Probes Classification

Following a review of research spanning the last 6 decades, electromagnetic field probes can be classified into different ways according to:

2.10.1 Type of Field

Early electromagnetic probes were introduced circa 1960 to measure the electric field (EF) [40] and magnetic field (MF) [41] separately from each other. At that time, the main applications of those probes were in characterizing different types of antennas and defining their coverage area, especially their electric field distribution. Therefore, it is not surprising to find hundreds of publications focussing on electric field only. However, designing and testing complicated electronic circuits demands more information relating to the voltages and currents of these circuits. These requirements present many opportunities for designing advanced probing solutions, where the aim is to measure both the EF and MF simultaneously, at the same position or at least in close proximity [42]–[47].

2.10.2 Number of Field Components

A probe is called Isotropic if it is sensing all the spatial components of the specific field (electric or magnetic) [43], [48], [49], see Figure 2-19. If it is not, then it is called an Anisotropic probe. The majority of the published researches and studies are about Anisotropic probes. Ideally characterizing a single component field can be easily done by measuring one or more of its properties like amplitude, frequency, phase and harmonic structure, but for a complex field like the electromagnetic field, the measurement becomes multi-faceted [50]. Electromagnetic fields consist of six orthogonal components. Three of them compose the electric part [51] and the remainder compose the magnetic part [52]. These components are varying with respect to time and to position as well. Although measuring any two-tangential components allow the calculations for all remaining field components according to the plane wave theory, it is expected that measuring all of them will ensure precise mapping of the total field distribution [53].

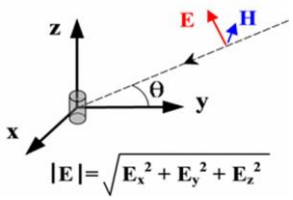

Figure 2-19 Components of Electric and Magnetic Fields [54].

2.10.3 Position of the Probe

The probe can be either located at a fixed position with respect to the source of radiation (stationary probe) or at variable position (movable probe). Movable probes provided the ability for field scanning and mapping over the whole area of measurement [55], see Figure 2-20. These probes are well documented and wildly used. However, their main drawback is the lack of accuracy of the measurement [56]. It is "inherently unrepeatable" [57], and any minor variation in the position of the probe, with respect to the Device Under Test (DUT), provides a different reading. Therefore, they are sometimes called "sniffer" probes [58] as they are more useful for relative measurements rather than the absolute measurements.

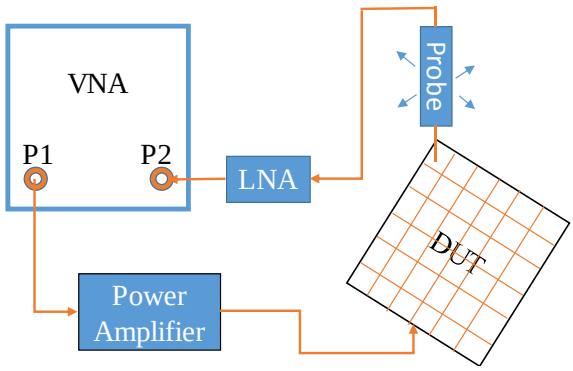

Figure 2-20 Movable probe within practical measurement setup [55].

To perform EMC measurements inside ICs, or any similar inaccessible structure, (where the movement of the probe is not applicable) the embedded stationary probe can present a sensitive and more accurate measurement of voltages and currents at their respective position [53], [59]–[63]. This, of course, limits their ability to generate an overall visualization of the spatial field distribution [64].

2.10.4 Power Requirements (Passive & Active probes).

Passive probes (no power is needed to activate the probe) like passive antennas [41], [52] (monopole, dipole or loop) or dielectric crystals [65]. They are generally simple in comparison with the active probes, but they have more limits on their dynamic range of sensitivity. The output of the passive probes is usually weak signals, especially if their size is small [63], compared with the noise level. This might be a source of error and uncertainty in measurements [66].

Within the last three decades, some studies were done to improve that by adding an amplification unit between the probe and the measurements tool [55], [67], [68]. Inserting

small size amplifier with low noise figures like LNAs (Low Noise Amplifiers) inside the probe and close to the sensing part increase sensitivity, provide insulation and decrease the impact of unwanted stray backup noise [69]. Power supplied to the probe can be either injected via a coaxial cable [70], [71] or transmitting it as a light through a fibre optic cable [72], [73] exploiting the so called "Power Over Fibre" technique [74], [75].

2.10.4.1 Power Over Fibre.

This method of power delivery through light is not a new one but nowadays it is attracting a lot of interest. The rapid developments in the industry of fabricating efficient photovoltaic cells [76] is one important reason for that attraction, see Figure 2-21.

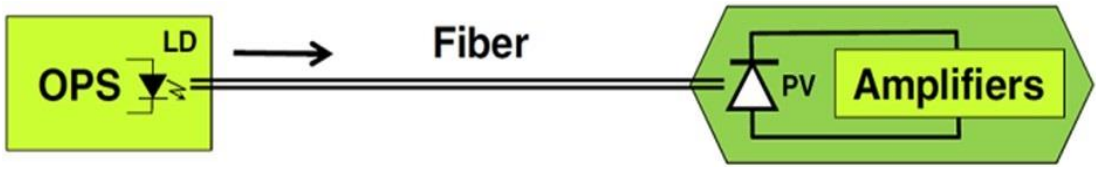

Figure 2-21 Feeding power to an amplifier through fiber [74].

To deliver optical power between two points, three essential parts are required, a transmitter to convert the electric power and emit it as light (high power laser diode, HPLS [77]), a medium allow that light to travel between the two points efficiently (fibre optic cable) and a receiver able to convert received light to electric power again (photovoltaic cell) [78].

2.10.5 Type of Material.

Since the early 1960's and up to now, the requirement for efficient and effective EMF probes is constantly growing. Dielectric, metal and semiconductors materials have been used in fabrication the sensing part of the EMF probes and a simple web search can return hundreds of articles on this subject. In the following sections, the advantages and disadvantages of probes that use a wide range of materials and material-radiation interactions are summarised.

2.10.5.1 Dielectric Probes.

The main part of these probes is a piece of dielectric (generally crystals). These crystals have one or more of their material dependant on an external electromagnetic field. The most popular dielectric materials are those modulate optical polarisation as a function of external electric field.

2.10.5.1.1 Electro-Optic Materials

Those materials that responded to the electric field are called electro-optic modulator EOM materials (Pockels effect). Complete measurement and field mapping systems employing these types of probes are now offered commercially [79]–[82].

The main advantages of these probes are the relatively broad bandwidth 20GHz [83], non-metallic parts and thus the minimal invasiveness [63], [84], [85] on the field under measurements. Another advantage of this type of probe is their compatibility with fibre optic cables [67]. This can significantly eliminate measurement error due to the scattering and disturbance [86] on the field due to the coaxial cable used with other types of probes. Furthermore, using fibre cable allows extending the distance between the probe and the measurements tool to tens of meters, while for coaxial cables, this is just about one meter or less in order to avoid attenuation at high frequency. This is important for measurements in harsh and/or noisy environments.

For decades the EO probes are made from the LiNbO3 crystal and many of them are based on the Mach-Zehnder (MZ) interferometer [87] which provide smaller size and simple construction compared with that shown in Figure 2-22 and also demonstrated in [67]. However, the main disadvantages are the limits on sensitivity [86], [88] (dependant on the size of the crystal), thermal stability [87], [89] and the trade-off between sensitivity and the spatial resolution [63], higher resolution means smaller probes (see Figure 2-22) with lower sensitivity. In addition to that, the MZ interferometer has some issues like the need for biasing voltage and their instability against temperature variation [87].

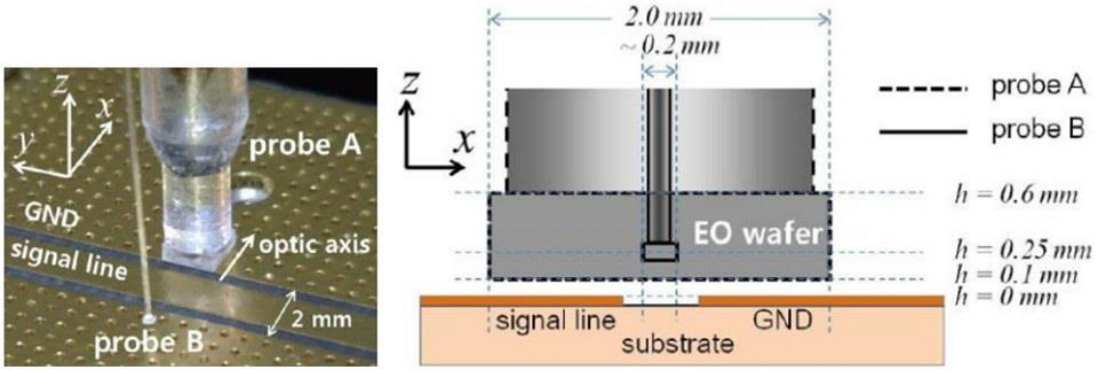

Figure 2-22 Comparison of two sizes of electro-optic probe [84].

Recent work with EO devices shows that polymer infiltrated silicon photonic crystal slot waveguides have EO coefficients of about 735 pm/V (2013) [90] and 1000 pm/V (2014) [91] which are much higher than that of the popular crystal LiNbO3 at 32 pm/V [92].

These devices have been used to demonstrate electromagnetic field probes with EO coefficient of 1000 pm/V giving an estimated minimum detectable electric field amplitude to be 2.5 V/m at 8.4 GHz [93], [94].

2.10.5.1.2 Magneto-Optic Materials

Those materials that responded to the magnetic field are called magneto-optic modulator MOM (Kerr effect). Magnetic field probes made from MO materials have the same advantages as the EO materials (except the bandwidth). Moreover, researchers in Japan [95]–[99] show the possibility of probes having a spatial resolution in the micrometre range.

The magneto-optic materials have the same sensitivity issue as EO materials and in addition to that, a narrower bandwidth and lack of stability are common issues in MO materials.

Efforts to solve these issues shows improvement in bandwidth [100] by using the $(BiG_dY)_3F_{e5}O_{12}$. However, the output level degraded to be very close to the noise floor, see Figure 2-23.

On the other hand stability improvements claimed in [100]–[102] leads to more complex and larger size probe structures. The impact of that is a lower spatial resolution which becomes in the range of millimetre.

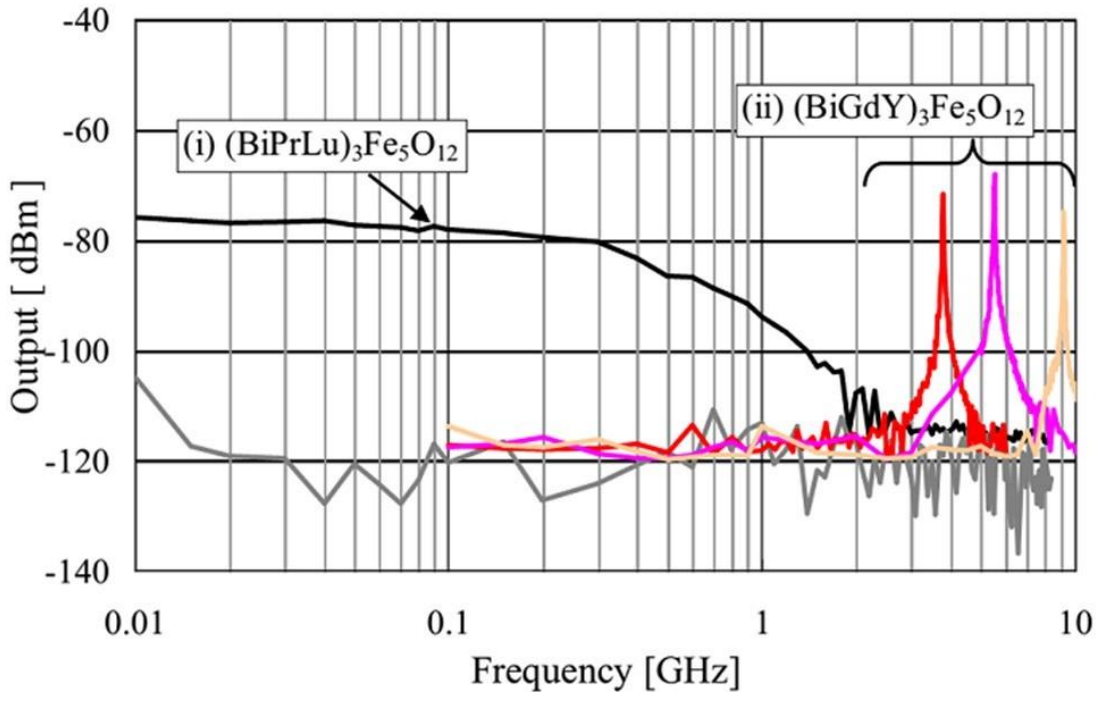

Figure 2-23 Frequency response of two types of magneto-optic materials [100]

2.10.5.2 Metallic Materials.

As the name indicates they are made from metal and they are just different types of antennas, monopole, dipole or loop …etc. used as a sensor to measure the electromagnetic fields. These types of probes are well documented [63] and they have been widely used over the last 5 decades due to their good sensitivity and well defined electrical properties [103]. Because of that, they are sometimes referred to as standard electromagnetic probes [104]. Many types of probes in this classification have been commercially realized with metal [105]–[108]. Different models for magnetic field probing with frequency bandwidth up to 18 GHz and spatial resolution started from 0.25 mm are provided by [109], see Figure 2-24.

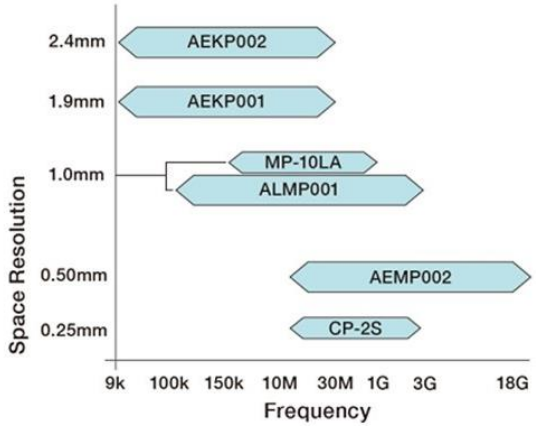

Figure 2-24 Different commercial models for magnetic field probing with frequency bandwidth and spatial resolution started from 0.25mm [60].

These probes are usually designed with an output impedance of 50Ω and come with standard connectors like BNC, SMA… etc. Therefore, they can be connected as a passive probe directly (via coaxial cable) to the measurements tools or to enhance their sensitivity, a standard amplification stage can be added in between.

Miniaturized on-chip metal probes for both electric and magnetic fields are demonstrated for a bandwidth up to 3 GHz in [47], [53], [59], [68]. By (2012) a claim of fabricating probes of 10 GHz bandwidth with 100µm spatial resolution had been presented in [61]. The main advantages of metal probes are the possibility to gather both the high spatial resolution and the high level of sensitivity [68] (unlike the EO probes). The magnetic field can be linearly and broadly (in term of bandwidth) quantified (as easy as it can be done for the electric field) by using the loop antenna. While the available MO materials are still showing limitations on their linearity, sensitivity and the frequency bandwidth

[100]). Furthermore, the fact they are just pieces of metal make their construction simple and low cost [45].

On the other hand, the main disadvantage is related to the fact that they are (and the coaxial cable connected to them) made from metal which disturbs the fields under measurement [69], [84], [86], [100]. One solution to reduce these effects; especially those which come from stray pick up is presented by Roman Kantor [103], [110], [111] the well-known "Kantor Probe". As a practical solution, the passive part of the Kantor probe, which in this study is an open coaxial cable, had been made very small (using non-standard coaxial cable) [103], [111]. This step allows the probe to have a significant gain and good spatial resolution as well. To overcome the degradation in sensitivity due to the size, a miniaturised preamplifier stage is installed inside the probe body, close to the sensing part [69], [103], [110], [111].

Further improvements towards minimizing field disturbance by making the probe floating with respect to the ground are presented in [72], [73], [112] by switching to the optical cable. The metal existed in the coaxial cable (transmission line) is replaced with fibre optic cable. This configuration demands that the power is remotely delivered to the probe via fire cable to feed both the optical transmitter and the pre-amplifier which is used in [72], see Figure 2-25. This maintains the required matching and buffering between the antenna output and input of the optical transmitter. In 2013 a commercial version, with 6 GHz frequency bandwidth, of the electric fields probe (0.15 mV/m – 150 V/m) and magnetic fields probe (0.3 µA/m – 1 A/m @ 2 GHz) gathering all the previous concepts is now available with ISO/IEC certificate [113].

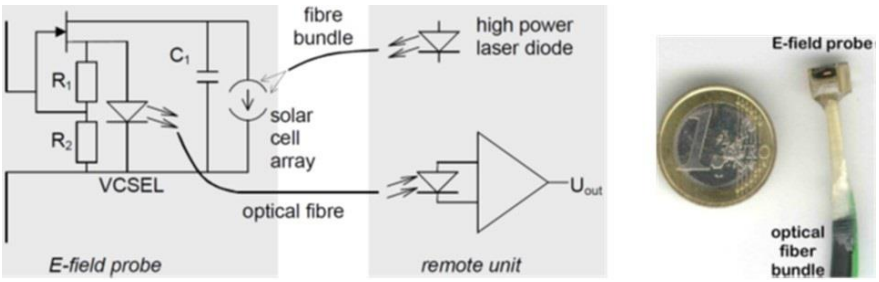

Figure 2-25 Active metallic electric field probe powered and communicate through fiber optic cables [72].

Many of the probes discussed above are movable probes which is essential for field visualization and mapping but for the sake of optimum accuracy, it is not as accurate as the case with the stationary probes discussed in 2.10.3. The problem of the uncertainty

and the lack of repeatability resulting from the change in the position of the probe with respect to the measurement point of interest still exists [56], [57]. A study in 2014 demonstrates the use of a matrix of small loop antenna distributed within the bottom ground plate of the printed circuit board (PCB) [54]. This might become a key solution for this problem in the future, see Figure 2-26.The current frequency bandwidth of this arrangement is up to 1GHz.

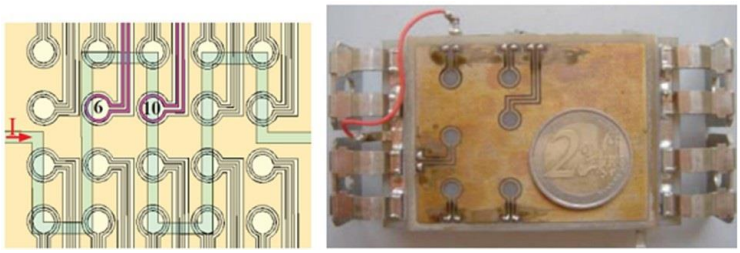

Figure 2-26 A matrix of small loop antenna distributed within the bottom ground plate of the printed circuit board (PCB) [54]**.**

2.11 Probing Inside Microwave Power Transistors

The structure of the microwave power transistor consists of the die (the active part of the transistor), matching devices, transistor leads and bond wires connecting between these parts, see Figure 2-27. Performance optimization of these parts leads to enhancing the gain, linearity and RF power efficiency [114]. The first step toward that is to scan these parts with a suitable probing mechanism to quantify their voltages and currents.

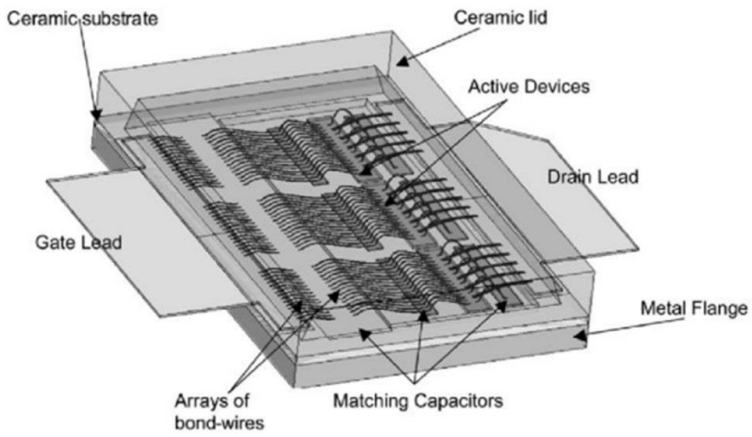

Figure 2-27 Microwave power transistor structure [115].

Selecting which type of probe is appropriate depends mainly on the mechanical and electrical properties of the DUT. Many types of probes had been reviewed in 2.10, however, a few options are applicable to microwave power transistor. For example, the

possibility of scanning only the top of the microwave power transistor limits the options to anisotropic probes.

The actual dimensions of the individual cells inside the die and bond wires are in the micrometre range. This range suggests the essential need of a miniaturized movable electric and magnetic probes to swiftly move and pick up the individual electromagnetic fields emissions inside the package of the transistor. Overcoming sensitivity degradation (due to the miniaturization) necessitate the use of the active probe versions.

In addition to the issues relating to probe dimensions, the probing process needs carefully consider the following parameters as well:

- High spatial resolution.
- Noise immunity (shielding).
- Bandwidth.
- Sensitivity.

According to these conditions and restrictions imposed by the mechanical and electrical properties of the microwave power transistor, metallic probes have an advantage because they are more likely able to satisfy all the above requirements.

Through this work, the most important parameter is the spatial resolution of the probe and thus it will be highlighted more than the remaining parameters.

2.12 High Spatial Resolution Probes

A common definition for the meaning and the limits of the expression “Spatial Resolution” is not present yet, since it is not dependant on the properties of the probe alone but it is mainly effected by the DUT as well [103], [116]. In many publications, it is quite possible to find similar claims being made for ‘record spatial resolution’ despite using different methods and devices under test used to quantify it.

It is important at this point to understand these methods and try to create some valid rules upon which reasonable comparisons and accurate quantification are achieved.

2.12.1 Track / Gap Width Spatial Resolution Definition

In this case, the DUT allows only one path for the electromagnetic energy to propagate to the load. This path is either a continuous microstrip line or multiple strips separated with gaps between them. For the first case, the spatial resolution is defined by the width of the track and the smallest width recognized by the probe is its highest spatial resolution

[117]–[119]. In the second case, the highest spatial resolution is defined by the smallest gap width the probe is able to recognize [120]–[122].

In this definition, the edges of the smallest width (a track or a gap) recognized by the probe are used to set the limit of the maximum spatial resolution. In spite of the fact that this does not accurately reflect the limits of the spatial resolution there are still recent publications that use this definition [123], [124]. Note that an infinitesimally small source of radiation would be measurable rendering this definition meaningless.

2.12.2 Multiple Parallel Sources Spatial Resolution Definition

In limited size environments crowded with electromagnetic sources (e.g. microwave power transistor), four factors are influencing the ability of the probe to differentiate between them. The first one is the relative size (usually the cross section of the monopole or the diameter of the loop antenna) of the probe tip with respect to the size of radiation sources (w). The second one is the distance between adjacent sources (g). Where (w) here represents the boundary of the individual source of the field while (g) is the opposite. The third factor is length (protrusion) of the probe tip (ℓ_p). It has been found that the required spatial resolution (R) will not exceed the value of this length [110].

$$R \leq \ell_p \tag{2-49}$$

The last factor is the distance between the probe tip and radiation source. The spatial resolution is inversely proportional to this factor. More details are discussed in chapter four and five.

Moving the probe perpendicular to a set of adjacent sources is a common procedure to test probe spatial resolution. Test fixtures that allow parallel paths for the electromagnetic energy are widely used by many researchers.

These test fixtures can be either PCB surface capacitor [103], [110], [111], [125], [126] (see Figure 2-28(A)), PCB surface meander line [51], [127]–[129] (see Figure 2-28(B)) or an array of PCB tracks (see Figure 2-28(D)) or wires that share the same input and output ports (see Figure 2-28(C)) [71], [130].

However, the predominant among these papers is the consideration of the width of the source finger/track as the spatial resolution without highlighting the impacts of the gaps between adjacent sources. While a few other publications [69], [71], [130] reported the width of the gap as a measure of the probes spatial resolution.

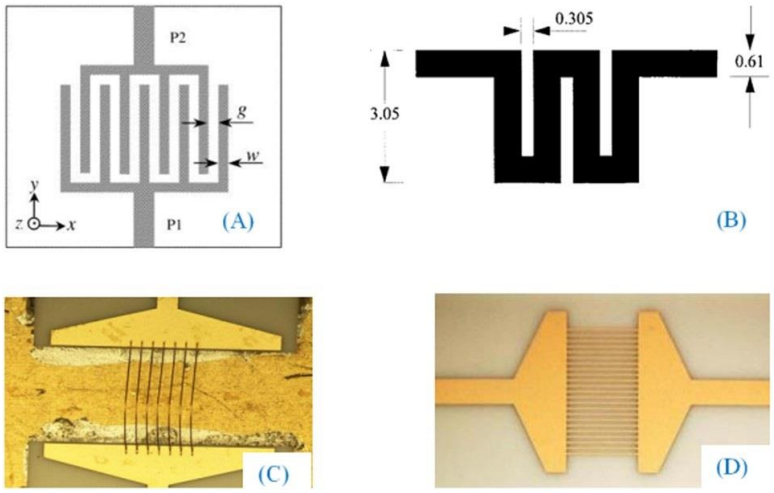

Figure 2-28 Deferent types of test fixtures used to determine probe spatial resolution. (A) PCB capacitor [103]. (B) PCB meander line [51]. (C) Wires array [71]. (D) PCB tracks array [130].

In 2015 an interesting definition introduced in [131], where the spatial resolution is given as the average of w and g

$$R_{wg} = (w + g)/2 \qquad (2\text{-}50)$$

Although this definition initially considered the case of the magnetic fields surrounding two wires carrying current in opposite directions, it can be generalized to cover the electric field as well due to the duality and similarity of electromagnetic fields behaviours (attraction between sources of opposite charges / currents and repulsion between sources of similar charges / currents).

In the next literature review, equation (2-50) will be applied, whenever it is possible, as a general definition of the spatial resolution. This will permit more rational comparison between the variation in the claimed spatial resolutions.

2.13 Literature Review

This literature review is limited to the metallic movable passive/active anisotropic voltage and current probes that claim to have a spatial resolution less than 1mm.The comparison will be based on:

- The spatial resolution.
- Size and length of the probe tip and distance to the DUT.
- Type and size of the DUT.
- Other parameters of the probe as they were referred to.

2.14 High Spatial Resolution Voltage Probes

2.14.1 Voltage Probing Using Stander Open End Coaxial Cable

In 1997, a research group in Germany, led by Ingo Wolff, demonstrate in [125] their voltage probe with spatial resolution = 100 µm. The structure was very simple just the usual open-end coaxial cable serving as a passive voltage probe. They had used standard semi-rigid 50 Ω coaxial cables (OD = 508 µm, ID = 112 µm and tip length = 300 µm) to scan at 7 GHz the surface of five fingers interdigital capacitor to examine the probe spatial resolution, see Figure 2-29(A).

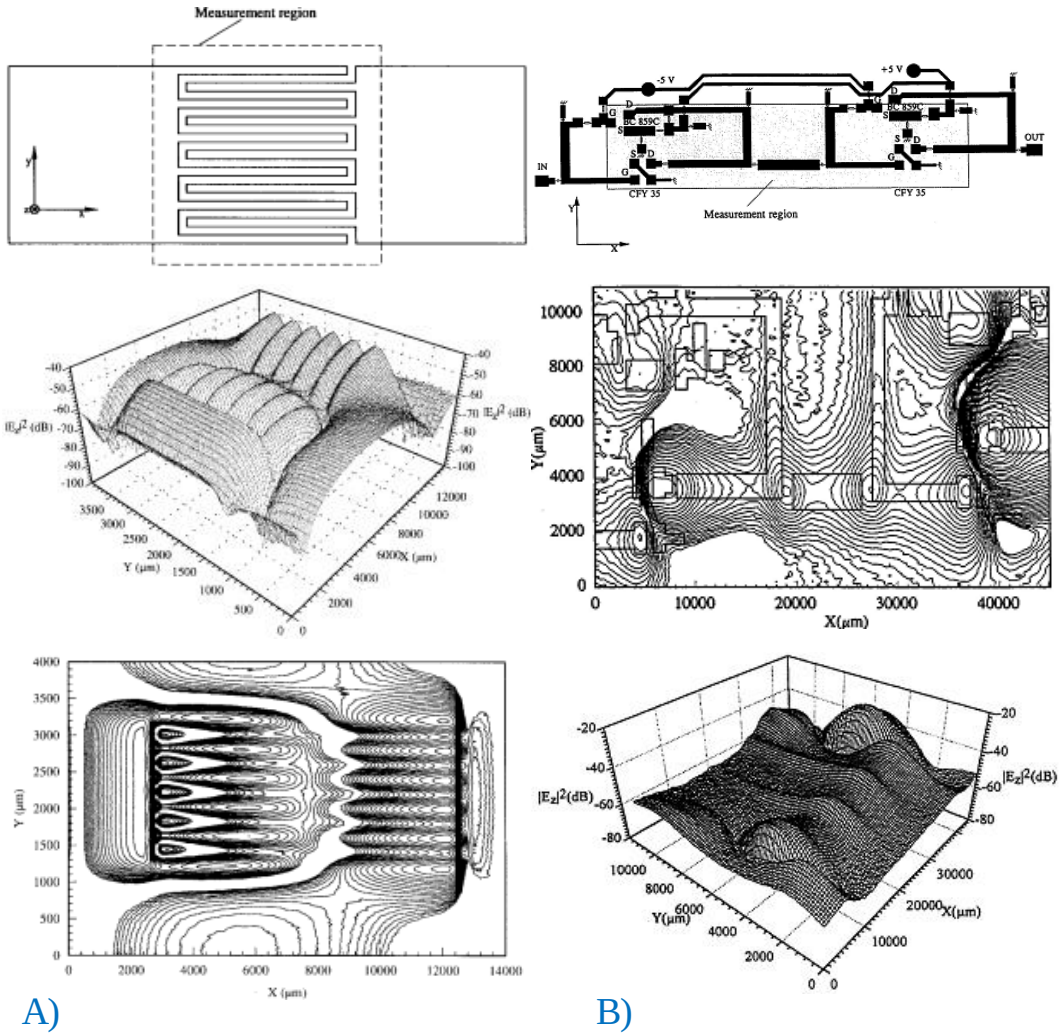

Figure 2-29 (A) Electrical field distribution for the five fingers integrated capacitor [126]. (B) Electrical field distribution for a 2.46 GHz amplifier [132].

The finger width was 100 µm and the total gap width was 300 µm. According to (2-50) the spatial resolution is 200 µm which it is twice the value announced. The total bandwidth is that of the coaxial cable (around 20 GHz).

The calibrated version of this probe demonstrated a sensitivity = 0.5 dBm at 1 GHz [126]. The minimum probe height above the test fixture was 20 µm. However, trials to scan the surface of two different amplifiers [51], [127], [132] at 100 µm height and at 2.4 GHz showed humble clarity (for such a relatively large amplifier (45 x 11 mm^2)). Two reasons were behind that: the large distance from the surface of the amplifier and the long length of the probe tip (300 µm) which allow the probe to couple to a relatively large area under it, see Figure 2-29(B).

Detailed characterization and comparisons between the theoretical (HFSS simulation) and the experimental results achieved in [120]–[122], [133], but without any improvement in the spatial resolution. Further characterization recently published (2016) focused on the calibration and the absolute voltage measurements (1-5 GHz) claimed to reduce the error from 8% to 5% [134].

2.14.2 Position Signal Differences Probing Technique

In 2003, Roman Kantor introduced two kinds of modification to enhance the spatial resolution of the electric field probe to more than twice that announced in 1997. These modifications are:

2.14.2.1 Miniaturized Non-Standard Coaxial Cable

In this miniaturized coaxial cable, the insulator was air, the outer and the inner conductor's diameters were 230 µm and 8 µm respectively. Within the body of the probe, a preamplifier is inserted to enhance the overall sensitivity, see Figure 2-30(A).

A PCB surface capacitor of four fingers of w = 40 µm width and g = 60 µm gap used as a source of radiation. Applying (2-50) on these figures results in a spatial resolution = 100 µm. In this part, Kantor demonstrates the effects of the inner conductor protrusion on the spatial resolution of the probe. Therefore, to gain higher spatial resolution the length of protrusion should be [103], [110], [111]:

- Equal or less than the desired spatial resolution.
- Equal or less than the diameter of the outer conductor.
- Much smaller than one-tenth of the operating wavelength.

2.14.2.2 Modulating the Vertical Position of the Probe

To avoid the difficulties of fabricating a voltage probe with extremely short protrusions, Kantor suggested the Position / Signal Differences (PSD) as a solution. Instead of making the protrusion ultra-short, he increased it to be in the range of 0.3-1 mm.

In this technique, the DUT is scanned twice at two different heights [103], [110], [111], see Figure 2-30(B). The differences between the results of these scans at each point are the final amplitude, see Figure 2-30(C), and phase Figure 2-30(D).

Another test fixture used in [111] with a track width = 20 µm and a gap width = 40 µm, from which the spatial resolution was reported to be 20 µm while according (2-50) to it is 30 µm

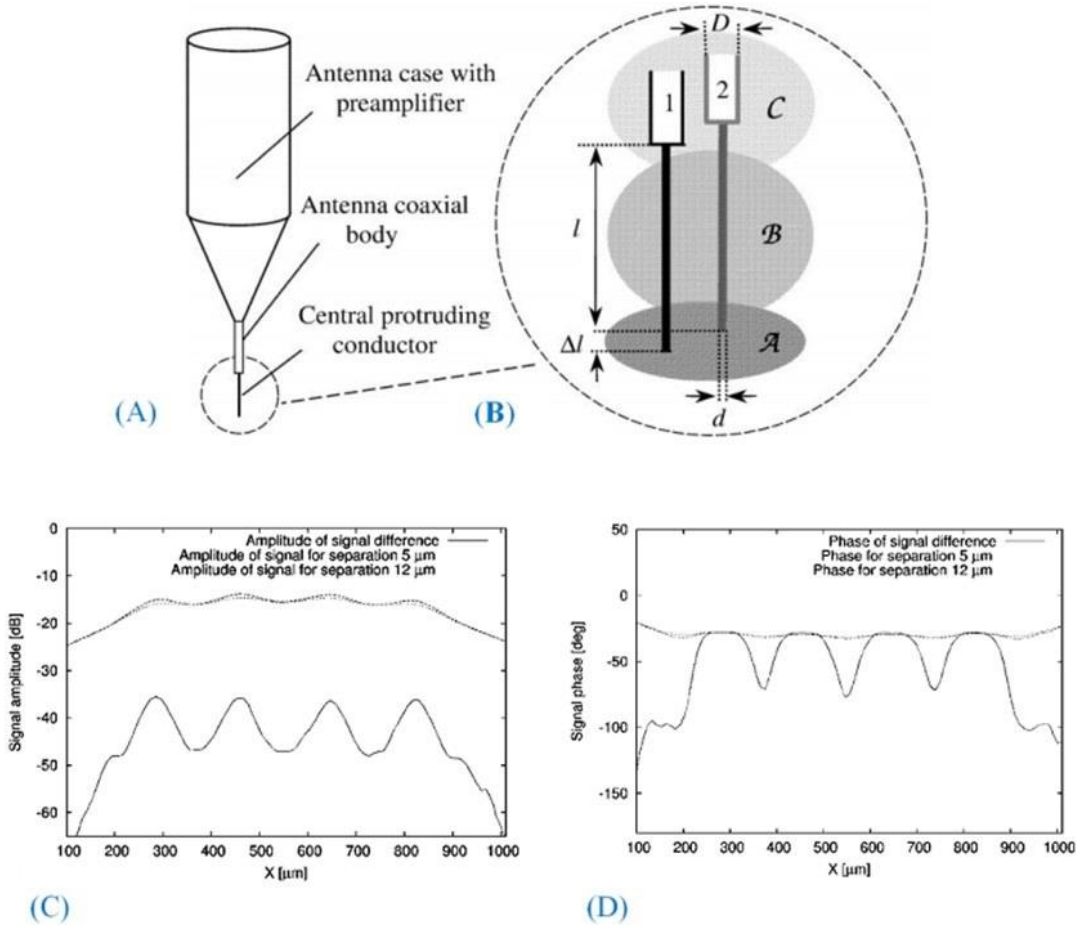

Figure 2-30 (A) Structure of the voltage probe. (B) Central protruding conductor. The two positions of the antenna corresponding to different heights above the surface of the device-under-test are indicated by 1 and 2. (C) Amplitude of the signal at 5 µm & 12 µm and the differences between them. (D) The phase of the signal at 5 µm & 12 µm and the differences between them [110].

The main advantage offered by the PSD technique is the flexibility in adjusting the protrusion while having the same spatial resolution of the same probe but with a very short protrusion.

This normally occurs once for each probe when it has been fabricated. However, this outcome will consume double scanning time and some mathematical calculations for all points of measurement at each measurement iteration.

Moreover, Kantor in [103] stated that "The PSD technique works well only with high gradient fields." This is due to the fact that the PCB capacitor test fixture had been terminated to ground at one terminal while exciting it with RF power at its resonance frequency at the other terminal.

2.14.3 Standard Open End Coaxial Cable with Micro Hole Aperture

In 2011, a modified version of the voltage probe, constructed from the standard open-end coaxial cable, was published by a research group from Japan. In this paper [129], they used relatively large size standard semi-rigid 50 Ω coaxial cables (OD = 2200 µm, ID = 510 µm and tip protrusion = 0 µm).

The end of the coaxial cable covered with conductive chip cap of 15 µm thickness. This chip is electrically connected to the outer shield of the coaxial cable for grounding purpose and had a through-hole width and length of 50 µm and 500 µm respectively. A 60 µm thickness insulating film had been used to prevent touching the inner conductor, see Figure 2-31(A).

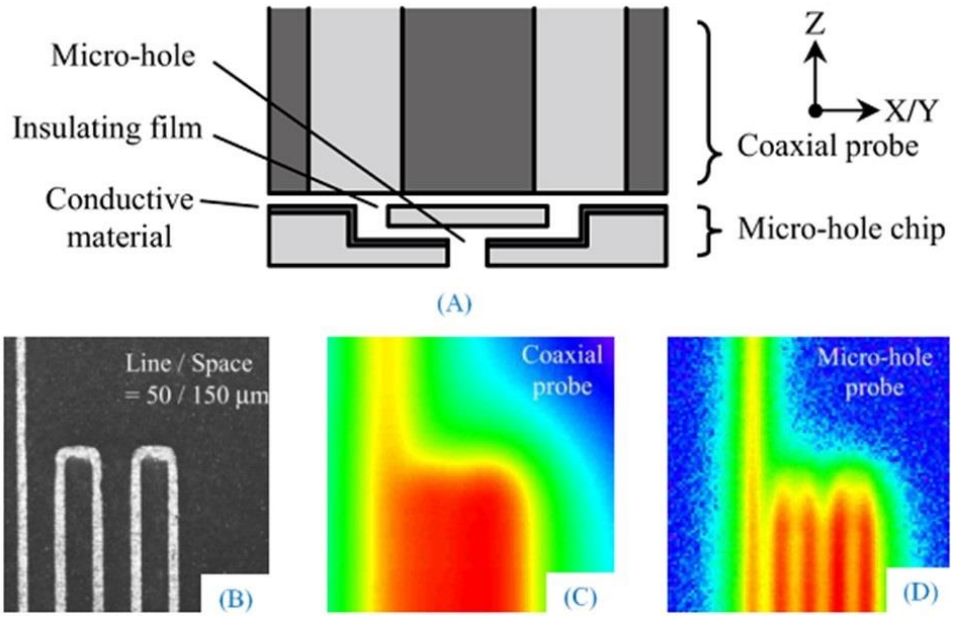

Figure 2-31 (A) Structure of the Micro Hole Aperture voltage probe. (B) PCB meander line test fixture of five fingers. (C) Spatial resolution of the open end coaxial cable without cap and has a protrusion. (D) Spatial resolution of the open end coaxial cable with protrusion = 0 µm and a conductive cap of 50 µm x 500 µm hole [129]

For this probe, the bandwidth was 10 GHz and the spatial resolution examined with a PCB meander line test fixture of five fingers of 5 µm track width and 150 µm gap width, see Figure 2-31(B). The announced spatial resolution was 72 µm while its value according to (2-50) is 100 µm, see Figure 2-31(C) and (D).

The good thing about this arrangement is the noticeable enhancement in the spatial resolution of a relatively large dimension' coaxial cable, where its inner conductor cross section area is 204282 μm^2. But on the other side, it has its own disadvantages which cannot be overlooked.

The large overall metallic cross section area (9 mm^2, this is equal or larger than the die area of many microwave transistors) is one issue. This does not only make this voltage probe unsuitable to smaller areas but also it can change markedly the field distributions in and around the DUT.

The other disadvantages here is the fact that the probe sensitivity is impeded within this arrangement. Sensitivity, as explained earlier in this chapter, is proportional to the length of the protrusion and inversely proportional to the height from DUT.

The micro hole technique required the protrusion to be zero and added a fixed separation from the DUT = 75 µm which mean less sensitivity. The Japanese team highlighted this drawback and tried to reduce its impact by changing the hole from a circle of 100 µm diameter to a rectangular hole of width = 50 µm and length = 500 µm. However, the rectangular aperture makes the probe response sensitive to its orientation, i.e. becoming anisotropic.

2.14.4 Voltage Probing Inside an Active Microwave Transistor

In 2010, Steve Cripps et al. reported an initial trial of voltage probing inside active power transistors [69]. The probe was constructed from a piece of 100 µm diameter wire passing through a glass tube with conductive paint on its outer surface to form an open end coaxial cable, see Figure 2-32.

This miniaturized coaxial cable is directly connected to the gate of a PHEMT transistor, preamplifier, (unlike Kantor design [110] where a passive matching circuit inserted in between which enhance the probe sensitive over a specific bandwidth only).

This preamplifier enhanced sensitivity and provided additional isolation against stray pickup as well [69]. The drain bond wires of two different GaAs PHEMT power

transistors, (10 W and 20 W respectively) were scanned by this probe and results observed at 2 GHz.

The bandwidth for this probe is limited by that of the PHEMT transistor at 4 GHz. A brass ferrule was added to encapsulate the preamplifier in [71]. The reported spatial resolution of the new probe was 100 µm tested above a set of bond wires.

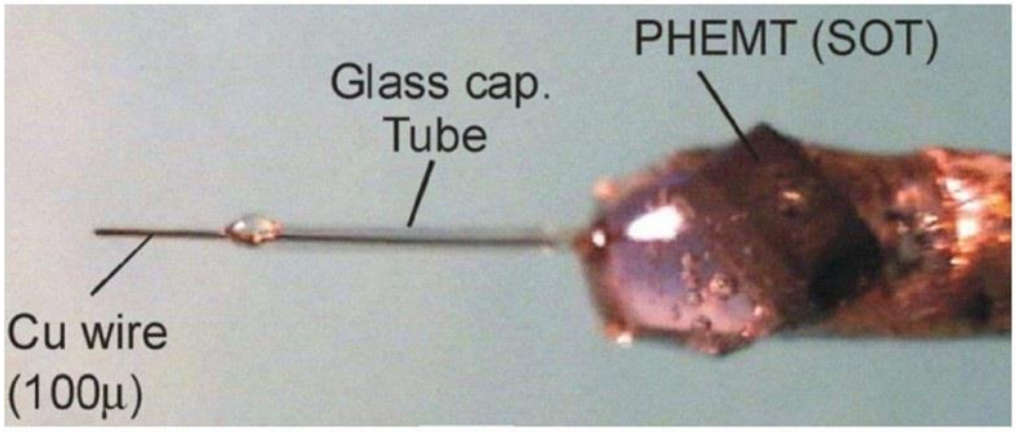

Figure 2-32 Electric field probe made of small open-end coaxial cable followed by a preamplifier [69].

In 2013 and 2015 Cripps and his group in Cardiff University, reported a modified and enhanced performance voltage probes [130], [135]. They solved the lack of shielding resulting from the usage of the conductive paint by using a Copper tube of 250 µm diameter, see Figure 2-33(A). Probe bandwidth raised to 6 GHz by replacing the PHEMT transistor with a MMIC preamplifier.

To enhance the spatial resolution of the probe, the protrusion was reduced to 25 µm. Demonstration of this improvement was achieved by using a well-defined test fixture of multiple parallel tracks of 25 µm width and 100 µm separation, see Figure 2-28(D). The reported spatial resolution was better than 100 µm while according to (2-50) it is 62.5 µm.

The improved voltage probe used to scan a 50 W LDMOS Doherty power amplifier at 2 GHZ. The ceramic lid removed to allow probe movements inside the LDMOS transistor, see Figure 2-33(B). Figure 2-33(C & D) shows the bond wires of gate region and the corresponding probe scan results respectively. The probe was able to recognize voltage differences between adjacent bond wires and locates the position of the deformity as well.

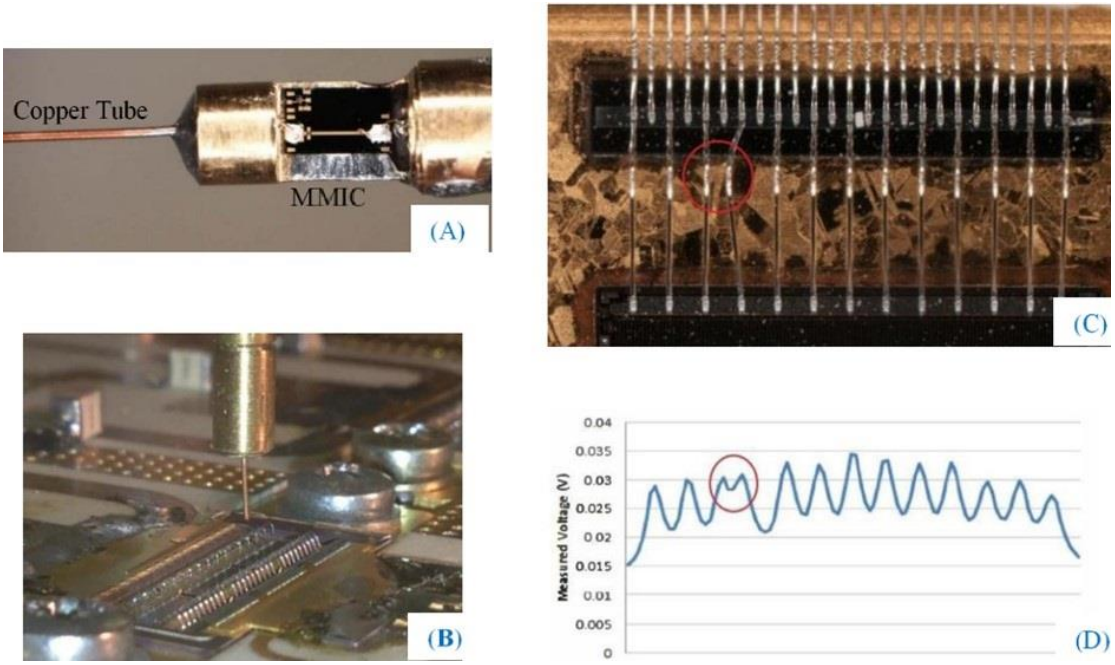

Figure 2-33 (A) Improved voltage probe made from copper and use a MMIC as a preamplifier [130]. (B) Voltage probe while scanning LDMOS power transistor [135]. (C) The gate region of the LDMOS transistor and the red circle around the deformity of two bond wires [130]. (D) Probe output after scanning the gate region of the LDMOS transistor depict the ability to recognize the deformity of two bond wires [130].

In 2012 a research group in Delft University reported the possibility to estimate the S-parameters of bond wires embedded in high power microwave devices [133]. This estimation based on the measurement of the electric field and a numerical reference module of the bond wires.

The probe made from a standard semi-rigid 50 Ω coaxial cable (OD = 800 µm, ID = 200 µm and tip length = 1000 µm) to scan an array of 33 bond wires (Diameter = 25 µm, Gap = 300 µm) at frequency range 1-5 GHz. By Appling (2-50) on theses dimensions, the spatial resolution is 162.5 µm. In this work, the aim was testing this technique rather than improving the spatial resolution.

Delft group reported in-situ characterization (based on electric field measurements only) of large LDMOS Doherty amplifier in [136], [137]. A smaller semi-rigid coaxial cable (OD = 500 µm, ID = 100 µm and tip length = 300 µm) used to enhance resolution. The drain bond wires of two different power rating LDMOS power transistors (100 W and 200 W) scanned at 500 µm above the bond wires.

This measurement was repeated at different levels of output power at 2.14 GHz. The smaller one has one die only and its scan results, amplitude and phase, are shown in Figure 2-34(A) while the larger one has two dies and their amplitude and phase results are shown in Figure 2-34(B).

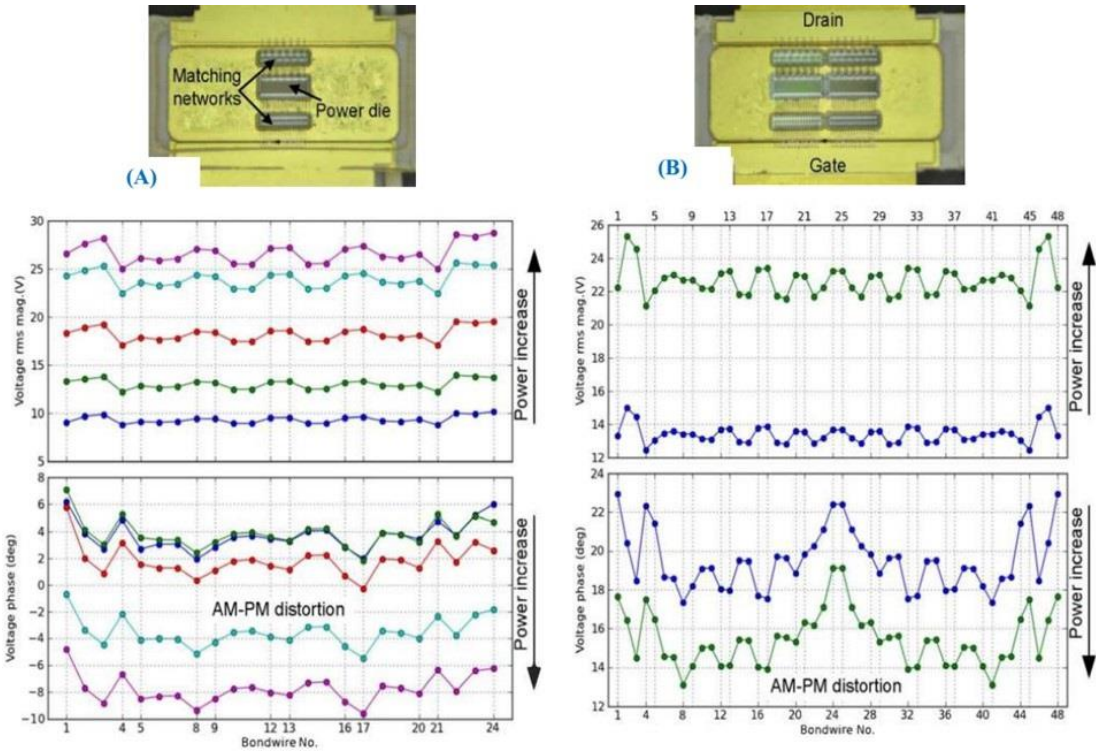

Figure 2-34 LDMOS power transistor output voltages (magnitude and phase) distribution at drain bond wires. (A) One die 100 W (B) Two dies 200 W [137]**.**

Examination of the results of both cases indicates that probe was far from capable of recognizing any of the nulls laying between any adjacent bond wires which reflects a modest spatial resolution. However, one cannot expect more than that from a standard coaxial cable with protrusion = 300 µm and positioned at 500 µm above the DUT.

In November 2016, a modified probe reported by Delft group with a 70 µm spatial resolution [138]. Three things lead to this spatial resolution enhancement:

- Miniaturizing the diameter of the probe tip to 10 µm, see Figure 2-35(A).
- Applying the PSD technique.
- Decreasing the spacing above the DUT to be within the range 15-65 µm.

Figure 2-35(B) illustrate the electric field variation along the die surface (Drain source fingers width are 70 µm) of 100 W power transistor after applying the PSD technique. The differences between scans results at 15 µm and 65 µm introduced a sharp

visualization of the maxima at the die fingers and the minima between those adjacent fingers.

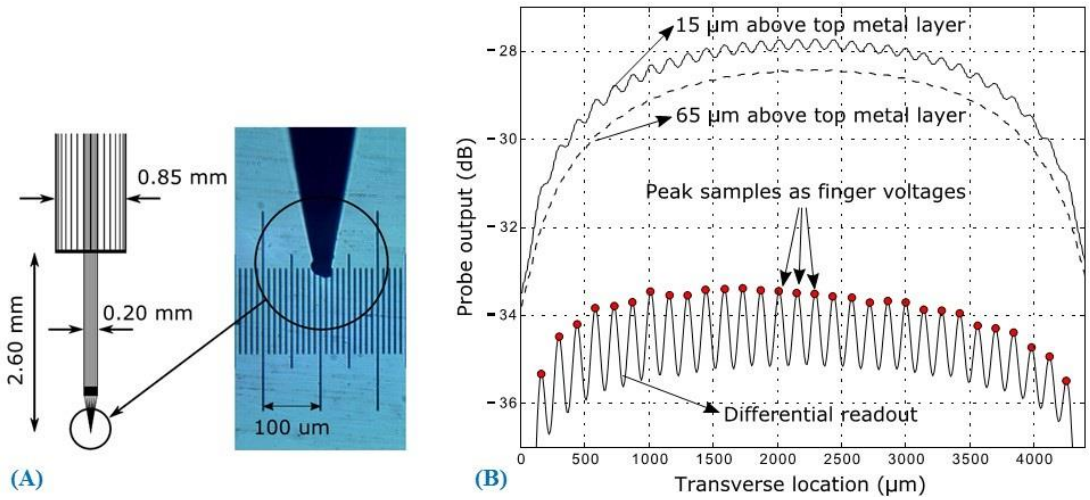

Figure 2-35 (A) Probe dimension details (standard open -end coaxial cable). (B) 100 W die scanned at two different heights with sharp visualizition of the maxima and the minima across the die surface [138].

2.15 High Spatial Resolution Current Probes

The magnetic field can be quantified either directly by using loop antenna or indirectly by quantifying the electric field by using a voltage probe and using its data to numerically estimate the magnetic field.

However, the vast majority of what has been published has been about the direct method of measuring the current as it is more realistic.

2.15.1 Direct Current Measurement

In the direct method of measurement, the loop antenna is the essential sensing part of the current probe. Unlike the monopole antenna used for voltage probing, which is only responding to the electric field, the loop antenna is responding to the magnetic and the electric field. The ratio between them depends on its symmetry and its relative orientation with respect to the DUT.

We will call this ratio the Electric Field Rejection Ratio EFRR. It is the electromagnetic field version of the Common Mode Rejection Ratio CMRR equation used in circuit applications.

In terms of loop parameters, it is given by (with reservation[2]) [139]

$$EFRR = \frac{V_{OH}}{V_{OE}} \tag{2-51}$$

$$EFRR \approx \frac{c}{4\pi bf} \tag{2-52}$$

Where, V_{OH} is the loop voltage in response to the magnetic field, V_{OE} is the loop voltage in response to the electric field, b is the loop diameter, f is the operating frequency and c is the speed of light. From which it can be estimated that the smaller the loop, the better EFRR results.

The EFRR ratio is one method among two that can be used to define the quality of the current probe. While the EFRR depends only on the data collected by the current probe itself (no external reference) the second method is more accurate as combines the data coming from an external voltage probe.

In the second method, the standing magnetic and electric field waves above a microstrip line are observed with a current and a voltage probe respectively. In the ideal case, the maxima and the minima of the standing magnetic wave are located at the minima and the maxima of the standing electric wave respectively (for more details refer to chapter three and five). Therefore, any deviation between these minima and maxima of these standing waves is considered as an indication of current measurement fidelity. This deviation will reflect how much electric field is absorbed by the current probe.

2.15.1.1 Methods of Improving the EFRR

There are two ways that can be used to totally or partially neutralise the impact of the electric field from the response of the current probe. The first improvement is obtained by preventing it from entering the probe. This means putting a barrier between them; commonly referred to as loop shielding. The other way is to cancel the effect after receiving it by either using a differential amplifier and/or a BALUN. Without doubt, prevention is much better than cure. However, it is not always possible to apply the appropriate shielding around the loop.

[2] In the reference [139] the equation (2-51) is given for near field measurements while its originally given in [217] and driven for far field measurements (E/H = 377Ω). However, we list it here for indication purpose only.

For similar reasons to what have been discussed earlier in this chapter, and in addition to the discussion above, this loop antenna should be miniaturized to enhance its spatial resolution and achieve higher EFRR as well.

This miniaturization must be for the loop and its shield if an accurate magnetic probe is needed. However, practically and due to the mechanical limits, it is not an easy task to fabricate a shielded movable loop with overall dimensions in the range of fractions of a millimetre.

Previous publications are distributed among unshielded loops (with and without differential amplifier/BALUN) and partially shielded loops. In the next literature review, the electric field rejection and the standing wave test are added, wherever it is applicable, to the list of compression parameters given in 2.10.5.

2.15.1.2 Unshielded Current Probe

Unshielded loops are the oldest version of metallic current sensing. This sensing part could be formed by a piece of wire or metallic track attached to a dielectric substrate. In both cases, it is either a single or a multi-turn (coil used to increase probe gain).

There are two kinds of coils: standard with two terminals and differential coil with three terminals. The latter is used to reduce the effect of the electric field by passing its induced voltage directly to the ground through the mid terminal.

2.15.1.2.1 Unshielded Passive Current probes

Movable current probes with miniaturized loop area (less than $1mm^2$) and application in microwaves circuits have been reported since 1989 with bandwidth in the range of 26 GHz. In that era, the focus of these reports [52], [140]–[142] were on showing the steps of manufacturing and the usability of their probes in the microwave current measurements. Therefore, no efforts have been made regarding probe spatial resolution or current measurement quality. However, one can expect from the size of the loop that the spatial resolution could have a similar value [143].

2.15.1.2.2 Unshielded Active Current Probes

The rapid developments in fabrication the integrated circuits provided the opportunities to fabricate on chip current probes with extremely small loops size (32 x 12 μm^2) and a high spatial resolution = 60 µm [144], [145] of single [144] or multiple turns (coil) [63], [145]–[151]. Moreover, it became possible to have not only a single loop/coil for one probe but also an array of loops/coils mounted on the surface of a planar current probe

[144]–[146]. These loops/coils (standard or differential) are cascade with one [146] or multi-stages of the differential amplifier to enhance the EFRR and sensitivity of the probe [63], [144], [145], [147]–[151], see Figure 2-36(A).

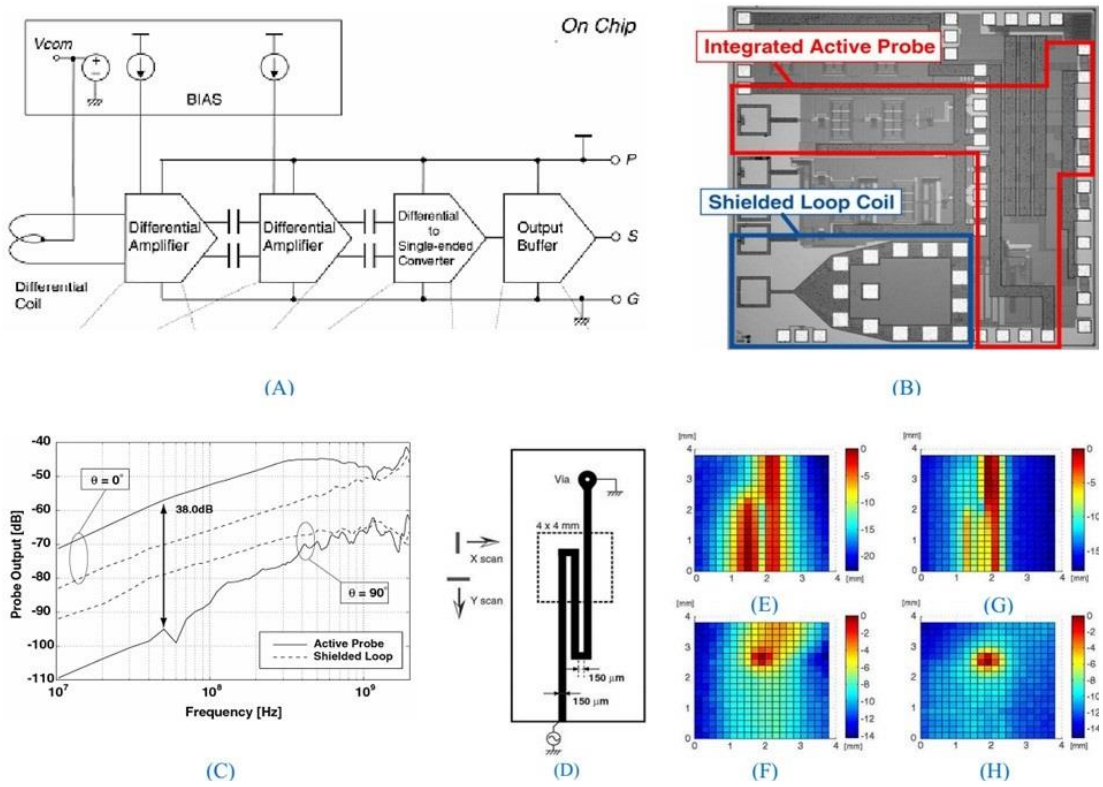

Figure 2-36 (A) Structure of the on-chip current probe. (B) Shielded and unshielded probes fabricated on the same chip. (C) The EFRR of the shielded and unshielded probe. (D) A PCB meander line test fixture of three fingers. (E) The response of the shielded probe to the magnetic field. (F) The response of the shielded probe to the electric field. (G) The response of the unshielded probe to the magnetic field. (H) The response of the shielded probe to the electric field [63].

Both the loop/coil and the stages of the differential amplifier are implemented on the same chip by using CMOS technology [149]. The fine accuracy of CMOS technology (65nm CMOS Process) [144], [145] permits loops/coils to have very good geometrical symmetry. The advantage of this geometrical symmetry combined with the effects of the differential amplifier and differential coil introduced unshielded current probe that might be able to defeat the shielded probes.

In 2006, a Japanese research group reported [63], [146] an interesting comparison, in terms of the EFRR and the spatial resolution. Two probes of the same dimensions (200 x

200 µm^2) fabricated on the same chip, see Figure 2-36(B), one of them was a shielded[3] coil and the other was unshielded cascaded with three stages of differential amplifiers.

Scanning the top of a microstrip line twice[4] by each probe at 100 µm height, showed that the unshielded probe had EFRR = 38 dBm at 50 MHz while the shielded loop had EFRR = 10 dBm, see Figure 2-36(C).

For the spatial resolution comparison, a PCB meander line test fixture of three fingers (150 µm width/gap) had been scanned twice[5] by each probe at 200 µm height, see Figure 2-36(D). The results illustrated that the unshielded probe had a better spatial resolution, see Figure 2-36(E-H). One thing can be deduced from Figure 2-36(F&H), is that in both cases the probes were unable to avoid the effects of electric field directly under it from transmitting to its output.

Despite all these features of the on-chip unshielded current probe, there is one drawback about their frequency response. The nature of CMOS technology does not allow a full coverage of the required microwave frequency band. The highest bandwidth reported was 3-3.3 GHz [144], [145], [148].

2.15.1.3 Partially Shielded Current Probe (Planar Loop)

A fully shielded wire loop antenna simply means the wire is surrounded by a metallic tube in a similar way to the structure of the coaxial cable. In 1996, a Japanese research group reported [152] a new shield loop antenna fabricated from printed circuit boards. The new loop consists of three layers of metal with insulators between them and they shared a gap at one end of the probe.

The top and the bottom layers were formed in a rectangular shape and they were connected to the ground at the far end opposite to the gap. The conductor in the middle formed a half turn pattern of the loop and its end, at the gap, terminated to the ground layers to complete the other half of the loop, see Figure 2-37(A). The induced voltage by the electric field in the top and bottom layers find their way to the ground. The magnetic field induced a current on the surface of the top and bottom layers.

---

[3] The geometrical nature of the on-chip planer loop/coil permits the shielded to be applied from the top and the bottom only [156]–[159] and thus it cannot be considered as a fully shielded loop/coli.

[4] In one scan the plane containing the loop is parallel to the microstrip line and in the other scan it is perpendicular.

[5] In one scan the plane containing the loop is parallel to the fingers and in the other scan it is perpendicular.

The gap is required to prevent a short circuit on this induced current. This current is passing through the opposite surface (facing the loop) in both layers to induce a voltage related to the magnetic field. With this structure, the new probe claimed to be insensitive to the electric field due to the shielding effect produced by the top and the bottom metal layers.

The name ”Planar Shielded Loop” was firstly reported [153] by the same group in 1999 and the reported probe was formed in a circular shape, see Figure 2-37(B). The bandwidth in both was below 2 GHz and their sizes were in the range of millimetres. This new design was the basis for many later designs of smaller size and wider bandwidth. Also, it was adopted by the European Computer Manufacturers Association (ECMA) [154] and the International Electrotechnical Commission (IEC) [155] standards in 2007 and 2008 respectively.

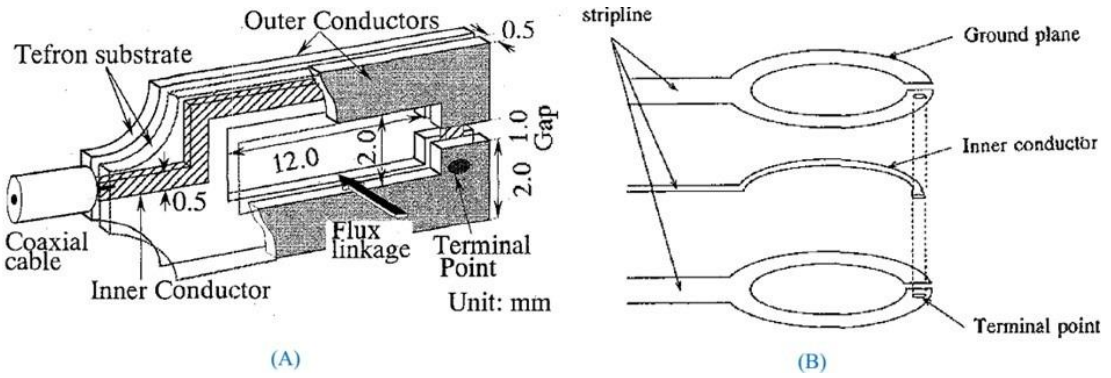

Figure 2-37 The structure of the planar shielded current probe fabricated from the printed circuit boards. (A) The rectangular shape [152]. (B) The circular shape [153].

On-chip CMOS technology was also used to fabricate this type of probe with high spatial resolution [156]–[159]. However, the issue of bandwidth limitation (3.3 GHz) is present here as well, see section 2.15.1.2.2.

The thin film technology and low temperature co-fired ceramics (LTCC) technology are both reported as an alternative approach in [116], [139], [160]–[165], thin layers of copper separated by either glass or ceramic insulators to enhance the bandwidth of the loop to around 20 GHz [164]. The smallest thin film probe was reported in Japan 2006 [116]. The outer dimensions of the loop were (50 x 22 μm^2) and the DUT had three parallel straplines of 5 µm width and 95 µm gap width scanned at height = 10 µm.

In this test fixture, all three strips shared the same input/output ports and therefore theoretically each one carries a current of the same magnitude and phase. This is a much

tighter arrangement compared with the case of reversed phase currents passed in adjacent strips (fingers) [116]. The reported value of the spatial resolution was 10 µm based on the location of the 6dbm drop from the peak, see Figure 2-38(A), while it is 50 µm if (2-50) applied to the track / gap widths. In this report, the standing wave test had been used to inspect shield effectiveness. Locations of the measured minima and maxima were compared with those calculated values for the electric and magnetic standing waves. Figure 2-38(B) illustrated the deviation between the measured and calculated locations.

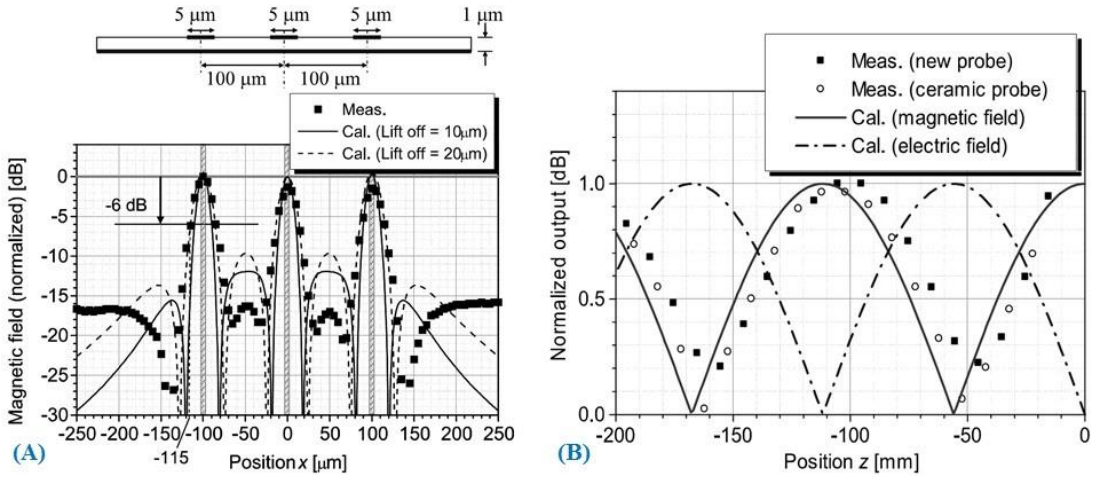

Figure 2-38 (A) Scan response of three parallel strips by the smallest thin-film current probe. (B) Standing waves along a microstrip line to inspect electric field rejection [116].

2.15.1.3.1 Planer Shielding Technique: Weak Points and Reported Solutions

The aim of the planar shielding technique is to support loop miniaturization with immunity against the unwanted effects of the electric fields. However, this description is not precise and not all the parts of the loop are fully screened.

The main weak points of the planar shielding are:

- One-half of the loop is present in the top and bottom layers and thus it is unshielded. The total voltages induced in the loops is the resultant of the magnetic field the electric field. A preliminary[6] solution to this issue reported in 2007 where all parts of the loop were etched to the central layer only, see Figure 2-39(A). This loop has two ports[7] and their outputs amplified and then differentiated by a 180 degree hybrid junction (BALUN) [163]. The EFRR value was 25 dB measured at

[6] In this solution only one among four issues is treated.

[7] In the original planer loop designee, it has one output port, while the other end is connected to the ground.

900 MHz. However, according to (2-51) this value is expected to decrease as the operating frequency increases.

- The top and the bottom of the loop are covered with metal layers while the two side edges and the edge facing the DUT are totally unscreened. Thus, the electric field emerges from all these edges and much more strongly from the facing edge where the distance to the DUT is the smallest and field lines are emerging perpendicularly.
- In addition to that, the part of the loop within the gap is sensitive to electric field from all directions.

While neither the facing edge and gap issues have been solved yet, there was a solution reported by a research group from National Taiwan University in 2011 to minimize the emergence of the electric field from the sides.

In this solution, the LTCC technology is used to implement a multi-layer planer current probe. A complete turn of the loop etched in the central layer before it is end terminated to the outer layers. Additional tracks added in parallel to the sides of the loop in the central layer and at the same location in the top and bottom layers. These tracks on each side are then connected together by using many vias distributed along their length to produce a via fences [164], see Figure 2-39(B). The improvement of this via fence was a 10 dB electric field rejection at 11.5 GHz.

To enhance EFRR in this kind of loop, a modified version of the via fences technique reported by the same research group in 2013 includes two other c shaped strips located above and under the half turn loop, see Figure 2-39(C). These strips etched in additional layers so that the total number of layers used in this structure were seven. An claim of 30 dB EFRR is reported over a wide bandwidth (0.05 to 17.8 GHz) [139], see Figure 2-39(D).

The announced spatial resolution was 140 µm estimated from scanning across the width of microstrip line[8] (width = 2000 µm). For comparison, the calculation of (2-50) in this situation gives a spatial resolution of[9] 930 µm.

[8] If loop size is small with respect to the width of the microstrip line then it is possible to recognize the high density distribution of the current at the edges of the microstrip line [161].

[9] Microstrip line edges might be considered as two separate tracks of 140 µm width and a 1720 µm gap between them.

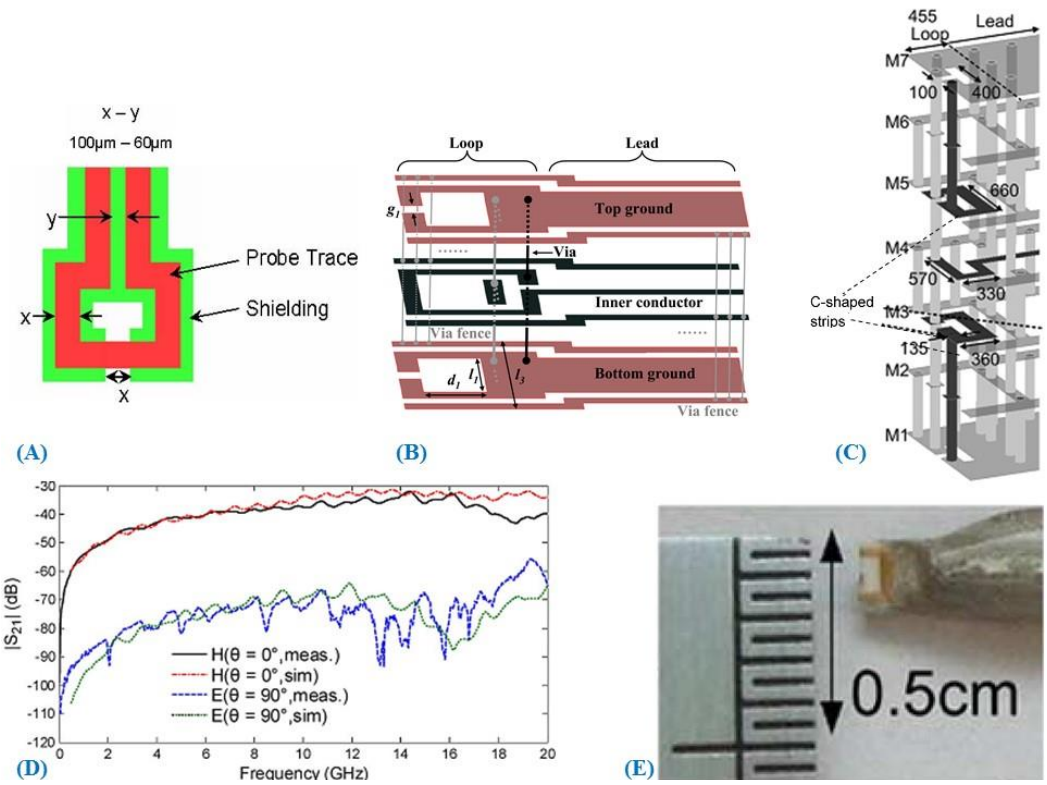

Figure 2-39 (A) The structure of the planar shielded current probe with all loop parts etched to the central layer [163]. (B) Loop side edges protection by using parallel tracks and via fence technique [164]. (C) Modified via fence technique by adding two c shape strips in separate layers above and below the central layer [139]. (D) Response to both the electric and the magnetic fields [139]. (E) The final probe tip size [139].

However, the impact of this EFRR enhancement are a factor of about 2.5 increase in the overall thickness of the probe and more complicated probe structure[10]. The loop aperture was 400 x100 µm^2 but the total probe tip width was 2 mm [139], see Figure 2-39(E). This extra width added to give the required mechanical support around the miniaturized loop. A two-millimetre width is quite large for many applications like scanning inside microwave power transistors.

In the same year, they reported a spatial resolution enhancement [165]. The Kantor technique applied here but instead of using a single loop to scan the DUT at two different heights, they used two loops sharing the same housing and located at two different heights. One of them has two turns each on a separate layer and clamping the second one

[10] In this designee 7 layers used in the fabrication of the probe instead of three in the original designee.

which has one turn located in the central layer with partial height overlapping, see Figure 2-40(A).

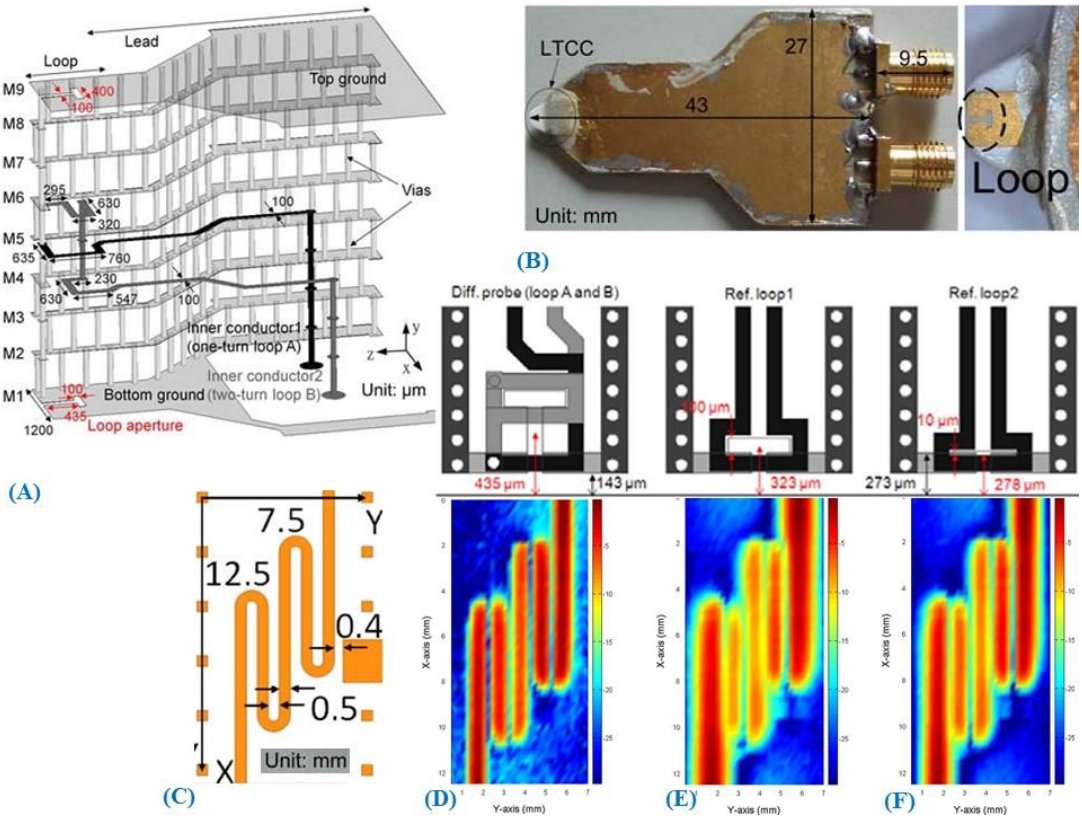

Figure 2-40 (A) Structure of the differential current probe. (B) It's actual size. (C) Test fixture used in spatial resolution test. (D) Differential probe scan result. (E) Scan result of a probe with 100 µm aperture width. (F) Scan result of a probe with 10 µm aperture width [165].

With this new arrangement, the probe becomes even thicker than their previous design (it has 9 layers instead of 7) and overall probe tip width was 1.2 mm. Figure 2-40(B) illustrates the actual size of this differential planer current probe and its tip.

The aperture for this differential loop was (400 x 100 μm^2) and the test fixture was a five finger meander microstrip line of track/gap width = 500 µm, see Figure 2-40(C).

For comparison purposes, this test fixture was also scanned with two other reference probes. One of them had the same aperture as the differential loop and the aperture of the second one was (400 x 10 μm^2). Spatial resolution results of the differential probe and the two reference probes are shown in Figure 2-40(D), (E) and (F) respectively.

2.15.2 Indirect Current Measurement

To avoid fabrication difficulties and structure complexity of the shielded current probes, an alternative method has been developed to calculate the current from voltage probe measurements [133], [136]–[138]. This calculation is basically based on defining the scattering parameters of the DUT and then to find it's related voltages, currents and impedances. Measuring the scattering parameters in a contactless manner is not new and firstly reported in 1992 [166].

To define these parameters either the electric field probe [125], [133], [136]–[138], [167], [168] or the magnetic field probe [166], [169]–[173] or both [174], [175] are used. This type of measurement is useful to test planar circuits/devices like open transmission lines (microstrip line) [174]. The unknown scattering parameters of the DUT are determined by inserting two microstrip lines before and after it and then quantifying electromagnetic field above them with one or two contactless probes connected to a VNA, see Figure 2-41(A).

In 2012, the group in Delft University reported their contribution to this type of measurement and extended it to include irregular structures like the arrays of bond wires [133]. In this development, the measurement process passes in two phases before having the final results. In the first one, the electric field emitted from each wire in the array is measured by a contactless voltage probe (open-end coaxial).

In the second phase, a three dimensions' numerical electromagnetic model of the bond wires array and the probe is generated by using HFSS simulation software. The excitation port within this simulation is then adjusted until the simulated electric field becomes identical to that value measured in the first phase [137]. Once that is obtained, the scattering parameters, voltage, current and impedance for each bond wire are numerically calculated.

A test fixture of 33 bond wires (diameter = 25 µm, length = 3 mm and pitch = 300 µm) was used to duplicate a drain bond wire array, see Figure 2-41(B). This procedure should be repeated for each operating frequency, Figure 2-41(C) shows the impedance of each bond wire at five different frequencies.

Whilst this development introduces an interesting perspective of the DUT (especially if the DUT is passive) it raises two concerns regarding applicability and accuracy when the DUT is active. Firstly, for each array structure, there must be an accurate modelling of the bond wires.

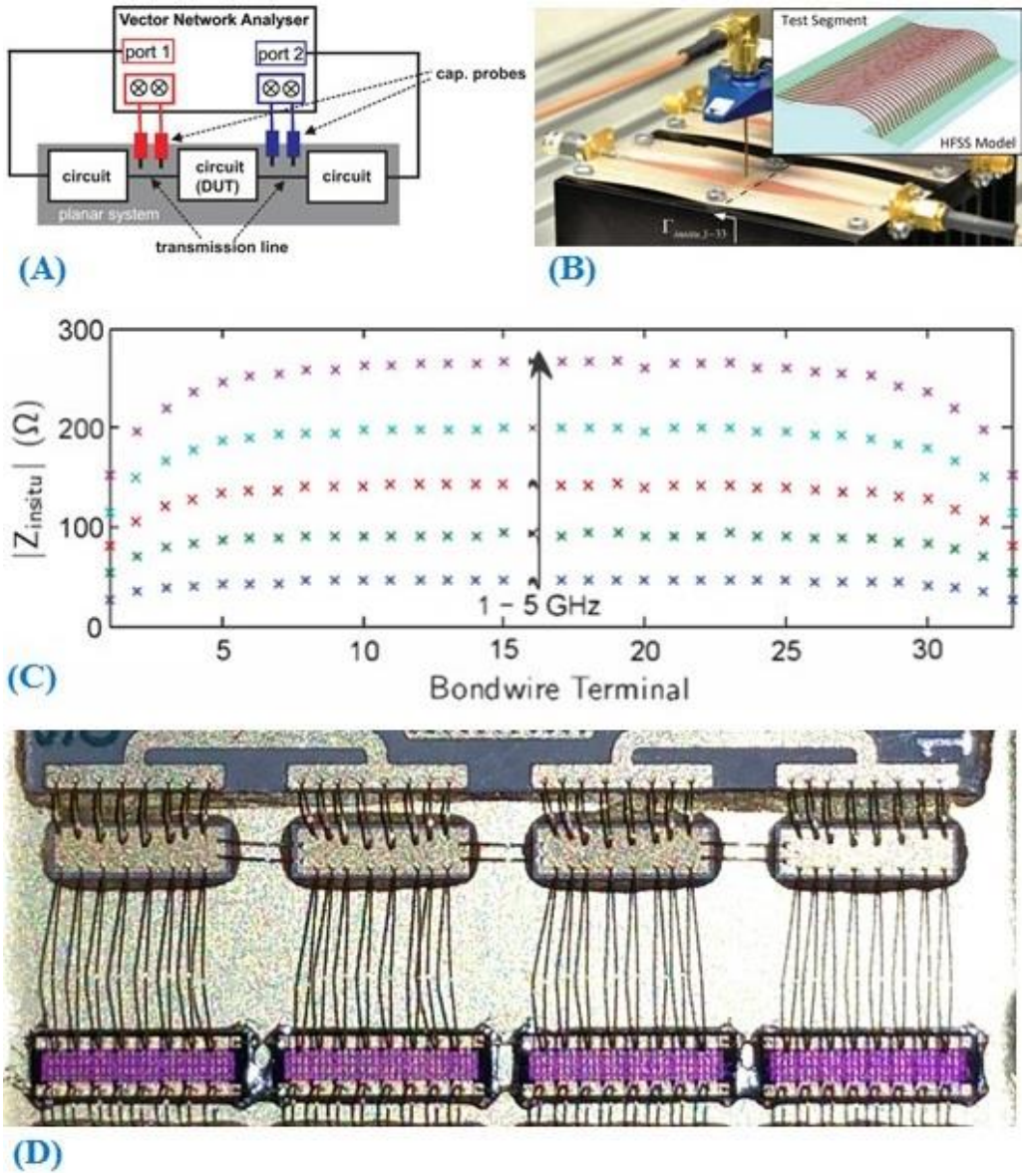

Figure 2-41 (A) Contactless scattering parameters measurement for planar microwave circuits [168]. (B) Bond wires test fixtures and its HFSS module [133]. (C) The individual impedance of each bond wire at five different frequencies [133]. (D) Microwave power transistor has bond wires of different shape and length.

This will require precise information about wire diameter, wire length, the separation between adjacent wires and the most importantly are the shape of each wire (in many cases, providers of the microwave transistors are using multiple wire shape and length in the same package to enhance the overall performance, see Figure 2-41(D)).

Secondly, in many practical cases, each bond wire or small group of them is/are connected to a nonlinear element (like the cell among an array of cells inside the die). This

nonlinearity could be inherent in the cell or due to the coupling effects within the array or all of these things together.

Simulation of such cases is still a misty area that welcomes a third-party investigation to clarify it. In fact, the main goal of all these efforts in the field of high spatial resolution contactless measurements is to introduce a real-time visualisation of how voltages and currents distributed among die cells.

2.15.3 Current Probing Inside an Active Microwave Transistor

To this author's best knowledge there are no earlier reports of a real-time direct contactless current measurement inside an active microwave power transistor. However, the only work achieved in this area was that done in Delft university [136]–[138] by using indirect measurements technique described in 2.15.2. Current distribution among drain bond wires arras of 100 W and 200 W LDMOS transistor reported in 2015, see Figure 2-42(A & B).

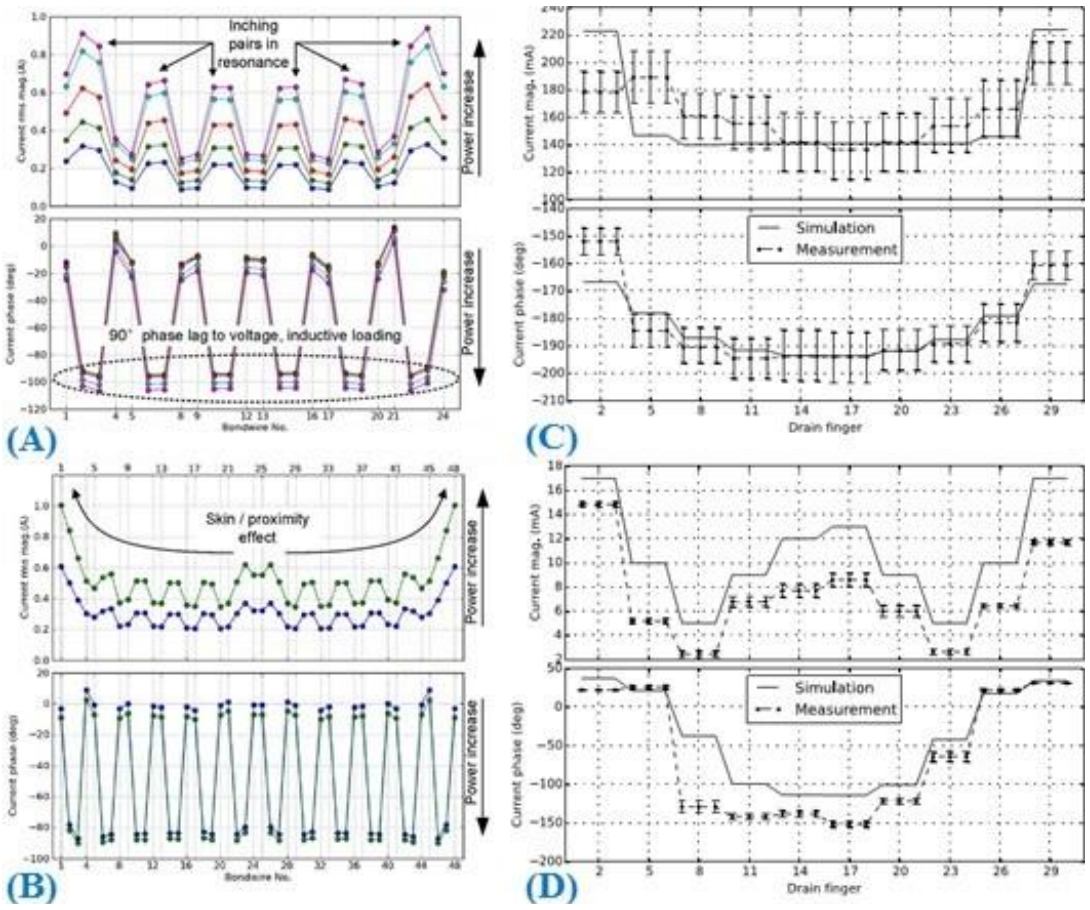

Figure 2-42 Current magnitude and phase at drain boondwires (A) 100 W LDMOS transistor [137]. (B) 200 W LDMOS transistor [137]. (C) GaN transistor fundamental harmoinc [138]. (D) GaN transistor second harmoinc [138].

In terms of spatial resolution, their best results were reported in 2016 after enhancing the spatial resolution of the electric field probe (refer to 2.14.4 and see Figure 2-35). This enhancement is also reflected in the result of the current calculations (included in the second phase of the indirect current measurements), see Figure 2-42(C & D).

3 MICROWAVE I-V MEASUREMENT SETUP AND FABRICATION REQUIREMENTS

3.1 Introduction.

The term ‘measurement’ in this chapter refers to the quantification of both current and voltage at microwave frequencies by comparing it to a reference signal. The item that is to have it’s I-V characteristics quantified is called the Device Under Test (DUT) and the device used to make the comparison is known as the measurement instrument together with the novel probes that have been developed in this research study. In the area of microwave applications, there are two fundamental domains within which one can perform a specific type of measurement, those are the frequency domain and the time domain. An example of the frequency domain measurement instrument is the Vector Network Analyser (VNA) and the spectrum analyser; for the time domain there are the oscilloscope and the sampling oscilloscope. Like many other types of RF measurements, contactless measurements of voltage and current required the DUT to be adequately excited by an RF power source and thus RF generators are also necessary. In addition to that, when a new probe has been fabricated, it needs to be characterized using well-known DUT. Such devices are used for verifications purposes and are called test fixtures. It has been shown, in chapter two, that contactless measurements are a function of the location

of the probe with respect to the DUT and therefore it is also necessary to have a proper mechanical system to accurately define the relative position of the probe. Finally, a central unit that manages the data captured and properly controls the whole process of the contactless measurement is a must. This chapter will briefly highlight all the above-mentioned topics.

3.2 Setup of Contactless Voltage and Current Measurements

A general contactless measurement setup that is applicable to both voltage and current measurements is illustrated in Figure 3-1. This setup is partitioned into three main levels:

1. Measurement Control and Data Management (MCDM) level.
2. Measurement Instruments (MIs) level.
3. Measurement Action (MA) level.

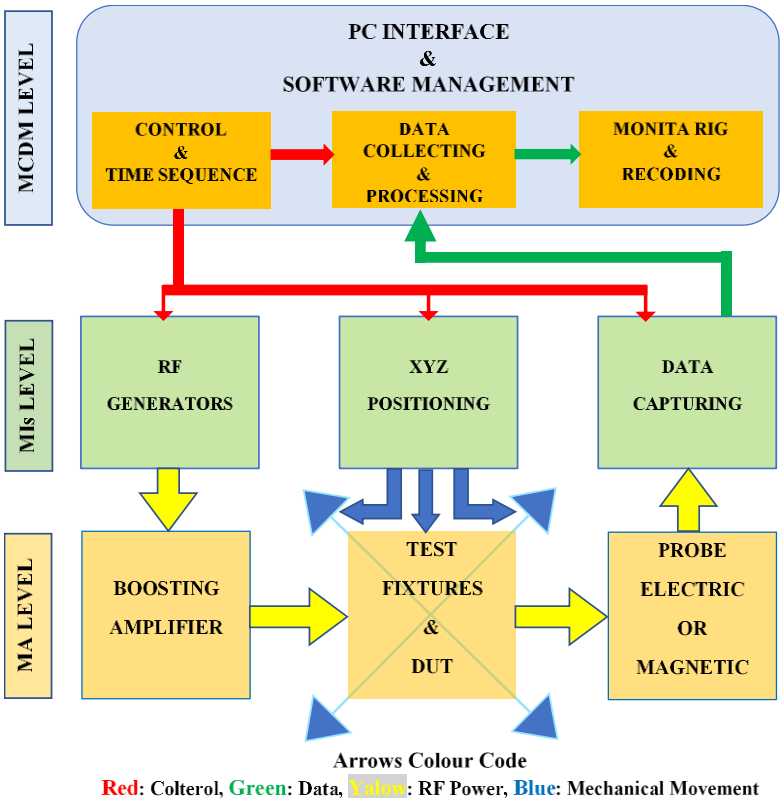

Figure 3-1 The setup of the contactless voltage and current measurement.

3.3 Measurement Control and Data Management

This is basically a computer with appropriate speed and data storage to run the management and control software. The initial values and the limits of measurement are defined prior the starting of the measurement process. Synchronization signals are

generated at this level and then sent to all the parts in the MIs level to ensure accurate timing slots for the positioning part and the capturing part. Captured data are then received, collected, processed and recorded for further analyses.

Through the whole measurement steps, monitoring and observation are accessible through the individual screen of each instrument and the overall measurement progress through the graphical interface provided by the MCDM level screen.

3.3.1 LabVIEW Programming

The main software used through this work is the Laboratory Virtual Instrument Engineering Workbench (LabVIEW). It is a robust software that manages instrument control, data acquisition, data processing and data presentation. LabVIEW uses a graphical programming language instead of the traditional high-level languages.

The basic units in programming with LabVIEW languages is known as virtual instruments (VIs). Theses VIs consist of the two graphical objects: the block diagram and the front panel. The former consists of various mathematical and logical functions while the later has a variety of controls, inputs parameters, and indicators, outputs parameters. Inside the block diagram, the flow of data between these functions is simply represented by wires.

LabVIEW can be installed on both Windows and Apple Macintosh and it supports many protocols like IEEE-488 (GPIB), RS232 and TCP/IP. These protocols are used to communicate with devices and instrument controlled by the LabVIEW program. LabVIEW acquires data from them and at the end of the execution these data are saved in an excel file with a record for all initial settings and inputs.

Through this work, five LabVIEW programs had been written to control and collect data from the MIs level devices and instruments.

The functions of these programs are:

1. Controlling the positioning system, see section 3.4.1.
2. Synchronous control and data acquisition from the RF power meter and positioning system, see section 3.4.3.
3. Synchronous control and data acquisition from the spectrum analyser and positioning system, see 3.4.4.
4. Synchronous control and data acquisition from the VNA and positioning system, see 3.4.5.

5. Controlling and data recording from the VNA in the frequency domain, see 3.4.5.

3.4 Measurement Instruments

At this level, three essential parts are required: the XYZ stage, the RF generator and the data capturing device[11]. The XYZ stage is holding both DUT and the probe and it is responsible for the relative location/ movement between them. Usually, this part remains without change regardless of the DUT type, or the type of the measurement or its domain. While the remaining parts in this level are changeable depending on the domain of the measurement and/or the parameters of the measurements. In the frequency domain, to measure the magnitude and the phase of the voltage or the current the VNA is used as an RF generator and for data capturing. To measure the magnitude of the harmonic content, a spectrum analyser with a separate RF generator is used.

In the time domain, the spectrum analyser is replaced with either an oscilloscope or a sampling oscilloscope to quantify the magnitude, the shape and the phase delay of the voltage or the current with respect to the original source signal.

In this level, it is essential for each part to have a proper interface to communicate with the MCDM level, such as the GPIB (General Purpose Interface Bus), USB (Universal Serial Bus) or any suitable Ethernet interface.

3.4.1 XYZ Positioning System.

The positioning system is utilized to automatically locate the relative positions of the probe and the DUT. The accuracy and quality of the positioning system can significantly influence the overall accuracy and the quality of the contactless measurement especially when it requires movements in the range of micrometres. Accuracy and quality are defined in terms of the smallest movement step allowed, repeatability and mechanical and thermal stability. The positioning system consists of three main parts: a mechanical stage, stepper motors and control. Among those parts, the mechanical stage is the most important, it should be stable and immune to mechanical vibration and thermal fluctuation especially for the Z axis (the distance between the probe and DUT).

[11] Sometimes become two when the RF generator and the data capture are included in the same device, like the case when the VNA is used.

In the contactless measurements, it is common to locate the probe at 5 μm or less above bond wires of a fully activated power transistor. If the mechanical instability of the stage is compromised, this could lead to uncontrolled physical contact between the probe and the wire under it. Usually under these circumstances, severe damage can occur, not only to the probe (electrically and mechanically) but also the transistor under test and the measurement tools. Selecting a mechanical stage of good quality can minimize mechanical vibration to a fraction of a micrometre.

Stage thermal expansion required more attention to minimize its impact. Metals like aluminium, steel, copper are commonly used in the structure of the stage, DUT and the probe. Thermal expansion coefficients of these materials are 0.23, 0.13, 0.17 μm/cm/C respectively. If for example, the temperature changed 5º then the length of a 10cm aluminium piece is changed by the amount of 11.5 μm. Such a variation can introduce permanent damage if it is larger than the distance between the probe tip and DUT. If not, then it has the potential to affect the overall accuracy of the measurement. Thermal expansion can be avoided or at least minimized to a fraction of micrometre by keeping the room temperature constant or/and designing the stage in a way that leads to a minimum temperature expansion coefficient. This can be accomplished by building the stage from materials that have opposite thermal expansion coefficient or/and use the flipped "U" shape in constructing the axis of the stage.

The other two important factors defining the quality of the positioning system are the minimum step size and the repeatability of the movements. Both factors are mainly related to the stepper motors characteristics. Minimum stepper motor step should be much smaller than the highest possible spatial resolution to produce smoother measurement responses and to enhance measurement repeatability as well. For example, a 2.5 μm and lower step size stepper motor should be used to a chive a spatial resolution of 25 μm. Stepper motor movements, under measurement conditions, need to be synchronized with the measurement process, therefore, the main controlling unit is used.

Positioning systems can be classified into two types: in terms of which part is moving with respect to the other. With the first type, the DUT is held still while the probe is moving across it. The advantage of this type is: easy to mount the DUT (especially when a water cooling heatsink is required) a smaller stepper motor is needed which means smaller step size is more likely possible. This type of stage is shown in Figure 3-2(A) and it has two stepper motors one for the X-axis and the other for the Z axis with a minimum

step size equal to 48 nm. The other option is the opposite and therefore it allows better observation to the movement through a microscope because the probe is held still and DUT is moving under it. This configuration is shown in Figure 3-2(B) where the minimum steeper motor step size is equal to 2.5 um.

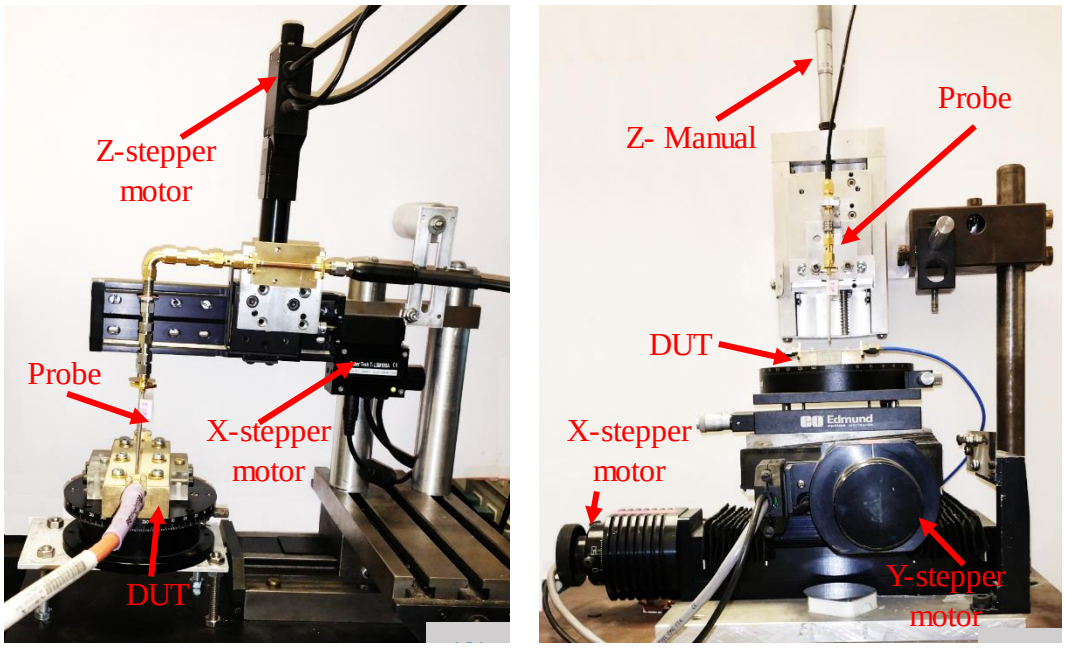

Figure 3-2 (A) XYZ stage with the probe moving across the DUT. (B) XYZ stage with probe still and the DUT moving under it.

The front panel of the LabVIEW programme that controls the movement along the X-axis and the program are given in Appendix one. This panel has control icons to determine step size, starting point, number of the steps, the direction of movement and the option automatically return to the zero position. Probe movement along the Z-axis is controlled through the Zaber software.

3.4.2 RF Generator.

An Agilent E4421B RF generator has been used to excite the DUT either directly or via a boosting amplifier, see 3.5. This generator can provide an RF signal up to 3 GHz at any value of power between +16 dBm and -136 dBm.

3.4.3 Power Meter.

An Agilent E4418B RF power meter has been used to measure the signal generated at the output of the probe. The front panel of the LabVIEW program that controls the power meter and the movement along the X-axis is given in Appendix two.

3.4.4 Spectrum Analyzer.

LabVIEW program written to controls the spectrum analyzer and the movement along the X-axis for harmonic measurement. The LabVIEW code for this type of measurement is given in Appendix three. The spectrum analyzer used through this work was a Hewlett Packard 1996A with 6 GHz bandwidth and remotely controlled via its Ethernet port.

3.4.5 Vector Network Analyzer.

The VNA HP8753E has been used for most of the measurements[12]. It is a relatively old model, it has only two ports with a 6 GHz bandwidth and very good sensitivity down to the range of -90 dB. Through this work, many calibration files were generated and saved in this VNA for a variety of setting options and different hardware attached to it through the measurements (cables, connectors, etc.…). The important setting for the VNA is the starting and ending sweep frequency, the number of points per sweep, sweep time, intermediate frequency bandwidth and the scattering variable to be measured. These parameters are made accessible at the PC through the front panel of the LabVIEW program which also controls the steps of the stepper motor.

The LabVIEW program for this instrument has been written to support more effective remote control by recalling pre-saved calibration files to match the different types of DUT, see Appendix four. In addition to that, and since the internal software of the VNA HP8753E is old, another LabVIEW program has been written to capture and record the date of the S-parameters in the case where the VNA is being used in a standalone setting. The front panel of this program and the program is given in Appendix five.

In order to perform an absolute contactless measurement, it is essential to calibrate the probe and to do a full calibration for the VNA as well. However, in many cases, the DUT needs a sufficient RF power delivered at its input (like microwave power transistors) and thus a boosting amplifier is located between the VNA and the input of the DUT, see section 3.2 and Figure 3-1.

For such an arrangement, see Figure 3-3, it is only possible to do a response calibration of the HP8753E and only the forward transmission measurement S_{21} is possible [176]. This limitation can be avoided in other VNAs like HP8753D Option 085 and other VNA that has jumpers to access its internal connection. For our case and under this

[12] Through this work, the only available VNA, for long term use, was HP8753E.

circumstance, the contactless measurement can be classified to be a relative measurement technique.

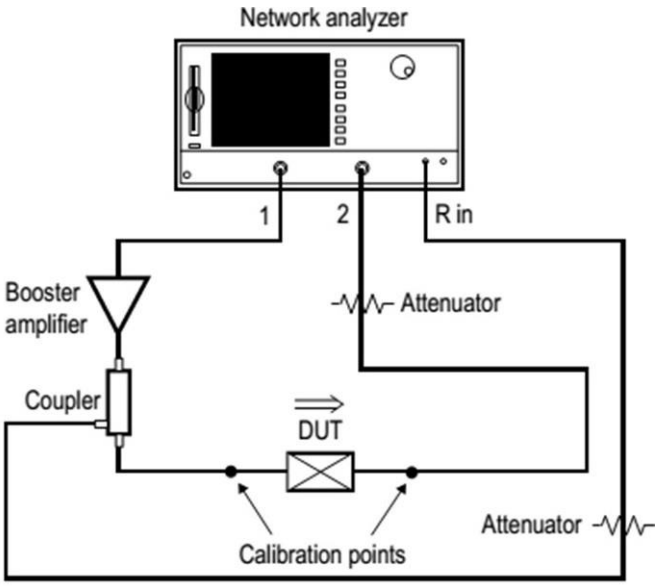

Figure 3-3 HP8753E calibration setup with boosting amplifier, only response calibration is possible [176].

The purpose of calibration is to correct the systematic errors [176]. These errors are related to the VNA and devices lying between it and the DUT and many of these errors are a function of the frequency. However, these errors are the same when the same measurement is repeated over and over at very close distance from each other (fraction of a millimetre). In another word, these errors look like common mode noise, their effects can be compensated through a subtraction process. In many applications, like the case of bond wires, what is important is the difference in magnitude and phase, between them rather than the absolute values. In fact, both the absolute and the relative measurements will lead to comparable results because error due to incorrect calibration is constant for a given hardware structure at a specific frequency.

3.5 Measurement Action Level

This level consists of three parts: The probe, the DUT and a boosting amplifier. This amplifier must have a sufficient RF power capability to excite the DUT. At this level, the setup should allow easy access to change any of its parts without affecting the remaining levels. The power and gain of the boosting amplifier stage depends on the DUT and through this work, three deferent power ratings of the amplifier (1 W, 3 W and 10 W) have been used, see Figure 3-4(A-C).

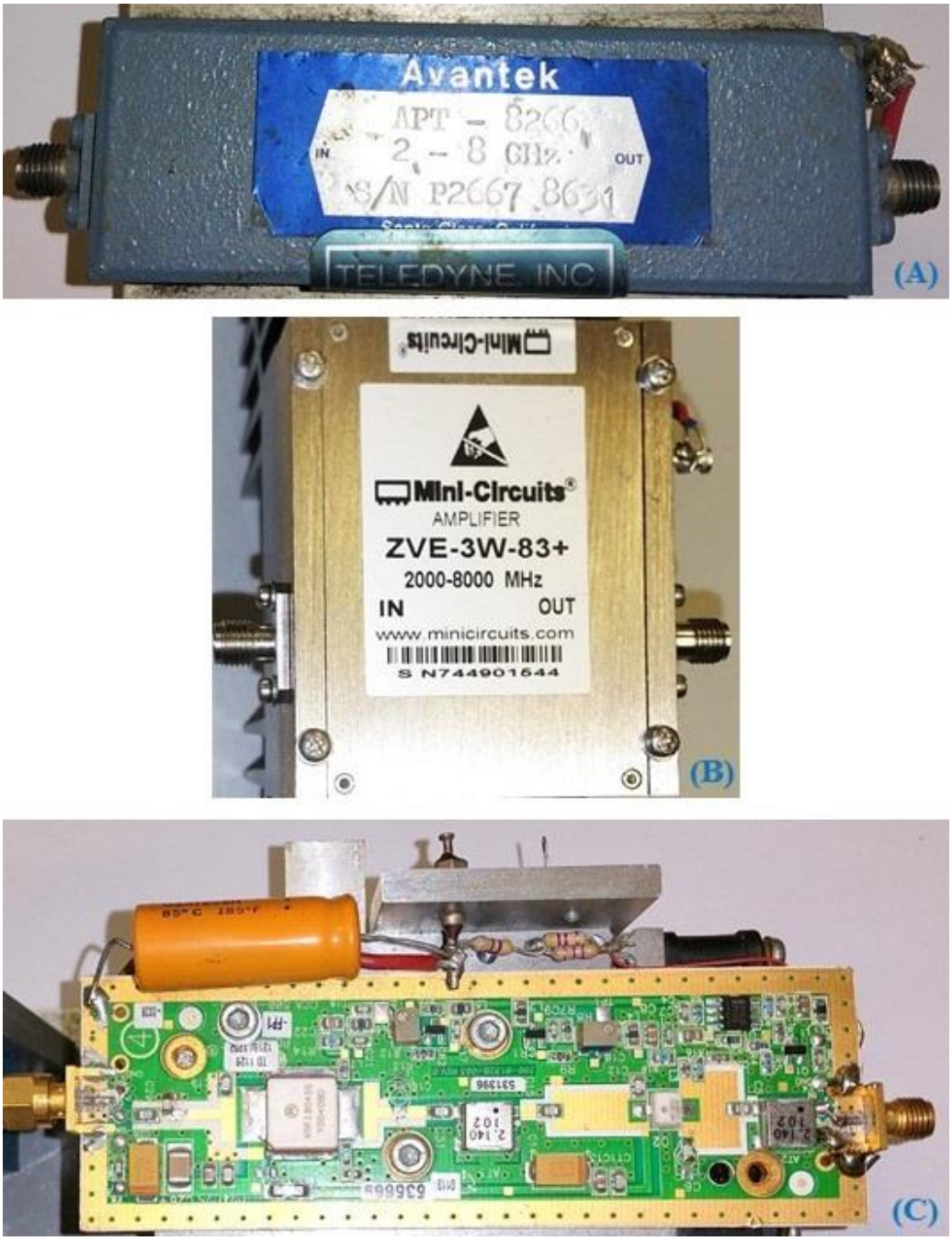

Figure 3-4 Boosting amplifiers. (A) 1 W, 2-8 GHz. (B) 3 W, 2-8 GHz. (B) 10 W, 2.4 GHz.

3.6 Generic Contactless Probe Structure

The generic structure of the contactless probes can be divided into three main units: the input interface unit, the transition unit and the output unit. The first and the second units are situated inside a container called the housing of the probe, see Figure 3-5.

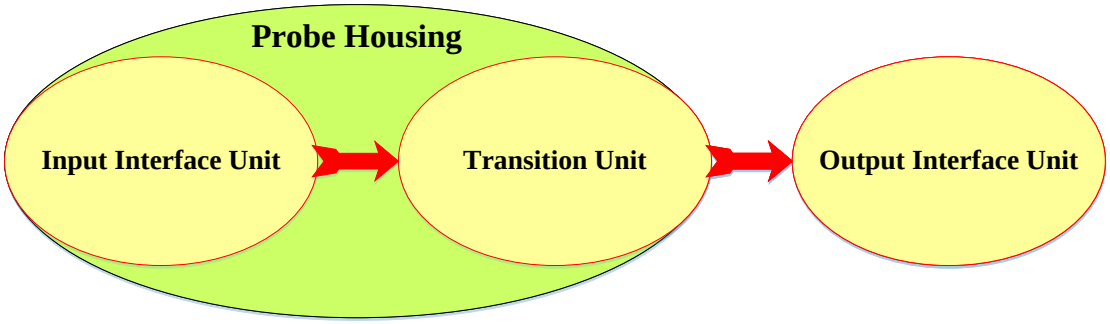

Figure 3-5 Structure of the generic contactless probe

3.6.1 Input Interface Unit

In this unit, the electromagnetic fields are converted to electrical signals. It has two essential parts: an antenna and an appropriate transmission line. The overall dimensions of these parts are miniaturized to the micrometre level to satisfy the high spatial resolution requirements inside microwave power transistors. Design details and fabrication procedures for these parts are discussed in chapter four and five.

3.6.2 Output Interface Unit

The function of this unit is to transmit the probe output signal to the next stage in the measurement system through a standard transmission line and compatible RF connector.

3.6.3 Transition Unit

The middle section is the transition unit. Here, two types of transition are achieved. The first type is the transition from the micro scale geometry of the input interface unit to the standard millimetre scale dimensions of the output interface unit. The second type is the electric signal transition which can be either through a direct electrical connection (passive probe) or via a preamplifier circuit (active probe).

The active version of the probe contains miniaturized electronic circuits and devices used to implement the preamplifier. More details are provided in chapter four and five.

3.7 Miniaturized Probe Housing Design and Fabrication.

A miniaturized tube followed by a small chamber with a movable cover are the main features of the probe housing. Both parts are made from metal and they contain the first and the second probe units, providing them with the required mechanical support and protection against noise as well.

Copper and brass tubes and rods have been used to fabricate the housing. Copper has better electric conductivity, but it is too soft to create miniaturized objects, therefore, brass, which it is much harder than copper, is preferred.

The parts of the input interface unit are contained inside the miniaturized brass tube. The antenna is situated at its far open end and the transmission line passes through it into the brass chamber.

Companies that manufacture microwave power transistors usually seal their products with a ceramic cover of 2-3 mm in height, see Figure 3-6. From which it can be assumed that if any metallic object is laid on the surface of the ceramic cover, it will not impact electromagnetic fields distribution inside them. Therefore, the length of the miniaturized tube is chosen to be 10 mm (which is much taller than the height of the ceramic cover) to ensure a safe minimum intrusion due to the metallic chamber. This assumption is also verified practically by the intrusive test in section 3.12.1.

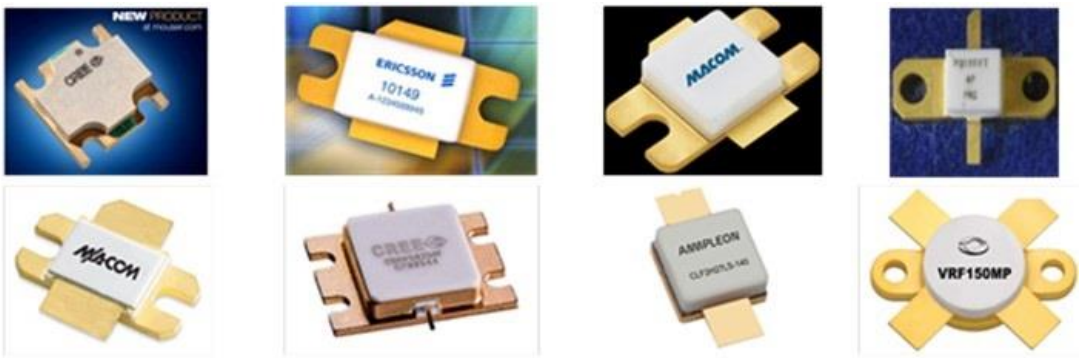

Figure 3-6 Different package of microwave power transistors with ceramic upper face cover.

The brass chamber contains the parts of the transition unit. It is a metallic structure fabricated from tubes and rods in a cylindrical shape with a removable cover for easy access. The chamber size is dependent on how many outputs the probe has and on whether is it active or passive. In the active probe version, this chamber offers the required shielded space to implement the micro electric and electronic circuit components necessary for the preamplifier.

Through this work, three versions of a miniaturized probe housing have been designed, manually fabricated, and used in the construction of the contactless probe. Designe details for these housings are illustrated in Figure 3-7.

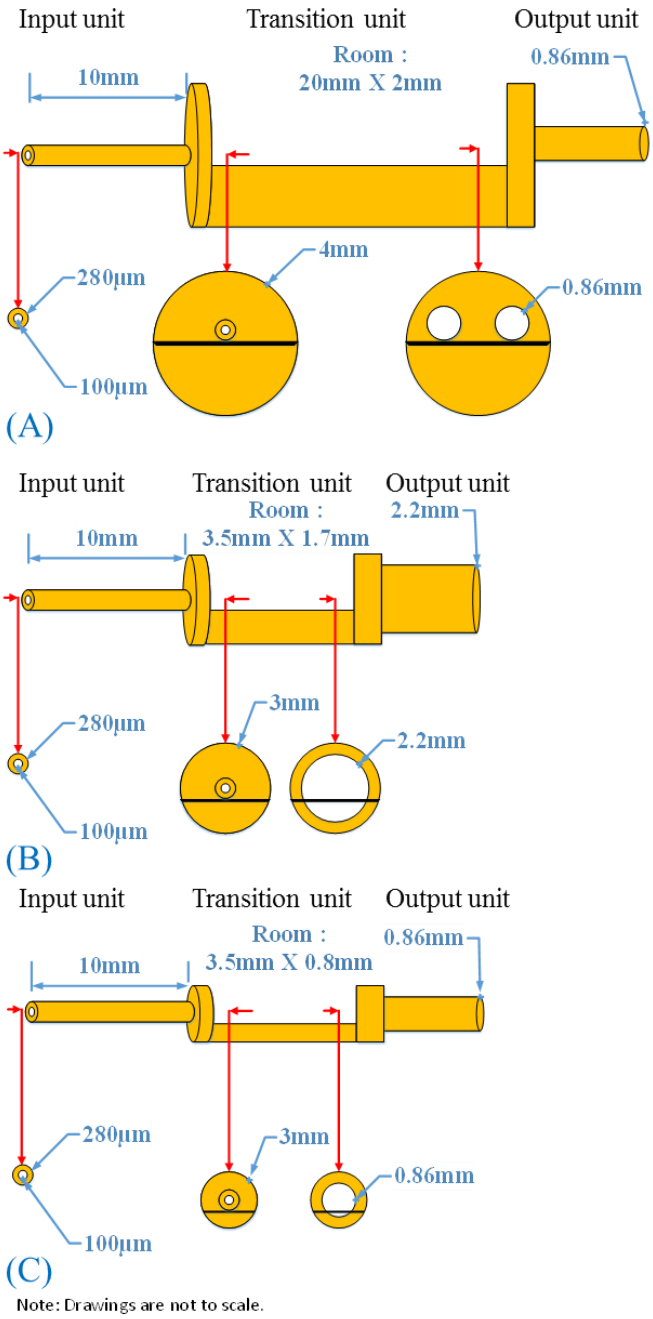

Figure 3-7 Design details of the three versions of the housing used to implement the mininaturized contactless probes. (A) Current probe. (B) & (C) Voltage peobe.

3.8 Micro Fabrication Requirements

Fabricating a new microwave device and/or microwave circuit is a challenge. Many factors should be considered especially those related to the size, relative positions and dimension aspects. However, handmade fabrication of a micro version of those microwave devices and circuits is an extremely difficult and time-consuming process.

The whole fabrication process needs to be conducted through an optical microscope which limits the allowed working space to a few centimetres only.

This involves the use of the various sets of precise micro tools. In fact, many of these tools have been manually fabricated either because they are expensive or unavailable.

Creating a successful and repeatable fabrication procedure is a result of intensive training in order to acquire sophisticated hand skills in this field. It also needs wide access to a various range of data resources about the electrical, mechanical, physical, and even chemical characteristics of the raw materials used for fabrication and implementation.

3.9 Fabrication Generic Materials

Many kinds of materials have been used in the fabrication of these probes. Some of them are common in both voltage and current probes while the remaining are specific to each one of them. These materials are divided into three groups according to the probe main units discussed above.

3.9.1 Materials Used in Implementing Input Interface Unit

Both types of the miniaturized antennas, the loop and the monopole, and their transmission line are fabricated from enamelled thin copper wire, AWG52, which has a 20 μm copper diameter. The copper is coated with 1.5 μm Polyurethane green insulator[13].

The traditional methods of removing this insulation layer from enamelled wires, by applying either heat or scratching it, are not applicable to this ultra-thin wire and thus chemical solvent materials are needed. After trying different materials, the Acetone works well but requires 5-6 hours to completely remove the insulation layer from the wire.

It is important to remove the wire soon after the insulation has dissolved, otherwise an unmovable black layer of copper dioxide forms on the wire surface. Alternatively, continuously wiping the wire with cotton and Acetone for 15-20 minutes yields the same result.

[13] This type of wire is usually available in three colours red yellow and green. However, it is better to choose the green or the red colour for easy distinguish the remove of the insulator while inspecting it under microscope.

Removing this insulation layer only from the ends of the wire demands precise wiping with a controlled amount of Acetone and for this purpose, we fabricated a simple but effective wiping tool using a half of cotton swab attached to a 5 ml syringe filled with Acetone.

3.9.2 Materials Used in Implementing Transition Unit

Materials used in this unit can be divided into three main categories:

3.9.2.1 Electronic Circuits Devices

Miniaturizing the size of the probe giving more functionality in a smaller space. Due to that, all the electronic devices used in implementing the transition unit are selected from the family of subminiature surface mount leadless packages. We choose active devices (transistor and /or amplifier) that is in an ultra-thin and small package WLP0402, 1 mm x 0.5 mm x 0.25 mm, see Figure 3-8.

For the passive parts (resistors, capacitors and inductors), we used the smallest packages sizes commercially available nowadays, 01005, 0.4 mm x 0.2 mm x 0.2 mm and 0201, 0.6 mm x 0.3 mm x 0.3 mm.

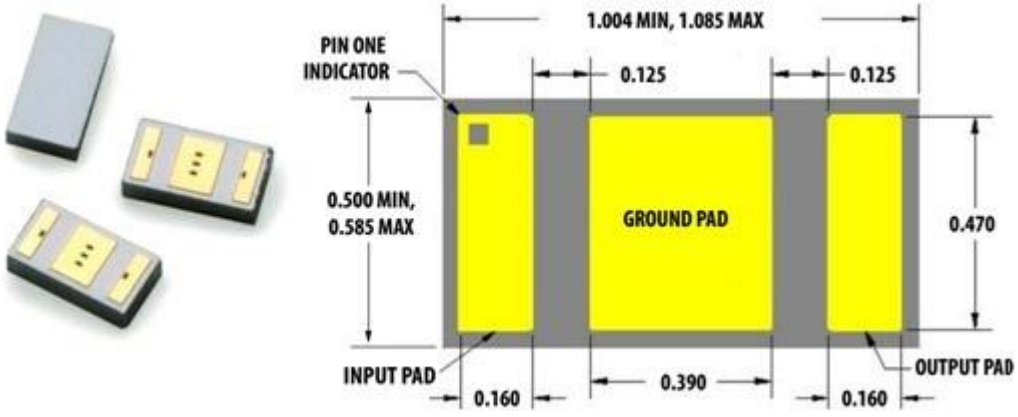

Figure 3-8 Photo of the WLP0402 package and its outline, all units are in millimetre.

3.9.2.2 Electric Connection Materials

Surface mounted devices are usually attached to the printed circuit board by using an automated soldering process. Automated soldering can offer the controlled amount of heat and accurate positioning of the soldering process. However, the cost of this technology is beyond the budget of this project. On the other hand, the manual soldering is not applicable to these miniaturized electronic circuits.

The alternative to the soldering technique is to use a conductive epoxy. The important factors in selecting the suitable conductive epoxy are its electric conductivity and its viscosity.

Silver conductive epoxy has the highest conductivity compared with other materials. The viscosity of the product depends on the density/size of the silver particles and the nature of the resin and hardener mixed with it. It is important here to have wide flexibility to create an ultra-small spot of the mixture at the required place.

Through the experimental tests on many brands of silver conductive epoxy, we found that the RS Pro Silver Epoxy Conductive Adhesive is the best choice. The resistivity of this product is less than 0.005 Ω/cm and the curing time is 24-36 hour at room temperature and it can be reduced to 20-30 minutes at 100° C. With this product, we were able to create ultra-small spots of less than 40 μm radius.

To create such small spots there is a need for an object with a tiny diameter and a strong enough structure to pick up the epoxy and move it to the desired place. The glass core of an optical fibre (diameter =125 μm) and a molybdenum wire (100 μm) were used to make a single bristle brush.

3.9.2.3 Printed Circuit Boards and Circuit Substrates

The function of the printed circuit board is to maintain electric connection between the devices. For this purpose, three sets of miniaturized gold printed circuits boards (2.5 mm x 1.5 mm x 0.25 mm) were designed and fabricated on an alumina substrate with a footprint that is compatible with the pads of the WLP0402 package, see Figure 3-9.

These designs were the preliminary version and through the work, some of them were subject to major modification to enhance circuit performance. However, due to limited financial resources and the high cost of fabricating a new set of these printed circuit boards, we adapted an alternative method to implement the electronic circuits. In this new technique, the electronic devices are mounted upside down and glued to an ultra-thin (125 μm) glass substrate (or only a thin layer of glue of small areas). This piece of glass is then glued to the internal metal base of the transition chamber (which acts as a reflecting ground plate under the bottom face the glass substrate), see Figure 3-10.

The dielectric constant of this type of glass (5.6) and the glue (2-3) are smaller than that of the alumina (9-11) and thus lower the capacitance introduced between the top layer and the ground layer.

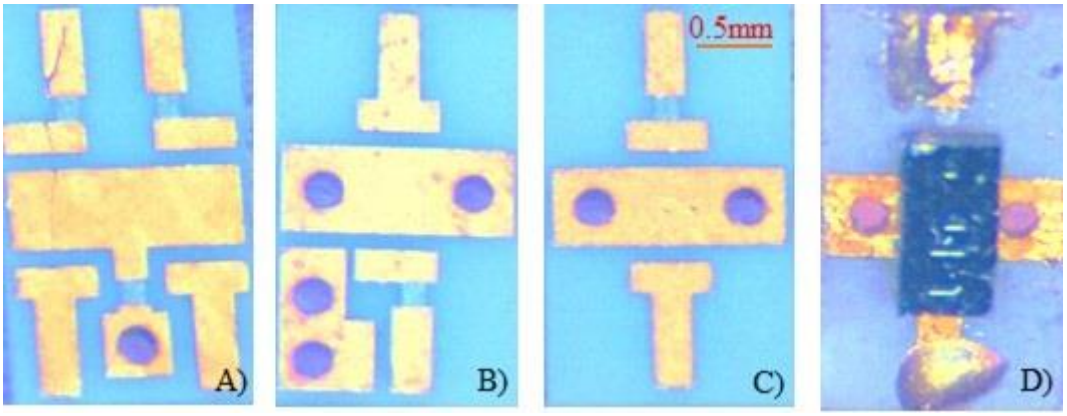

Figure 3-9 Miniaturized alumina printed circuit boards. A) PCB for the currnt probe with diffrintial loop antenna. B) PCB for the currnt probe with single end lop antenna. C) PCB for the voltage probe. D) PCB for the voltage probe with miniaturized amplifiere attached to it.

Among many types of glues, that have low viscosity and thickness, we found that the new generation of liquid plastic ultraviolet light curing adhesives is more suitable. The ultraviolet light cures the liquid plastic in less than 10 seconds. This light-controlled curing permitted wide flexibility to correct the position and/or relocate the piece. The final step is to make the electric connections with silver conductive epoxy on the top face of the electronic devices, see Figure 3-10.

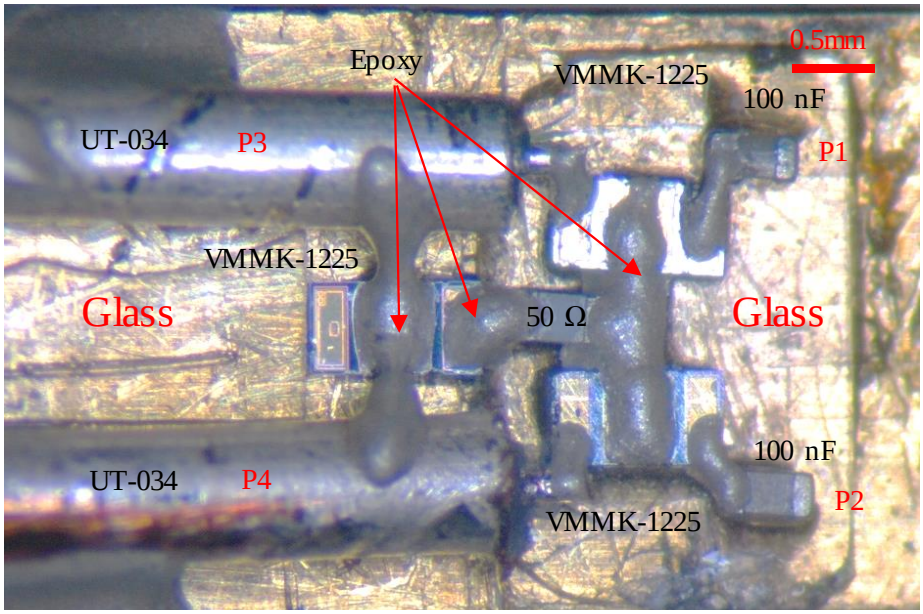

Figure 3-10 Thin layers of glass used as a substrate inside the transition unit. The complet circuit diagram is shown in Figure 5-15 and 5-16.

The main advantages of this technique over the traditional printed circuit boards are:

- Enhancing overall probe sensitivity (see section 4.10.1) by eliminating the additional shunt capacitor introduced by the PCB between the pads of the active device and the ground plate especially at the input side (depending on the area of metal connected to that pad). The value of this capacitance for the PCB shown in Figure 3-9 is around 0.15 pF.
- All connections can be visually inspect and modified before epoxy curing.
- Reducing the spacing between the elements of the circuit which means a smaller area for implementation and smaller electrical length compared to the operating wavelength.
- Rework and circuit modification is easier to do, scratching the cured conductive link with a sharp needle is sufficient to remove it.
- The thin glass substrate allows more free space inside the transition chamber.

3.9.3 Materials Used in Implementing Output Interface Unit

Materials used in this part are a 50 Ω coaxial cable and appropriate RF connector. Miniaturized coaxial cables are commercially available in different sizes and can be either flexible or semi-rigid. Although the miniature flexible cables are mechanically easier to deal with, their bandwidth is limited[14] and their low-quality shielding makes them inappropriate to use in high electromagnetic field density environments.

The smallest semi-rigid coaxial cable UT013 (outer diameter = 330 μm) is mechanically fragile and terminating it with the standard RF connector is not possible. Therefore, we have selected the UT034 50 Ω semi-rigid coaxial cable. The outer diameter = 860 μm and the inner diameter is 200 μm which is smaller than the pad width of the electronic device packages attached to it see Figure 3-8 and Figure 3-10.

The end of the UT034 can be attached to the standard female SMA connectors to support probe compatibility with the other parts of the measurement system.

3.10 Environments of Real Measurements

Before proceeding to describe methods of measurement verification, it is more appropriate at this point to introduce three important devices and their geometrical details.

[14] They are initially fabricated for WIFI applications. For example, the miniaturized flexible 1.13 mm coaxial cable has a 6 Ghz bandwidth.

These parts are commonly found inside microwave transistors and quantifying their voltages and currents can lead to their required optimization.

The first is the bond wires that connect the semiconductor inside a device to the remaining parts, such as the leads, matching capacitors, and the dies inside the transistor. The second is the die itself which it is an array of the identical cells connected in parallel.

The last device is the microstrip transmission lines. The importance of the microstrip line comes from the fact that they exist in many microwave applications and circuits inside microwave transistors as well. For example, the ends of any bond wire are either connected to a pad located on a semiconductor die or to a lead. For both cases (the pad and lead) represent the upper conductor of a microstrip line isolated from the ground plane by an insulator (the substrate layer under the semiconductor or the insulator under the lead). Those mini microstrip lines are either feeding to or receiving from bond wires / dies and they are having their impacts on them.

3.10.1 Bond Wires

Bond wires, like any other wire, are electrically connecting two parts. This method of connection is widely used in semiconductor fabrication. It is accurate, fast and safe in connecting between miniaturized parts. Bond wires are usually arranged in groups or arrays inside a transistor, like a drain or the gate bond wire array. The following sections are intended to describe the arrays of bond wires and their main geometrical and electrical characteristics.

3.10.1.1 Bond Wires Geometrical Characteristics.

Bond wires are normally distributed in arrays of wires made from high conductivity metals and the range of their diameters extends from 5 µm to 500 µm [177]. However, practically they are classified into: fine bond wires (< 20 µm), standard or thick bond wires (25 µm to 100 µm) and heavy bond wires (125 µm to 500 µm) [178], [179].

Pitches between bond wires mainly depend on the wire diameter, bonding area and the dimension of the tool (Capillary or Wedge) used to bond them. Thus, pitches between bond wires are also classified into three groups: ultra fine pitch (< 50 µm) with fine wires only, fine pitch ((75 µm to 190 µm, standard wires) and (250 µm to 700 µm, heavy wires)) and standard pitch ((125 µm to 280 µm, standard wires) and (350 µm to 1150 µm, heavy wires)) [178], [179], see Table 3-1.

Table 3-1 Bond wire diameters and width of the pitches between them [179].

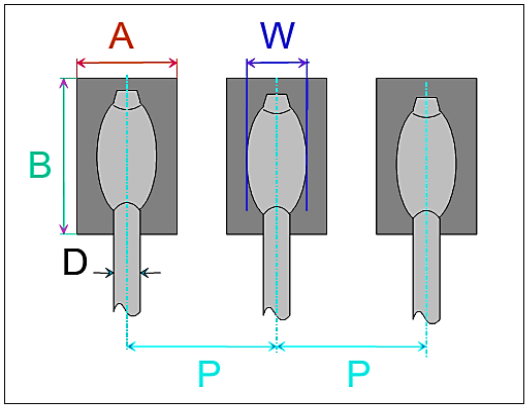

A pad width W bond width

B pad length P pitch

D wire diameter

wire D	standard				cutting edge			
	A	B	P	W	A	B	P	W
1Mil	100µm .004in	125µm .005in	125µm .005in	45µm .0018in	50µm .002in	75µm .003in	75µm .003in	38µm .0015in
2Mil	125µm .005in	150µm .006in	200µm .008in	75µm .003in	90µm .0036in	125µm .005in	140µm .0056in	70µm .0028in
3Mil	180µm .0072in	200µm .008in	250µm .01in	125µm .005in	120µm .0048in	170µm .0064in	150µm .006in	112µm .0045in
4Mil	200µm .008in	280µm .0112in	280µm .0112in	130µm .0052in	150µm .006in	220µm .0088in	190µm .0076in	130µm .0052in

wire D	Heavy wire							
	A	B	P	W	A	B	P	W
5Mil	250µm .01in	300µm .012	350µm .014in	150µm .006in	175µm .007	250µm .01in	250µm .01in	150µm .006in
6Mil	250µm .01in	500µm .02in	400µm .016in	200µm .008in	230µm .0092in	320µm .0128in	250µm .01in	180µm .0072in
10Mil	400µm .016in	800µm .032in	600µm .024in	320µm .0128in	350µm .013in	500µm .02in	350µm .013in	300µm .012in
20Mil	800µm .032in	1300µm .052in	1150µm .046in	650µm .026in	660µm .0264in	950µm .038in	700µm .028in	600µm .024in

Two main geometries are used, the wire (widely used) and the ribbon (used for high-frequency applications to increase the surface area and reduce unwanted coupling [180], [181]) and they are made either from copper, aluminium or gold.

The cost, method of bonding and the properties of these materials are the important factors that classify the applications they are used for. Table 3-2 illustrates nominal range of dimensions for each type of material and for both geometries.

Table 3-2 Bond wire size range for gold, aluminium and copper in comparison with dimensions range of the ribbon [182].

	Au	Al	Cu	Ribbon
Wire Size Range (µm)	15-51	25-250	15-76	12-51(thick) 51-250(wide)
Min. Recommended Pitch (µm)	35	75	35	N/A
Min. Recommended Bond Pads (mils)	2 x 2	3.5 x 3.5	2 x 2	3 x 3

For commercial devices, the largest size bond wire that can be attached to it mainly depends on the bonding area (pad area) at the semiconductor metal contact [183]. In a microwave application, it is needed to make the total area of the semiconductor small compared to the operating frequency. For this reason, it is rare to see wires of diameters larger than 50 µm used in microwave devices. In fact, many publications [180], [182],

[184], [185] indicate that for microwave applications, 50 µm is the upper limit of the wire size.

3.10.1.2 Bond Wires Electrical Characteristics.

The designer of microwave devices needs to consider many factors before selecting the proper size of the bond wire, like the size of the bonding area, impedance matching and most importantly, the current handling capability for the cases of power transistors. The size for microwave applications extends from 18 µm to 50 µm [183] (a slightly wider range from 12.5 µm to 50 µm is given in [184]). However, in the microwave power transistors, where the demand is for high current capability, the 25 µm or thicker diameter is often used [183]. The electric characteristic of the bond wires in Figure 3-11 can explain the reasons behind this selection.

The bond wire self-inductance is inversely proportional to its diameter and a noticeable decrease is shown in Figure 3-11(A) for diameters thicker than 25 µm (which mean higher current capability). The opposite of this behaviour is illustrated in Figure 3-11(B) for the bond wire capacitance.

The fusing current value is defined as the amount of current that causes the wire to melt. As expected for any conductor, the value of the fusing current increases as the diameter of the conductor increase, see Figure 3-11(C).

For safe operation, the rated current should be kept around the 50% of the fusing current [184]. For example, a 1 Amp current requires three 25 µm gold bond wires and with aluminium wires, it needs seven wires. For the same conditions, nine gold wires of 15 µm diameter would be needed.

In contrast to fusing current, the DC resistance decreases and goes below 450 mΩ per 10 mm length for gold bond wires diameters ≥ 25 µm, while it is around 2 Ω for 15 µm, see Figure 3-11(D).

The last important property is the AC resistance of the bond wire which is a function of the frequency. At high frequency, the effect of the skin depth becomes dominant and thus the effective cross-section area, that is allowed for the current to pass through, becomes smaller [180]. In Figure 3-11(E) the AC resistance of the 25 µm (1 mil) gold bond wire increased by the ratio of 3.19 as the frequency increased from 100 MHz to 1 GHz.

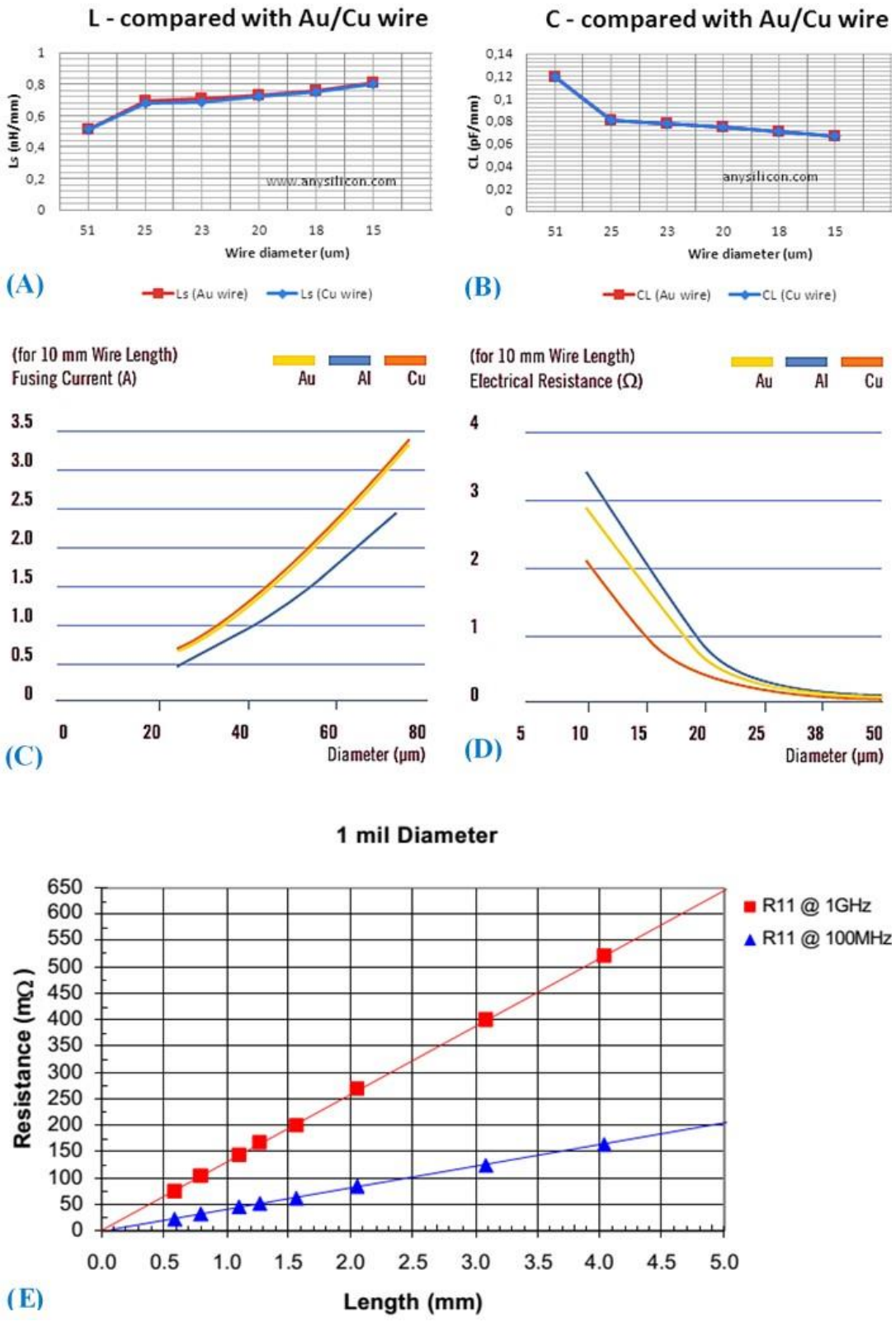

Figure 3-11 The electric characteristic of the bond wire. (A) Inductance variation with wire diameter [186]. (B) Capacitance variation with wire diameter [186]. (C) Fusing current variation with wire diameter[187]. (D) DC resistance variation with wire diameter[187]. (E) AC resistance variation with wire frequency for 25 µm (1 mil) gold bond wire [188].

3.10.2 Layout of Transistor Die

Microwave transistors with high power capabilities usually consist of an array of smaller transistors (cells). Each of the individual cells consists of at least three parts: source, gate and drain (FET transistor), see Figure 3-12(A).

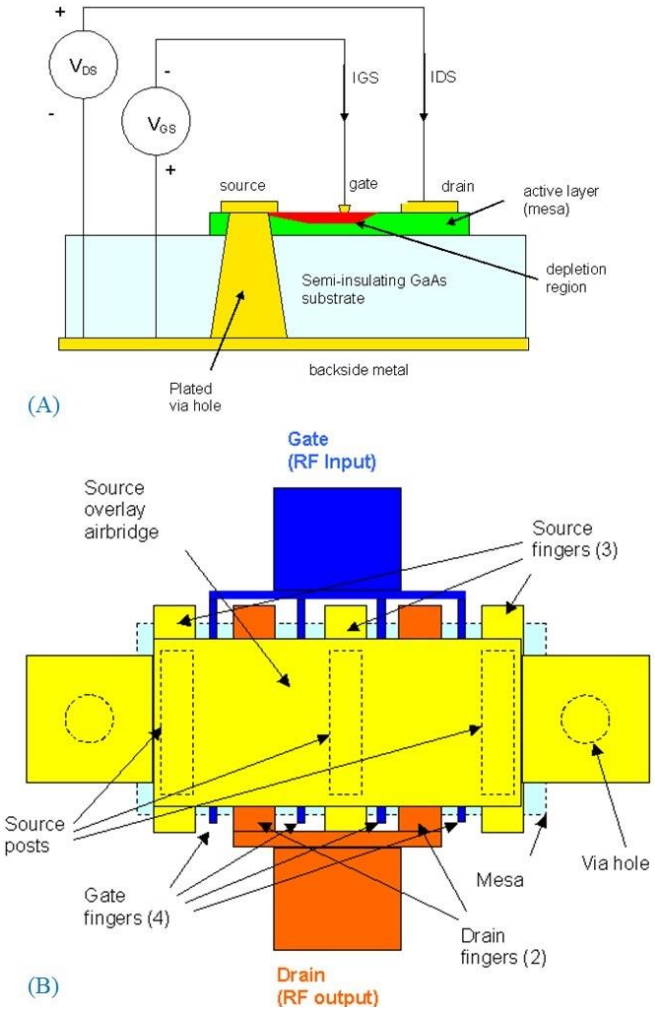

Figure 3-12 (A) structure of a transistor. (B) Bottom surface view of RF transistor die [189].

These three terminals of each cell are connected in parallel respectively and sharing one large physical structure called the die. The gates, sources and drains of these small transistors are distributed along the surface of the die and look like a chain of strips (fingers) with a repeated sequence, see Figure 3-12(B).

Unlike the case of the currents passing through the bond wires where all of them are carrying current in the same direction, currents through adjacent source-drain fingers are in opposite directions. This will introduce much stronger electromagnetic fields between them. Depending on the number of cells per die, if it is even or odd, the fingers at the

edges of the die are either of the same or different types respectively, see Figure 3-13. Large transistors have more than one die, if the edges of the adjacent dies are of similar types then a bridge wires connect these similar ends.

Information about the finger dimensions is not usually addressed in the datasheets of the devices. Larger finger width allows higher current handling capabilities while the wider spacing between fingers reduces thermal resistance which in turn improves power disruption among them. However wide finger/space means larger die as well and this can affect the overall performance of the die [115]. Because of that, the choice of the finger/ space width is a trade-off between the two issues.

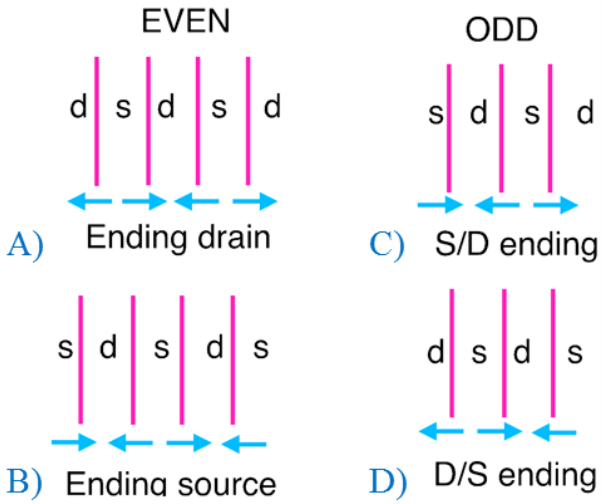

Figure 3-13 The number of fingers per die is either even or odd and the fingers at the edges of the die are either of the same or different types respectively [190]. A) Both eands are drain. B) Both eands are source. C) First end is source and the last is drain. D) First end is drain and the last is source.

3.10.3 Microstrip Line.

The microstrip line is a transmission line and its geometry include three layers, the top strip and the bottom ground plane are conducting materials while the middle layer is an insulating material (substrate). Copper or gold are usually used to implement the strip and ground plane due to their electrical and mechanical characteristics. The dielectric layer could be made from Polytetrafluoroethylene (PTEE), Ceramic, Silicone, Gallium Arsenide or Alumina [191]. The width (W) of the strip, thickness (h) of substrate and the dielectric constant ($\mathcal{E}$) of the substrate identify the value of the characteristic impedance of microstrip transmission line, see Figure 3-14, and it is given as follows [192]

$$Z_o = \frac{60}{\sqrt{\varepsilon_{eff}}} \ln\left(\frac{8h}{W} + \frac{W}{4h}\right)(\Omega) \qquad for\ \frac{W}{h} \leq 1 \qquad (3\text{-}1)$$

$$Z_o = \frac{120\pi}{\sqrt{\varepsilon_{eff}}\left[\frac{W}{h} + 1.393 + 0.667\left(\frac{W}{h} + 1.44\right)\right]}(\Omega) \qquad for\ \frac{W}{h} \geq 1 \qquad (3\text{-}2)$$

$$\varepsilon_{eff} = \frac{\varepsilon + 1}{2} + \frac{\varepsilon - 1}{2}\frac{1}{\sqrt{1 + \frac{12h}{W}}} \qquad (3\text{-}3)$$

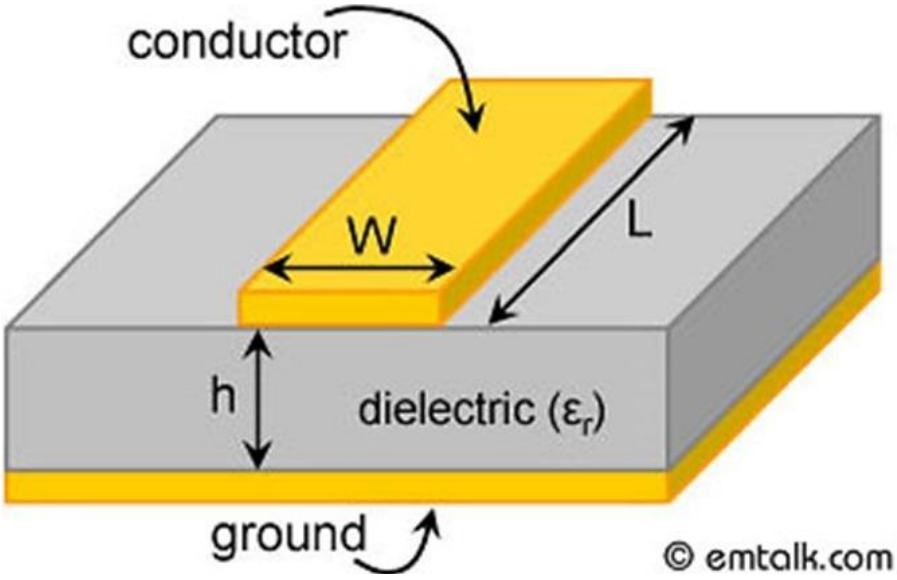

Figure 3-14 Microstrip transmission line structure [193].

3.10.3.1 Microstrip Line Current Distribution across its Width.

At DC and low frequency, the distribution of the current across the width of the strip conductor is uniform [194]. As the operating frequency increases the skin effect losses increases and thus the AC resistance of the strip increases too, see Figure 3-15(A). Therefore, the electric charges diverge away from the core of the strip towards its surface to be confined in its skin [194].

With the existence of the ground plane under the strip, an electrical attraction occurs between the opposite charges on the bottom surface of the strip and the top surface of the ground plane [195].

These effects concentrate the current in the edges [161], [196] and the bottom [195] of the strip line to produce current distribution like an inverted umbrella [197], see Figure 3-15(B).

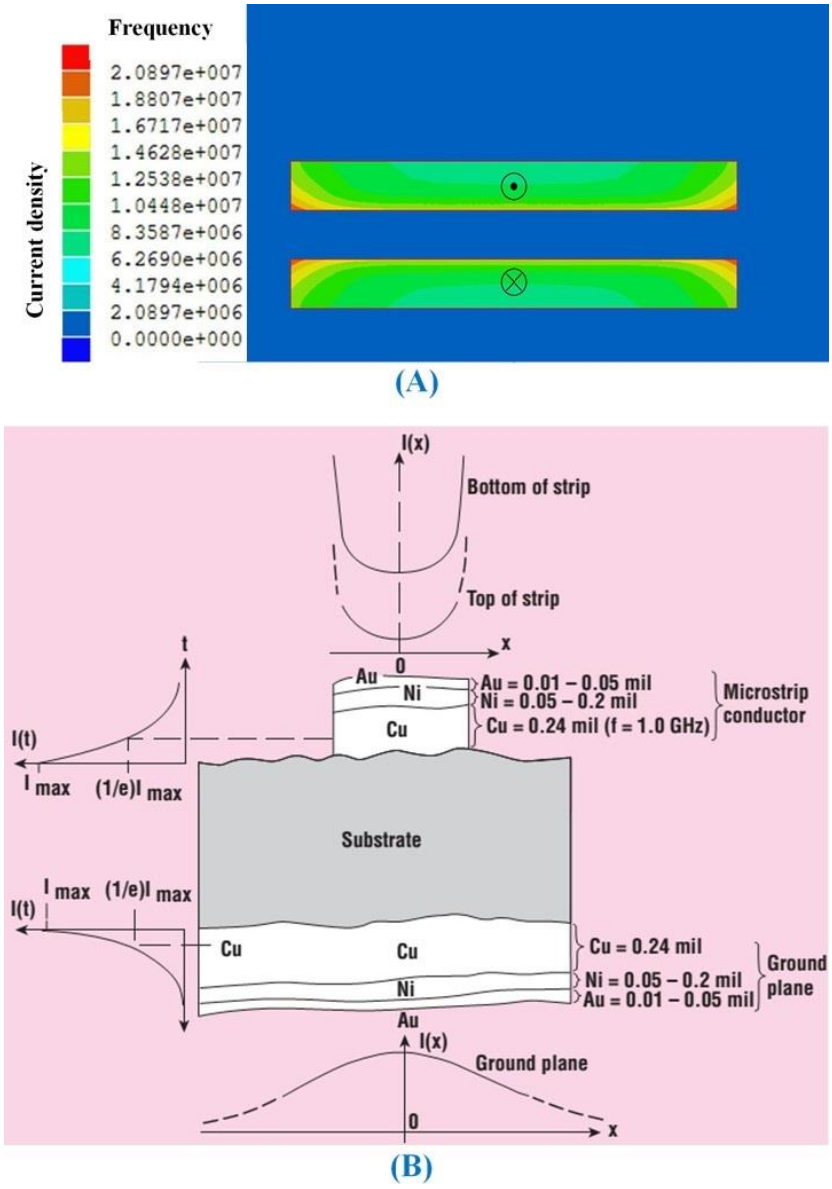

Figure 3-15 (A) Current distribution in the cross-section of two parallel plates as a function of the operating frequency [195]. (B) A cross-section of the microstrip line showing the inverted umbrella shape of the current distribution [192].

3.10.3.2 Microstrip Line Current and Voltage Distribution along its Length.

Like any transmission line, see Figure 3-16(A), distribution of the voltage and current along the length of the microstrip line is decided mainly by the load that terminates it. If the load impedance is equal to the microstrip line characteristic impedance, ($Z_o = R_o = R_L$), given in (3-1) & (3-2) then matched termination takes place.

Therefore, the whole incident power is absorbed by the load and no reflected power returns to the source. Observation of voltage and current wave (as a function of position) shows a uniform (constant level) distribution for both [191], see Figure 3-16(B).

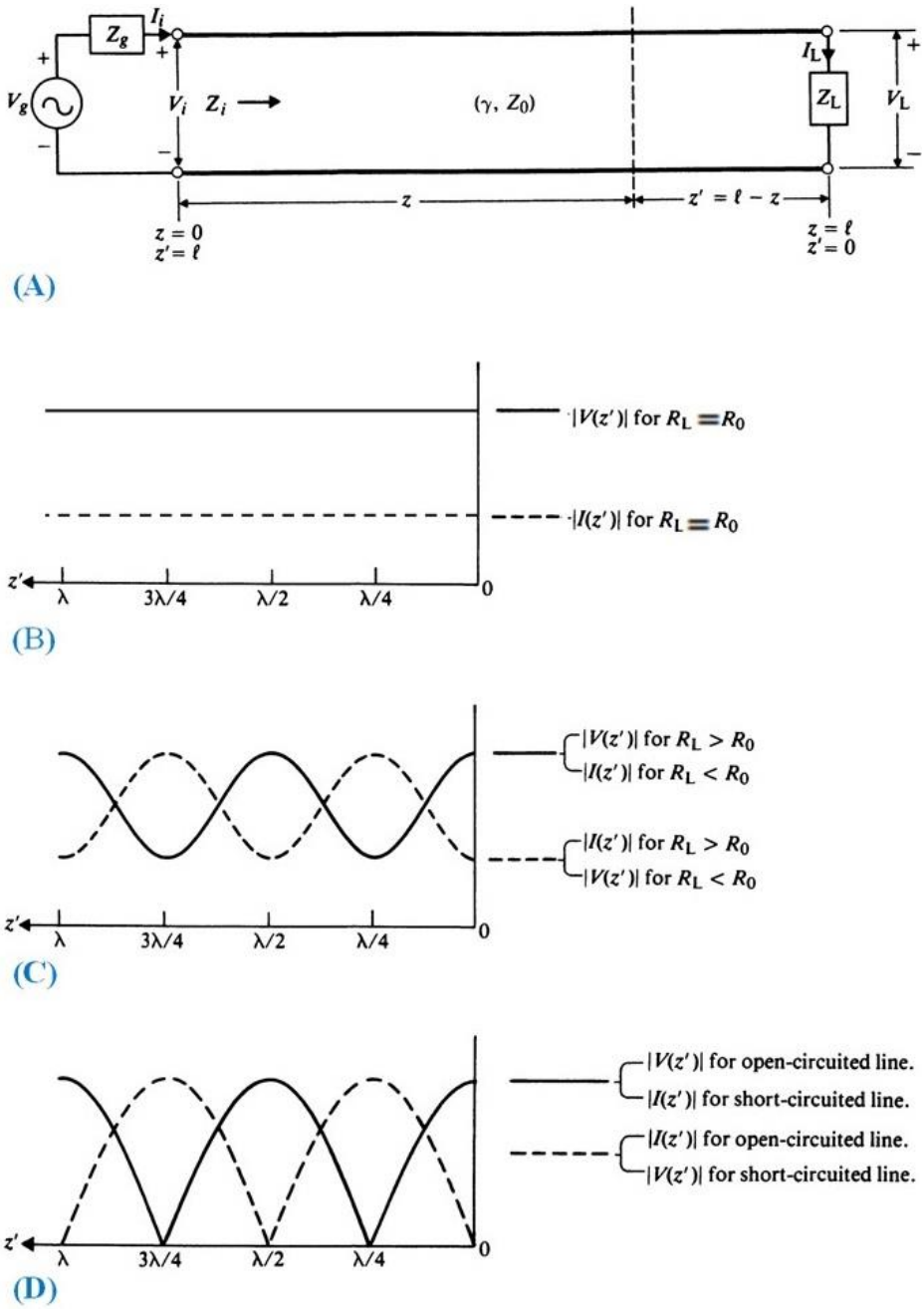

Figure 3-16. (A) A transmission line terminated with load impedance Z_L. (B) Voltage and current waves on matched termination $R_o = R_L$. (C) Voltage and current waves on mismatched termination $R_o \neq R_L$. (D) Voltage and current waves on short and open termination [198].

Any other value for load, larger or smaller than the characteristic impedance of the microstrip line (mismatching) ($Z_o = R_o \neq R_L$), leads to a percentage reflection of the incident power from the load toward the source. Thus, for the case of mismatching termination, both voltage and current signals has two waves travelling along the microstrip line in opposite directions between the load and the source. The net result of

those waves introduces what it is known as the standing wave for the voltage and the current respectively. They have a repetitive pattern that makes it look like a still wave along the length of the microstrip line. The standing wave of the current has its minimal and maximal values at the same location where the maximal and minimal of the voltage standing wave are respectively, see Figure 3-16(C). Those minimal and maximal values occur at an integer multiple of the quarter of the operating wavelength. A 90˚ phase shift between the standing wave of the current and the standing wave of the voltage always exists due to the reflection effect where the current wave inverting its direction of movement and phase (right-hand rule). Full reflection of the incident power occurs in two cases, when the load impedance is a short circuit and when it is an open circuit. For those cases, the minimal values of the standing waves become zero while the maximal values become double, see Figure 3-16(D).

3.10.4 Microstrip Taper Line

The bond wire can be treated as microstrip lines [199] and thus their characteristic impedance can be estimated [200] using (3-1). For a 25 µm bond wire with average height from the ground = 500 µm, it is approximately 260 Ω. Large power microwave transistors have many bond wires connected to the device leads in parallel to reduce overall wire inductance [201] necessary to handle high current requirements.

If for example, a transistor has an array of 20 bond wires and are connected to one of its leads then the estimated[15] total impedance under the above conditions can be less than 13 Ω. Microwave standard characteristic impedance is either 50 Ω or 75 Ω. Therefore, to avoid the reflection of the microwave power, either internal [185], [202] and/or external [203] matching device and/or circuit is required [204].

One of the most popular matching devices is the microstrip taper line due to its broadband response. Unlike the ordinary microstrip line where it has a constant characteristic impedance along its length, the characteristic impedance of the microstrip taper line is varied along its length. This dependency on the length could be either in the form of steps or continuous variation. There are many shapes of the continuous taper used to match microwave power transistors, like the linear taper, the exponential taper or the

[15] This estimation is for illustration purpose only and it does not reflect the actual values. Mutual effects between bond wires and semiconductor effects are not considered here. More precise calculations are required for realistic approximations.

Klopfenstein taper [203]. The narrow side of the taper has the high value of impedance while the wide side has low impedance.

The matching circuit could be inside the microwave transistor completely, and thus having narrow leads connected to the normal microstrip line, or part of it is outside the transistor, and therefore transistor leads are wide and flat with subsequent connection to a microstrip taper line, see Figure 3-6.

3.11 Miniaturized Test Fixtures

Three miniaturized test fixtures have been created to simulate three practical cases of bond wires to be used in probe testing and verification. These test fixtures are fabricated from thin film circuits to emulate the drain bond wires array inside power transistor, see Figure 3-17.

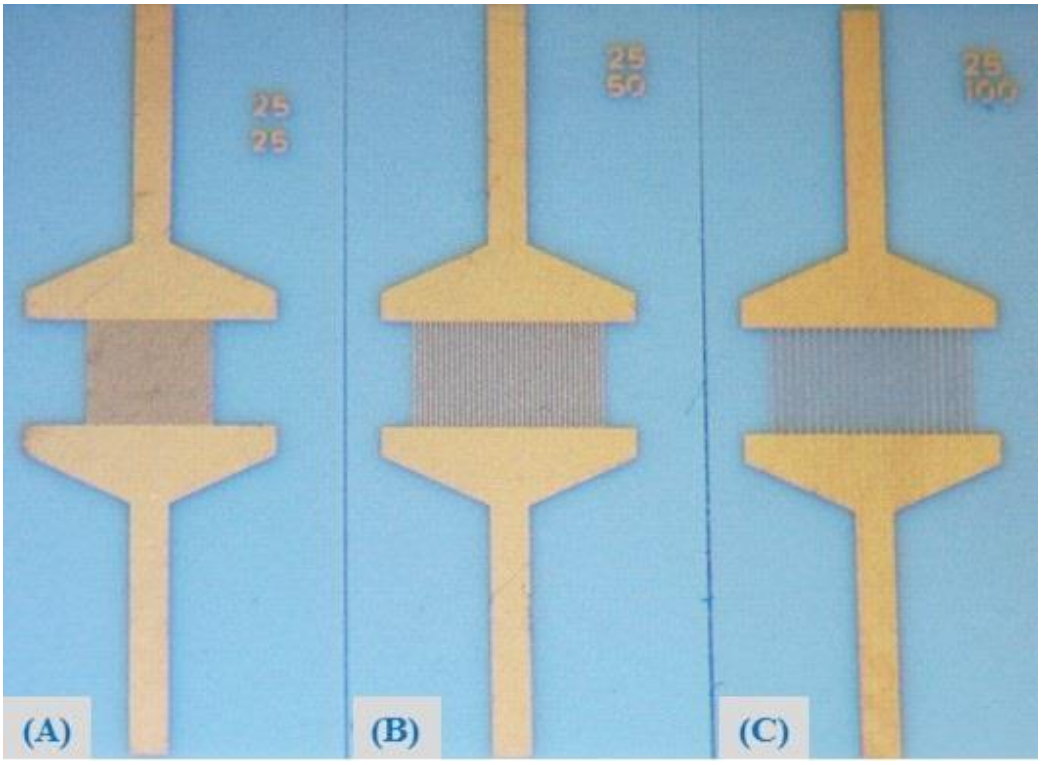

Figure 3-17 Miniaturized test fixtures. (A) 36 fingers of 25 µm width and 25 µm gap. (B) 30 fingers of 25 µm width and 50 µm gap. (C) 25 fingers of 25 µm width and 100 µm gap.

Three pieces of alumina of 250 µm thickness, 11.5 mm length and 4.5 mm width were used as a substrate for these test structures. The bottom layer is covered with a gold ground plane. The top layer is two 0.7 mm gold tracks where the width widens in the middle to two flat manifolds spaced by 1.5 mm (linear microstrip taper). These manifolds

are connected by a parallel array of gold fingers. The first test structure is for ultra-fine spatial resolution tests and has 36 fingers, with both 25 µm width and 25 µm spacing, shown in Figure 3-17(A). The second one is for fine spatial resolution test and has 30 fingers of 25 µm width and 50 µm spacing, shown in Figure 3-17(B). The last one is for standard spatial resolution test and has 25 fingers of 25 µm width and 100 µm spacing, shown in Figure 3-17(C).

3.12 Non-Intrusive Probing

In an ideal situation, the measurement should be non-intrusive so that the DUT has no variation in any of its properties while it is under measurement. However, in practical cases, each measurement might have its own impacts on the DUT.

Putting a metal object close to an electromagnetic source can affect the field distribution and thus might change its properties. It is clear that these effects are proportional to the size of the metal object and to the density of the electromagnetic sources within the DUT as well. The important thing here is the amount of change, if it is very small then this measurement can be described as a non-intrusive measurement.

In microwave circuits, the scattering parameters are widely used to define the important properties of the DUT. For passive components like the test fixtures shown in Figure 3-17, the four parameters for the input and output ports are the same ($S_{11} = S_{22}$ are the reflection coefficients and $S_{21} = S_{12}$ are the gain coefficients). Measuring these parameters before and after the presence of the probe in the vicinity of the DUT can provide an insight into the impacts of the probe.

3.12.1 Testing the influence of the Probe Transition Unit[16]

As shown in section 3.7 the whole body of the contactless probe is fabricated from metal and the largest cross-section of the transition unit is 4 mm, see Figure 3-7. On the other hand, the highest density of the electromagnetic fields is that of the test fixture shown in Figure 3-17(A).

In this test, the transition unit is moved away from the test fixture and both S_{11} and S_{21} are measured at different heights above the test fixture, 1 µm, 1 mm, 10 mm and 10 cm, see Figure 3-18(A) and (B) respectively. In both measurements, the change in these

[16] The input unit removed from the probe in order to inspect only the influence of the transition unit.

parameters increased with frequency and it is much clearer for the case of S_{21}. In addition to that, the largest variation can be seen between the 1 µm and 1 mm while the measurements at 1 mm, 10 mm and 10 cm are almost the same. These results emphasize the assumption given in section 3.7 regarding the length of the input unit (the brass tube in Figure 3-7).

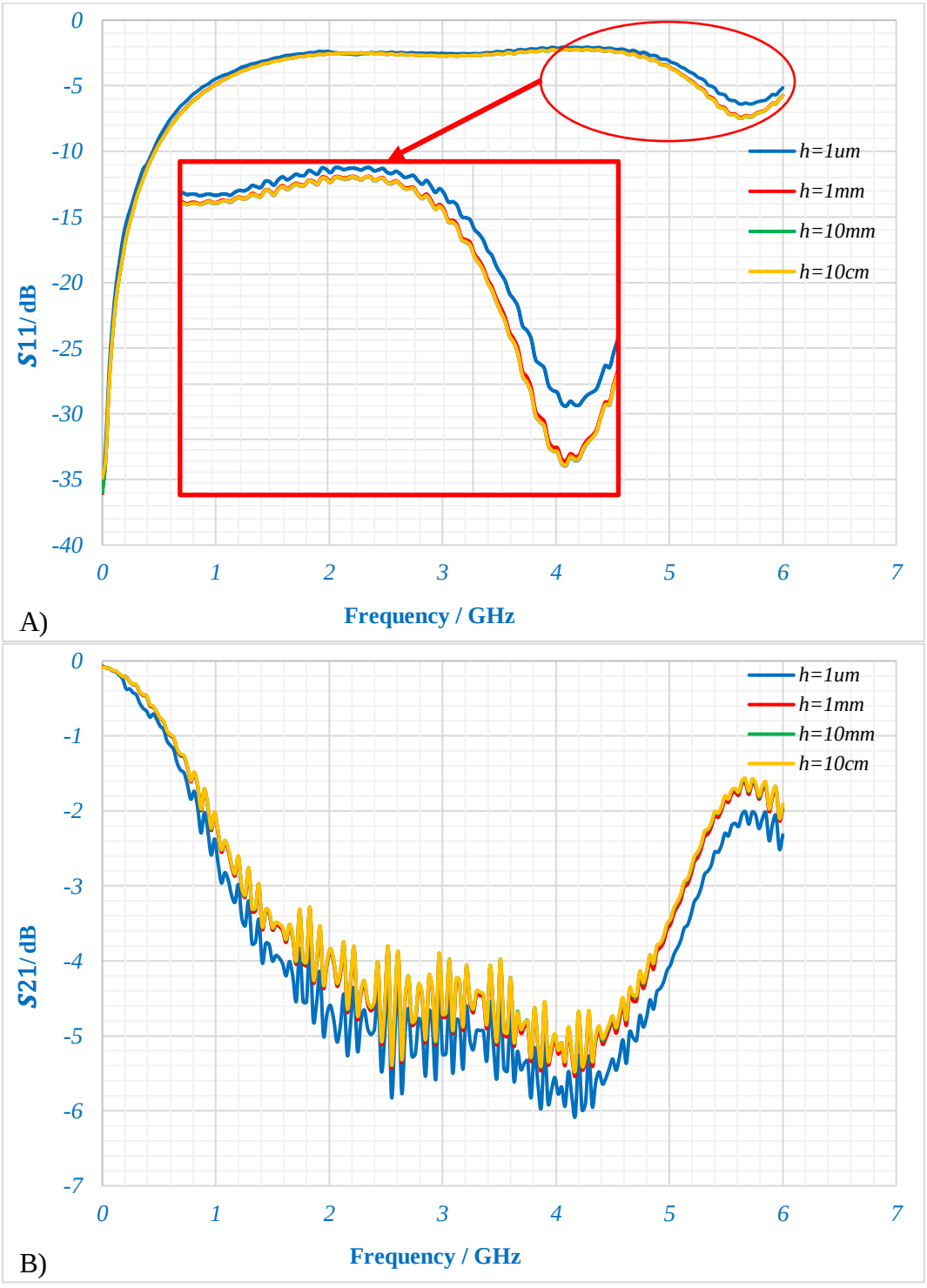

Figure 3-18 Influence of the presence of the transition unit on the S_{11} and S_{21}.

3.12.2 Testing the influence of the Probe Input Unit

The same previous tests are repeated here with an input unit (10mm brass tube) attached to the transition unit at different heights from the DUT (1 um, 1 mm and 10 cm). The results are shown in Figure 3-19(A and B) indicate that differences in the values S_{11} and S_{21} are very small, and the largest differences are 0.12 dB and 0.085 dB respectively. Under these conditions one can confidently claim that the contactless voltage and current probes are non-intrusive probes.

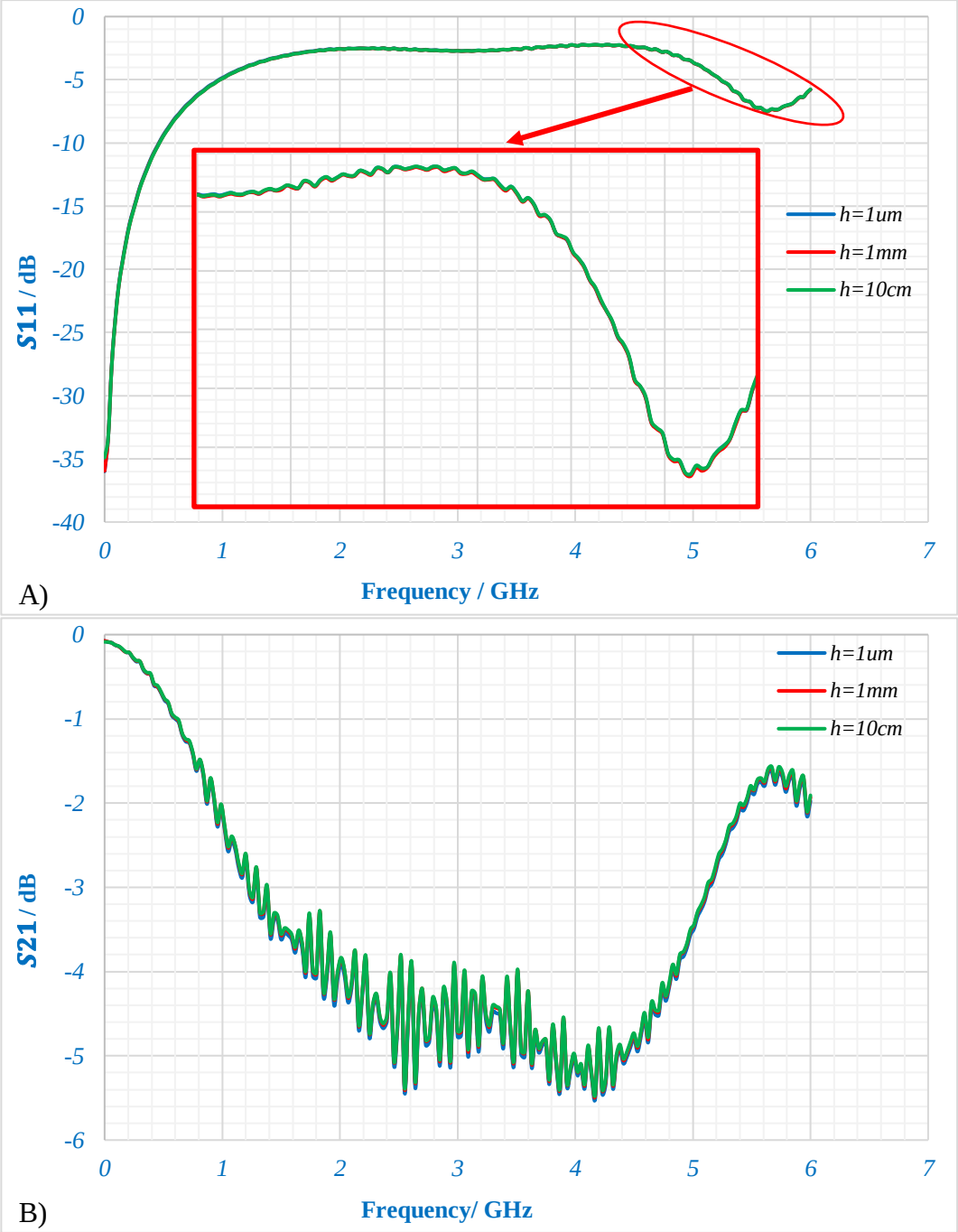

Figure 3-19 Influence of the presence of the input unit on the S_{11} and S_{21}

3.13 Measurement Verification.

Newly fabricated devices need to be tested and evaluated against the purpose they were created for. The contactless probes within this work have been fabricated mainly to serve inside microwave power transistors to measure voltage and current differences among bond wires. There are three important tests to be applied to these probes to examine their spatial resolution, bandwidth and fidelity of the measurement.

Before applying these test to the miniaturized voltage and current probes we applied them to 'scaled-up' probes fabricated from standard coaxial cables, see Figure 3-20(A-C) The results of these test are used as a reference to compare within the next chapters.

Figure 3-20 Contactless probe fabricated form stander coaxial cables. (A) Voltage probe. (B) Shielded current probe. (C) Unshielded current probe.

3.13.1 Measurement Fidelity verification.

Theoretical analyses, provided in chapter two illustrate, two important facts regarding the fidelity of the voltage and current measurement. The first one being that: the voltage probe can only sense the electric fields and it is immune to magnetic fields. The second fact is that: the current probe mainly responds to the magnetic field, but it is not inherently immune from the electric field and it needs external support to enhance current measurement fidelity. It is imperative that any alleged current probe should be subjected to two rigorous tests, the standing wave test and EFRR test, to demonstrate that current is being truly sensed, in the absence of any voltage pickup.

3.13.1.1 Standing Wave Test

Based on the details given in section 3.10.3.2, the fidelity of the current probe could be examined by traversing the length of a microstrip transmission line that has a high VSWR pattern (e.g. using an open/short circuit termination), see Figure 3-21. Such a test must show current minima (nulls) at the voltage maxima positions, and a suitable voltage probe must also be used to demonstrate that the voltage peaks do indeed interlace with the current minima.

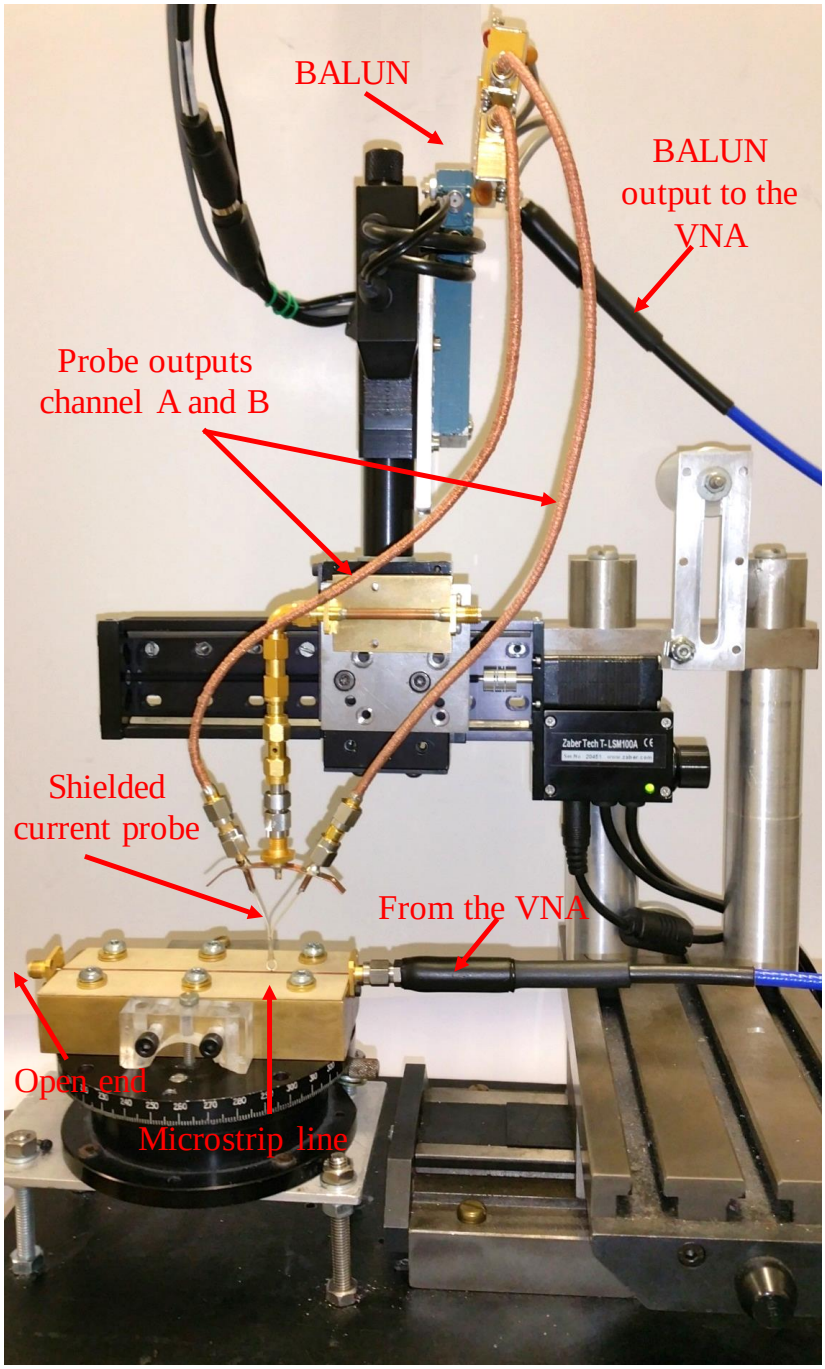

Figure 3-21 Setup for the standing wave measurements along a microstrip transmission line terminated with open load.

Three probes have been used in this test: the voltage probe, see Figure 3-20(A), the shielded current probe, see Figure 3-20(B), and the unshielded current probe, see Figure 3-20(C). Each of them scans a 10 cm microstrip line terminated with open load at one end and fed with 1mW at 6 GHz at the opposite end. The orientation of the loop antenna is parallel to the length of the microstrip line to pick up the magnetic field around the microstrip line. The BALUN used to subtract the outputs of the current probe and its output is connected to the VNA.

Figure 3-22 shows the results of these scans where the nulls of the shielded current probe are located almost at the maxima of the voltage probe. These results agree with theory given in section 3.10.3.2.

On the other hand, the nulls of the unshielded current probe are offset from the voltage probe maxima locations because this probe is picking up both the electric and magnetic field components.

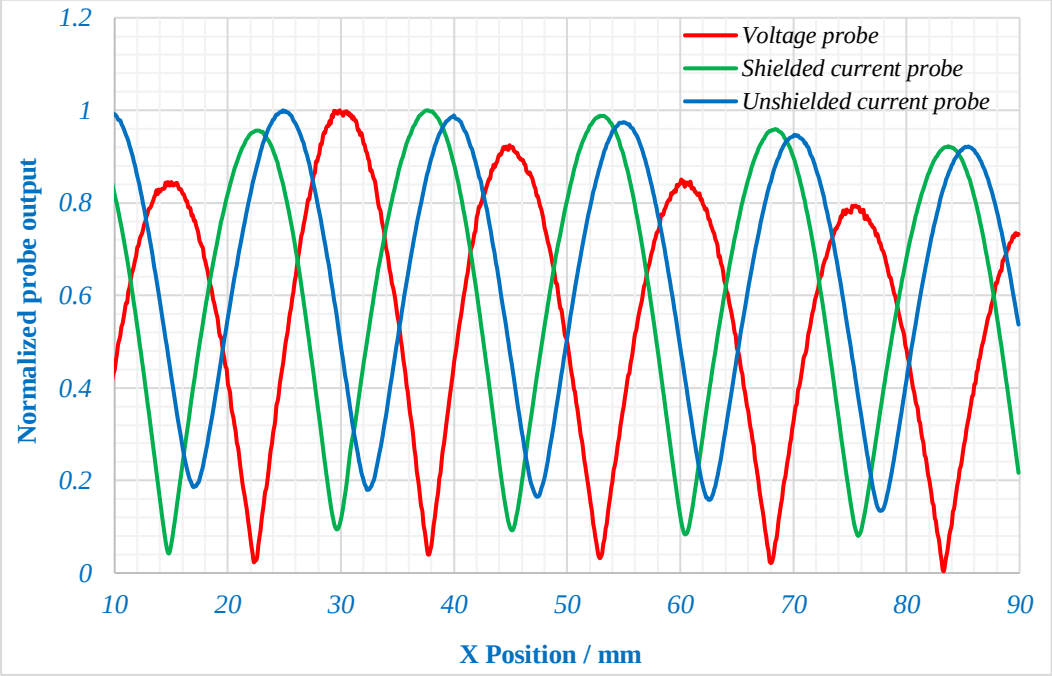

Figure 3-22 Results of the standing wave test.

3.13.1.2 EFRR Test

As explained in chapter two the output voltage of the loop antenna is a function of the angle between the plane containing the loop and the plane containing the path of the current. If this angle is set to zero-degrees, then this output voltage is mainly induced by the magnetic field and if it is set to ninety degrees, then this voltage is mainly induced by the electric field.

Using the shield and the differential loop one can reject the presence of the electric field significantly so that the loop antenna can be considered as a current sensing device. Equation 2-51 defined this rejection, EFRR, in terms of the ratio between the loop output voltage at zero-degree angle and the loop output voltage when the angle is at ninety degrees. The highest the value of the EFRR the better the current probe is.

To apply this test on the current probes fabricated from the standard coaxial cables we used the shielded probe shown in Figure 3-20(B). The setup for this test is the same as the previous setup, shown in Figure 3-21, but instead of moving the probe, it is placed at a fixed location above microstrip line loaded with 50 Ω.

The frequency of the VNA is swept over its whole range (30 KHz – 6 GHz) twice. In the first scan, the orientation of the loop is set to be parallel to the length of the microstrip line to measure loop response to the magnetic field in dB.

In the second scan the orientation of the loop is set to be perpendicular to the length of the microstrip line to measure the loop response to the electric field in dB. The magnitude of S_{21} of these two scans are shown in Figure 3-23, where the average value of the EFRR = 26 dB and the maximum is 42 dB at 0.3 GHz while the lowest value is 11.9 dB at 4.86 GHz.

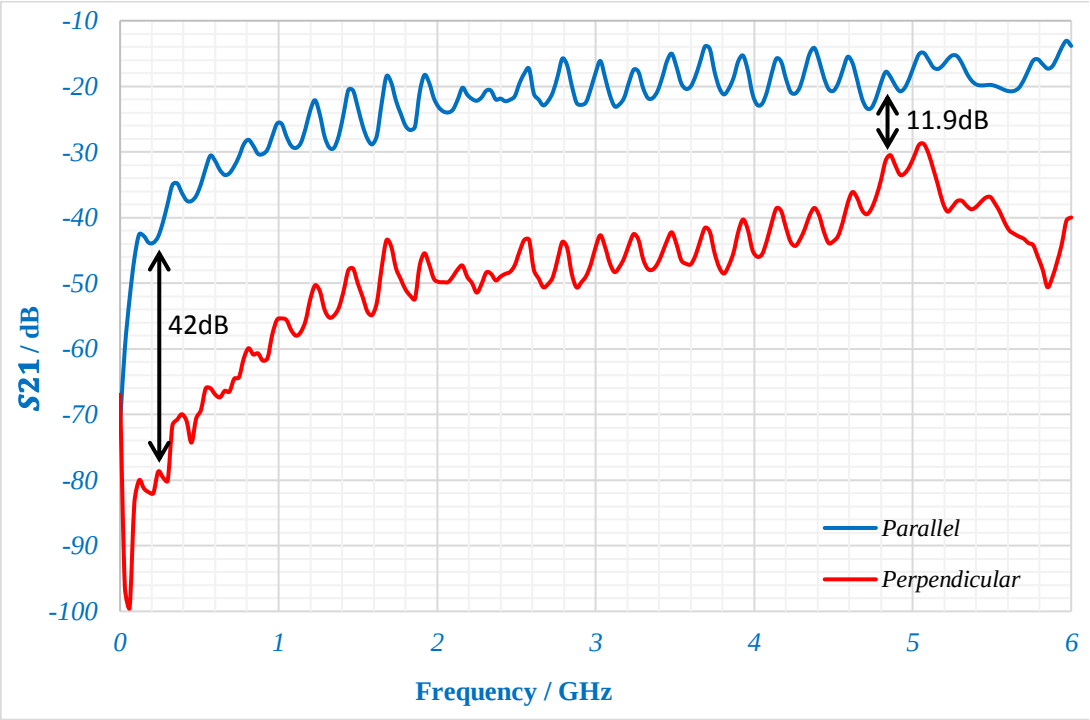

Figure 3-23 Results of the EFRR test.

3.13.2 Bandwidth Verification.

The bandwidth of the contactless probe can be obtained by placing the probe at a fixed location above the microstrip line and instead of moving it, a standing wave pattern is generated by terminating the microstrip line with short/open circuit load. The sweep of frequency at this fixed location shows the voltage/ current nulls traversing the probe tip and suggests a probe bandwidth [197].

In this test all three probes shown in Figure 3-20 are used here but each of these probes is kept still above the microstrip line at a location close the source side and the other end is terminated with open load. The frequency of the VNA is then swept to draw repetitive nulls and maxima for each probe, see Figure 3-24. The nulls of the shielded current probe occur at locations (in the frequency domain) close to the maxima of the voltage probe while those of the unshielded probes are displaced more than that.

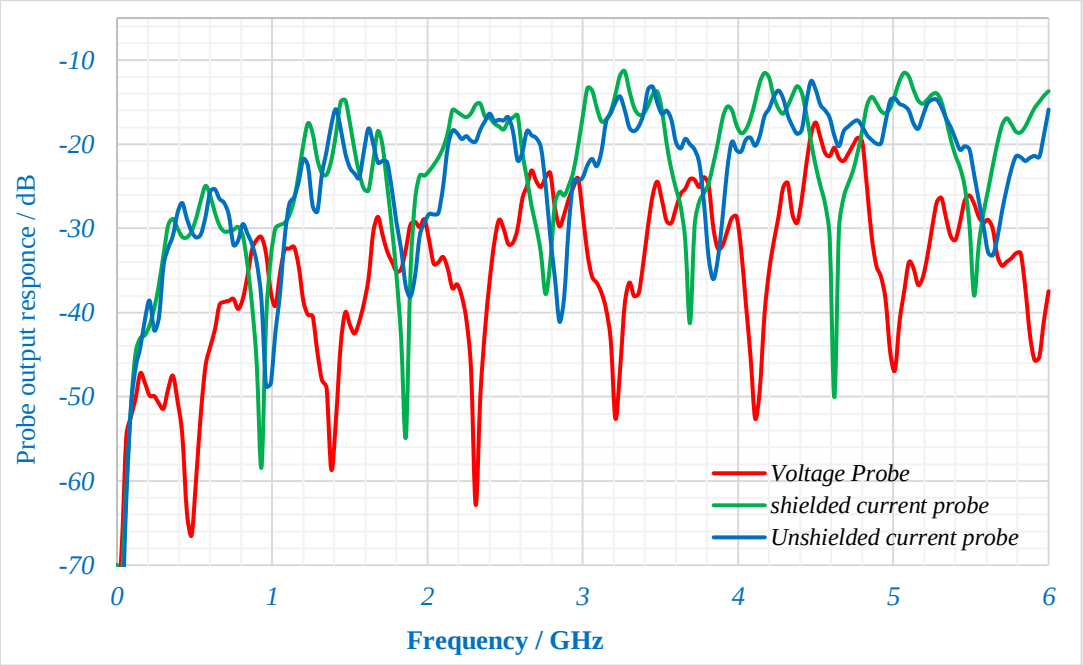

Figure 3-24 Results of the band width test.

3.13.3 Spatial Resolution Verification.

In a contactless measurement, the probe spatial resolution means its ability to recognize certain field components around a specific source among other adjacent sources. Four factors are affecting probe spatial resolution, two of them related to probe dimensions and its location with respect to the source and those will be discussed in detail in chapter four and five. The remaining two factors are the geometry of the source and the distances separating it from the adjacent sources, see sections 3.10.1 & 3.10.2.

4 VOLTAGE PROBE REALIZATION AND TESTING

4.1 Introduction

To design and implement a voltage probe with high spatial resolution it is essential to identify what is affecting the spatial resolution and how that can affect the sensitivity of the probe. Those two factors are the most important and they are discussed here in detail.

This chapter will focus on the influences of the geometrical aspects on both factors and through this chapter we establish design criteria. To address these criteria, scaled-up versions of the probes have been fabricated from standard coaxial cables, being much easier to fabricate and to handle compared with the miniaturised probes. Once the important characteristics have been deduced, one can then proceed to design and fabricate miniaturized contactless voltage probes with some overall optimisation.

In addition, the methods of enhancing probe sensitivity are discussed and examined. A 25 μm spatial resolution voltage probe has been implemented with the capability of having a passive gain at the desired operating bandwidth. Finally, the characteristics of the newly fabricated voltage probe are tested experimentally.

4.2 Contactless Voltage Probe Structure

The main three building blocks or units of the active probe are discussed in chapter three. Figure 4-1 illustrates these units for the active version of the contactless voltage probe: The input unit, the transition unit and output unit are represented by the input coaxial cable, the low noise amplifier and output coaxial cable respectively.

The geometry of the input coaxial cable affects both the spatial resolution and the sensitivity of the contactless voltage probe. Unfortunately, one general observation being that an improvement in one leads to a degradation in the other.

However, since sensitivity can be improved by acting on other parameters of the active probe, the geometry design tends to favour spatial resolution as its main target.

One way, among others, to enhance voltage probe sensitivity is to directly cascade the input coaxial cable with a low noise preamplification stage to produce an output signal compatible with the next stages of the measurement system, see section 3.2.

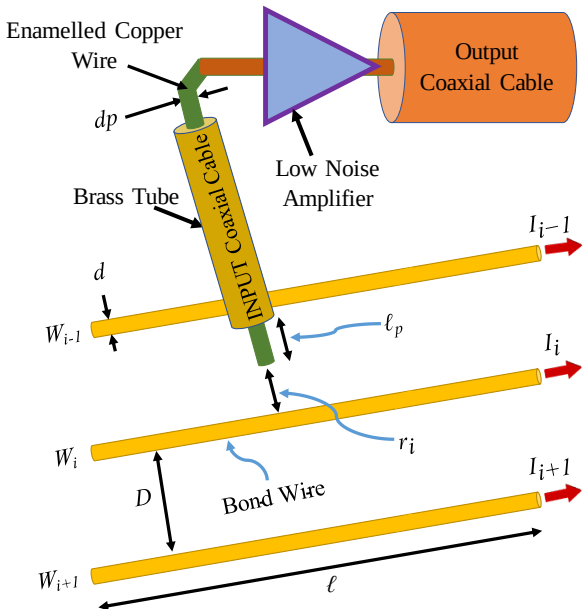

Figure 4-1 The main three elements of the active contactless voltage probe: the input coaxial cable, the low noise amplifier and the output coaxial cable.

4.3 Parameters Affecting Voltage Probe Spatial Resolution

In principle, the spatial resolution of any contactless probe is a function of the geometrical aspects of both the probe and the DUT. Practically, however, the geometry of the DUT cannot be modified to enhance the spatial resolution, therefore, we have only those of the

voltage probe and it is these probes that are subject to modification in order to gain the desired spatial resolution.

Although the voltage probe structure is relatively simple (a coaxial cable with one end open circuit), the influence of its geometry on its spatial resolution and sensitivity is relatively complex to analyse and therefore quantify. The geometry of the voltage probe tip has three parameters that affect its spatial resolution: protrusion length of internal conductor (ℓ_p), diameter of the internal conductor (d_p), internal diameter of the outer conductor (D_p). In addition to those parameters the distances between the active area of the probe and the DUT (r) have significant influence on the spatial resolution.

To keep the focus on the case of microwave power transistor, the DUT will be assumed to be an array of bond wires ($W_{i-1} - W_{i+1}$). These wires each share a proportion of the current (I_{DS} for Drain current and I_{GS} for Gate current) and ultimately transfer the RF power to to and from the DUT. For simplicity here, the length of each wire is (ℓ) and the spacing between any adjacent wires is (D) and the diameter of each wire is (d). In some practical devices, the bond wires can have slightly different lengths and shapes in order to augment the input/output matching characteristics.

The capacitive coupling between the probe tip and the elements of the array induce a displacement current given in (2-42). At specific values for the wire length and the electric current, the probe output voltage can be simplified to:

$$v_O = Kf^2 \frac{A}{r^2} \tag{4-1}$$

Where (K) is the probe constant, (f) is the frequency of operation, (r) is the distance between the probe tip and the DUT and (A) is the total surface area of the tip that exposed to the electric field lines.

The spatial resolution can be defined in terms of the maxima and the minima that appear while the probe is scanning across the adjacent wires. The maxima represent the regions of high field intensity above each wire, see Figure 4-2(B), and the minima represent the regions of low field intensity above the middle area between adjacent wires, see Figure 4-2(C). (Note that both of these figures illustrate a cross section that is perpendicular to the current flow.) This, of course, is based on the assumption that an equal voltage is present on each wire. Otherwise, the minima location could be anywhere in the region between them. In a direction parallel to the flow of current, the probe tip is exposed to the full length of the wire and the distance from the active interaction area of the probe can

have any value between (r_i) and ($r_i + \delta_{rm}$), see Figure 4-2(A). Similarly, the distances between array elements, on both sides of the maxima or minima locations, and the active area of the probe can have any value between (r_i) and ($r_{i\pm1} + \delta_{rm}$), where (δ_{rm}) is the maximum distance increment and ($r_{i\pm1} + \delta_{rm}$) represents the upper length boundary for each case, see Figure 4-2(B& C). The height of the probe from the plane containing array elements is measured at the maxima location and it is equal to r_i in Figure 4-2(A & B). Otherwise, (r_i) is the distance from W_i to the probe tip at any location.

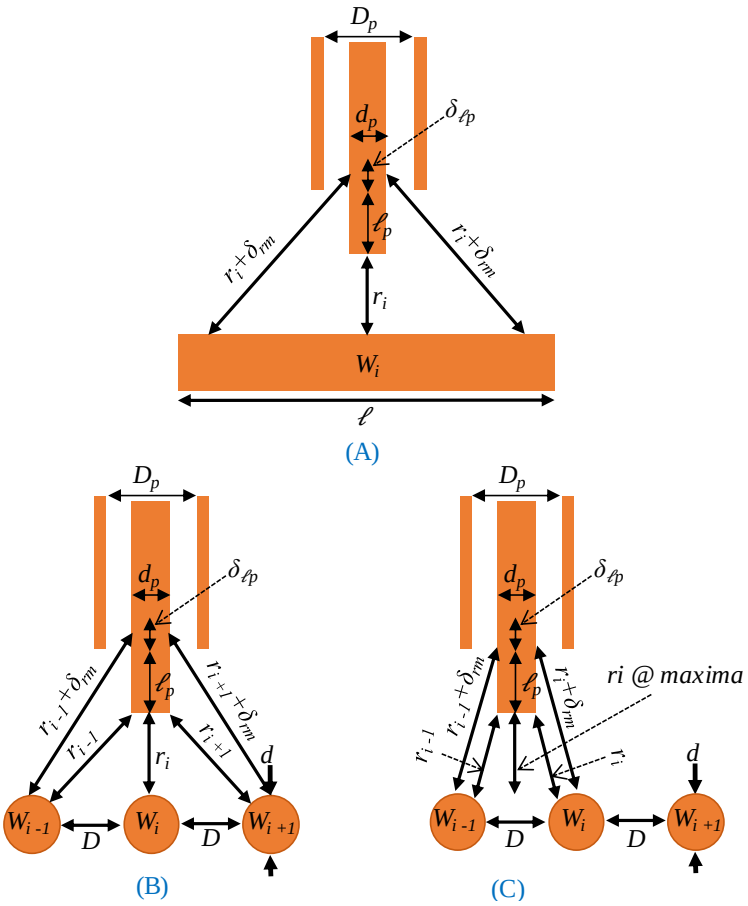

Figure 4-2 Definition of the geometrical parameters of the voltage probe and the distances to its active area: (A) Wire under probe tip. (B) Maxima location. (C) Minima location.

According to (2-39), the probe active area has two parts: the cross-sectional part (A_{dp}) and the cylindrical part ($A_{\ell p}$). The relative size and position of the probe tip with respect to the array elements will define whether the probe is interacting with one DUT element alone or whether the probe is sensitive to many adjacent DUT elements simultaneously. The significance of this is highlighted in section 2.9.2 where the concept of virtual shielding is introduced.

The proportion of the field received by each respective area, at any of these two locations (maxima and minima), depends on the distances between them and the elements of the array. For example, at the maxima locations, the field received by the cross-sectional area is dominant due to the short distance to the DUT element. In contrast, at the minima locations, the influence of cross-sectional area recedes as the distance between adjacent wires and the cylindrical area become shorter. Therefore, the effect of this area becomes dominant. The proportion to the overall signal each area provides can be quantified independently.

4.3.1 Influence of the Cross-sectional Area on the Spatial Resolution

This section shows the relationship between the diameter of the internal conductor and the spatial resolution. The cross-sectional area is given as:

$$A_{d_p} = \frac{\pi {d_p}^2}{4} \tag{4-2}$$

It can have one or three sub-areas at the maxima location, while it has three sub-areas at the minima locations.

At the maxima locations:

- if $d_p<D+d$ then A_{dp} can be modelled as a single area as it will receive only the electric field emanating from the wire directly under it, see Figure 4-3(A).
- if $d_p>D+d$ then A_{dp} can be modelled as three separate areas as it will receive the electric field emanating from three adjacent wires, see Figure 4-3(B).

At the minima locations:

- if $d_p<D$ then A_{dp} can be modelled as three separate areas, two side areas receiving the electric field emitted from the adjacent wires around it and in the middle sub-area will receive no field lines, see Figure 4-3(C).
- if $d_p>D$ then A_{dp} still has three divisions but the effectiveness of the side fields become dominants and thus preventing the probe from recognizing the null.

These four possibilities indicate that, where high spatial resolution is required, the diameter of the internal conductor should be smaller than the smallest gap distance between any adjacent DUT elements or wires. The main drawback to specifying an extremally miniaturized probe is the impact a small d_p has on lowering the output voltage provided by the voltage probe; which, in turn results in low sensitivity.

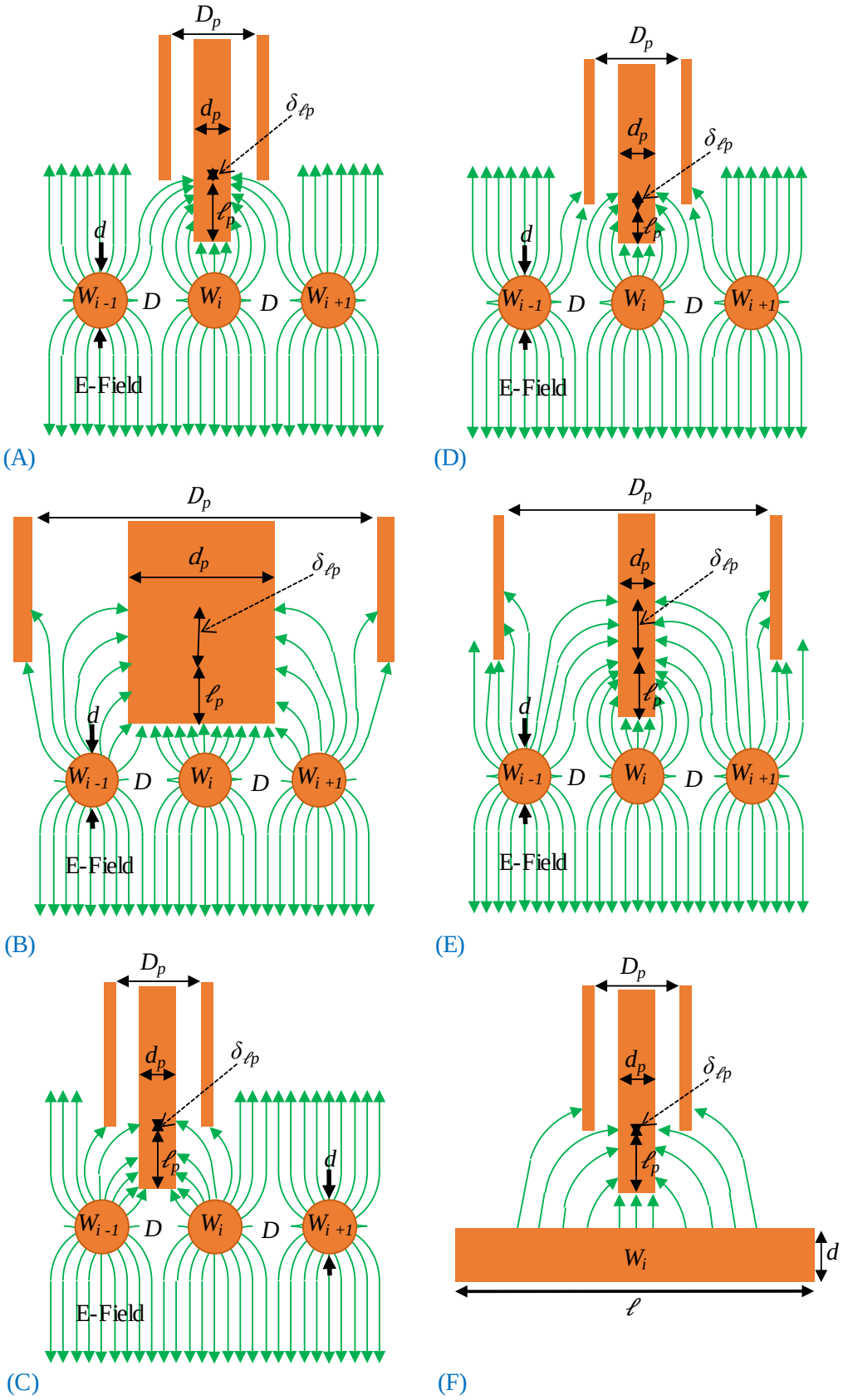

Figure 4-3 The influences of voltage probe parameters on the amount of electric field lines received by each part of its active area at maxima and minima locations (for details refer to sections 4.3.1 & 4.3.2).

4.3.2 Influence of the Cylindrical Area on the Spatial Resolution

This section illustrates the influence of the remaining probe geometrical parameters (length of protrusion and the internal diameter of the outer shield) on the spatial resolution. The cylindrical area is given by:

$$A_{\ell_p} = \pi d_p * (\ell_p + \delta_{\ell_p}) \quad (4\text{-}3)$$

Where, ($\delta_{\ell p}$) is the variation to the length of the probe tip due to the changes in D_p, see Figure 4-3(A, B, D & E).

At the maxima locations:

- if d_p<D+d then $A_{\ell p}$ will be surrounded (totally or partially depending on the value of ℓ_p+$\delta_{\ell p}$) with the electric field lines emitted from the wire under it. Where the coupling is exclusively from the wire below ((ℓ_p+$\delta_{\ell p}$) < (D+d)/2) then a so-called self-shielding occurs, blocking the fields from other wires, see Figure 4-3(D). If a partial coupling occurs ((ℓ_p+$\delta_{\ell p}$) > (D+d)/2) then the upper part of cylinder can be divided into four longitudinal sub-areas. The two sub-areas on the sides of the cylinder will receive the field lines from the adjacent wires W_{i-1} and $W_{i+1.}$ The contribution from these side areas (in comparison to that of the cross-sectional area) is very low due to the large distance (any value between $r_{i\pm1}$ and $r_{i\pm1}$ +δ_{rm}) from W_{i-1} and $W_{i+1,}$ see Figure 4-3(E).

  The front and the rear sub-areas are receiving field lines radiated along the length of the wire W_i. This enhances the magnitude of the output signal and spatial resolution, see Figure 4-3(F).
- For the case of d_p>D+d, it will be the same situation as that of the partially coupled case. The exception here is that cylindrical part of the whole protrusion can be divided into four sections and not just the upper portion.

At the minima locations, $A_{\ell p}$ has two parts only receiving electric field lines from the wires on the sides of the minima, see Figure 4-3(C). The distances from these wires to the cylindrical part becomes shorter (compared to those at maxima locations), see Figure 4-2(A & B).

If D approaches the value of d then these distances approach the value of r_i at the maxima locations. As a result, a higher output voltage is introduced reducing the probe's ability to differentiate between the minima and maxima locations.

Therefore, a maximum in spatial resolution can be achieved when both the length of the protrusion and the internal diameter of the outer shield are approaching their respective minimum.

The limit for the protrusion is zero, while the limits for the internal diameter of the outer shield is equal to the diameter of the internal conductor. This, of course, will increase the shunt capacitor to the ground (as it works as a voltage divider with the coupling capacitor) and hence reducing the overall sensitivity of the probe.

4.4 Quantification of the Spatial Resolution and Sensitivity

As shown in chapter two, there is no common definition given for the spatial resolution. The wire/gap width definition ($R_{wg} = (w + g)/2$, see section 2.12.2 for more details) provides a numerical description of the probe's spatial resolution in terms of geometrical aspects and this is a very important parameter. However, it just quantifies the probe's ability to recognize the existence of the wire/gap (black and white, i.e. contrast). It is more appropriate to associate it with the geometry of the DUT rather than the geometrical parameters of the probe.

This is clearly shown in the cases of testing a group of probes that have some variation in their geometrical aspects by the same DUT. All of them can have the same numerical value of the spatial resolution. Therefore, in many cases, to say which one is the best, the images of the DUT, created by an X-Y scan from each probe, need to be carefully examined, see Figure 2.29, 2.31, 2.36 and 2.40.

Instead of adapting the visual evaluation of the spatial resolution, we considered the ratio between the maxima and the minima voltages at the output of the probe as a new method of quantification. This technique permits the evaluation to be based on a range of numerical figures and thus provide more accurate comparison between different probes.

$$R_v = \frac{Output\ voltage\ at\ the\ maxima}{Output\ voltage\ at\ the\ minima} \tag{4-4}$$

Where, (R_v) is the spatial resolution quantified by output voltages ratio.

To make the comparisons easier, the line graphs of many scans results on the same chart have been normalized. The results of each scan are individually normalized to their highest values. This will create a single reference for all scans results at their maxima while the depth of the minima will indicate how high the spatial resolution is.

The other important factor in a probe's specification is its sensitivity. In contrast with the spatial resolution, this factor is proportional to the size of the probe active area and inversely proportional to the square of the distance from the probe active area to the DUT.

A similar method is used when comparing the sensitivities of a group of probes. Normalization is applied again, but this time it is with respect to the highest value among all scan results shown on the same chart. This allows all the line graphs to have the same scale and thus a better sensitivity comparison is introduced.

4.5 Experimental Validation of the Geometrical Aspects

In this section, we will experimentally inspect the influence of the voltage probe parameters (d_p, ℓ_p & D_p) on its spatial resolution and sensitivity. To keep the focus on the open end coaxial cable only, the ordinary coaxial cables are used to create the passive version of the contactless voltage probe. Three different sizes of semi-rigid 50 Ω coaxial cable (UT-034, RG405 and RG402) are used to implement passive open end coaxial cable voltage probes.

A three finger PCB test fixture (2 mm X 41 mm X 0.7 mm) is used to simulate the EM field environment of a bond wire array, see Figure 4-4. The width of each finger and the gap between any adjacent fingers is 0.3 mm and finger length is 11 mm.

The frequency of operation is set to 1 GHz to maintain negligible voltage variation along the finger length. The lowest scanning height (h) above the test fixture is set to 50 µm. Total scanning length is 6 mm and the scanning step size is set to 50 µm.

Input power delivered to this test fixture is 1 mW introduced by a VNA and the other end is terminated with a 50 Ω load.

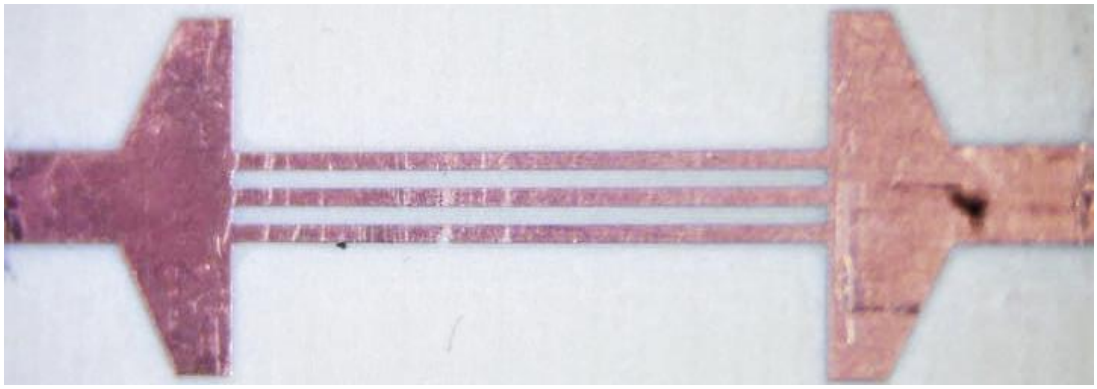

Figure 4-4 A three fingers PCB test fixture (22 mm X 4 mm X 0.7 mm) used to simulate the environments of bond wires array of 0.3 mm track/gap width.

4.5.1 Influence of ℓ_p on the Spatial Resolution and Sensitivity

Four probes with different protrusions (0 µm, 180 µm, 500 µm and 1000 µm) are fabricated from the UT-034. The deepest null (highest spatial resolution = 1.48) is shown in the scan results of ℓ_p = 0 µm, see Figure 4-5(A). In contrast to that, the highest level of sensitivity is achieved at ℓ_p = 1000 µm, see Figure 4-5(B). The array effect causes the electric field around the side wires to be lower than that around the middle wire, while imperfections from cutting of the probe tip introduce a minor asymmetry around the middle. Such imperfections can be eliminated by precision machining.

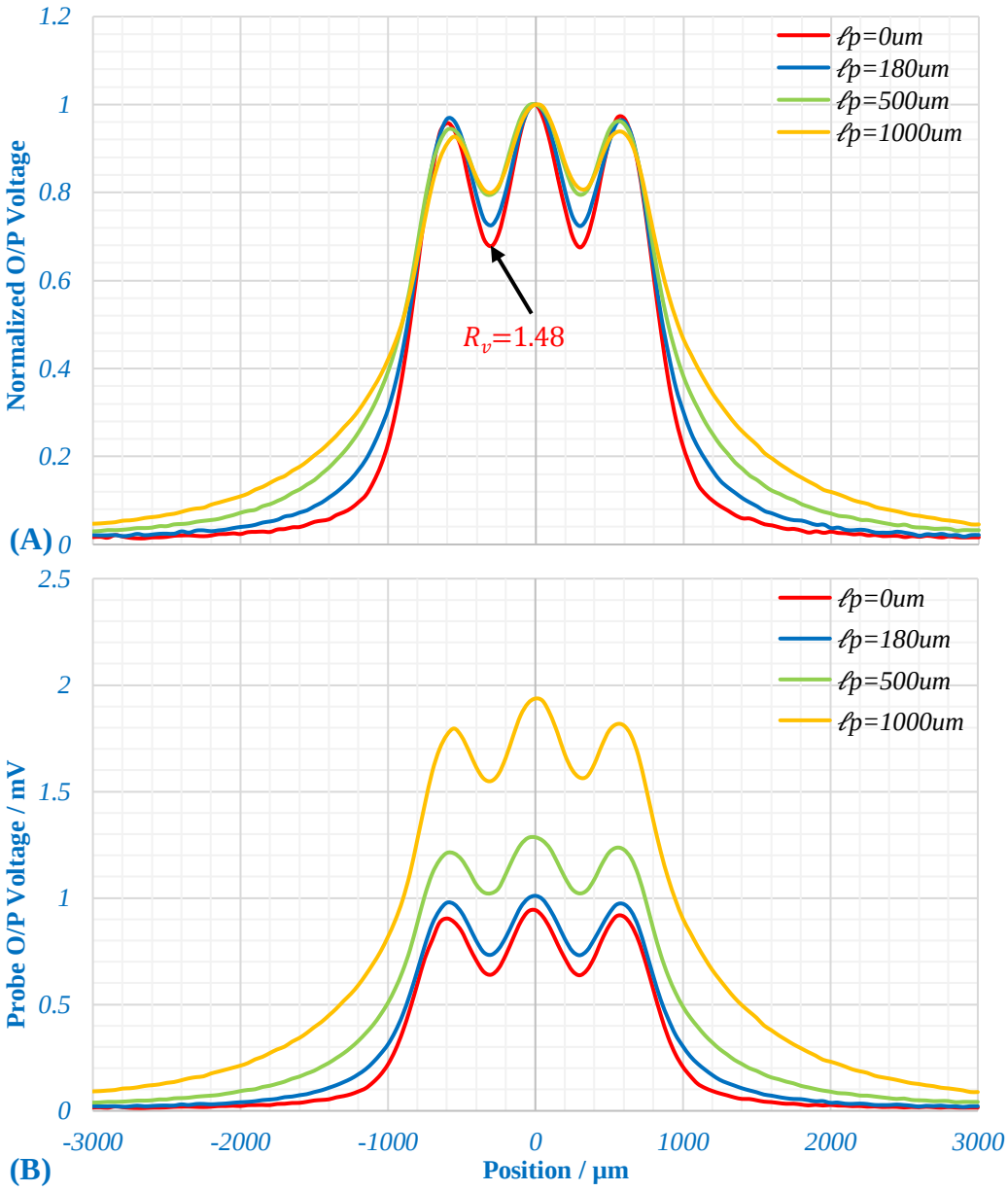

Figure 4-5 The influence of ℓp on the voltage probe ability to recognize variation in: (A) Spatial resolution. (B) Sensitivity.

4.5.2 Influence of d_p on the Spatial Resolution and Sensitivity

The internal diameters of each of the three coaxial cables (UT-034, RG405 and RG402) are: 200 µm, 510 µm and 910 µm respectively, and the protrusions for each is 500 µm. The impact this has on the spatial resolution and sensitivity are shown in Figure 4-6. The smaller the internal diameter of the probe tip the deeper the null introduced ($R_{V_r} = 1.196$). As d_p becomes $>2D+d$, the probe fabricated from RG402 becomes unable to recognize the minima locations at all, see Figure 4-6(A). Figure 4-6(B) shows the strong influence of cross-sectional area of the probe tip on its sensitivity.

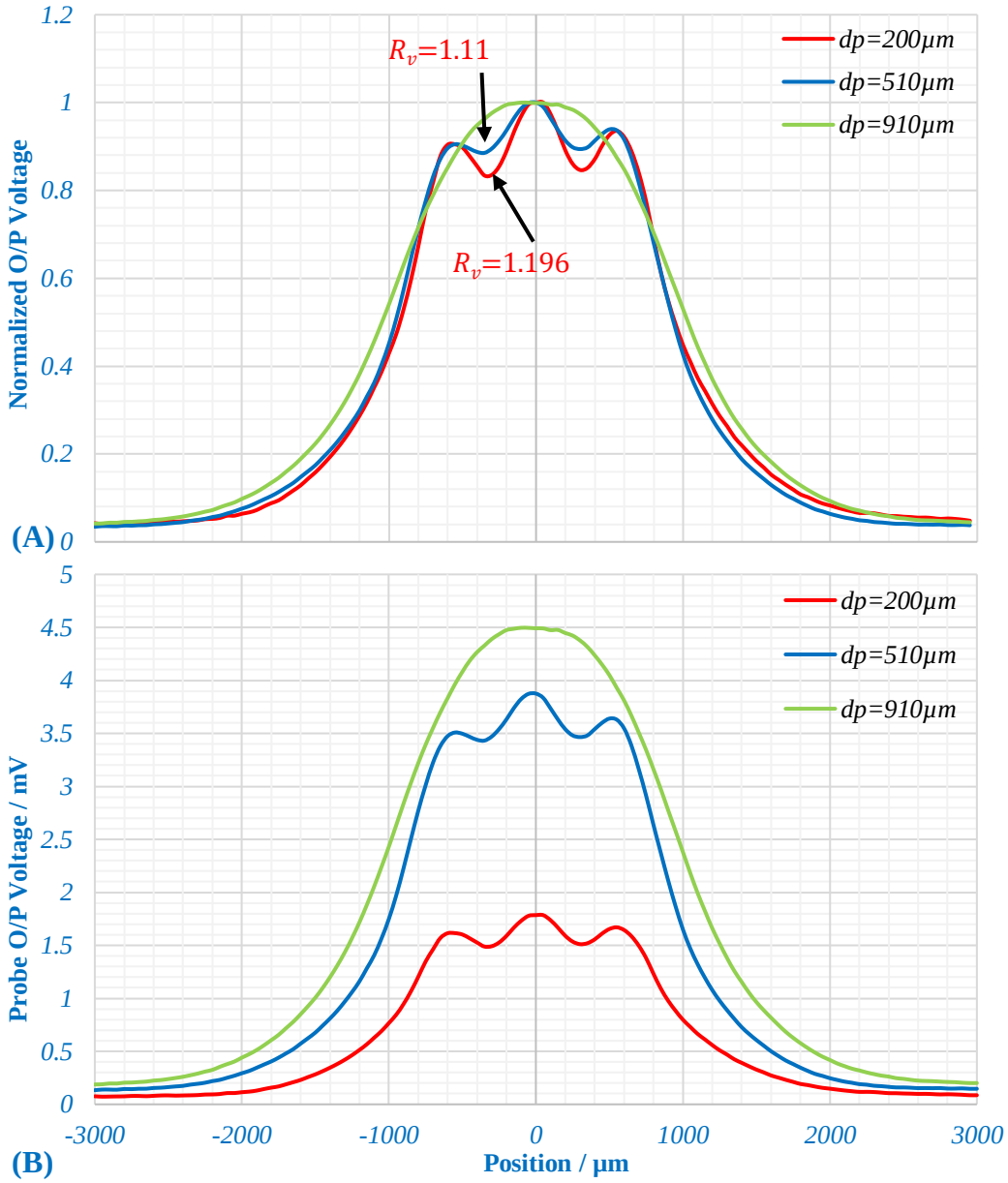

Figure 4-6 The influence of d_p on the voltage probe ability to recognize variation in: (A) Spatial resolution. (B) Sensitivity.

4.5.3 Influence of D_p on the Spatial Resolution and Sensitivity

The values of D_p for (UT-034, RG405 and RG402) are: 0.66 mm, 1.67 mm and 2.97 mm respectively. To examine only the effect of D_p on the spatial resolution and sensitivity all remaining parameters must be the same. The protrusions of all probes are set to 500 µm and the internal conductors in RG405 and RG402 are replaced with that of the UT-034. Figure 4-6(A) illustrates the negative influence of D_p on the spatial resolution. The difference between the null depths are not large (D_p is translated to $\delta_{\ell p}$ and $\delta_{\ell p} < \ell_p$).

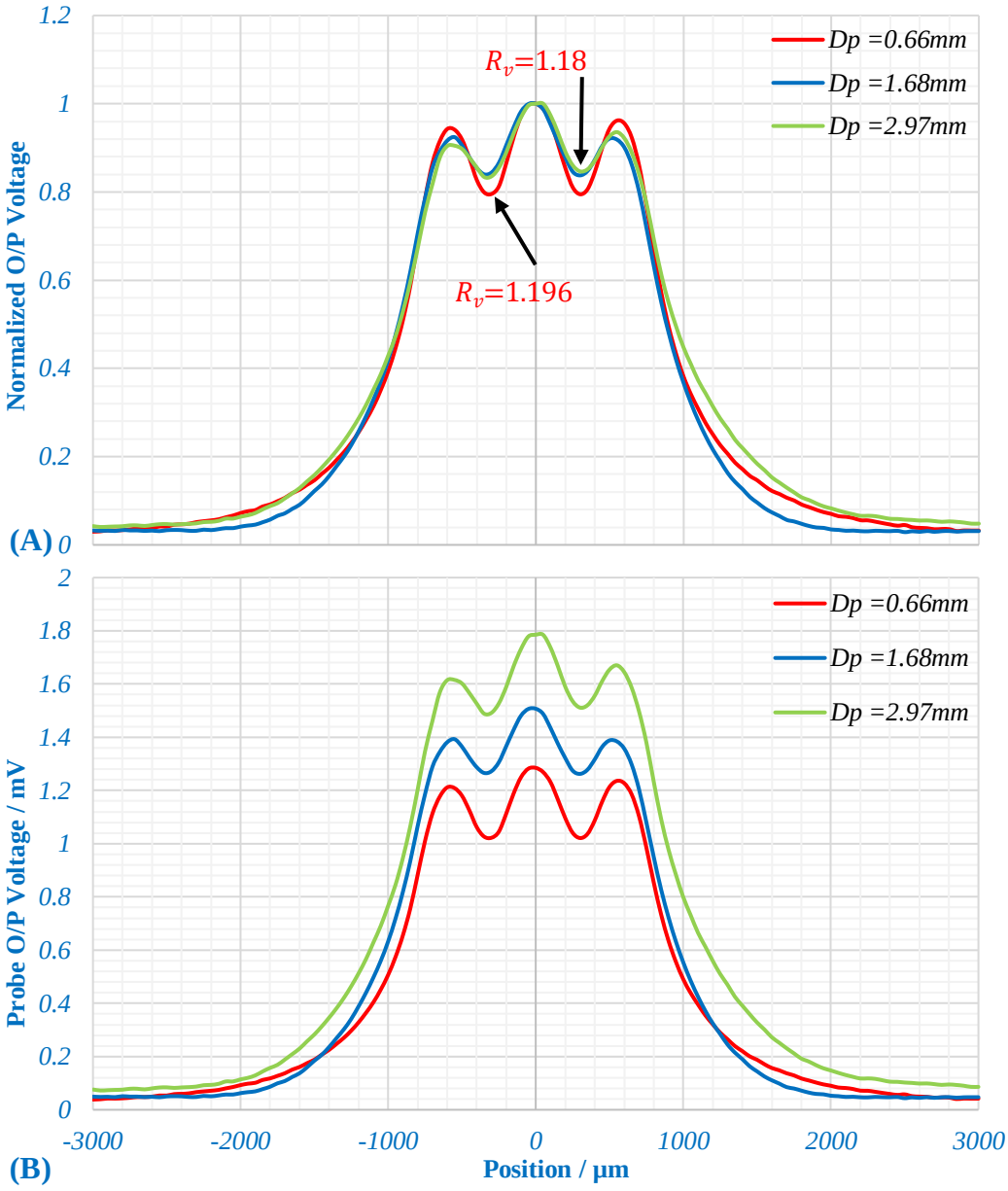

Figure 4-7 The influence of D_p on the voltage probe ability to recognize variation in: (A) Spatial resolution. (B) Sensitivity.

In addition to that, the results from RG405 and RG402 are close to each other because D_p in both is larger than the total width of the DUT (width of 3 tracks + 2 gaps = 1.5 mm). Therefore, approximately all electric field lines are entering the shield apertures. The sensitivity is proportional to D_p but with a smaller amount of variation, see Figure 4-6(B).

4.6 Influence of *h* on the Spatial Resolution and Sensitivity

As shown in 4.5 highest spatial resolution is achieved by the smallest coaxial cable UT-034 with zero protrusion. Therefore, this voltage probe is used to inspect the effects of probe height from the DUT on its spatial resolution and sensitivity. At h = 50 µm the spatial resolution is 1.48 while at h = 300 µm it drops to 1.06, see Figure 4-9(A).

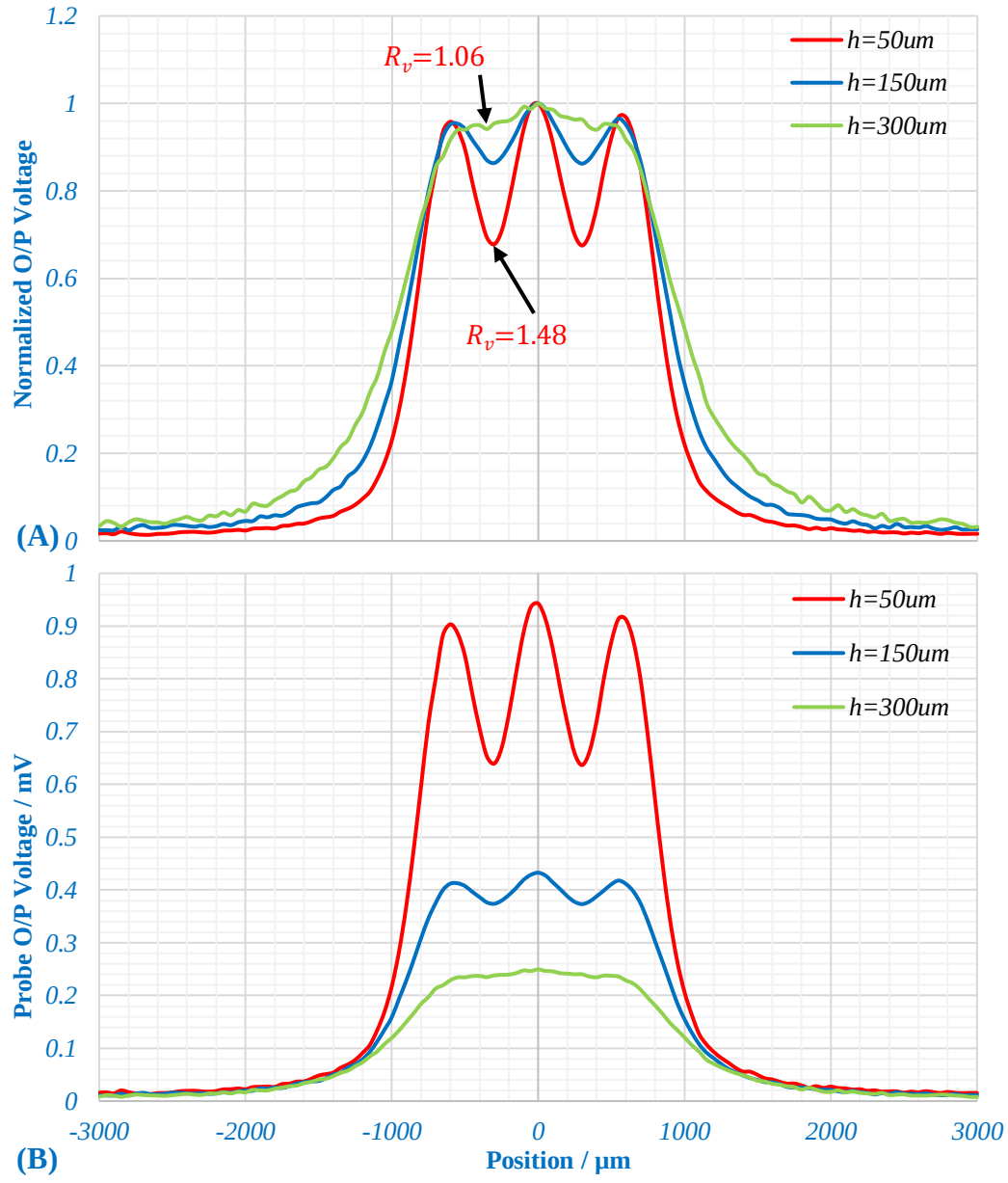

Figure 4-8 The influence of *h* on the voltage probe ability to recognize variation in: (A) Spatial resolution. (B) Sensitivity.

Correspondingly, the magnitude of the probe's sensitivity is reduced by 75% as the height increases from 50 µm to 300 µm, see Figure 4-9(B).

Voltage probe response is inversely proportional to the increments in its height and it has an exponential trend, see Figure 4-9. Plotting the variation in probe responses, at both the maxima and minima locations, shows that the differences between them reduces with an increase in probe height. When the magnitude of this height approaches the value of the gap width between adjacent tracks, the difference drops to about 3% of its value at h = 50 um.

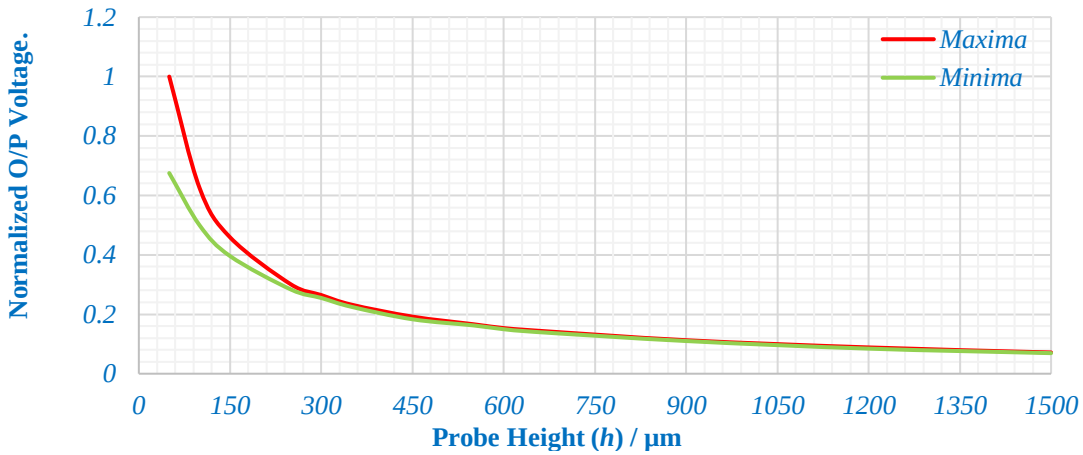

Figure 4-9 Relationship between voltage probe height and its response at both the maxima and minima locations.

4.7 Enhancing Voltage Probe Spatial Resolution

The geometrical analyses and the experimental validation illustrates that the cylindrical part of the probe active area is degrading the spatial resolution. Reducing the capacitive coupling to the cylindrical area is the key factor for this issue. One solution is to prevent the occurrences of this unwanted coupling by miniaturizing the active protrusion of the probe, $\ell_p+\delta_{\ell p}$, see sections 4.3.2, 4.5.1 and 4.5.3.

The other way is to eliminate the unwanted coupling by differentiating it from the total output response. The 'position signal difference technique' was introduced as a method to achieve that, see section 2.14.2.2. This required scanning the DUT twice at two different heights and then subtracting the results of these scans and hence minimising the unwanted effects of the cylindrical area. In the next sections, the effectiveness of this technique is examined, and the results are then compared with those of the miniaturization technique, see section 4.5.1.

4.7.1 Effectiveness of Position Signal Difference Technique (PSDT)

In this test, the UT-034 is used to fabricate a voltage probe that has a 1000 µm protrusion in order to compare its results with those of the zero-protrusion case. The test fixture was scanned four times at the following probe heights: 50 µm, 100 µm, 300 µm and 2000 µm. The results of the last three scans are then subtracted from those captured at 50 µm resulting in three sets of data: PSD 50-100 µm, PSD 50-300 µm and PSD 50-2000 µm respectively. The result of PSD 50-100 µm shows a noticeable improvement in the spatial resolution ($R_{V_r} = 2.46$) due to this technique. The influence of increasing the height of the probe resulting in lowering the corresponding spatial resolution (2.46, 1.67 and 1.32 respectively), see Figure 4-10(A).

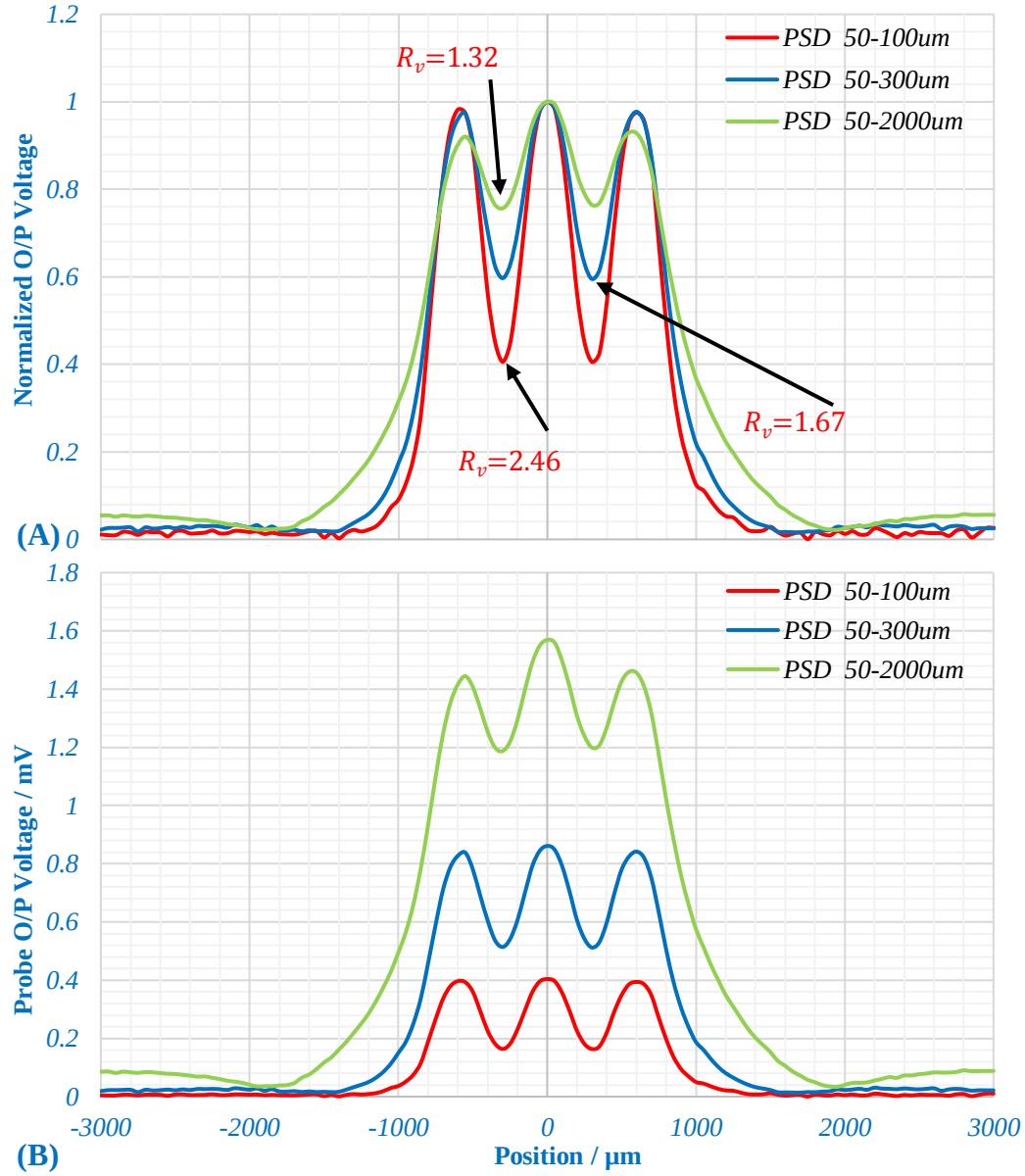

Figure 4-10 The effectiveness of the position signal difference (PSD) technique in terms of: (A) Spatial resolution. (B) Sensitivity.

In contrast with the results obtained in 4.6, the sensitivity here is proportional to the probe height, see Figure 4-10(B).

4.7.2 The PSDT Versus the Zero Protrusion Technique (ZPT)

The comparison between the ZPT and the PSDT is based on the scan results obtained in 4.5.1 and 4.7.1 respectively. The voltage probe used in the former has zero-protrusion and for the latter it has a protrusion = 1000 µm. The PSDT applied to the latter one at two heights 50 µm and 100 µm while the scanning height for the first is 50 µm. Figure 4-11(A) shows that the PSDT introduces a superior improvement (about 66%) in terms of spatial resolution over that of the ZPT. The reason beyond this improvement is that with ZPT the influence of D_p is still degrading the spatial resolution while through the PSDT this effect is eliminated.

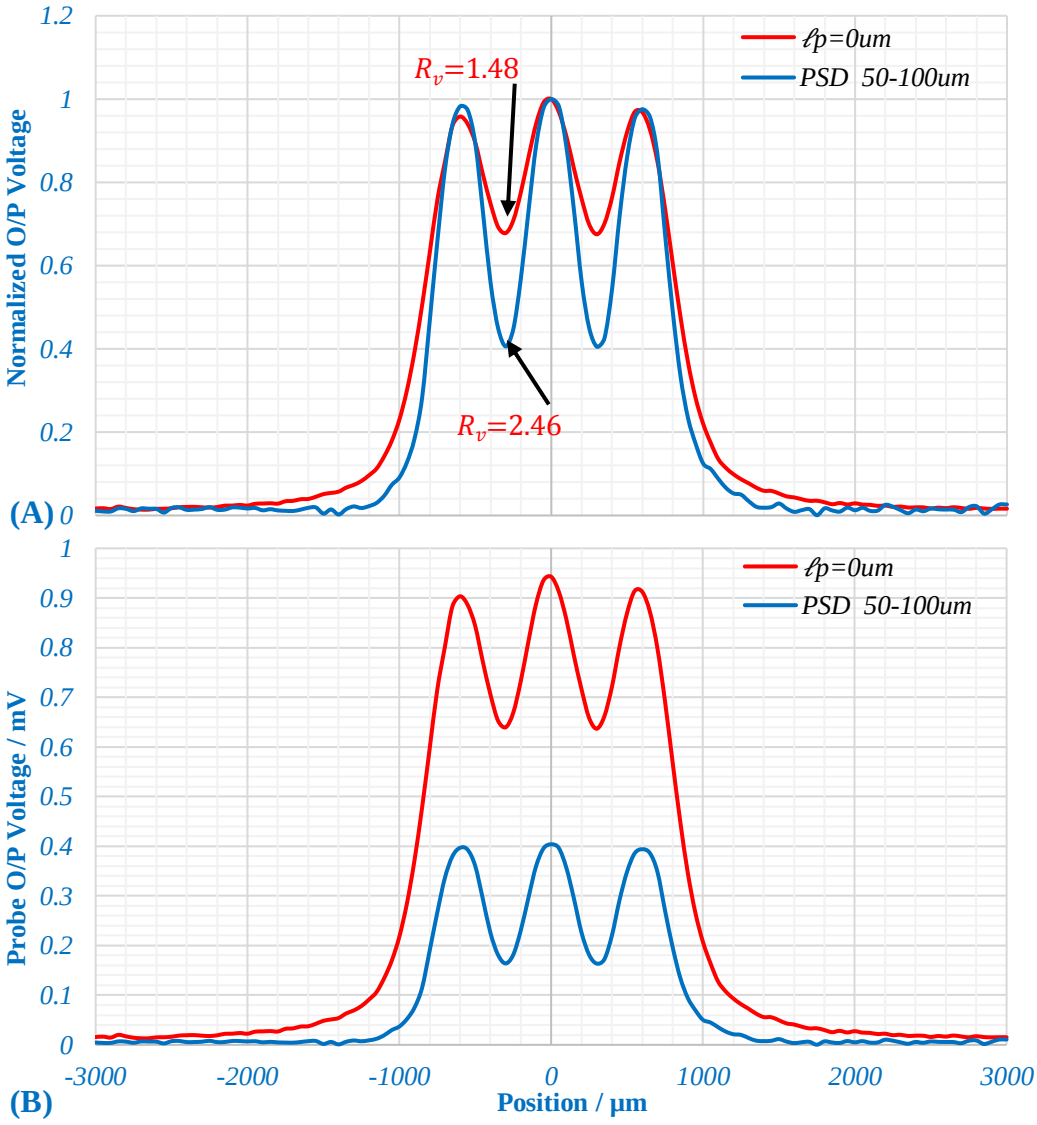

Figure 4-11 Comparison between the PSD technique and the zero-protrusion technique in terms of: (A) Spatial resolution. (B) Sensitivity.

On the other hand, the sensitivity dropped to about 40% of that compared with the zero-protrusion probe, see Figure 4-11(B). However, this is the outcome of the subtraction process which is performed after completing both PSD scans and it cannot be considered as the real sensitivity of the probe. In fact, the actual sensitivity in both PSD scans (at h = 50 µm and h = 100 µm) is higher than that of the zero-protrusion probe (at h = 50 µm), see Figure 4-12.

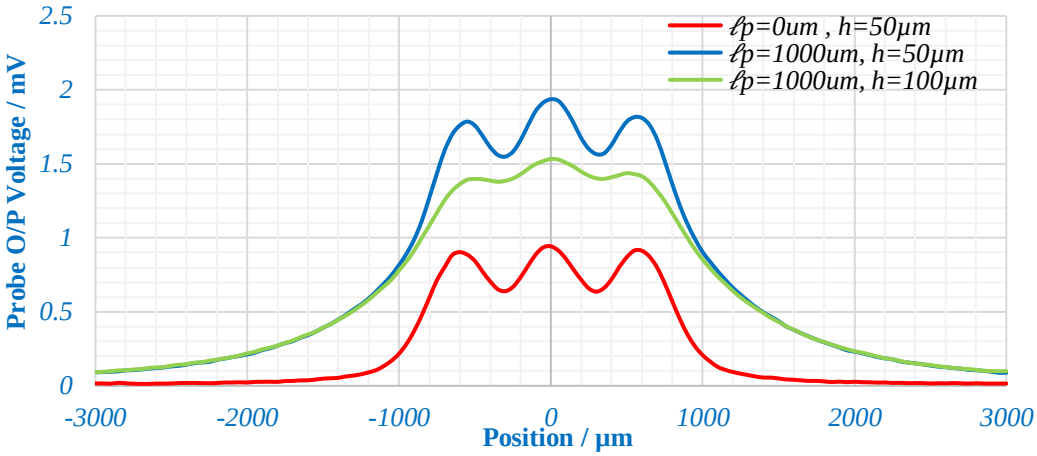

Figure 4-12 The actual sensitivity of a voltage probe of 1000um protrusion at two heights (50µm and 100µm) compared to that of zero-protrusion at 50µm height.

4.8 Essential Criteria for the Design of a High Spatial Resolution Voltage Probe

Based on the conclusions and results previously obtained, through the geometrical analysis and the experimental validation, the requirements for designing a voltage probe with high spatial resolution can be classified as follows:

- Essential requirement: -

  The diameter of the internal conductor should be smaller than the sum of the wire & the gap widths. However, to obtain deep nulls it should be smaller than the smallest distance separating any adjacent wires. The smaller the better in terms of spatial resolution but this impacts overall sensitivity.

- Enhancement requirements: -

  1. The internal diameter of the shield should be the smallest. The limit is the diameter of the internal conductor. However, this will increase the shunt capacitor to the ground and thus reducing the sensitivity of the probe.
  2. Probe tip protrusion should be kept as small as possible. Best results obtained when it is reduced to zero.

3. Applying the PSDT allows significant improvements in terms of voltage probe spatial resolution and partial improvement in terms of sensitivity as well. To achieve these improvements, the difference between the heights of the scans should be smaller than the distance separating adjacent wires. However, this will consume twice of the scanning time.

4.9 Electrical Characteristics of the Open End Coaxial Cable

The main electrical characteristics of any coaxial cable are: - Characteristics impedance (Z_{Cox}), total distributed capacitance (C_{Cox}), total distributed inductance (L_{Cox}) and cut off frequency (f_C). These characteristics are given by [38]:

$$Z_{Cox} = \frac{138.2}{\sqrt{\varepsilon_r}} \log \frac{D_p}{d_p} \quad in\ \Omega \tag{4-5}$$

$$C_{Cox} = \varepsilon_r \frac{24.146}{\log \frac{D_p}{d_p}} \quad in\ pF/m \tag{4-6}$$

$$L_{Cox} = 0.459 \log \frac{D_p}{d_p} \quad in\ uH/m \tag{4-7}$$

$$f_C = \frac{7.5}{\sqrt{\varepsilon_r}(D_p + d_p)} \quad in\ GHz \tag{4-8}$$

In a similar manner to the calculation of the spatial resolution, the above set of equations interpret the strong dependency on the inner conductor diameter d_p and the inner diameter of the shielding conductor D_p. Greatest spatial resolution is achieved at (D_p / d_p) =1, see section 4.3.2, and the value of Z_{Cox} becomes equal to zero ohm.

However, this also means zero voltage introduced at the output of the probe. The length of the coaxial cable (L) in normal application (long coaxial cable) attenuates the signal strength. But for the voltage probe case, this input coaxial cable has a short length (few millimetres) and thus the influence of the attenuation is negligible here. However, in open end coaxial cable, the length can significantly impact the sensitivity of the voltage probe.

4.10 Methods of Enhancing Voltage Probe Sensitivity

Up to this point, the main focus was on enhancing the spatial resolution of the voltage probe. For each enhancement achieved the sensitivity degraded, the only exception here is the PSDT enhancement. However, even for this exception, the improvement in

sensitivity due to tip protrusion extension is bounded by the height of the bond wires to avoid unwanted effects, see section 4.13.

The spatial resolution and sensitivity are sharing the opposite dependency on the geometrical boundary conditions, while the sensitivity is also a function of the electrical boundary conditions: -

- Frequency of operation

  Although the sensitivity according to (4-1) is proportional to f^2, it is not possible to modify the frequency of operation to enhance its sensitivity.

  It is useful at this point to define the minimum bandwidth requirements. The target bandwidth of this type of measurement is the frequency range of mobile networks, 0.5 GHz to 4 GHz. To easily compare the impedances over this bandwidth, each capacitance or inductance is followed by brackets containing its range of impedance.

- Impedance matching

  Maximum signal power transfer, and thus high sensitivity, occurs if all impedances are matched. However, under capacitive coupling conditions, impedance matching is difficult to achieve especially at the input of the probe.

  Practically, miniaturization of probe active area leads to a smaller capacitive coupling to the DUT and thus higher capacitive impedance XC_c (hundreds of Kilo Ohm range) introduced to the input of the voltage probe. For example, if the probe tip has a 20 µm diameter and zero protrusion length and it is at a 10 µm height from the DUT then from (2-40) C_c = 0.278 fF (1.14 MΩ ≥ XC_c ≥ 143 KΩ), where C_c is calculated for the cross-sectional area only. Matching such a large input impedance will require large size matching devices (i.e. larger probe size). Moreover, it is difficult to implement (if that is at all possible without increasing the size of the probe active area) at the input of the probe to avoid further probe intrusion on the DUT. In addition to that, on the other side of the coaxial cable maintaining a fixed reflection (or optimally zero reflection) over the whole range of operating frequency is not easy to achieve due to the nonlinear input characteristics of the active device [205].

- Increasing signal gain

  This is the most common way used to enhance voltage probe sensitivity. A suitable size of low noise amplifier is added at close proximity to the probe active area.

- RF power reflections between the electrical parts of the probe.

  If it is not easy or even possible to avoid the impacts of the inherent mismatching problem in the voltage probe, then it is worthwhile exploiting this as an advantage. Impedance mismatching between the internal parts of the voltage probe means a portion of the incident power is reflected between them. The superposition of the incident and the reflected waves introduces a standing wave. If the position of the standing wave maxima is adjusted to the desired location of measurement, then a higher sensitivity is achieved. This is the case of semi-resonant probes.

4.10.1 Sensitivity Enhancement by Adding Gain

This technique is based on compensating the lack of sensitivity due to the small size of the active area of the voltage probe by introducing a voltage gain. FET transistors/ amplifiers are preferred over the BJT transistors/amplifiers in voltage probe applications. The FET transistors are more compatible with voltage driving schemes rather than current driving schemes. In addition to that, the FET transistors are more easily adapted to work under self-biasing conditions. This feature is of a great importance in simplifying the probe structure and miniaturizing its size as well.

At microwave frequencies, the capacitor between transistor gate and source (C_{gs}) has a strong influence on the overall gain that can be achieved from it. The value of C_{gs} depends on the characteristic of the FET transistors and the selected point of operation.

For the wafer scale FET transistors (WLP0402, 1 mm x 0.5 mm x 0.25 mm), that have been selected for voltage probe implementation, C_{gs} may have any value within the range 0.3 pF (1061 Ω ≥ XC_{gs} ≥ 133 Ω) to 1.41 pF (225 Ω ≥ XC_{gs} ≥ 28 Ω), see Figure 4-13 and the data sheets of VMMK-1218 [206]and VMMK-1225 [207]. Where XC_{gs} is the impedance of C_{gs} over the rang of frequency 0.5 GHz to 4 GHz.

In addition to that, if a standard PCB is used with these transistors/amplifiers then the capacitance between the top metal layer connected to the input of the device and the ground layer is combined with C_{gs} see section 3.9.2.3.

If it is possible to connect the gate of the transistor directly to the monopole (the active area of the probe) without the intermediate transmission line, then the range of the required voltage gain can be easily estimated from the voltage divider equation. The

capacitively coupled voltage is divided between the coupling capacitance C_c and the input capacitance of the transistor C_{gs}.

However, the available wafer-scale transistors/amplifiers are still relatively large to achieve that, see Figure 3.12, and therefore, the coaxial cable is needed to geometrically match this difference in size.

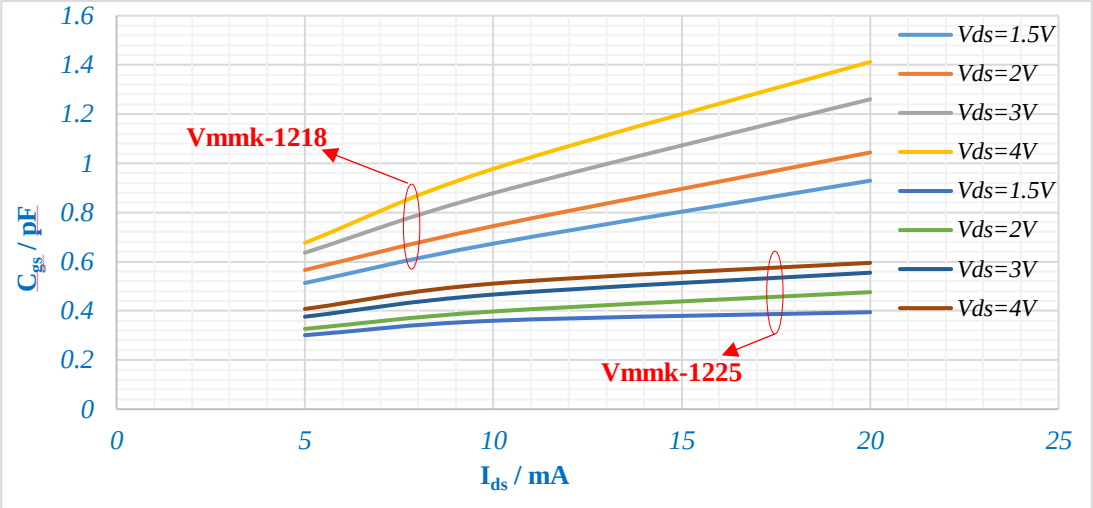

Figure 4-13 The relation between the value of C_{gs} and V_{ds} and I_{ds} for the VMM-1218 and VMMK-1225

To ease the calculations, we can suppose the length of the intermediate coaxial cable to be 1mm (extremely small compared with smallest operating wavelength 70mm). Thus, the coaxial cable can be replaced with its lumped capacitive (XC_{cox}) and inductive (XL_{cox}) impedances, see Figure 4-14.

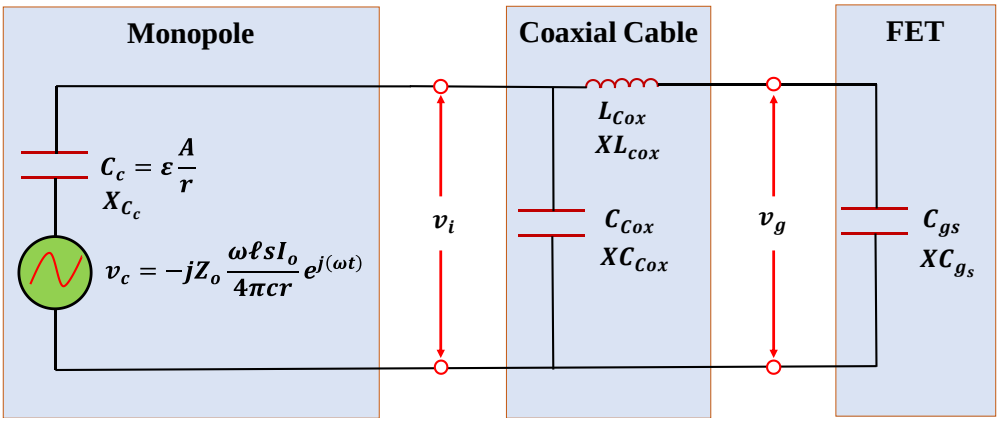

Figure 4-14 The equivalent circuits of the monopole, the lumped equivalent circuit of the coaxial cable and the input impedance of the FET transistor/amplifier.

As indicated in the previous sections, the best geometrical boundary condition regarding spatial resolution are the worst regarding sensitivity. Through this work, the smallest

coaxial cable we were able to fabricate has a central conductor of 20 µm diameter and the ratio (D_p / d_p) is equal to 3 with air as the dielectric. By applying these conditions to (4-6) & (4-7) yields $C_{Cox} = 0.05$ pF (6366 Ω ≥ XC_{Ccox} ≥ 796 Ω) and L_{Cox} =0.22 nH (0.69 Ω ≤ XL_{cox} ≤ 5.53 Ω) respectively.

From these calculations, it can be seen that the total contribution from the coaxial cable parameters is so small compared with that of the X_{Cc} and thus we can assume for this case, that the gate of the FET is directly connected to the monopole antenna.

The effect of the monopole antenna is modelled by a voltage source cascaded with the coupling capacitor see Figure 4-13. This model is based on the analysis given in chapter two and from (3-52), C_c = 0.278 fF (1.14 MΩ ≥ XC_c ≥ 143 KΩ), this value is calculated for zero protrusion length of the central conductor and 10µm probe height from the DUT.

Based on the above calculations and assumptions, the voltage divider ratio between the gate voltage and the capacitively coupled voltage is given by

$$\frac{v_g}{v_c} = \frac{C_c}{C_c + C_{gs}} \tag{4-9}$$

The first thing obtained from (4-9) is that the range of signal degradation between the source voltage and the gate voltage is -61 dB to -74 dB. In terms of voltage, for 0 dBm power delivered to the input of the DUT, the range is 0.04 µV ≤ v_g ≤ 0.2 µV. This voltage is beyond the sensitivity threshold of many instruments. Inserting an amplification stage in the path of the signal with proper gain can solve this issue. The question is where to place this amplifier?

Using an external amplifier is simple and it easy to implement with any desired gain and even with automatic gain control to provide a flat response over the entire bandwidth of interest. However, transmitting this weak signal over a coaxial cable to the external amplifier would not enhance the sensitivity as it becomes attenuated due to transmission losses which make the total signal to noise ratio practically worse. The alternative is to put the amplification stage as close as possible to the source of the signal to avoid unwanted noise pick up and thus enhancing the signal to noise ratio. This will, of course, limit the options to those transistors/amplifiers that have an extremely small package like the wafer scale WLP0402, at 1 mm x 0.5 mm x 0.25 mm [206]–[208]. In addition to that, such a transistor/amplifier would not be able to offer all the required gain; however, the important thing is to offset transmission losses and noise until reaching the input of the external amplifier.

The other interesting feature of equation (4-9) is the possibility to have flat frequency response present at the input of the amplifier. The bandwidth of the amplifier, for this case, is the final limit of the voltage probe bandwidth. However, this is only valid for the case of an extremely short coaxial cable between the monopole and the amplifier.

Regarding the environment inside microwave power transistor, it is essential to minimize field disturbances as much as possible. To do that, the main body of the probe needs to be far enough from the probing area. That means a longer length for the input coaxial cable.

Figure 4-15 highlights the frequency response at the output of the voltage probe at three different operation points. The input coaxial cable has 6mm length and $Z_{Cox} = 107\Omega$ cascaded with a VMMK-1218 transistor.

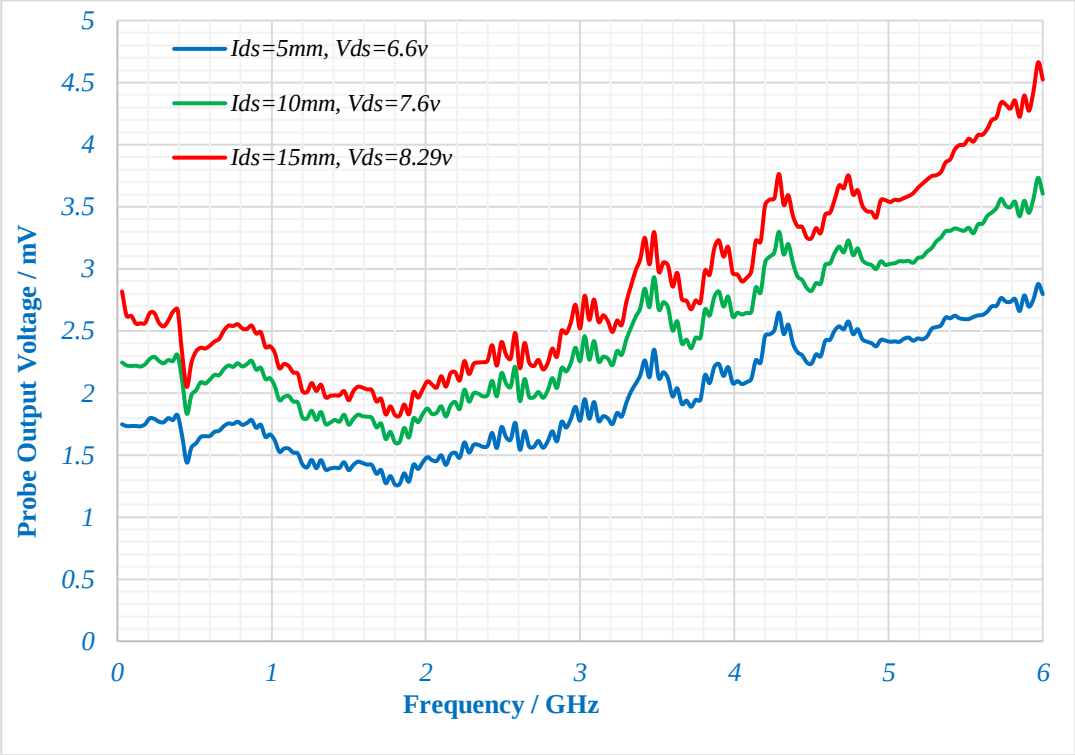

Figure 4-15 Frequency response of the voltage probe that has: input coaxial cable of 6 mm length feeding the VMMK-1218 transistor biased at 5 mA, 10 mA and 15 mA.

Although the gain of this transistor is decaying from 21 dB to 14 dB for the range from 2 GHz to 6 GHz [206], the response is flattened due to the dependency of the capacitively induced voltage v_c on the frequency and the standing wave generated due to the mismatching between the transistor and the coaxial cable, see section 4.10.2.

4.10.2 Sensitivity Enhancement by Controlling the Standing Wave Pattern

The equivalent circuit of the voltage probe shown below is applicable for any length of coaxial cable; represented by its characteristic impedance instead of the lumped capacitor and inductance.

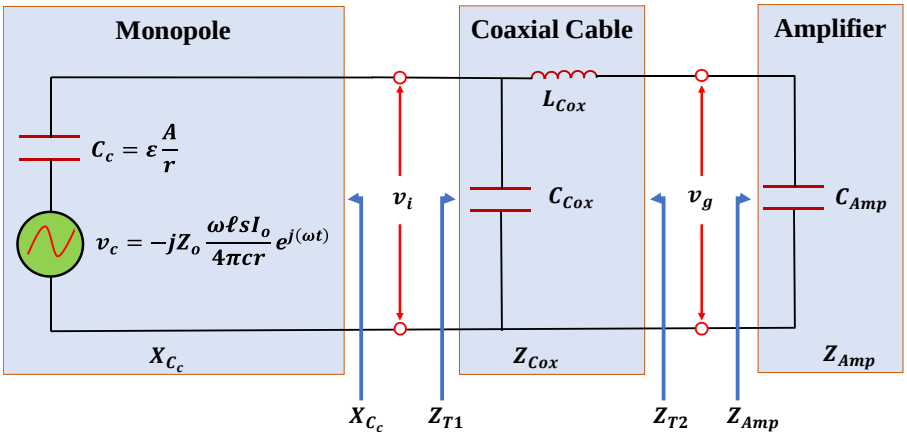

Figure 4-16 The equivalent circuits of the monopole antenna (XC_c), the equivalent circuits of the input coaxial cable (Z_{Cox}) and the input impedance of the low noise amplifier (Z_{Amp}).

By applying the transmission line theory for a low loss coaxial cable (due to its short length), the total impedances seen at each end of the coaxial, (Z_{T1}) and (Z_{T2}) cable are given by [191]: -

$$Z_{T1} = Z_{Cox}\left[\frac{Z_{Amp} + jZ_{Cox}\tan(2\pi L/\lambda)}{Z_{Cox} + jZ_{Amp}\tan(2\pi L/\lambda)}\right] \quad (4\text{-}10)$$

$$Z_{T2} = Z_{Cox}\left[\frac{XC_C - jZ_{Cox}\tan(2\pi L/\lambda)}{Z_{Cox} - jXC_C\tan(2\pi L/\lambda)}\right] \quad (4\text{-}11)$$

Both impedances are changing their values periodically depending on the ratio L/λ [11]. The only exception to that is when perfect impedance matching occurs. This would not be possible at the front end of the coaxial cable, i.e. that terminated with monopole, due to the very large value of XC_C.

At the other end, perfect matching is possible but not for the whole frequency range due to the non-linearity of the active device. These conditions lead to creating multiple reflections and thus a standing wave generated along the coaxial cable. As the mismatching between Z_{T2} and Z_{Amp} increases, the difference between the maxima and the minima increase as well.

In this case the amplifier input impedance, Z_{Amp}, represents the load and if its capacitive component, C_{Amp}, is large (the case of FET transistor), then it behaves as a reactive load. A reactive load cannot dissipate incident energy. This energy is stored and then reflected back into the coaxial cable. Because of that, a pure standing wave is generated with significant contrast between maxima and minima.

The coaxial cable under these conditions known as resonant transmission line [205]. The pattern, rate of repetition and the locations of the minimum and maxima, of this standing wave depends on the ratio L/λ. For a specific operating frequency, the position of the first maxima can be modified by changing the length of the coaxial cable.

If this length is adjusted so that the first maxima occurs at the connection point between the coaxial cable and the input leads of the amplifier, then this amplifier will amplify the input signal at the peak of this standing wave.

To show the influence of the standing wave on the voltage probe sensitivity, two voltage probes with different lengths for the input coaxial cable 6 mm and 24 mm are constructed, see Figure 4-17. The remaining parameters of the voltage probes are: d_p = 20 µm, (D_p / d_p) = 6, ℓ_p = 150 µm and the transistor is VMMK-1218 biased at 15 mA. Probe tip height from the DUT is 10 µm.

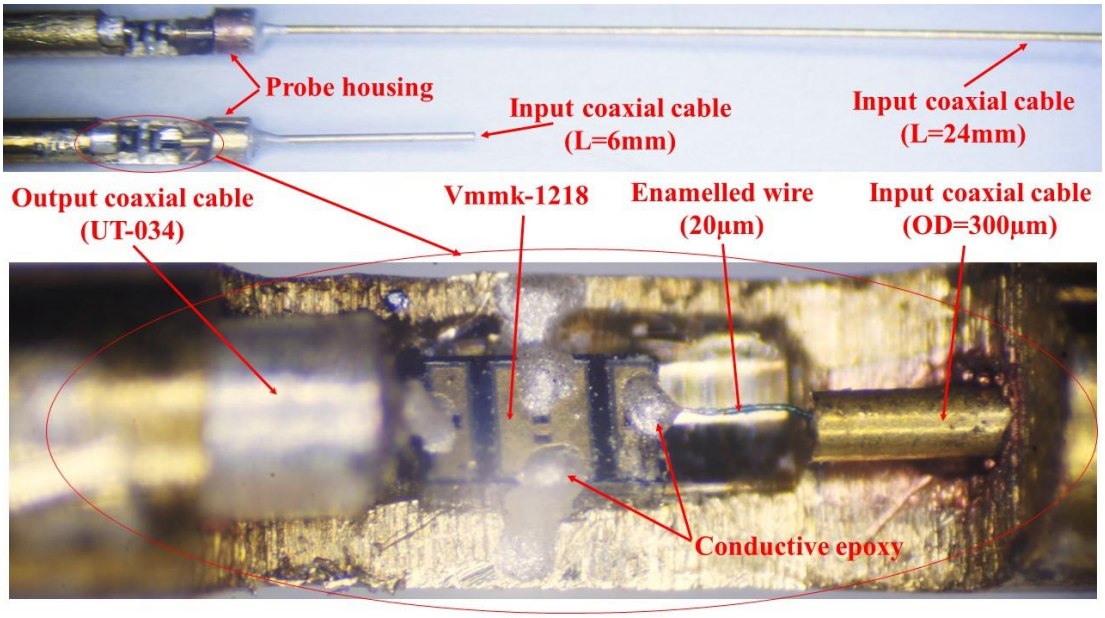

Figure 4-17 Two voltage probes with different lengths for the input coaxial cable 6mm and 24mm and similar internal structure.

Results of this study are shown in Figure 4-18. Increasing the length of the input coaxial cable by a factor of four gives rise to the shifting of the position of the standing wave maxima to be at 3.69 GHz with about 19 dB improvement in the forward transmission parameter S_{21} of the voltage probe.

The 3 dB bandwidth of this response is about 400 MHz and the 6 dB bandwidth is about 930 MHz. Microwave transistors are usually tested at single tone (the desired carrier frequency), however, with this large side bandwidths, it is possible to test them under realistic modulation conditions which are not normally more than 10% of the carrier frequency.

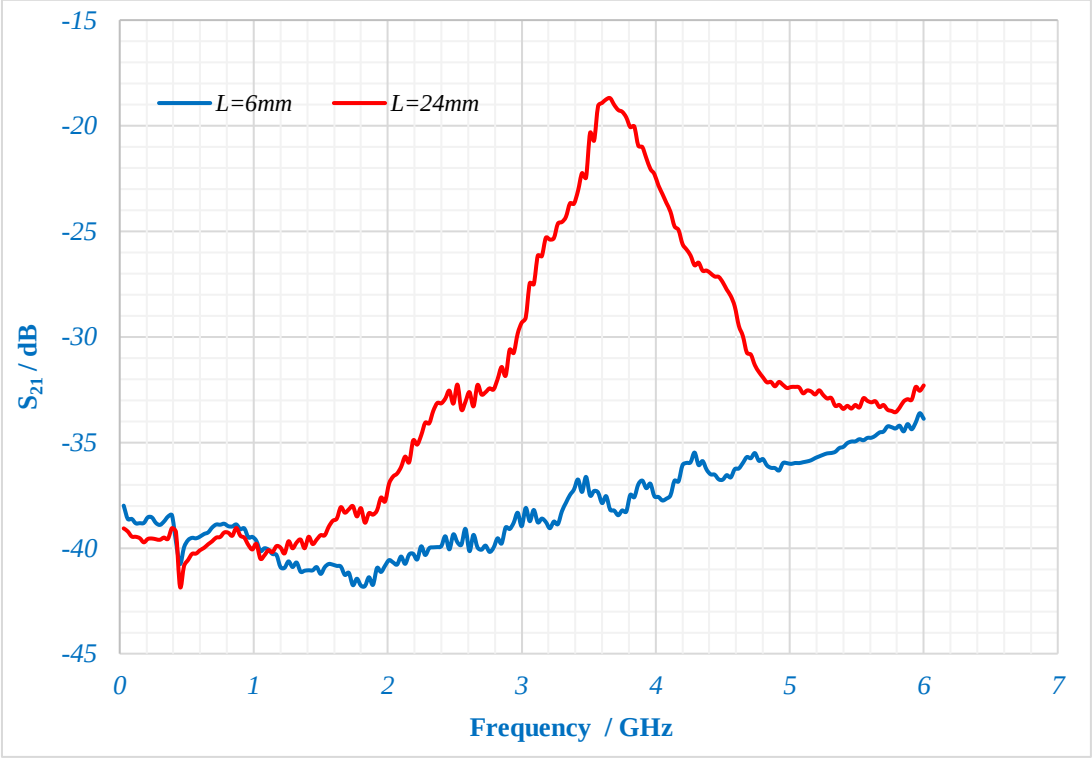

Figure 4-18 The forward transmission parameter S_{21} of the voltage probe at two different lengths of its input coaxial cable, 6mm and 24mm.

4.10.2.1 Voltage Probe Schematic Modelling and Simulation

Due to the limited resources of this project, the experimental results shown demonstrate the voltage probe response up to 6 GHz (the bandwidth limit of the VNA used in this measurement). Within this bandwidth it is not possible to validate the above concepts as the repetition of the standing wave is not clear.

The ADS schematic simulation has been used as a third-party method of verification of the standing wave technique. In this simulation, the operating frequency has been

extended to cover the whole bandwidth of the VMMK-1218 which is 18 GHz [206]. The schematic module of the above voltage probe is shown in Figure 4-19.

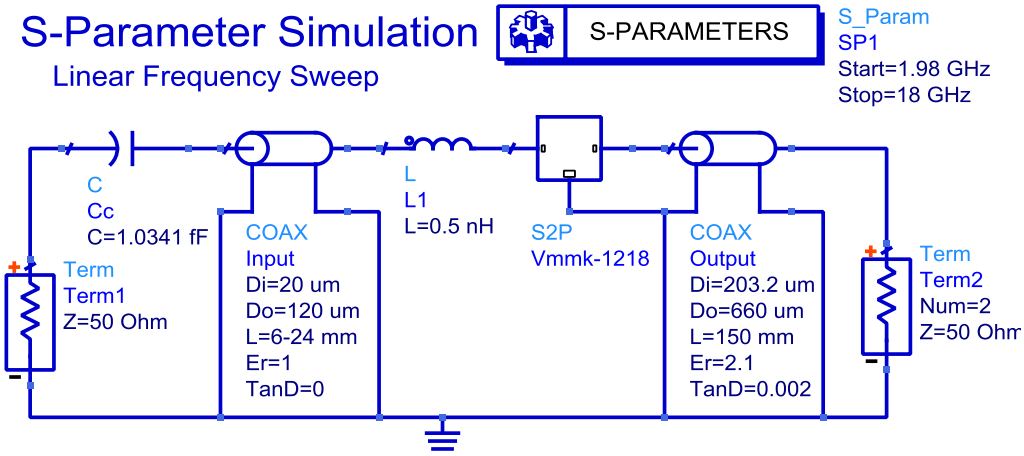

Figure 4-19 The ADS schematic model of the voltage probe for two lengths of the input coaxial cable, 6mm and 24mm.

The results of the simulation are shown in Figure 4-20, from which it can be seen that the standing wave pattern is clear for both cases. The voltage probe with the long input coaxial cable has three maxima. While for the voltage probe with the short input coaxial cable, the first maxima is appearing at about 9.9 GHz.

In general, a good agreement has been achieved with the experimental results shown in Figure 4-18, regarding both the location of the first maxima and the difference in magnitude at this maximum.

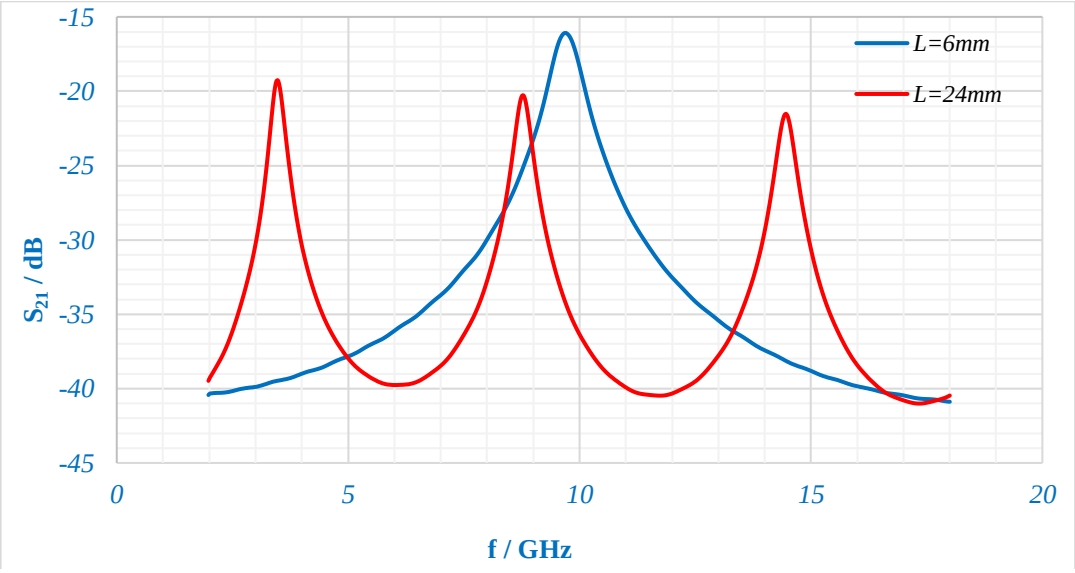

Figure 4-20 The forward transmission parameter S_{21} of the tow voltage probes connected to the short (L=6mm) and long (L=24mm) input coaxial cables.

However, the difference between the simulation and the experimental results appears in the general trend of the response with respect to the frequency. In the experimental result, the general trend is proportional to the frequency. This is due to the influence of the coupling voltage v_c, see Figure 4-16, and the influence of the generated standing wave. This proportionality is partially compensated for by the drop in the gain of VMMK-1218 (loss 17 dB over the range 2-18 GHz, see Vmmk-1218 datasheets [206]) resulting in a gradual rise in the response. While this coupling voltage, v_c, is modelled in ADS with Term1, see Figure 4-19, which has a flat frequency response and thus the simulated response is gradually damping.

The relation between the location of the first maxima (in the frequency domain) and the length of the input coaxial cable has a decaying exponential trend, see Figure 4-21.

Figure 4-21 The location of the first maxima (in the frequency domain) with respect to the variation in the length of the input coaxial cable.

4.10.2.2 Alternative Method to Control Standing Wave Pattern

The results in Figure 4-21 suggests that, in order to have a standing wave maximum at 2 GHz, the length of the input coaxial cable needs to be extended to about 48.7 mm. For large values of the ratio (D_p / d_p) (for example $(D_p / d_p) = 6$) it is easy to push an ultra-thin wire of 20 µm diameter inside a brass tube that has a 120 µm internal diameter (the shield) over a length of 50 mm or more is relatively easy.

But for small values of the ratio (D_p / d_p) (for example $(D_p / d_p) = 3$) it is difficult to achieve that for more than 30 mm due to the mechanical friction between the wire and

the internal walls of the tube. In addition to that, the long coaxial cable introduces more attenuation.

This limitation can be avoided by adding inductance in series between the input coaxial cable and the leads of the amplifier (L1 in Figure 4-19). The discrete surface mounted inductance, with their wide range of values, can be used in the implementation. The only problem here is if the exact value of the inductance is not known (which is quite common) then each time the inductance is replaced, the probe must be left until the conductive epoxy hardens, see section 3.9.2.2.

Alternatively, the protrusion length of the central conductor of the input coaxial cable (unshielded length) can be extended inside the housing of the voltage probe to create a wire inductance, see Figure 4-22. This protrusion then can be easily adjusted so that maximum voltage gain occurs at the desired frequency.

The self-inductance of the 20 µm wire is about 0.9 nH/mm and thus to create a large inductance one or more loops need to be formed inside the boundary of the voltage probe housing. Increasing the value of the inductance L1 from 0.5 nH[17] to 9.5 nH inside the voltage probe that has an input coaxial cable length of L = 6 mm, shifts the location of the first standing wave maxima (in the frequency domain) from 9.8 GHz to 3.66 GHz.

However, this alternative approach reduces the gain of the voltage probe by about 3 dB compared with that of the long input coaxial cable voltage probe, L = 24 mm, see Figure 4-23. It is also lowering the 3db bandwidth to about 330 MHz.

Figure 4-22 The wire inductance created by extending the central conductor of the short input coaxial cable (L = 6 mm) inside the housing of the voltage probe.

[17] The space between the end of the coaxial cable and the leads of the VMMK-1218 is about 0.6 mm and the inductance of the unshielded central conductor for this length is about 0.5 nH, see Figure 4-17.

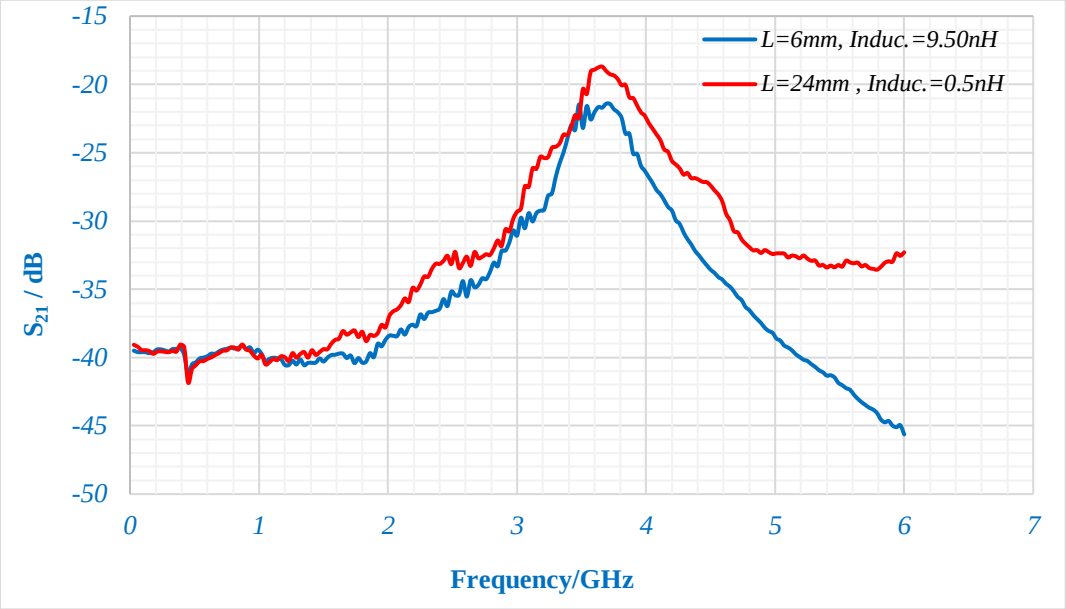

Figure 4-23 Comparison between the locations (in the frequency domain) of the first standing wave maxima generated by the long input coaxial cable and that of the short input coaxial cable after cascading it with wire inductance of 9.5 nH.

4.11 Narrowband Voltage Probe Applications

The previous result shows that the standing wave technique, under certain conditions, can add a considerable amount of gain at the expense of narrowing the bandwidth. This can be quite useful in extending the range of microwave transistors that this type of measurement is applied to. Large power transistors usually have a large spacing between their bond wires and generate strong electromagnetic fields as well, see section 3.10.1.1. This allows more flexibility in selecting probe critical dimensions and thus sensitivity is not an issue in these cases.

In contrast, for the case of small and medium scale transistors (low power transistors), the spacing between bond wires is much smaller and the generated electromagnetic fields from them are much weaker. Thus, the issue of sensitivity becomes an important factor once again.

The simple solution of adding more gain inside the probe is limited by the available free space and most important: the low noise figure of the selected preamplifier. Therefore, any enhancement that improves signal to noise ratio even as low as one dB extra is beneficial. The standing wave technique can offer around 15-20 dB passive gain to enhance the signal to noise ratio at the input of the preamplifier.

4.12 Broadband Voltage Probe Applications

Large microwave transistors, tested under high power operating conditions, usually generate multiple harmonics of the operating frequency. Therefore, it is more convenient to have a broad band probe to capture the second or even the third harmonics in a single scan. A noticeable flatness in the voltage probe frequency response can be achieved by inserting a resistor in series with the input coaxial cable and input of the amplifier. The tuning and optimization functions offered by the ADS software suggest the approximate value of this resistor. Cascading the short input coaxial cable (L = 6 mm) with 118 Ω introduces a flat frequency response up to 10 GHz with less than 0.5 dB variation. While for the case of the long input coaxial cable (L = 24 mm) the ripple is minimised to less than 2 dB, over the same range of frequencies, when the resistance is adjusted to 110 Ω.

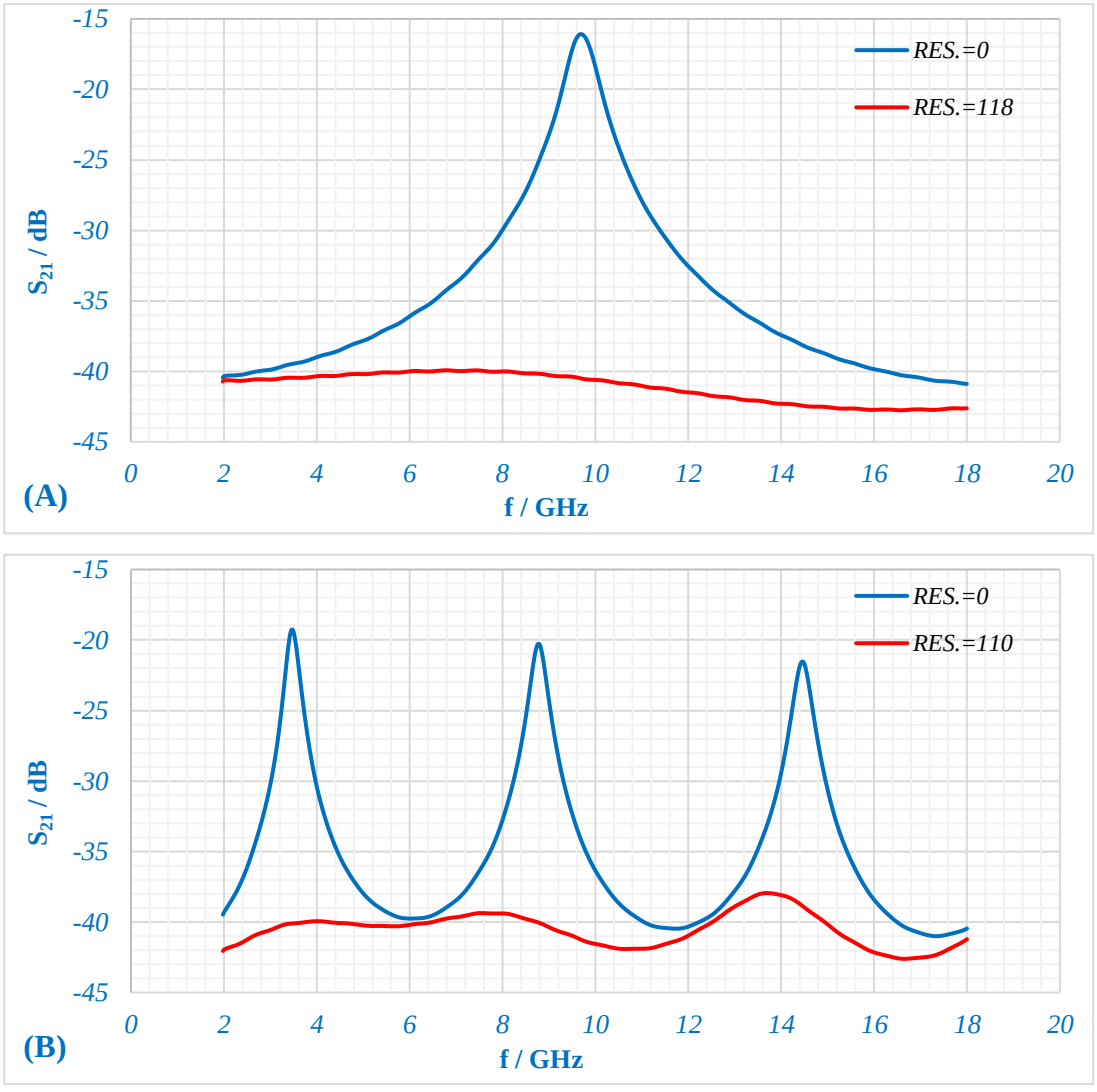

Figure 4-24 The influence of adding a resistor (in series with the input coaxial cable) on the frequency response of the voltage probe. (A) *L* = 6 mm. (B) *L* = 24 mm.

4.13 Resolution Target and the Ordinary Coaxial Cable Limits.

The aim of this work is to design and implement a contactless voltage probe with a 25 µm wire/gap spatial resolution. The smallest coaxial cable commercially available, that can be used to implement such a contactless probe, is the UT-013. Its outer diameter is 330 µm, inner conductor diameter is 79 µm and the dielectric diameter is 200 µm.

This coaxial cable can work fine with arrays of wires that have gap width (between wires) larger than 79 µm. If the diameter of wires is 25 µm then the spatial resolution (according to equation 2.50) is 52 µm. Therefore, a voltage probe fabricated from the UT-013 cannot be used to scan bond wires of 25 µm wire/gap width array, see Figure 4-25(A). The alternative is miniaturizing the diameter of the internal conductor to be smaller than 25 µm, see Figure 4-25(B).

There are two ways to achieve this miniaturization: either sculpting the end of the internal core as Delft group did [138], see Figure 2-35(A), or fabricate a miniaturized coaxial cable as Kantor did [103], see section 2.14.2.1.

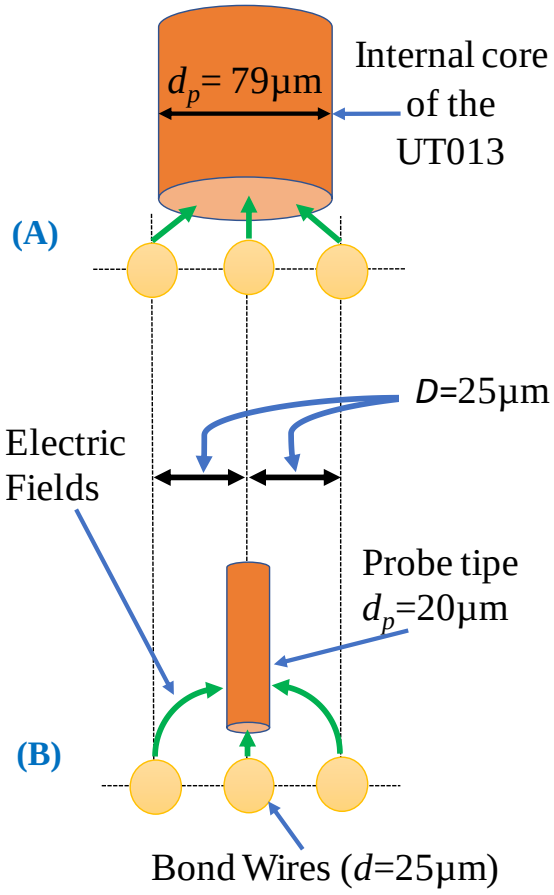

Figure 4-25 The internal core of UT-013 above bond wires array (25 µm wire/gap width) compared with 20 µm copper wire as a probe tip above the same array.

The sculpting approach is much simpler but, on the other hand, it maintains the overall size of the coaxial cable. This means more unnecessary disturbance to the electromagnetic field distribution and less freedom to move inside the microwave power transistor. This can be a real challenge, especially when scanning over a narrow die where bond wires of the gate and drain become very close to each other, see Figure 4-26. In such circumstances, it becomes a challenge to avoid accidentally touching the bond wires and thus destroying the probe and the transistor.

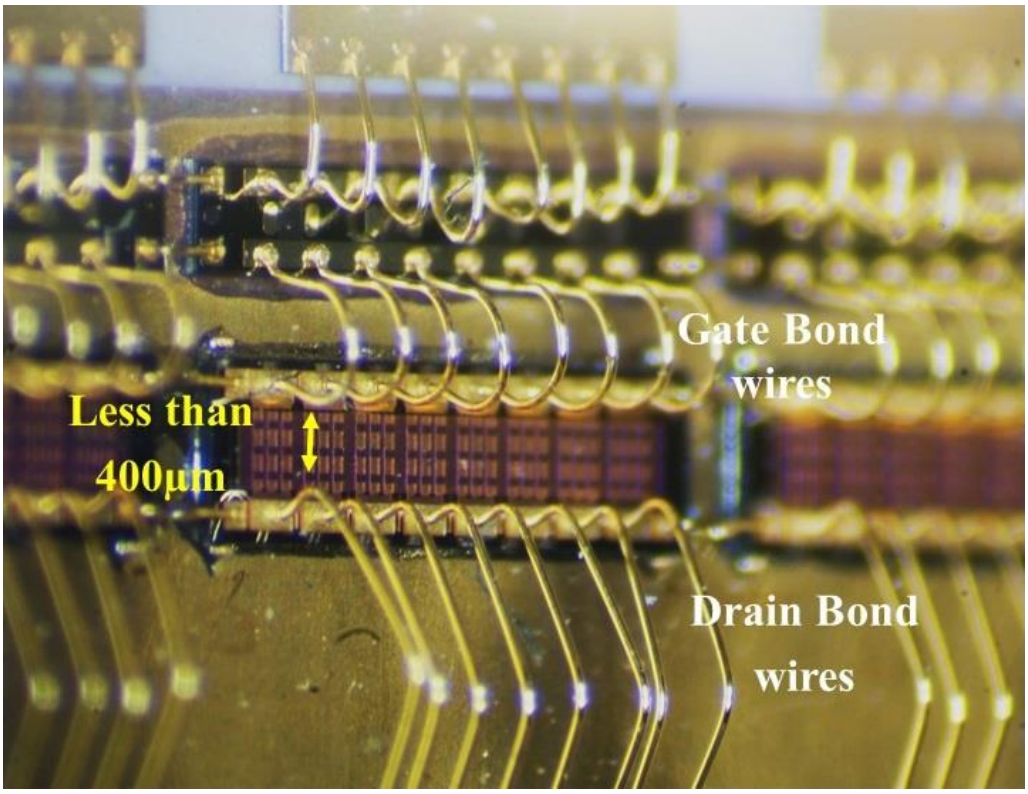

Figure 4-26 Drain and gate bond wires attached to a narrow die inside microwave power transistor.

Making the protrusion of the probe longer than the highest bond wire can partially help in minimalizing these issues, but on the other hand, this will increase the amount of noise picked up by the probe. This, of course, will require the PSDT to be applied, as it is the only possible way to enhance the spatial resolution of this voltage probe.

Fabricating ultra-miniaturized coaxial cables demands more effort to realize; however, after all it provides more freedom to move inside microwave power transistors. In addition to that all possible types of spatial resolutions enhancements, see section 4.8, can be applicable to it.

4.14 Fabricating Miniaturized Contactless Voltage Probe

The main parts of this contactless voltage probe are shown in Figure 4-27. The semi-rigid coaxial cable RG-405 is used to implement the output coaxial cable with a length of about 10cm and one of its ends is terminated with a female SMA connector for compatibility with standard measurement tools. The other end of the RG-405 is terminated to the low noise amplifier inside the probe housing.

The miniaturized input coaxial cable is attached to the other end of this housing. The silver conductive epoxy is used for the mechanical support and the electrical connections (ground path) between these parts.

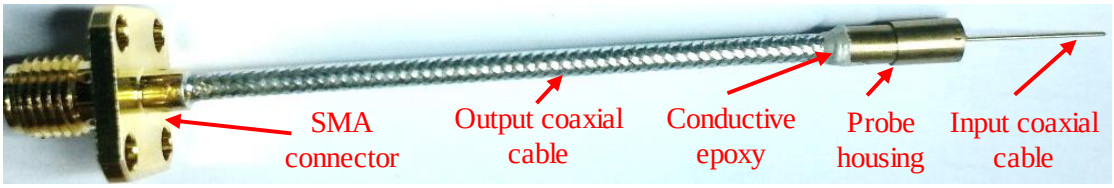

Figure 4-27 The main parts of the miniaturized contactless voltage probe.

4.14.1 Details of the Miniaturized Input Coaxial Cable

To achieve a 25 µm spatial resolution, the input coaxial cable is locally fabricated by hand from enamelled thin copper wire and miniaturized brass tube. Selecting the desired size of the wire and the tube is mainly subject to their availability.

The available brass tube has an outer diameter = 300 µm and an inner diameter = 100 µm. By applying the first rule stated in section 4.8, the diameter of the central conductor of the input coaxial cable is selected to be a 20 µm.

This wire is extremely soft and thus it is difficult to control its protrusion and position inside the brass tube. To solve this issue, the wire is firstly inserted through a glass tube of outer diameter = 80 µm and an inner diameter = 50 µm, see Figure 4-28.

This of course increases the distributed capacitance of the input coaxial cable from 0.035 pF/mm to 0.046 pF/mm (due to the increase in the total dielectric constant from 1.05 to 1.33).

However, this new value of the distributed capacitor is less than 50% of that of the UT-013 (0.095 pF/mm). The characteristic impedance of this input coaxial cable is 84 Ω. The length of this input coaxial cable is set to 10 mm and the protrusion of the central conductor is 10 µm.

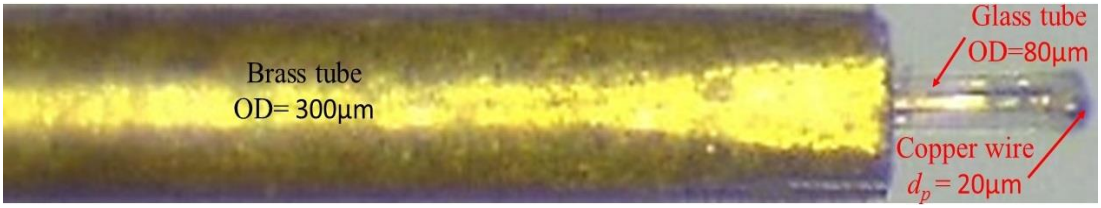

Figure 4-28 Structure of the input coaxial cable.

4.14.2 The Low Noise Pre-amplifier

The internal structure of the miniaturized voltage probe is shown in Figure 4-29. The active part of this probe is implemented by using a sub-miniature chip wafer scale amplifier VMMK-3603. It is an E-mode ultra-thin PHEMT technology with a low noise figure (NF = 1.4-1.9 dB). This amplifier has a positive slope gain (small signal gain = 15.5-19.5 dB) over a bandwidth from 0.1 GHz to 8 GHz [208].

This technology from Avgo requires no negative voltage to bias the input of the amplifier. In addition to that, for this amplifier, the input biasing circuit is completely embedded within its package so no additional components are needed to be connected to its input lead.

This self-biasing technique offers two important advantages. Firstly, it reduces the unwanted shunt capacitance to the ground because it eliminates the need for external discrete devices to bias it.

Secondly, it simplifies the fabrication process of the voltage probe because in this case only one biasing voltage is required for the amplifier[18]. The only DC biasing required for this amplifier is supplied to its output port, through the output coaxial cable, using a commercial broadband bias tee.

The printed circuit board (PCB) used with this amplifier is a 1.5 x 2.5 x 0.25 mm gold patterned alumina substrate and embedded in it a 70 Ω resistor to make the frequency response flat, see Figure 4-29(A).

The PCB output port is connected to a semi-rigid coaxial cable RG-405. On the input side, the 20 µm wire from the input coaxial cable is directly connected to the input port of the PCB, see Figure 4-29(B & C).

[18] If the self-biasing is not present then the amplifier will need two biasing circuits and voltages, one of them is connected to its input lead while the other is connected to the output lead.

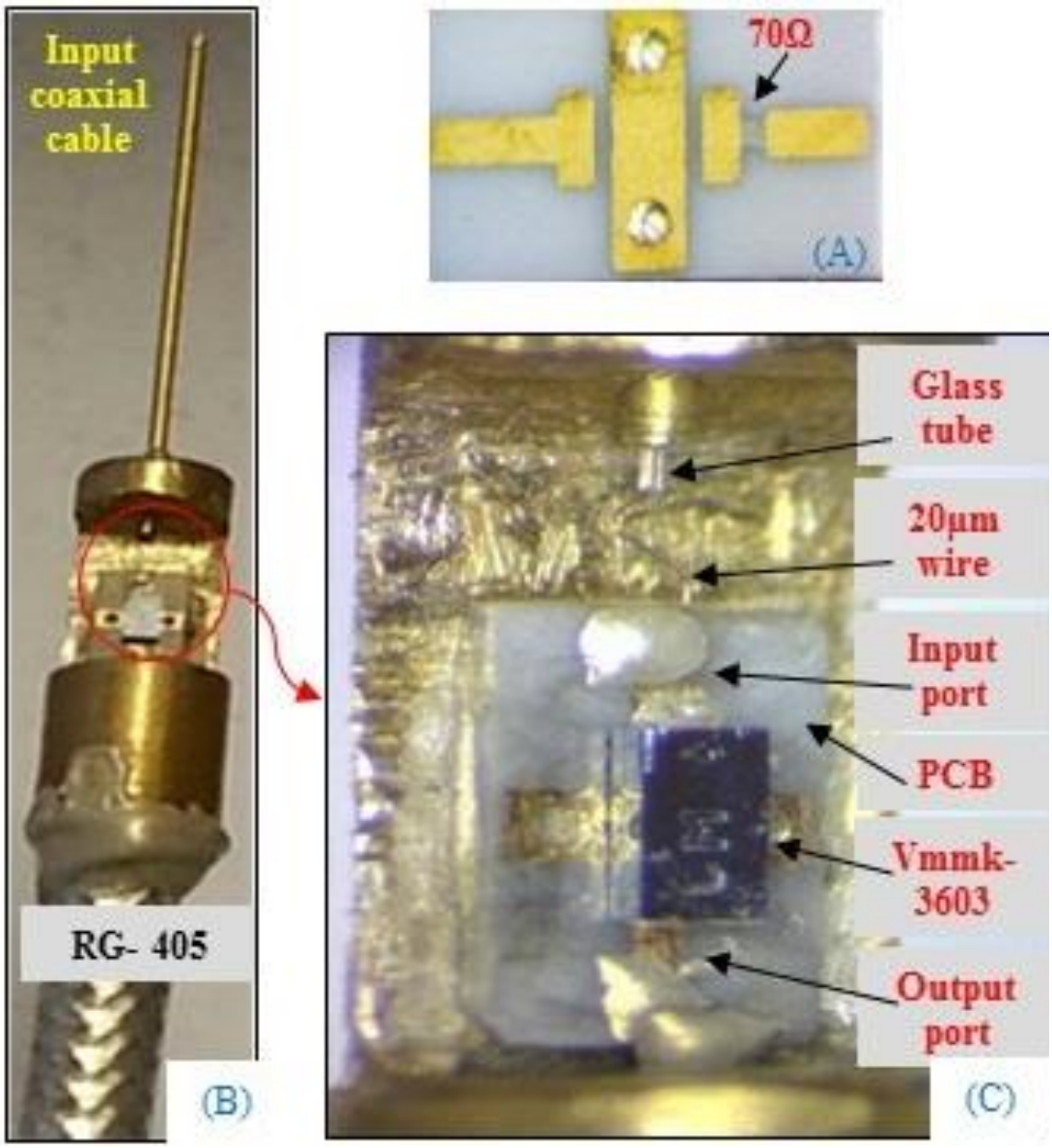

Figure 4-29 Internal structure of the miniaturized voltage probe. (A) The alumina printed circuit board. (B) & (C) The connection inside the housing of the probe.

4.14.3 Measurement Setup

The main parts of the measurement system include a vector network analyzer and stepper motors driven Z-X-Y stage under LabVIEW control, see Figure 4-30(A). Movement step size in this measurement setup can start from 48 nm with a maximum scan length of 100 mm in the X-axis and 50 mm in the Z-axis, see Figure 4-30(B).

The LabVIEW code allows spatial scanning and simultaneous logging of both magnitude and phase information at each point.

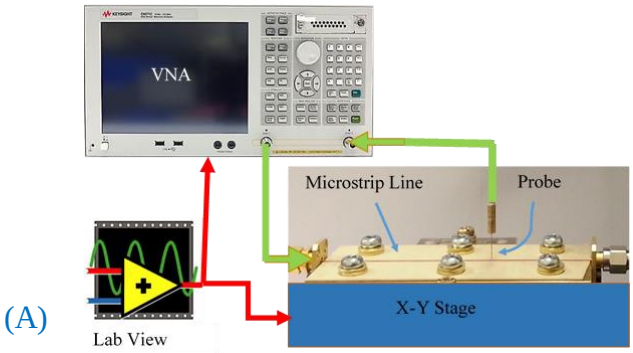

(A)

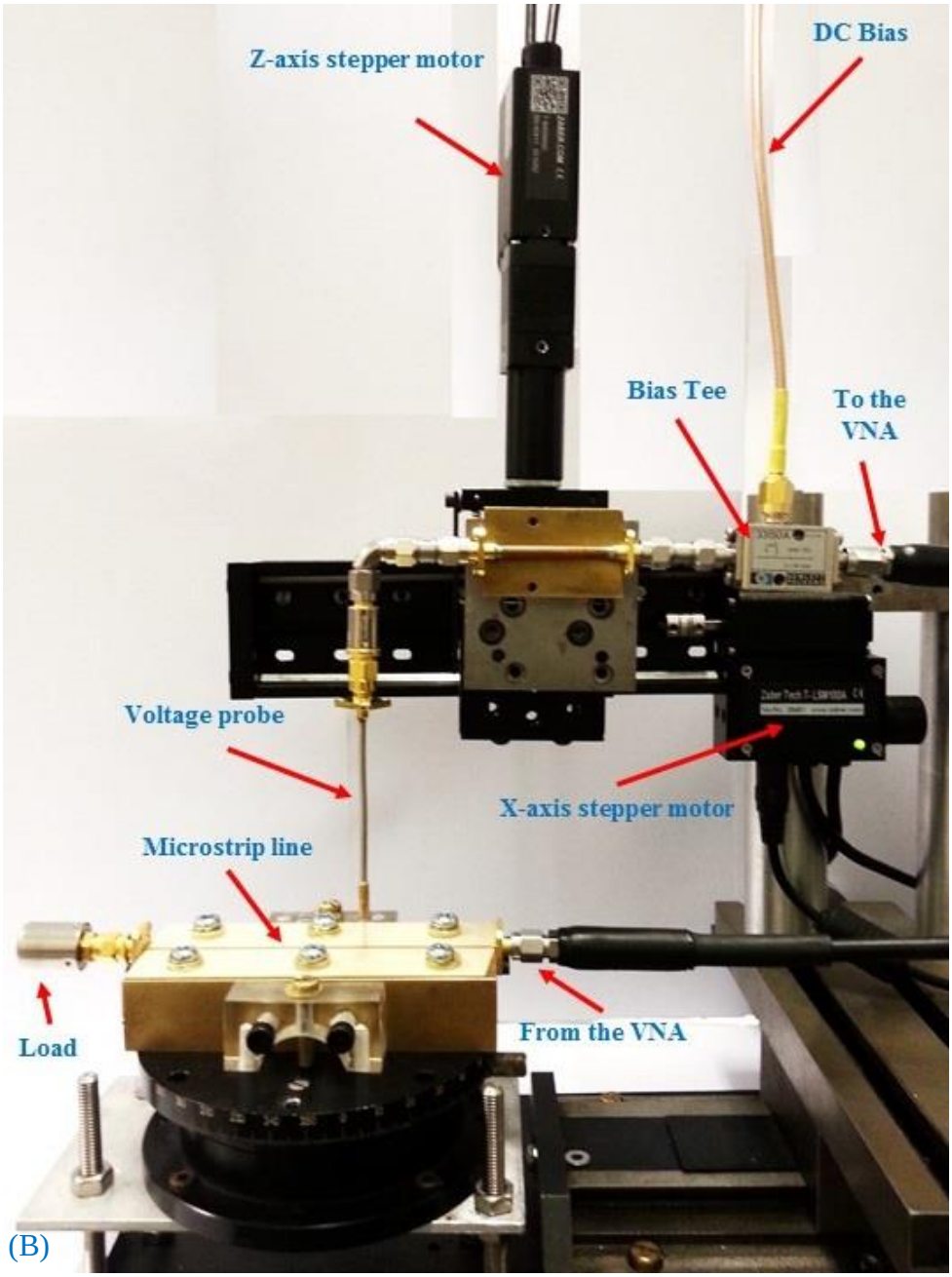

(B)

Figure 4-30 (A) The main parts of the measurement setup. (B) The parts of the XYZ stage.

4.14.4 Testing the Miniaturized Contactless Voltage Probe

A simple proof of concept is to scan the E-Field distribution over a well-known microwave device such as the microstrip line. In this case, a 50 Ω microstrip line of 100 mm length and 1.62 mm track width, fabricated from Rogers PCB TMM3, was used, see Figure 4-30(B).

Figure 4-31 and Figure 4-32 illustrate the influence of the protrusion length ℓ_p on the resolution and the sensitivity of the probe. At a very low protrusion setting, ℓ_p = 10 µm, see Figure 4-31, the edges of the copper track of the microstrip line are sharper. Also, the width is more clearly defined than the case of ℓ_p = 100 µm, see Figure 4-32.

In contrast with ℓ_p = 100 µm, the voltage probe at ℓ_p = 10 µm is able to recognize height variation at the surface of the copper track of the microstrip line at h = 1 µm and 10 µm. As previously explained the improvement in the resolution is clear as ℓ_p and h decrease.

The cost of this improvement in resolution is a reduction in the overall sensitivity. At ℓ_p = 10 µm the measured values of E-Field intensity for all scans are at least 5.4 dBm lower than those for the case of ℓ_p = 100 µm. For example, the E-Field intensity for ℓ_p = 10 µm is about -55 dBm at h = 200 µm while for ℓ_p = 100 µm it reaches a similar value at h = 2000 µm.

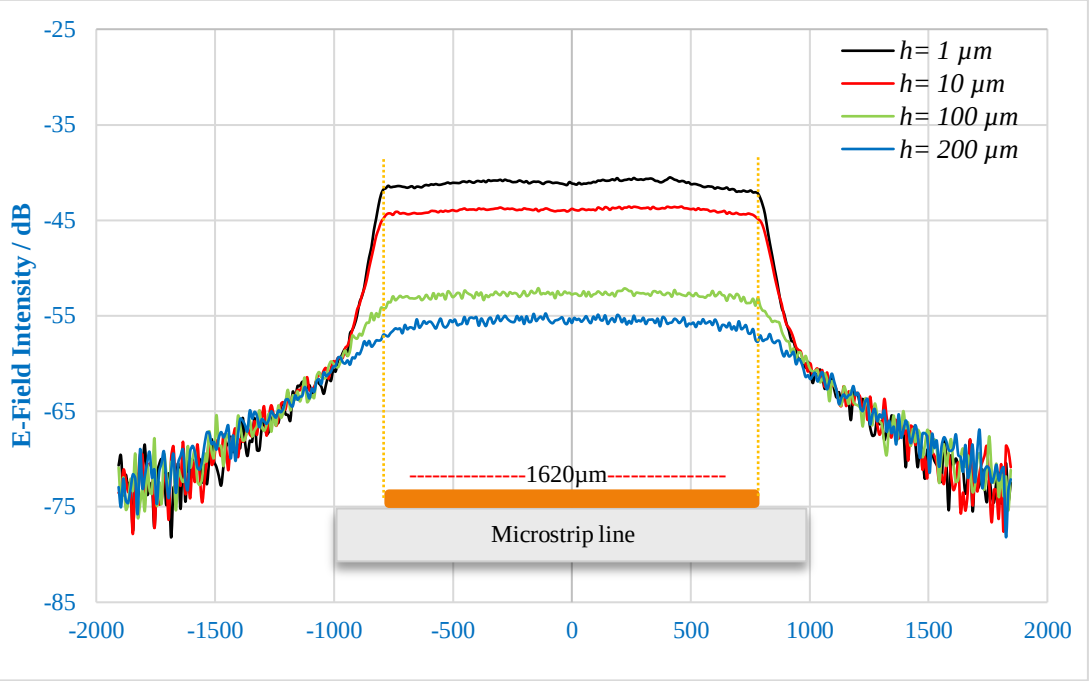

Figure 4-31 E-Field intensity scan results across the width of the microstrip line. The probe tip length is set to ℓ_p = 10 µm. The scans are for four values of h = 1, 10, 100 and 200 µm.

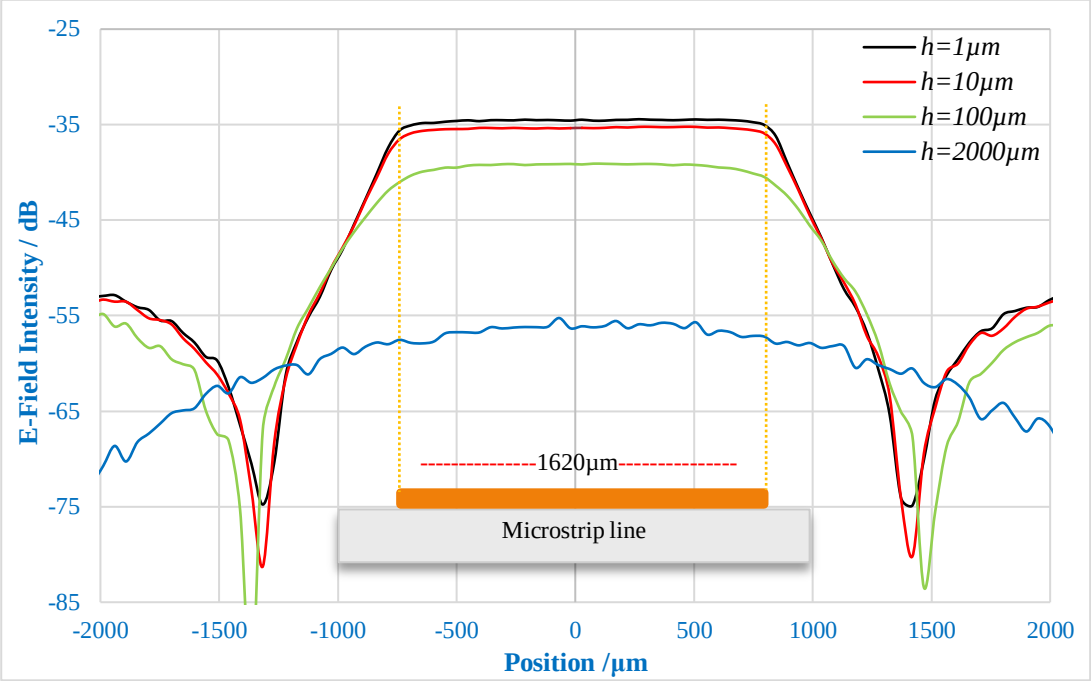

Figure 4-32 E-Field intensity scan results across the width of the microstrip line. The probe tip length is set to ℓ_p = 100 µm. The scans are for four values of h = 1, 10, 100 and 2000 µm.

The results in Figure 4-31 demonstrates the effect of h on the spatial resolution of the voltage probe. It indicates that an appropriate assignment of both ℓ_p and h is critical for obtaining the required spatial resolution. For example, fixing ℓ_p = 10 µm and increasing h to 100 µm changes the shape of the response in Figure 4-31 to be very similar to that when ℓ_p = 100 µm at h = 100 µm in Figure 4-32. Voltage probe response for both cases, ℓ_p = 10 µm and ℓ_p = 100 µm, when h is varied from 1–1100 µm is shown in Figure 4-33. The trend lines are decaying in an exponential like manner.

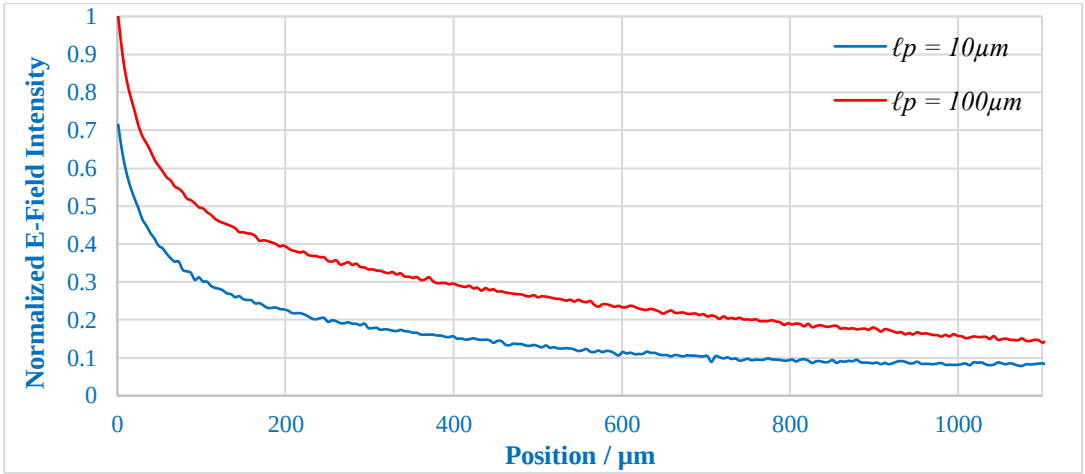

Figure 4-33 Voltage probe response as a function of h at ℓ_p = 10 µm and ℓ_p = 100 µm.

4.14.5 Spatial Resolution Test

To test and prove the high spatial resolution of this miniaturized voltage probe, we used a thin film circuit to emulate the drain bond wires array inside small to medium size transistor. Alumina of 250 µm thickness, 11.5 mm length and 4.5 mm width was used as a substrate for this test structure. The bottom layer is the ground plane. The top layer is a 0.7 mm track width widened in the middle to two flat manifolds spaced by 1.5 mm. These manifolds are connected by a parallel array of 36 fingers, with both 25 µm width and spacing, shown in Figure 4-34. The power delivered through this fixture was three watts to replicate the case of medium scale microwave transistor. The spatial resolution scan for this test fixture clearly shows the capability of this probe in resolving the varying electric field intensity between the gold fingers as shown in Figure 4-35.

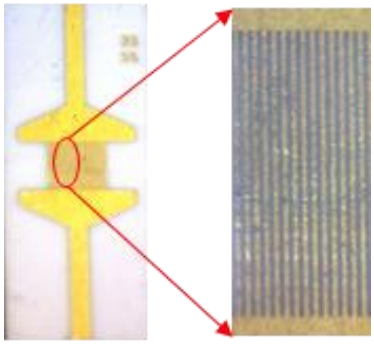

Figure 4-34 Thin film circuit used to simulate bonds wires array inside transistor. It consists of 36 fingers of 25 µm width and 25 µm spacing

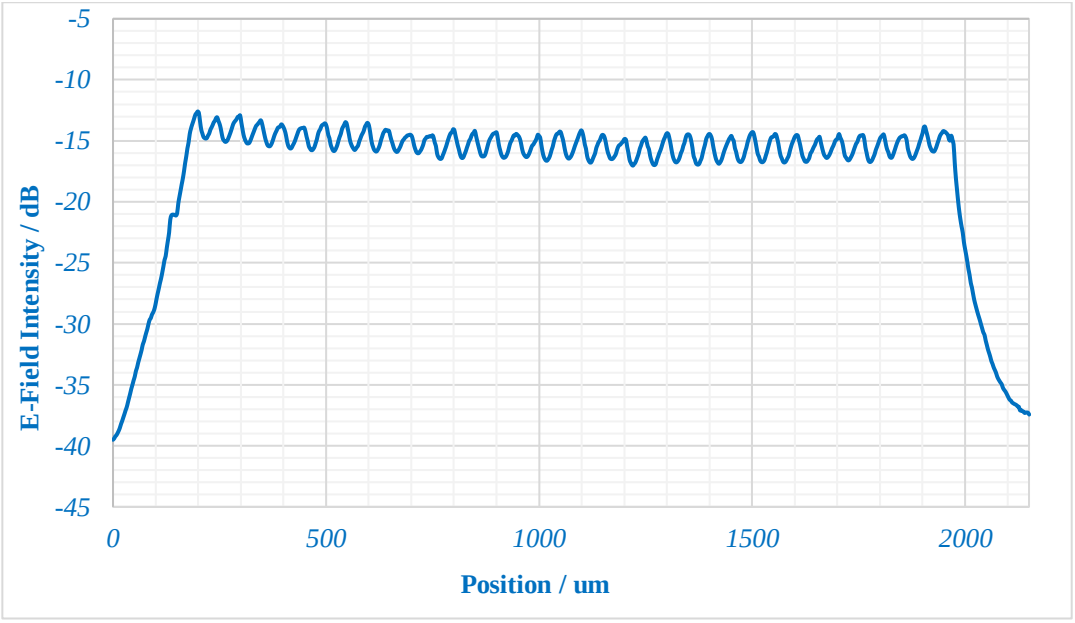

Figure 4-35 A 25 µm spatial resolution tests results of the voltage probe.

4.14.6 Bandwidth Test

The bandwidth of the probe was obtained by placing the probe at a fixed location above the microstrip line. Instead of moving the probe a standing wave pattern is generated by terminating the microstrip line with short circuit load. The sweep of frequency at this fixed location shows the voltage nulls traversing the probe tip and suggests a probe bandwidth up to 7 GHz as shown in Figure 4-36

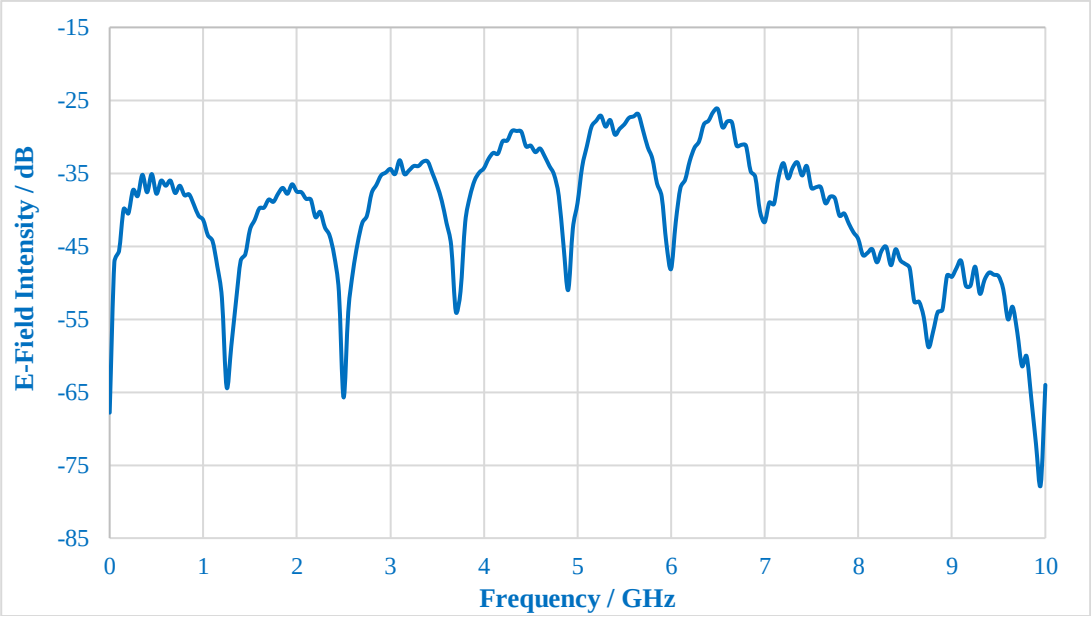

Figure 4-36 The frequency response of the voltage probe measured at fixed location above a microstrip line terminated with short circuit load.

4.15 Conclusion

A broadband voltage probe with high spatial resolution has been developed and the design criteria presented in this chapter. This probe has demonstrated an ability to measure directly the voltages on adjacent tracks that are spaced by a distance of 25 µm, with a useful bandwidth up to 7 GHz. The developed voltage probe is thus claimed to have the capability to measure the electric field distribution at a resolution four times finer than previously reported probes. Furthermore, through the gain enhancements, it is possible to utilize time domain oscilloscope-based measurements for the purposes of two-dimensional waveform engineering.

5 CURRENT PROBE REALIZATION AND TESTING

5.1 Introduction

In a similar manner to the design procedure presented in chapter four, this chapter will highlight the influences of the geometrical aspects on the spatial resolution and sensitivity of a non-contact current probe. The first step in this design procedure considers the 'scaled-up' current probes in order to assess the relevant design criteria and then adapt those features to the design of the miniaturized current probes.

The preliminary design of the current probe has relied on the ability of the differential amplifier and BALUN only to reject the influence of the electric field. Consequently, it failed in the current probe fidelity test, see Figure 5-24 . As a result of this poor fidelity, a novel method of shielding the loop antenna was introduced in order to improve probe's rejection of the electric field.

The performance of this new design is then characterised through different types of tests in order to verify its specification (spatial resolution, sensitivity and bandwidth) and measurement fidelity (standing wave test and EFRR test).

5.2 Contactless Current Probe Structure

The essential parts of the active contactless current probe are shown in Figure 5-1. The loop antenna and the brass tube are within the input unit, the low noise differential amplifier is the transition unit and the output unit are implemented by two coaxial cables.

The geometrical aspects of the loop antenna are controlling both the spatial resolution and the sensitivity of the contactless current probe. For the same reasons discussed in 4.2, the degradation in sensitivity, due to the miniaturization of the loop antenna, is compensated by cascading the loop antenna with a low noise pre-amplification stage (in this case a differential amplifier). This differential amplifier also contributes to the enhancement of the fidelity of the current measurement, by reducing the effect of the electrical field component. The inputs to the differential amplifier each have a signal that is proportional to the intensity of the magnetic field that are 180° out of phase; these outputs are then subtracted. This subtraction can either be performed within the measurement instrument if it has multiple input ports or by using the balanced to unbalanced (BALUN) converting devices.

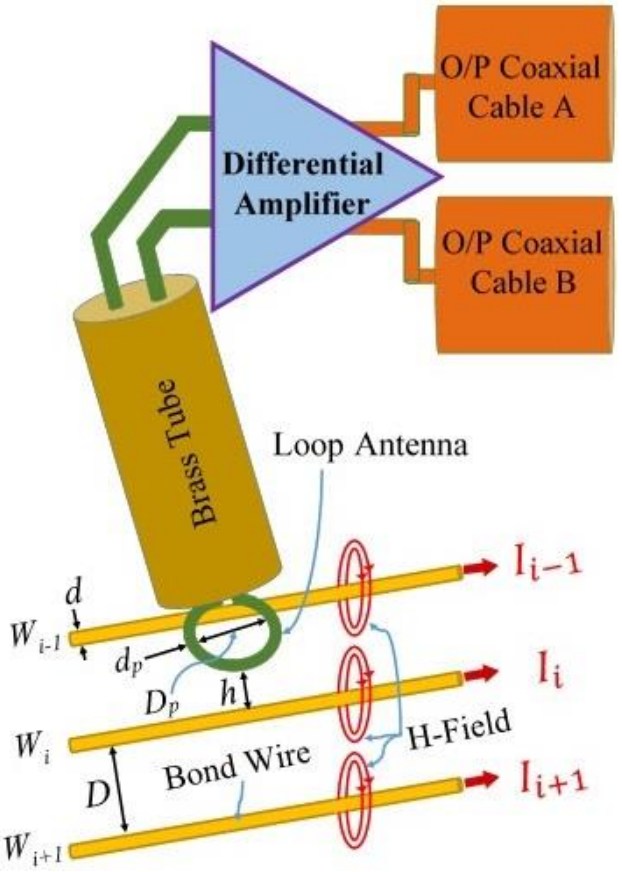

Figure 5-1 The main three units of the active contactless current probe: the loop antenna, the low noise differential amplifier, and the output coaxial cables.

5.3 Parameters Affecting the Spatial Resolution & the Sensitivity

The geometry of the loop antenna is defined by two parameters: the cross-sectional diameter of the conductor forming the loop (d_p) and the internal diameter of the loop aperture (D_p). These geometrical aspects combined with separation distance from the DUT (h), see Figure 5-2, are affecting the current probe's spatial resolution and sensitivity.

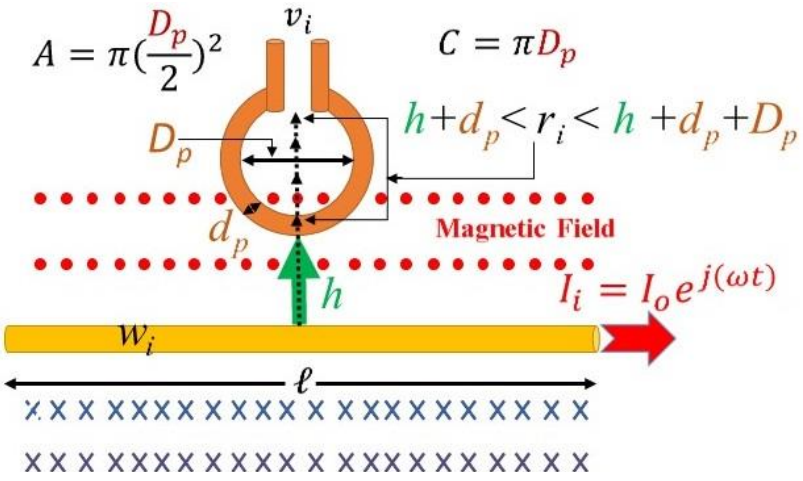

Figure 5-2 The parameters defining the geometry of the loop antenna and the distance from the wire (W_i).

The inductive coupling, between the loop antenna and one wire element (W_i), within the wire array of the DUT, induce a voltage at the terminals of the loop given in (2-46), see Figure 2-16. At specific values for the wire length and the current flowing, this induced voltage can be simplified to:

$$v_i = Kf\frac{A}{r_i^3} \tag{5-1}$$

Where, (K) is the probe constant, (f) is the frequency of operation and (A) is the aperture area of the loop antenna that exposed to the magnetic field lines, which is given by:

$$A = \pi\left(\frac{D_p}{2}\right)^2 \tag{5-2}$$

The radius (r_i) of the magnetic field lines crossing the aperture of the loop, see Figure 5-2, is given by:

$$(h + d_p) \leq r_i \leq (h + d_p + D_p) \tag{5-3}$$

and for the side wires ($W_{i\mp1}$) within the wire array, see Figure 5-1, the value for the radii are given by:

$$\sqrt{(h+d_p)^2+(D+d)^2} \le r_{i\mp1} \le \sqrt{(h+d_p+D_p)^2+(D+d)^2} \qquad (5\text{-}4)$$

Where, (d) is the cross-sectional diameter of the wire and (D) is distance separating between any adjacent wires. In practical conditions, to gain higher spatial resolution and sensitivity, the value of h is chosen to be much smaller than d_p, see section 5.5.

The contour lines of the magnetic field, around a single wire, have a circular shape and share the same centre with growing radius toward infinity. The superposition of fields coming from adjacent wires, carrying currents in the same direction change contour shape to be more elliptical in the near field. The highest magnetic field intensity (the maxima) can be seen above any wire within the array, while lowest intensity (the minima) occurred in the area between any two adjacent wires, see Figure 5-3.

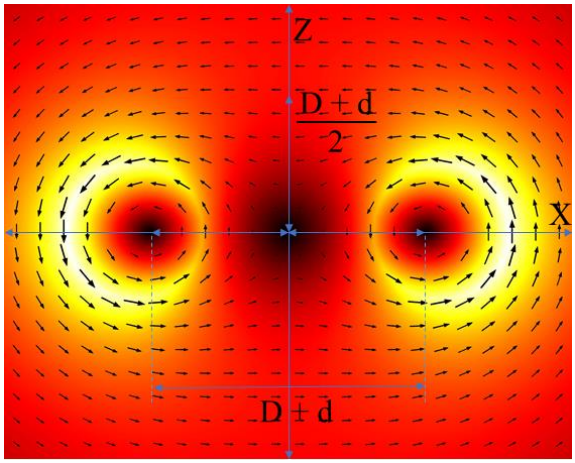

Figure 5-3 Magnetic field intensity around two parallel wires carrying currents in the same direction [209].

The ability of the current probe to recognizes these maxima and minima depends on the relative values of d_p and D_p with respect to d and D at a specific height. If the currents in these adjacent wires are equal, then the location of the minima is directly[19] between them at X = 0 and Z = 0. In terms of the DUT parameters, this point is located at (D+d)/2 from each of the side wires. As the observation point moves away from this point along the Z axis, the presence of the minima diminishes until the intensity of the magnetic field reaches a similar level to that directly above the side wires at the same height, see Figure 5-3.

[19] This special case is considered here for illustration purpose only, practically the location of the minima could be anywhere between the adjacent wires depending on the currents passing through them.

Based on the similarity between the case of the voltage probe and the current probe, many of the concepts discussed in sections 4.3 and 4.4 (like DUT parameters and the definitions of the spatial resolutions in terms of probe output voltage rather than the spatial aspects) are applicable for the current probe as well.

5.3.1 The Influence of d_p on the Spatial Resolution and the Sensitivity

Since the cross-sectional diameter of the loop increases the separation between the DUT and the active aperture of the loop from the bottom and the sides, it is appropriate to keep d_p small with respect to d and D_p. However, when the priority is to design a miniaturized current probe, this may not always be satisfied. As a result, both the sensitivity and the spatial resolution of the current probe are negatively impacted.

Having a piece of high conductivity metal (copper), very close to a localised magnetic field distribution, will have the effect of shielding that field from the sensing loop. Only those field lines that have a radius larger than the dimensions of this piece of metal may be detected. In terms of spatial resolution, the loop antenna cannot recognize the minima and maxima if its cross-sectional diameter is larger than $(D+d) / 2$.

The relationship between the sensitivity and d_p is given by (5-1), (5-3) and (5-4).The impact of d_p on the spatial resolution can be seen at the minima locations where there is a limited margin (along the Z-axis) to sense the variations in magnetic field intensity, see Figure 5-3. If $d_p > (D+d)$ then the wires under the probe will look like a single wire and thus the magnetic field intensity inside loop aperture has a uniform level, see Figure 5-4(A). As the value of d_p decreases toward $(D+d) /2$ the current probe begins to differentiate the locations of the minima and maxima under it, see Figure 5-4(B).

If $d_p < (D+d) /2$, see Figure 5-4(C) - (F), then the intensity of all the magnetic fields (partially or totally depending on the value of $(d_p + D_p)$) crossing the loop aperture will vary over the distance $(D+d)$ and hence a noticeable spatial resolution will be achieved. The highest spatial resolution can be achieved when $d_p + D_p < (D+d)$, see Figure 5-4(E), in this case, the intensity of all the magnetic field lines crossing the aperture fluctuate in response to the locations of maxima and minima.

5.3.2 The Influence of D_p on the Sensitivity and the Spatial Resolution

Enlarging the aperture of the loop antenna leads to increased energy coupling from the magnetic field crossing it and therefore the current probe may have a higher sensitivity, see (5-1) and (5-4).

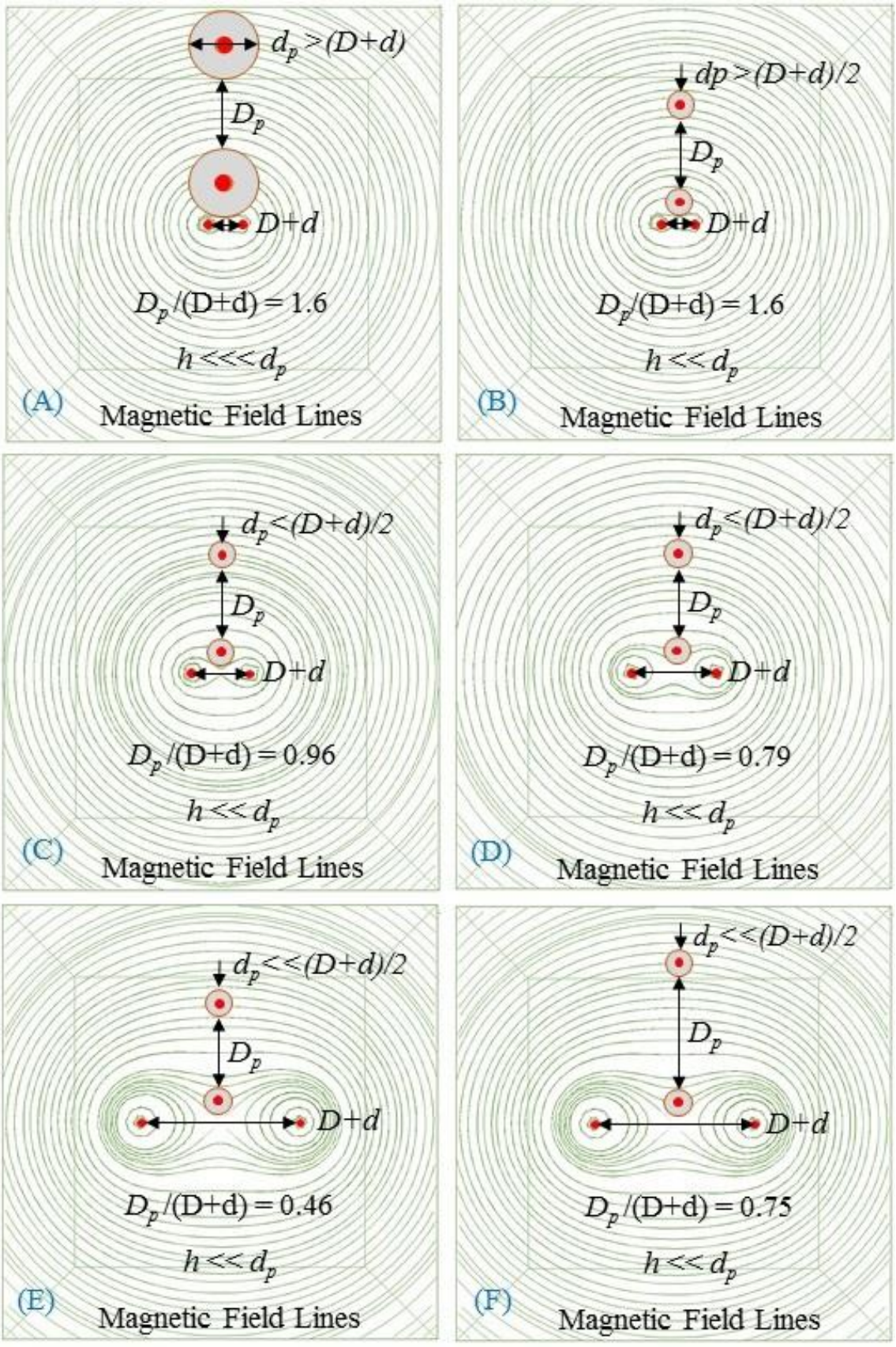

Figure 5-4 The influence of the geometrical parameters of the loop antenna on the spatial resolution and the sensitivity of the current probe.

In contrast, the spatial resolution is inversely proportional to the ratio between D_p and (D+d). If the essential condition d_p< (D+d) /2 is satisfied, then the former ratio may define how far the probe is able to differentiate the variation in magnetic field intensity at the minima locations, see Figure 5-3 and Figure 5-4(C) - (F).

In this case, the highest spatial resolution occurs when the value of (d_p + D_p) becomes much smaller than (D+d). Under these circumstances, the intensity of the magnetic field crossing the loop aperture will strongly vary, over the distance (D+d), in response to the location of the minima and maxima, see Figure 5-4(E). Otherwise, this response becomes a matter of percentage ratio between two parts of the magnetic field crossing the loop aperture, one has a variable intensity and the other has a constant intensity.

5.4 Experimental Validation of the Loop Geometrical Aspects

In this section, we will experimentally inspect the influence of the loop antenna parameters (d_p and D_p) on the spatial resolution and sensitivity of the contactless current probe. To keep the focus on the loop antenna only, the ordinary coaxial cables are used to create the passive version of the contactless current probes.

Two different sizes of semi-rigid 50 Ω coaxial cable (UT-034 and RG405) are used in this implementation. The size of the smallest loop aperture, which is possible to create from these coaxial cables, is limited by their geometrical and mechanical properties.

Four PCB test fixtures (22 mm X 41 mm X 0.7 mm) are used to emulate the environments of multiple bond wire arrays, each has three fingers. The width of each finger is 0.3mm and the finger length is 11mm. To test more possibilities of the ratios d_p / (D+d) and D_p / (D+d), the gaps separating between adjacent fingers is set to: 1.1, 2.0, 2.5 and 4.5 mm, see Figure 5-5.

To keep the size of the loop smaller than the length of these fingers, we used only two sizes for the loop aperture 2.2 mm and 3.6 mm. The frequency of operation is set to 500 MHz to ensure a small circumference of the loop with respect to the operating frequency (C = π D_p << 10% λ).

The lowest scanning height (h) above the test fixture is set to 50 µm for all measurements (unless otherwise stated). Total scanning length (across the fingers) is 18 mm and scanning step is set to 50 µm.

The input power delivered to this test fixture is 1 mW introduced by a VNA and the other end is terminated with the 50 Ω load.

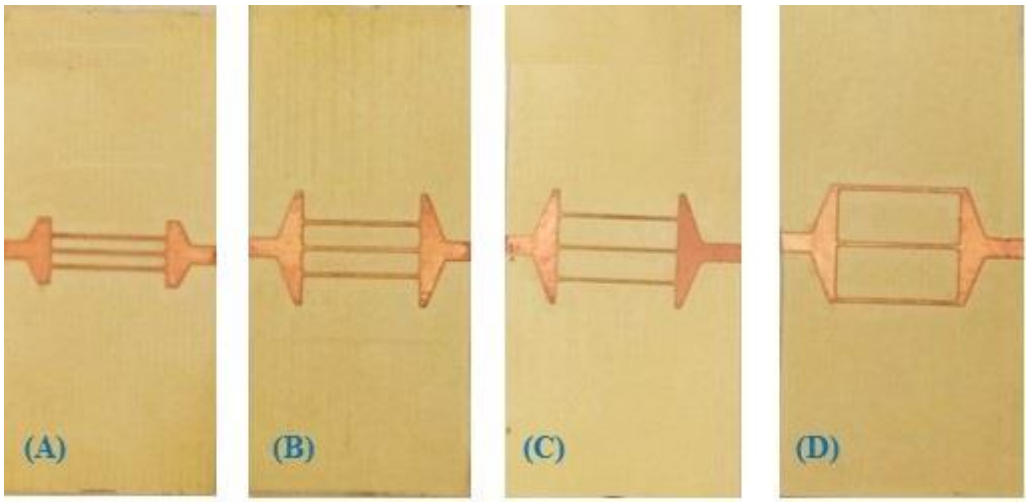

Figure 5-5 Four PCB test fixtures (22 mm X 41 mm X 0.7 mm) used to simulate the environments of bond wires array of 0.3 mm track width and gap width equal to (A) 1.1 mm. (B) 2 mm. (C) 2.5 mm. (D) 4.5 mm.

5.4.1 Influence of d_p on the Spatial Resolution and Sensitivity

To examine the effect of increasing d_p on the spatial resolution and the sensitivity of the current probe, two probes of the same loop aperture, D_p = 2.2 mm, were fabricated from the cables UT-034, d_p = 0.86 mm, and RG405, d_p = 2.2 mm.

These passive current probes are then used to scan the set of test fixtures shown in Figure 5-5(A) - (D), at the following values of the ratio d_p / (D+d), 1.57 & 0.61, 0.96 & 0.37, 0.79 & 0.3 and 0.46 & 0.18 respectively.

Figure 5-6(A) - (D) shows that there is a strong negative relationship between the spatial resolution of the current probe and cross-sectional diameter of the loop antenna. At large values of the ratio d_p / D+d, the current probe becomes unable to recognize the fingers and the gaps between them. This can be clearly seen in Figure 5-6(A), where the probe created from the RG-405 introduces a wide signal plateau in the centre of the structure.

This negative influence decreases as the ratio d_p / (D+d) decreases and additional enhancement can be achieved when this decrease is combined with a decrease in the ratio D_p / (D+d), see Figure 5-6(C) - (D).

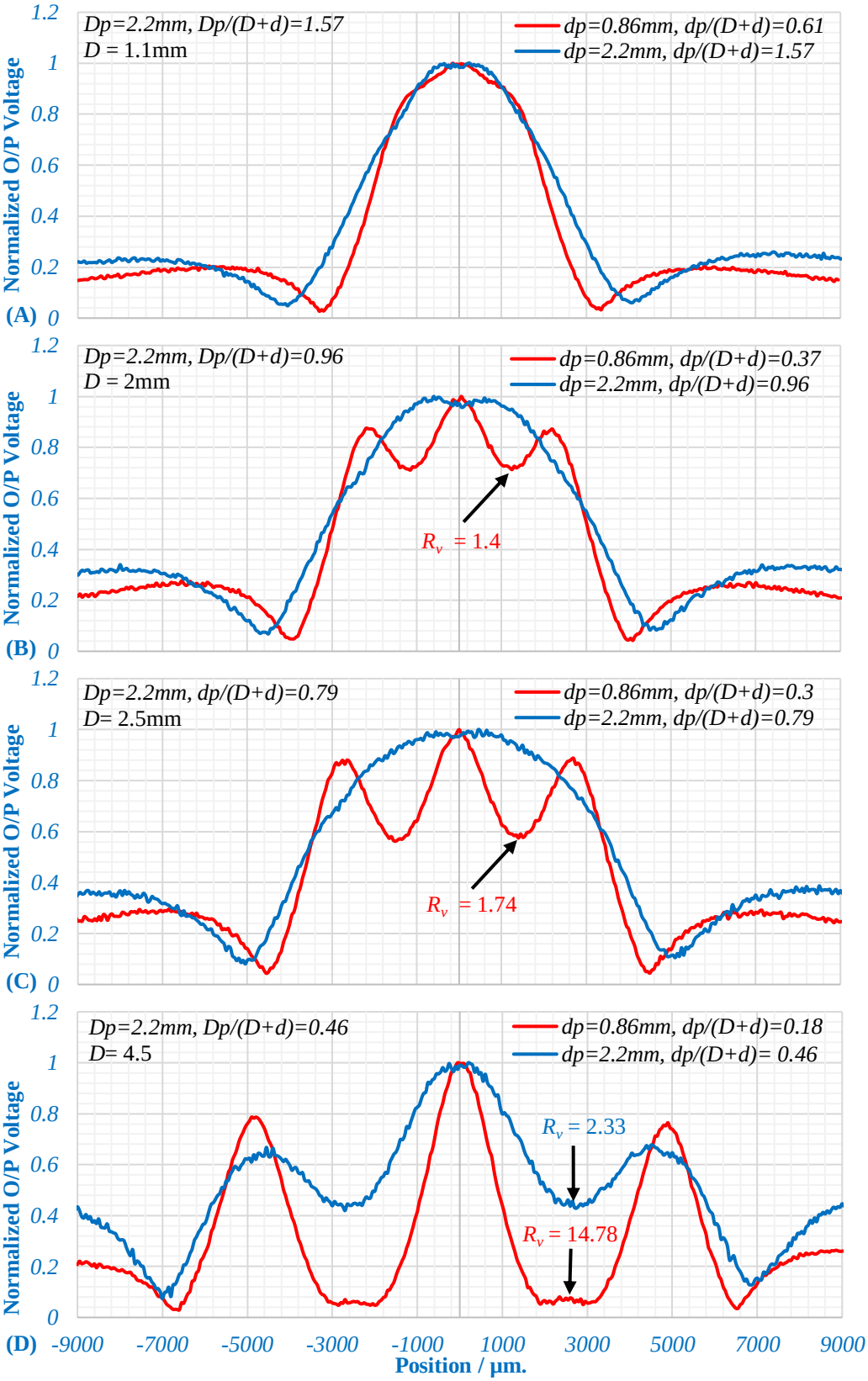

Figure 5-6 The influence changing d_p (from 0.86 mm to 2.2 mm) on the spatial resolution of the current probe (D_p = 2.2 mm) at the following values of the ratio d_p / (D+d): (A) d_p / (D+d) = 0.61 & 1.57. (B) d_p / (D+d) = 0.37 & 0.96. (C) d_p / (D+d) = 0.3 & 0.79. (D) d_p / (D+d) = 0.18 & 0.46.

For example, at D_p / (D+d) = 0.46, the spatial resolution recorded its highest values: R_v = 14.78 at d_p = 0.18*(D+d) (the loop implemented by the UT-034) and R_v = 2.33 at d_p = 0.46*(D+d) (the loop implemented by the RG-405), see Figure 5-6(D). In addition to that, the latter offers better spatial resolution than that achieved by the UT-034, R_v = 1.74, in Figure 5-6(C). This improvement is due to the reduction in the ratio D_p / (D+d) from 0.79 to 0.46. However, this improvement is at the expense of the accuracy in locating the maxima positions. For this case, the thin loop is more accurate than the thick loop.

In terms of the current probe sensitivity, the experimental results are shown in Figure 5-7 (A) - (D) agree with the qualitative geometrical analysis given in section 5.3.1. The sensitivity of the current probe degraded as the cross-sectional diameter of the loop increased. The loop fabricated from RG-405 increases the height between the DUT and the lower threshold of the loop aperture and thus the sensitivity of this loop is always lower than that of the loop formed from the UT-034 by at least 20% for all ratios of D_p / (D+d).

5.4.2 Influence of D_p on the Spatial Resolution and Sensitivity

To examine the impact of increasing D_p on the spatial resolution and the sensitivity of the current probe, two probes with different loop apertures, D_p = 2.2 mm, and D_p = 3.6 mm, were fabricated from the UT-034, d_p = 0.86 mm. Both are used to scan the set of test fixtures, see Figure 5-5(A) - (D), at the following values of the ratio D_p / (D+d): 1.57 & 2.57, 0.96 & 1.57, 0.79 & 1.29 and 0.46 & 0.75 respectively.

In terms of spatial resolution, results are shown in Figure 5-8(A) - (D) support what has been achieved during the previous sections. The essential factor here is reducing the ratio d_p / (D+d) as much as possible while the size of the loop antenna aperture has a complementary role only. Enlarging loop aperture area by about 37% reduced the spatial resolution and the effectiveness of this reduction is inversely proportional to the the value of d_p / (D+d), see Figure 5-8(A) - (D).

In contrast with this trend of change in the spatial resolution, the influence of enlarging the aperture area of the loop antenna on the sensitivity of the current probe is positive and yields a more efficient coupling. Results shown in Figure 5-9(A) - (D) illustrate that the large aperture introduces more gain and thus better sensitivity (the improvement is more than 40%) in all four cases.

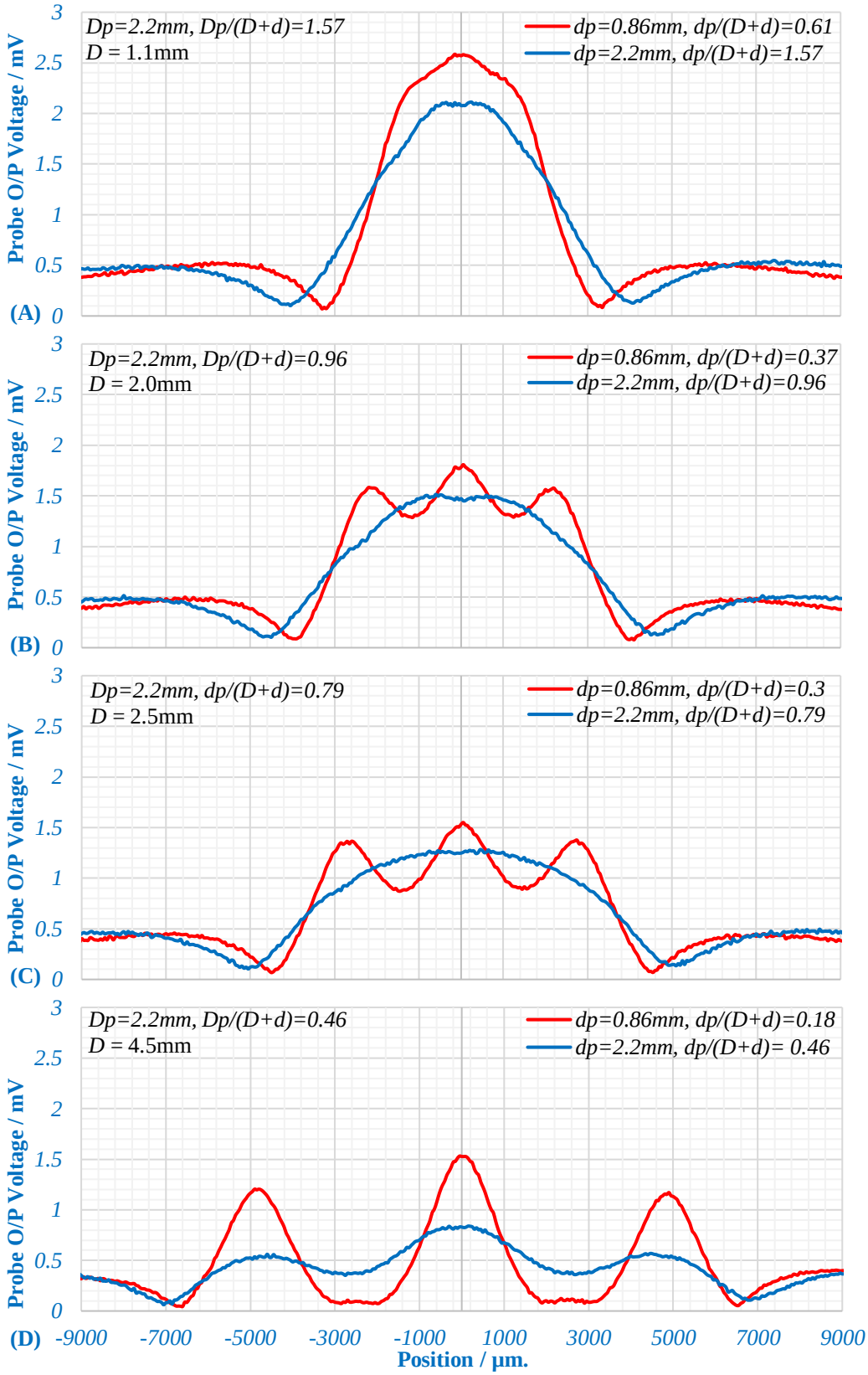

Figure 5-7 The influence changing d_p (from 0.86 mm to 2.2 mm) on the spatial resolution of the current probe (D_p = 2.2 mm) at the following values of the ratio d_p / (D+d): (A) d_p / (D+d) = 0.61 & 1.57. (B) d_p / (D+d) = 0.37 & 0.96. (C) d_p / (D+d) = 0.3 & 0.79. (D) d_p / (D+d) = 0.18 & 0.46.

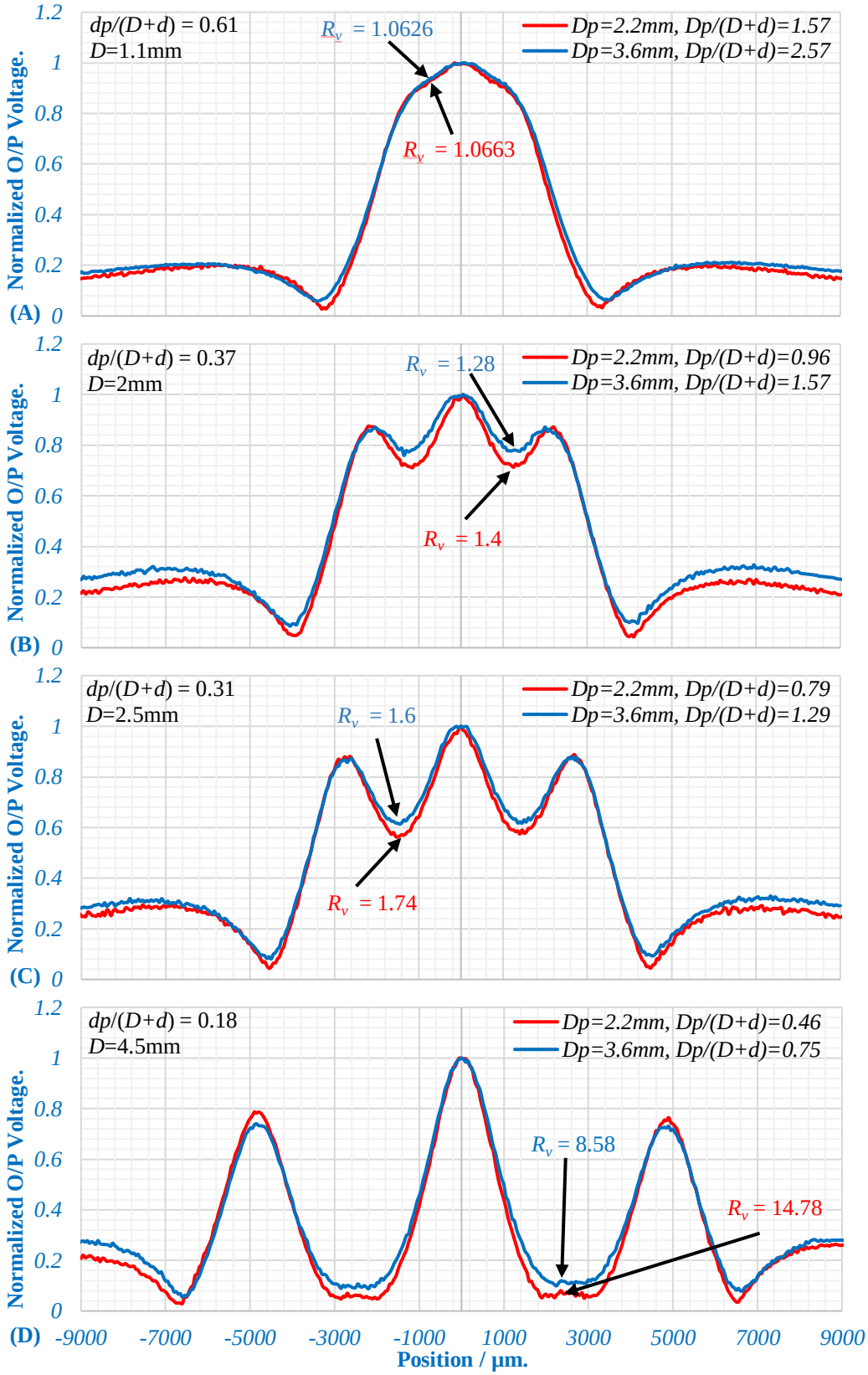

Figure 5-8 The influence changing D_p (from 2.2 mm to 3,6 mm) on the spatial resolution of the current probe (d_p = 0.86 mm) at the following values of the ratio D_p / (D+d): (A) D_p / (D+d) = 1.57 & 2.57. (B) D_p / (D+d) = 0.96 & 1.57. (C) D_p / (D+d) = 0.79 & 1.29. (D) D_p / (D+d) = 0.46 & 0.75.

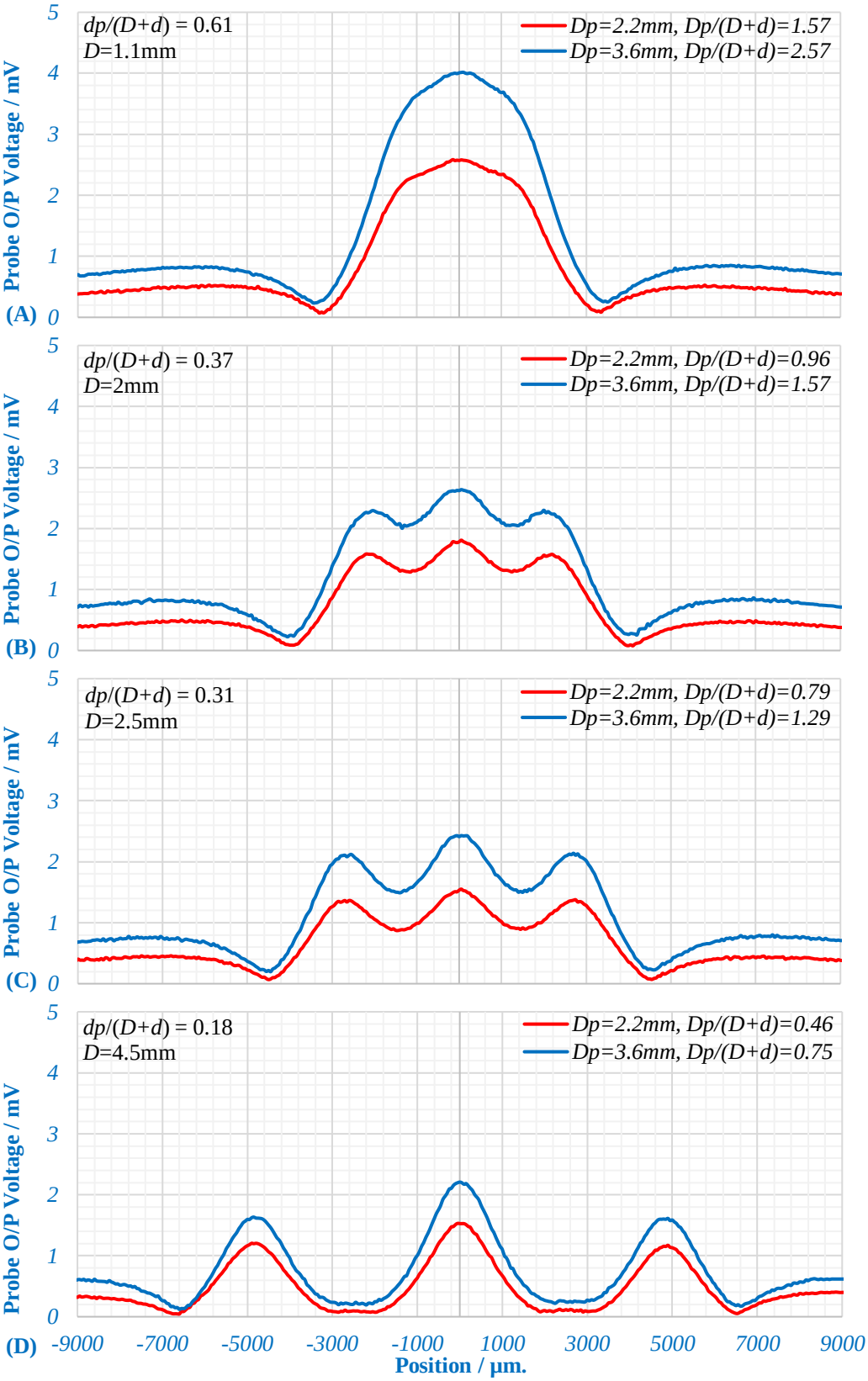

Figure 5-9 The influence changing D_p (from 2.2 mm to 3,6 mm) on the spatial resolution of the current probe (d_p = 0.86 mm) at the following values of the ratio D_p / (D+d): (A) D_p / (D+d) = 1.57 & 2.57. (B) D_p / (D+d) = 0.96 & 1.57. (C) D_p / (D+d) = 0.79 & 1.29. (D) D_p / (D+d) = 0.46 & 0.75.

5.5 Influence of h on the Spatial Resolution and Sensitivity

The radii of the magnetic field contours crossing the aperture of the loop antenna are affected by three factors d_p, D_p and h. To examine the effect of increasing h on the spatial resolution and the sensitivity with correlation to (D+d), a single probe is used in this test. It is fabricated from the UT-034, d_p = 0.86 mm and it has a loop aperture, D_p = 2.2 mm. Three scans were performed across the set of test fixtures shown in Figure 5-5(B) – (D), at the following values of the ratio (D_p+d_p) / (D+d): 1.33, 1.09 and 0.637 respectively.

Figure 5-10(A) – (C) show the inverse proportionally between current probe height and its spatial resolution. The impacts of this degradation can be noticeably reduced by decreasing the ratio (D_p+d_p) / (D+d).

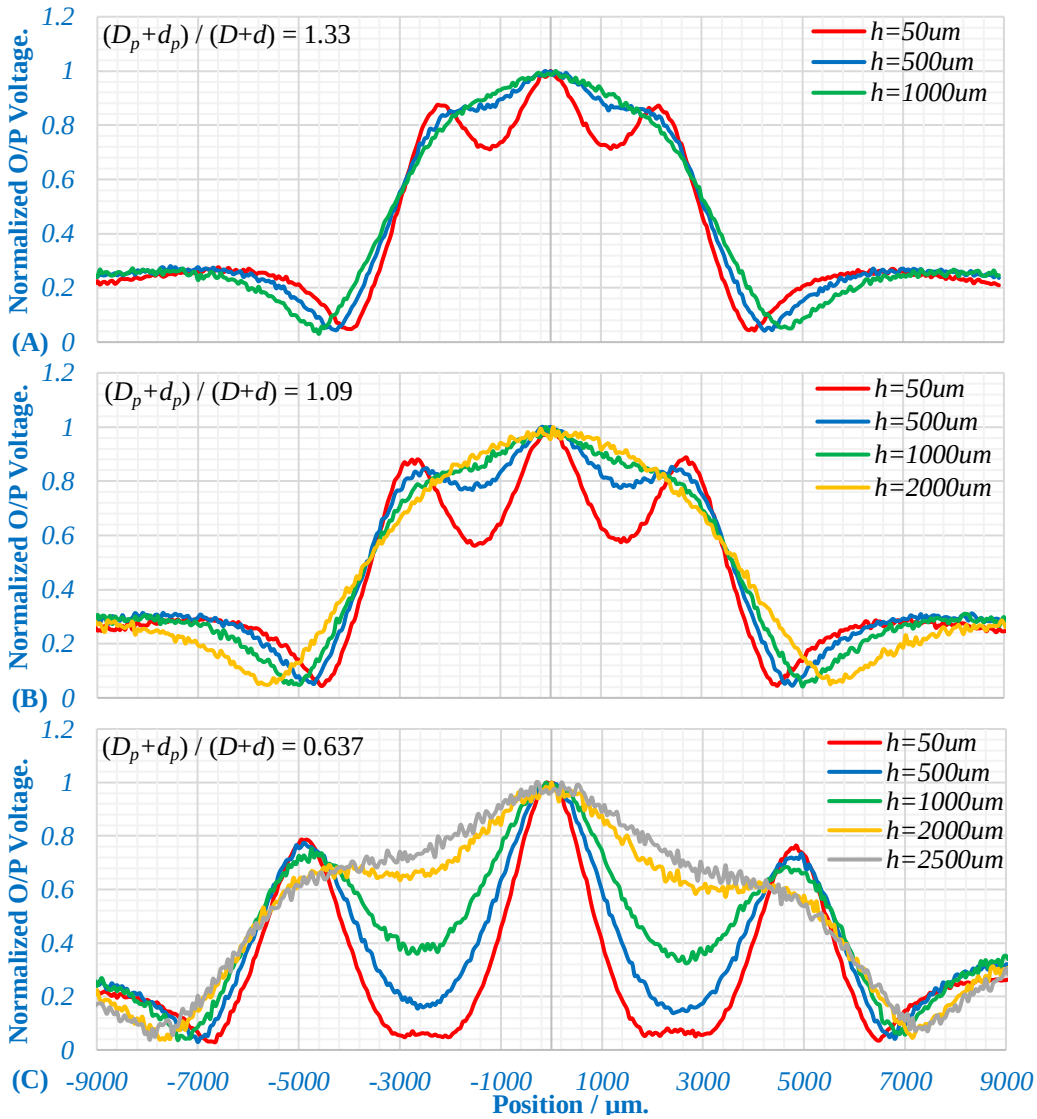

Figure 5-10 The influence changing h the spatial resolution of the current probe) at three different values of (D_p+d_p) / (D+d): (A) (D_p+d_p) / (D+d) = 1.33. (B) (D_p+d_p) / (D+d) = 1.09. (C) (D_p+d_p) / (D+d) = 0.637.

This ratio defines the percentage of the magnetic field that crosses the loop antenna aperture that has a spatially independent intensity to that which has a variable intensity in response to the maxima and minima locations. The spatially varying field is hardly recognized at h = 1000 µm when this ratio is equal to 1.33, see Figure 5-10(A), while it is still better than that at h = 2500 µm for the case of $(D_p+d_p) / (D+d)$ = 0.637, see Figure 5-10(C). Similarly, the sensitivity of the current probe is inversely related to its height above the DUT, see Figure 5-11(A) - (C). But in contrast with the case of the spatial resolution, the influences of the ratio $(D_p+d_p) / (D+d)$ on the sensitivity is negative. Finally, the variation in current probe output voltage at the minima and maxima locations in response the variation in height is shown in Figure 5-12(A) – (C) for each of the three values of the ratio $(D_p+d_p) / (D+d)$.

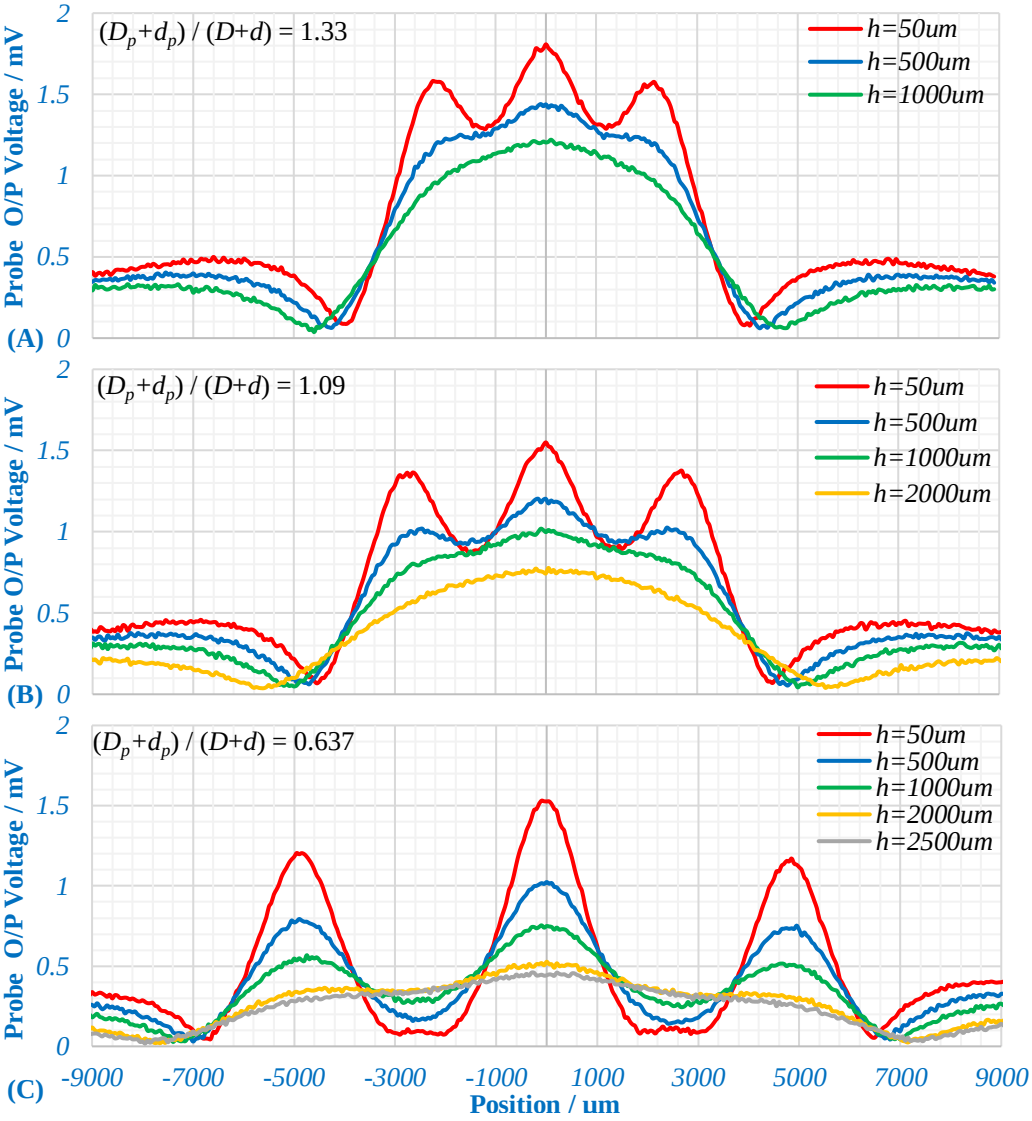

Figure 5-11 The influence changing h on the sensitivity of the current probe at three different values of $(D_p+d_p) / (D+d)$: (A) $(D_p+d_p) / (D+d)$ = 1.33. (B) $(D_p+d_p) / (D+d)$ = 1.09. (C) $(D_p+d_p) / (D+d)$ = 0.637.

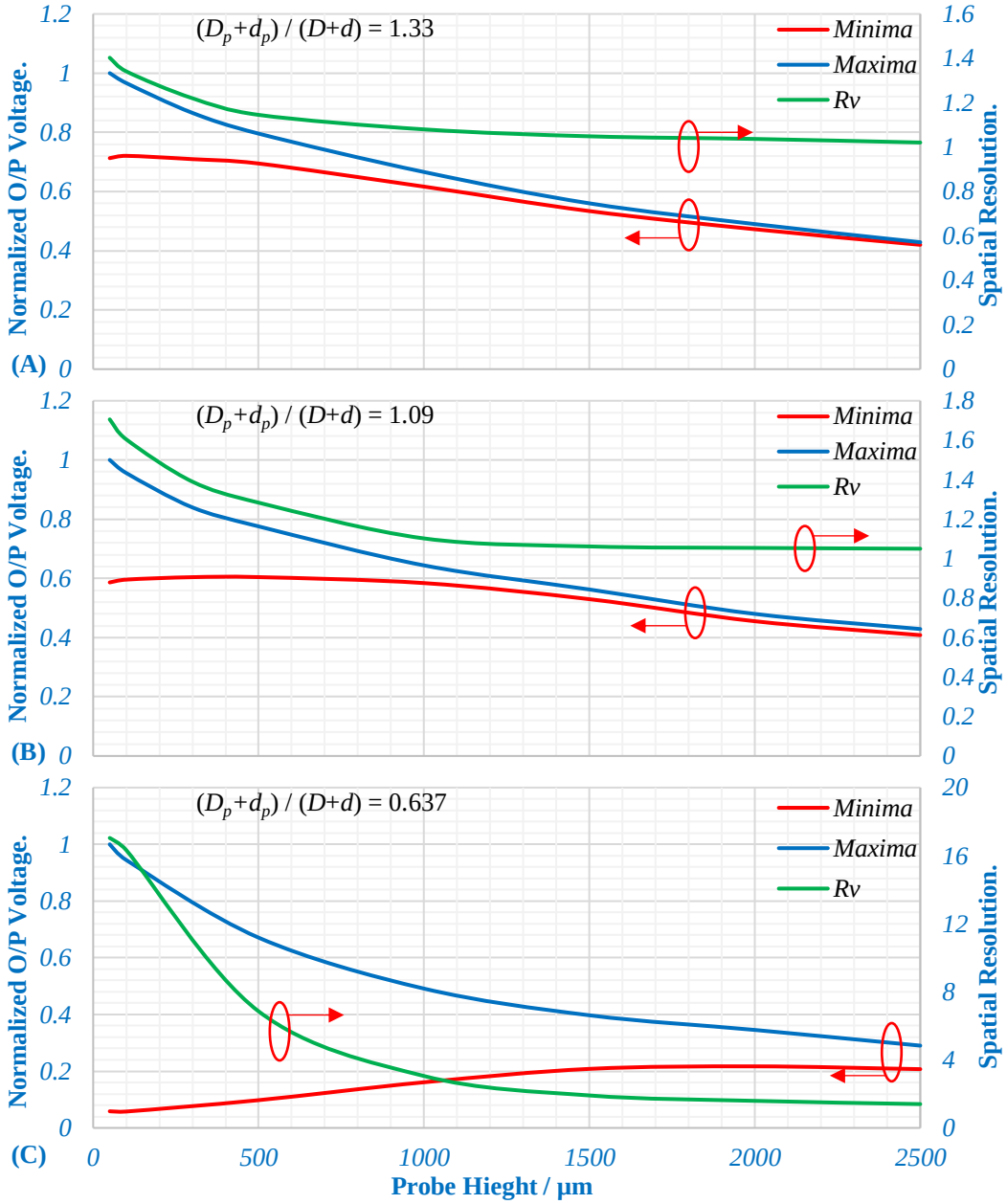

Figure 5-12 The Relationship between current probe height and its response at both the maxima and minima locations.

5.6 Criteria to Design High Spatial Resolution Current Probe

Based on the conclusions and results previously obtained, through the qualitative geometrical analysis and the experimental validation, the requirements for designing a current probe with high spatial resolution can be classified as follows:

- Essential requirement:

  The diameter of the conductor forming the loop antenna should be smaller than the sum of the wire gap widths. However, to obtain deep nulls it should be smaller than the 50% of this sum.

- Enhancement requirements:

  Reducing the size of the aperture of the loop antenna can improve the spatial resolution. A significant improvement is achieved if $(D_p+d_p) / (D+d) <1$.

5.7 Differential Amplifier

The miniaturized loop antenna provides weak signals and thus a pre-amplification is necessary to enhance the signal to noise ratio and improve the sensitivity of the current probe. The pre-amplification stage could be either a single-ended or dual-ended stage depending on the signal applied to it.

With this loop antenna, there is the flexibility to have either a single-ended output (one end of the loop antenna is connected to ground) or a dual-ended output (differential output). If a single ended approach is used, then a preamplifier stage similar to that used with voltage probe is needed here to enhance the sensitivity.

Taking the output from both loop ends can help in improving current measurement fidelity by offering more rejection to the common mode 'noise' (mainly the electric field radiation) picked up by the loop antenna itself and/or by its leads.

There are two possible topologies that can be used to amplify the differential signals [210]. In the first instance, two separate single end amplifier stages (like VMMK-3603) are connected to one of the loop output ends [163], [210], see Figure 5-13(A).

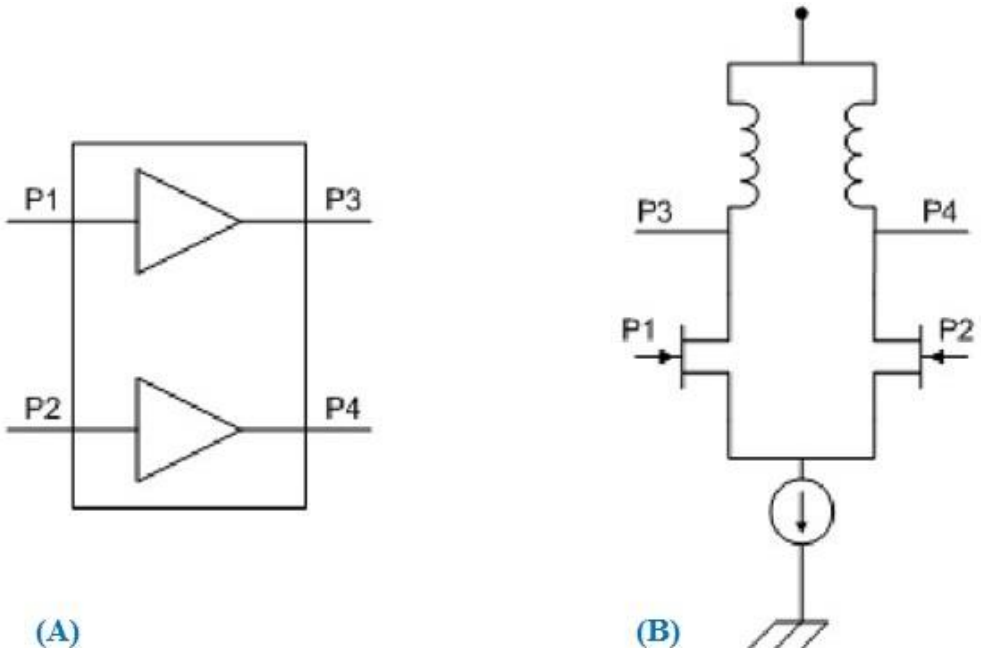

Figure 5-13 Topologies of amplifying differential signals (A) By using two single end amplifiers (B) By using differential amplifier [210].

In this case, both the common mode and the differential mode signals receive the same amount of amplification without rejection at this level. The amplified signals are then subtracted either by the measurement instrument (if it has multiple input ports) or through a BALUN (if the measurement instrument has one input port only). Although this method is very simple and easy to implement, its total common mode rejection ratio is not high because the common mode noise is initially amplified and then attenuated.

The differential amplifier is the second topology [63], [210], see Figure 5-13(B). This type of amplifier introduces high gain to the differential signals and low gain to the common mode signals and therefore higher common mode rejection is achieved. Outputs of the differential amplifier are then differentiated either by the measurement instrument (if it has multiple input ports) or through a BALUN (if the measurement instrument has one input port only).

5.7.1 Implementation of the Differential Amplifier

The enhancement-mode pseudomorphic high-electron-mobility-transistor (E-PHEMT) offers many advantages over other types of FET transistors in terms of linearity, wide dynamic range, high gain, broad bandwidth, low noise figure and the need for a single dc supply [211]–[213]. These features, combined with the ultra-small chip scale package developed by Avago Technology, provide an ideal solution for building a miniaturized differential amplifier from these discrete transistors.

The VMMK-1218 and the VMMK-1225 are both sub-miniature 0402 (1 mm x 0.5 mm x 0.25 mm) Surface Mount Leadless Package devices. From their datasheets [206], [207], they are broadband (18 GHz & 26 GHz respectively) and have a low noise figure (0.7 dB & 0.8 dB respectively) while their gain is (10.2 dB & 12.2 dB respectively). Based on these figures the VMMK-1225 has higher gain and wider bandwidth with only 0.1 dB higher in terms of the noise figure. Therefore, the VMMK-1225 was selected to implement both the differential amplifier and the current source, see Figure 5-13(B).

5.7.1.1 Differential Amplifier and Current Source Biasing

Usually, transistors require two biasing circuits to identify the location of the operating point, one of them controlling its input and the other delivering the required power through its output circuit.

A single stage of the corresponding differential amplifier with current source needs five biasing circuits: two for each of the pair differential transistors and the fifth to control the

gate of the current source transistor. This means more complexity overall and more physical space needed to implement it.

The VMMK-1218 and VMMK-1225 have another advantage that makes them more suitable for use in a confined area like the miniaturized current probe. For these transistors, if the DC voltage connected to the drain is raised while the gate is left floating without a DC biasing voltage, then it will operate in a self-biasing mode and amplify the RF signal introduced at the gate.

Driving the differential pair to work in a self-biasing mode reduces the number of biasing components to only three. The DC supply for this biasing circuit is supplied through three paths, each is terminated with an SMA connector, see Figure 5-14.

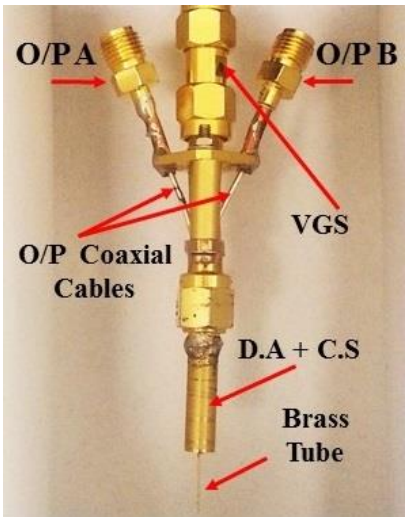

Figure 5-14 Current probe structure and the paths to DC and RF currents to and from the differential amplifier (D.A) and the current source (C.S).

The SMA connector in the middle is used to both mechanically secure the current probe to the XYZ stage and also to provide the required DC biasing to the gate of the current source. The side SMA connectors terminate the ends of the two output coaxial cables and allow paths to both the DC biasing currents and the RF signal currents to propagate to and from the drains of the differential pair. The separation between the AC and the DC component is achieved via two Bias Tee stages, see Figure 5-15.

The schematic of the differential amplifier (D.A), the current source (C.S) and the biasing circuits are shown in Figure 5-15. Inside the probe, only the differential amplifier transistors and the current source transistors are implemented, see Figure 5-16. T1 & T2 are the differential pair and T3 & R4 are connected in series to form the current source. P1 and P2 are the input ports receiving the signal from the loop antenna. P3 and P4 are

the output ports of the differential amplifier and P5 provides the DC voltage to the gate of the current source. Bias Tee 1&2 feed power to the drains of the differential pair through P6 & P7 and allow only the RF signal at the ports P9 & P10.

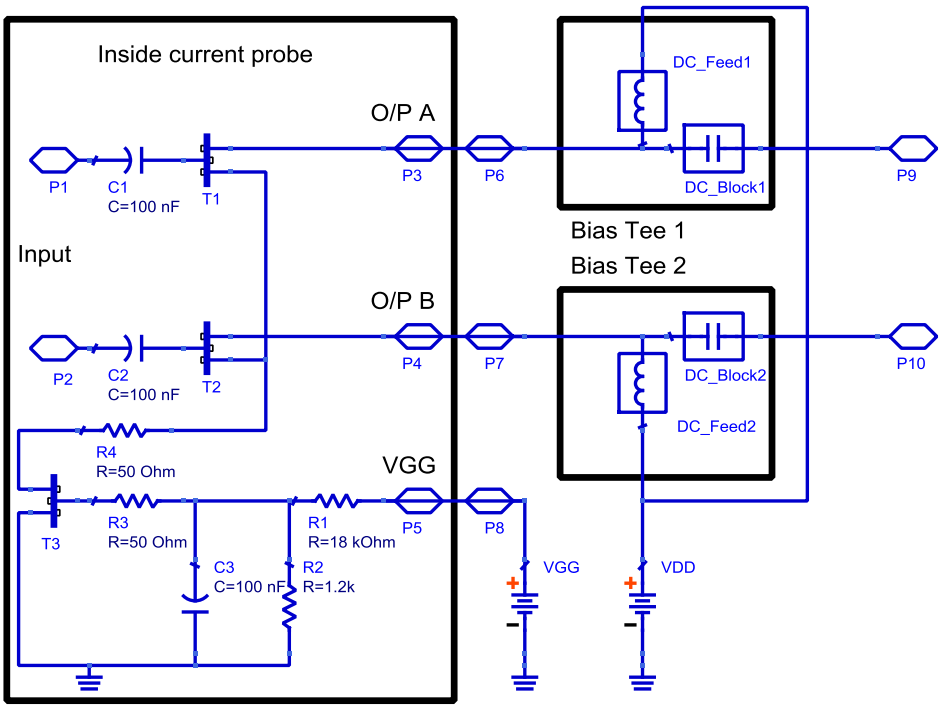

Figure 5-15 The schematic of the differential amplifier and its biasing circuits.

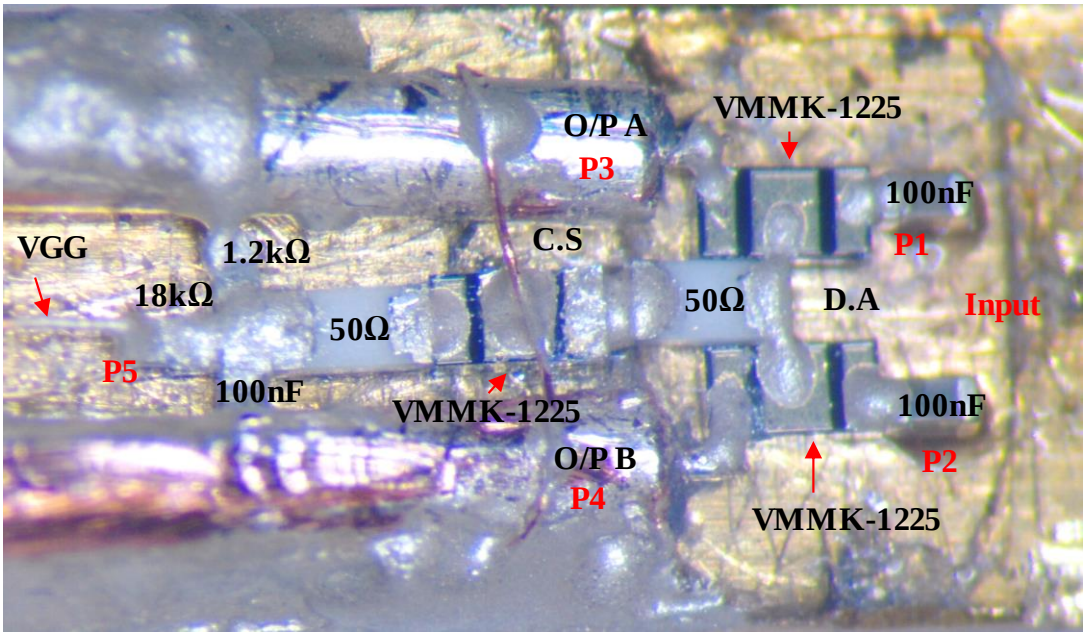

Figure 5-16 Current probe structure and the paths to DC and RF currents to and from the current source (C.S) and the differential amplifier (D.A).

From the data sheet for VMMK-1225, the maximum drain current is 50 mA and the maximum power dissipation is 250 mW. Therefore, to be in the safe area of operation, the maximum current in each branch of the differential amplifier should not exceed 20 mA so that the total current passing in the current source is 40 mA.

To find out the best location of the operating point, the ADS software is used here to simulate the differential amplifier and the current source. The DC characteristic (relation between drain current and V_{DD} at different values of the gate voltage) of the differential amplifier is shown in Figure 5-17 and from which it can be seen that the location of the operating point is mainly controlled by the voltage at the gate of the current source.

The optimum location of the operating point is at IDS = 10 mA for each branch at VDD = 10 V and the intersection of those lines is at VGS = 0.625 V.

To drive the differential amplifier and the current source from the same power supply the values of the voltage divider R1 and R2 are selected to be 18 KΩ and 1.2 KΩ respectively.

The capacitor C3 serves as a filter to bypass any noise to the ground and keep the current source stable. C1 and C2 prevent any DC current circulation between the gates of the differential amplifier.

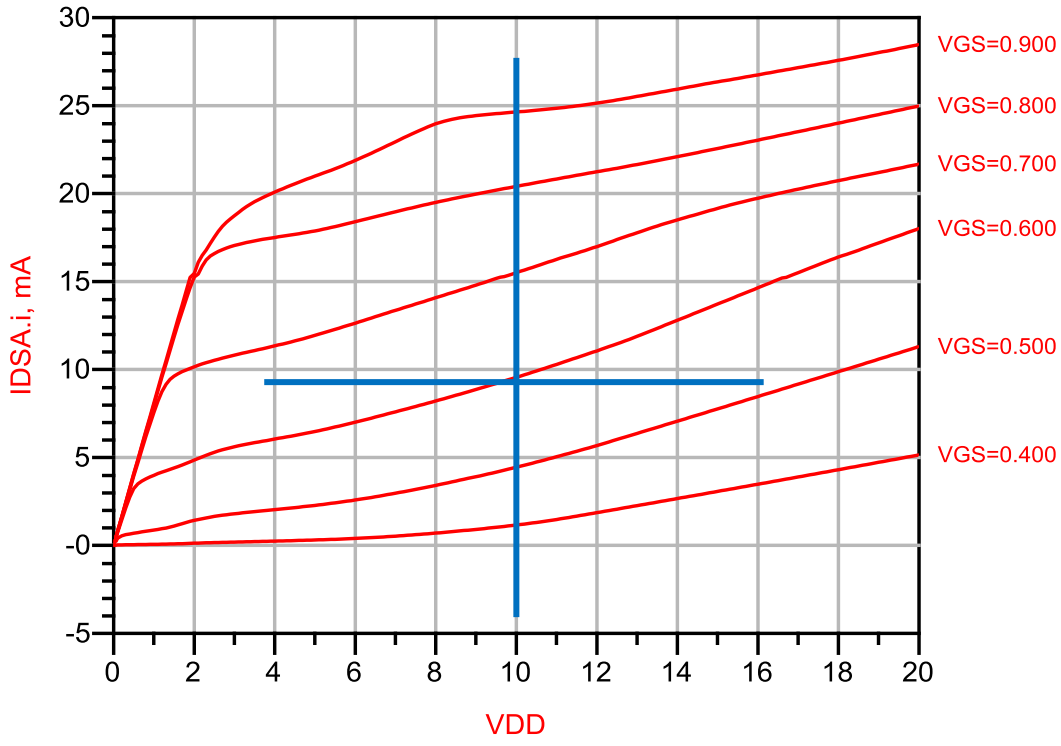

Figure 5-17 DC characteristics of the differential amplifier where the location of the operating point is at IDS = 10 mA and VDD = 10V.

5.8 Preliminary Design of the Miniaturized Loop Antenna

As shown in the previous section, to increase the spatial resolution of the current probe, the cross-sectional diameter of the conductor forming the loop antenna must be decreased. One way to reduce this cross-sectional diameter is to remove the shield around the loop antenna. This means picking up both the magnetic and the electric field radiation and then electronically processing these signals and attenuate the effect of the latter. The idea of this design is based on the assumption that the differential amplifier will be capable of rejecting all the unwanted effects of the common mode signal (electric field).

To examine this possibility, the printed circuit board has been used to implement an ultra-thin loop antenna, of 5 µm gold layer thickness and 30 µm track width, attached to a miniaturized alumina substrate (250 µm X 250 µm X 10 mm), see Figure 5-18(A). The aperture for this rectangular loop antenna has an internal width = 75 µm and the length = 200 µm. Ends of the loop are terminated with two parallel tracks of 55 µm width and 50 µm spacing between them with ground shielding layer under them on the bottom side of the substrate. This transmission line connects the loop signal to the differential amplifier. The substrate is then inserted inside a copper tube of 400 µm inner diameter and 600 µm outer diameter to shield the whole structure and only the loop area is protruded out of it, see Figure 5-18(B).

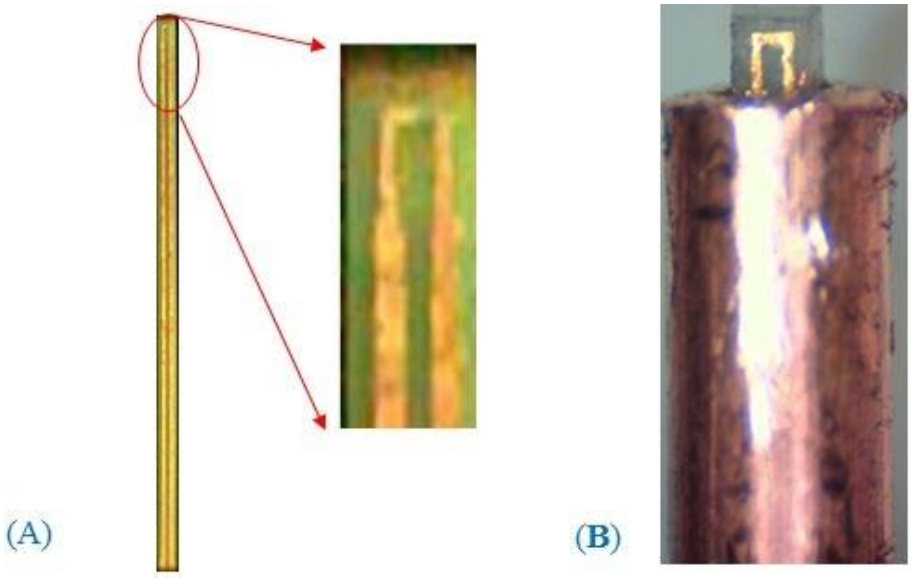

Figure 5-18 Structure of the miniaturized alumina current probe. (A) The loop antenna and the transmission line. (B) The copper tube shielding the transmission line.

5.8.1 Spatial Resolution Test

This probe is scanned across a test fixture consisting of a parallel array of 36 fingers (25 µm track width and 25 µm spacing between fingers), see Figure 5-19, and the results obtained from this scan are shown in Figure 5-20 at 3 GHz. The general trend in the variation of this current signal shows peaks on the edges of the array and a signal minimum in the central area, an inverted umbrella shape, which means this current probe is able to recognize current variation across the whole array structure. However, this probe was unable to recognize the current variation due to the individual fingers.

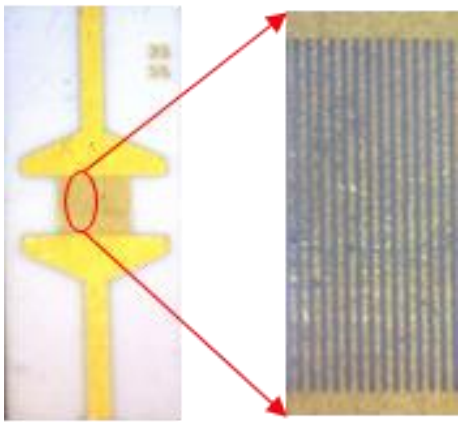

Figure 5-19 Thin film circuit used to simulate bonds wires array inside transistor. It consists of 36 fingers of 25 µm width and 25 µm spacing.

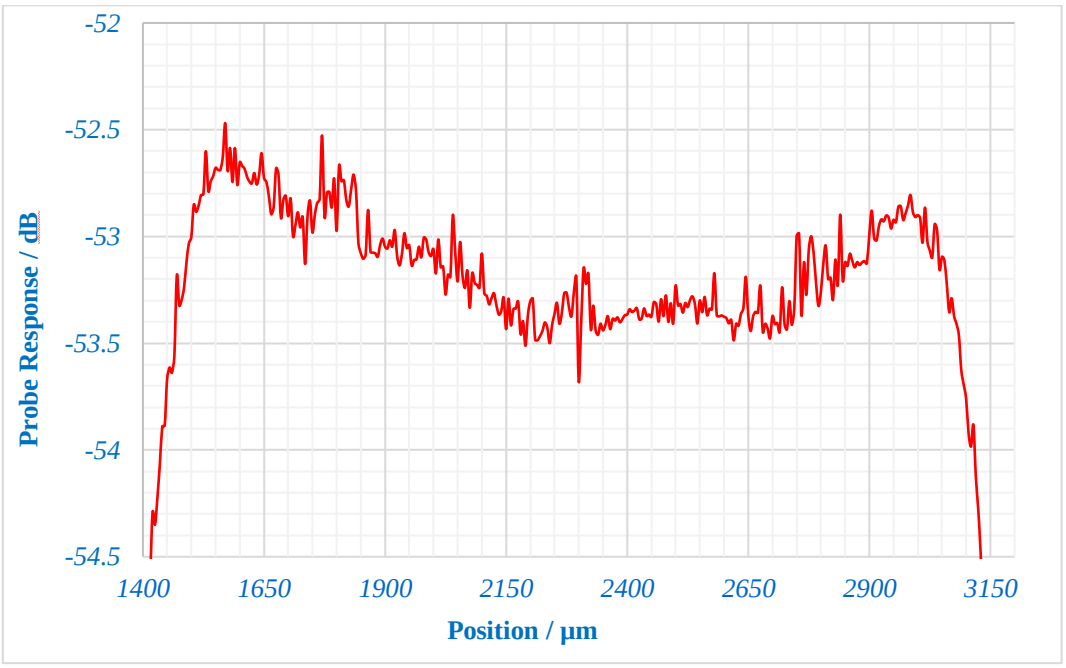

Figure 5-20 Spatial resolution test result across the 36 finger test fixtures (25 um track/gap width) with loop antenna protrude out from the copper tube.

In order to investigate the reason behind this lack of spatial resolution, the protrusion of the substrate is reduced so that all of the loop antenna is now shielded with the copper tube, see Figure 5-21. The purpose of this arrangement is to reduce the effect of the magnetic field and only allows the electric field along the Z-axis to be effective and picked up through the bottom facing side of the loop antenna. The previous scan is repeated with this modified current probe and the result is shown in Figure 5-22 where the variation between array fingers is recognized. Comparison with previous scan results indicates that the effect of the electric field is transmitted through a differential amplifier to the output of the probe.

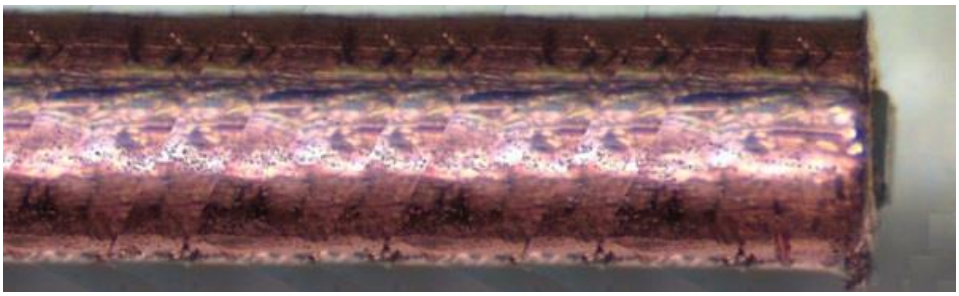

Figure 5-21 The modified current probe after shielding all the loop antenna inside the copper tube to minimize the effects of the magnetic field.

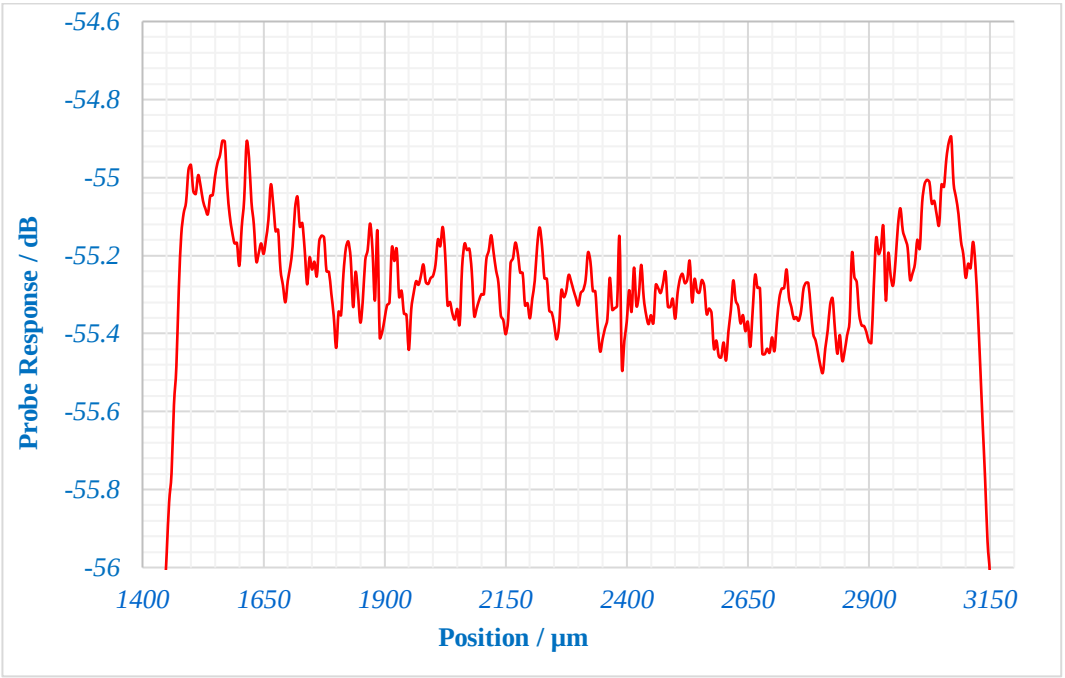

Figure 5-22 Spatial resolution test result across the 36 finger test fixtures (25 µm track/gap width) with all the loop shielded with the copper tube.

5.8.2 Standing Wave Test

Based on the above considerations, it is imperative that any alleged current probe should be subjected to a rigorous test that can demonstrate that current is being truly sensed, in the almost complete absence of voltage pickup.

A good candidate for such a test is to traverse the length of a microstrip transmission line that has a high VSWR pattern (e.g. using an open circuit termination). Such a test must show deep nulls at the voltage maxima positions, and a suitable voltage probe must also be used to demonstrate that the voltage peaks do indeed interlace with the current maxima. In this test, a 50 Ω microstrip line is used with the following details: 50 mm length, 1.1 mm line width, 1.28 mm dielectric thickness and 10.2 dielectrics constant, see Figure 5-23.

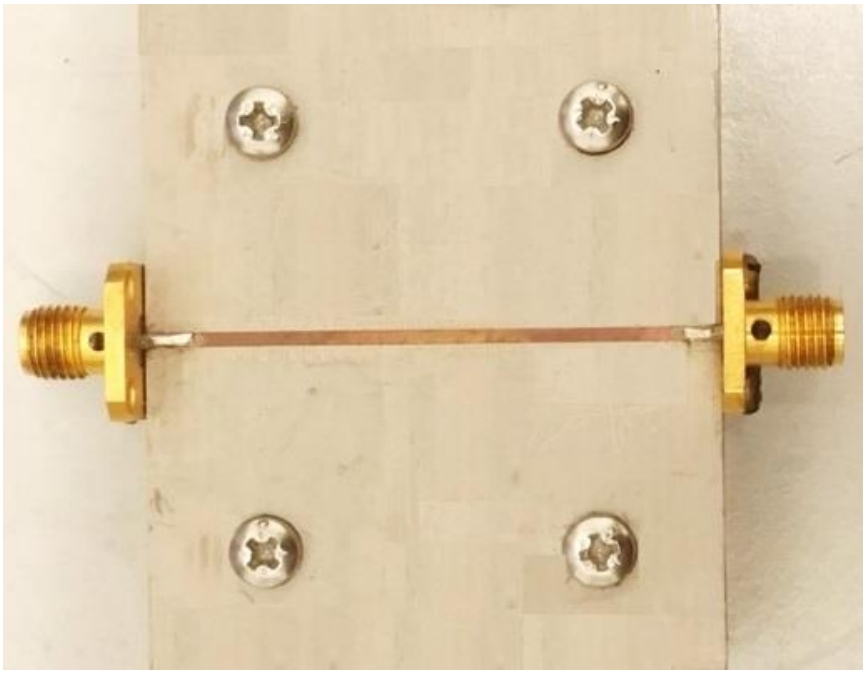

Figure 5-23 The microstrip line used in the standing wave test.

The standing wave (current and voltage) is generated above the microstrip line at 3 GHz by terminating it with open circuit load and then scanned twice. The first scan is made with the voltage probe previously fabricated, see chapter four, and in the second scan with the unshielded current probe (with the loop antenna protruded out of the copper tube).

Results of these scans are shown in Figure 5-24. Comparing locations of the minima and maxima of both scan results shows the difference of about 2.5 mm. This verifies the fact that the output of this probe is proportional to the superposition of the electric and magnetic fields.

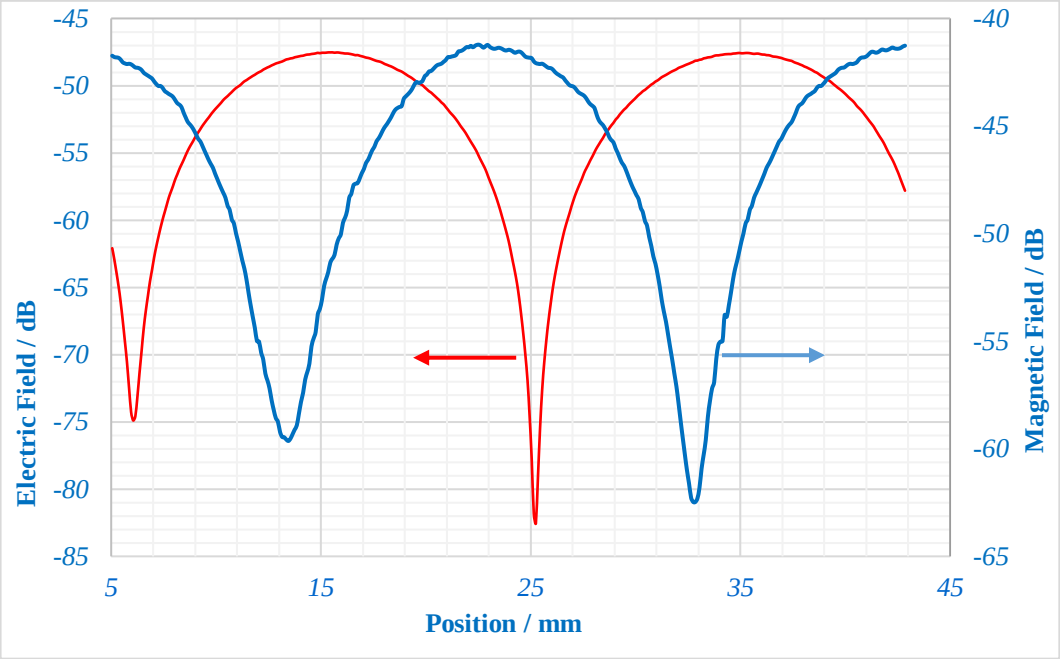

Figure 5-24 The results of the standing wave test along open end microstrip line.

5.9 Current Probe and the Problem of Electric Field Coupling

A magnetic field probe fundamentally requires a closed loop in order to couple into the magnetic field and thus generate an induced circulating current. Clearly, as the size of the loop is reduced the induced current drops in proportion to the probe loop area, whereas the capacitive coupling will drop approximately in proportion to the linear dimensions of the loop.

The problem in the particular application of probing high-power microwave transistors is that the corresponding voltage swing at the bond-wire can be tens of volts, and even the tiniest capacitive coupling between the probe and the wire can cause a much larger voltage coupling. In principle, it can be argued that if a differential amplifier is used across the loop terminations and the geometry is sufficiently symmetrical, the electric field pickup will be an even mode excitation which is rejected by the differential amplifier.

In practice, however, we find that the electric field intrusion can be sufficiently asymmetric[20] such that it appears as a small but significant component of the overall signal presented to the microwave differential amplifier. As such it is necessary to

[20] As an example, for this asymmetry, the dielectric of the substrates, alumina, works as a magnifier for the electric fields and thus the top face of the loop antenna will receive weaker electric fields compared with that received by its bottom face attached to the alumina substrate.

augment the common mode rejection through the design of a loop structure that reduces the electric field pickup.

5.10 Options Available to Fabricate Miniaturized Loop Antenna.

Current probing inside a microwave power transistor requires not only the loop size to be very small, but also the overall size of the current probe to be very small with respect to the dimensions inside it.

Using the ordinary coaxial cables is not an option here because of the smallest coaxial cable, UT-013, has a cross-sectional diameter equal to 330 µm. With this size, only heavy bond wires with heavy patches will be resolved; furthermore, none of these bond wire arrays are present in the microwave transistors studied, see section 3.10.1.1.

Alternatively, the planar loop antenna technique offers good miniaturization capability regarding loop size, but the overall size of the probe is not compatible with this measurement environment (inside microwave transistors), see Figure 2-37, 2-39 & 2-40.

The multi-layer structure of this type of probe needs a relatively thick and wide substrate to offer the necessary mechanical support and electrical shielding from the sides of the probe. In addition to that, in all previously reported versions of this type of loop structure, the problem of receiving electric field from the DUT, through its bottom facing side, is yet to be solved.

These limitations might explain why, since 1996 and until now, none of these planer current probes have been reported for current measurements in a tight environment like that inside microwave transistors.

As a result, one more essential condition is added to the design criteria in section 4.8, which is the necessity of making the actual size of the current probe equal or at least very close to the loop size.

To satisfy the above requirements, in designing a high spatial resolution current probe suitable for probing inside microwave power transistors, a new version of the planar current probe has been developed. The shield around the loop antenna is assembled by using multiple loops of metal and conductive epoxy.

5.11 Multiple Loop Shielding Technique (MLST)

In this new technique, the same essential three metal layers of the planner loop antenna structure are used: front and rear side shielding layers and in the middle a track to form

the loop antenna layer, see section 2.15.1.3. In this new technique, instead of using the usual flat copper layers and tracks in implementing the planner loop antenna, we used extremely thin copper wire (20 µm diameter) to form three adjacent loops.

The insulation layer between these copper rings are established by using enamelled copper wire (1.5 µm insulation layer) for the middle loop. In the first design, these loops are pre-formed around a 125 µm diameter rod of glass (the glass core the of fibre optic cable), see Figure 5-25(A). Glass offer good visibility under a microscope, but it can be easily broken while winding the wires. To avoid this problem the glass rod was replaced with molybdenum wire, see Figure 5-25(B). The diameter of this wire is 100 µm and will serve to enhance the spatial resolution also.

The ends of the wire loop are then twisted together to create a strong bundle which provides the necessary mechanical support for all three loops. In addition, the twisting enhances rejection to the common mode signals.

The outer circumference of the three adjacent rings is then painted with high conductivity silver epoxy. Both the bare copper loops and the epoxy serve to shield the electric field component from the current pick-up loop. In addition to this, the epoxy contributes to keeping the three loops contiguous with each other and adds more mechanical support for the entire structure, see Figure 5-26.

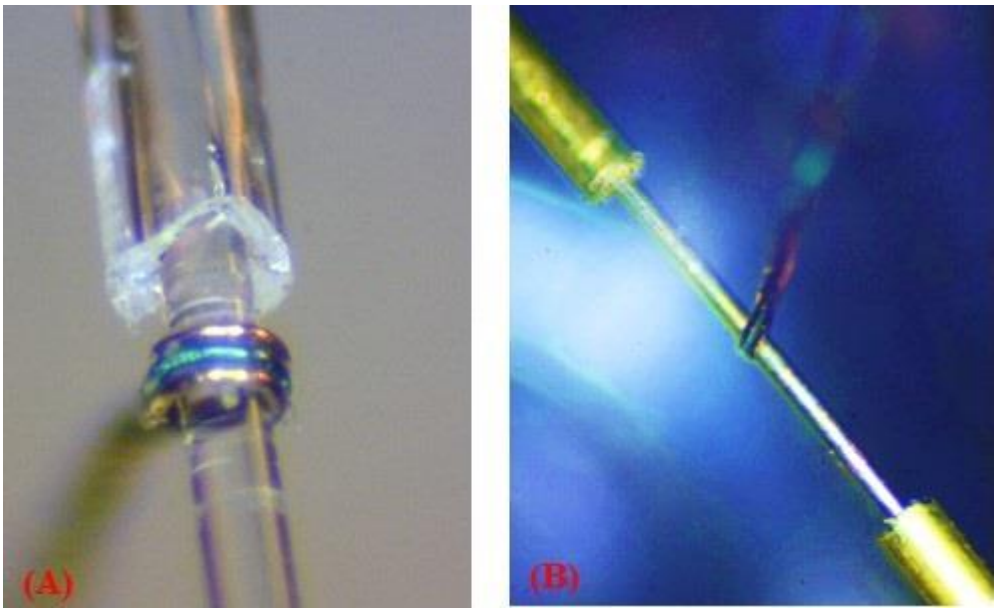

Figure 5-25 The structure of the developed shielded loop antenna. In the middle is the enamelled copper loop antenna and the other uncoated copper loops are the side shield. (A) Loops formed around the core of fiber optic cable. (B) Loops formed around wire.

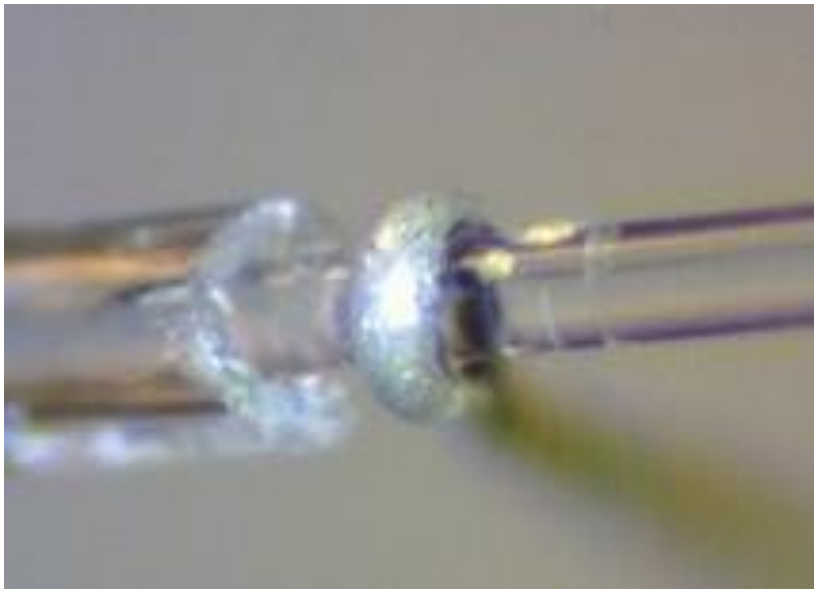

Figure 5-26 High conductivity silver epoxy covering the circumferences of the three loops to shield the loop antenna.

The loop structure and part of the twisted leads are then soaked in thin, fast drying and non-conductive glue to gain more physical strength and offer electrical insulation. Finally, the wires are mechanically secured and electrically shielded in an EDM brass tube in order to terminate the leads to the transition unit of the current probe (inputs of the differential amplifier); while the loop antenna emerges at the other end of the brass tube to capture the magnetic field energy from the DUT, see Figure 5-27.

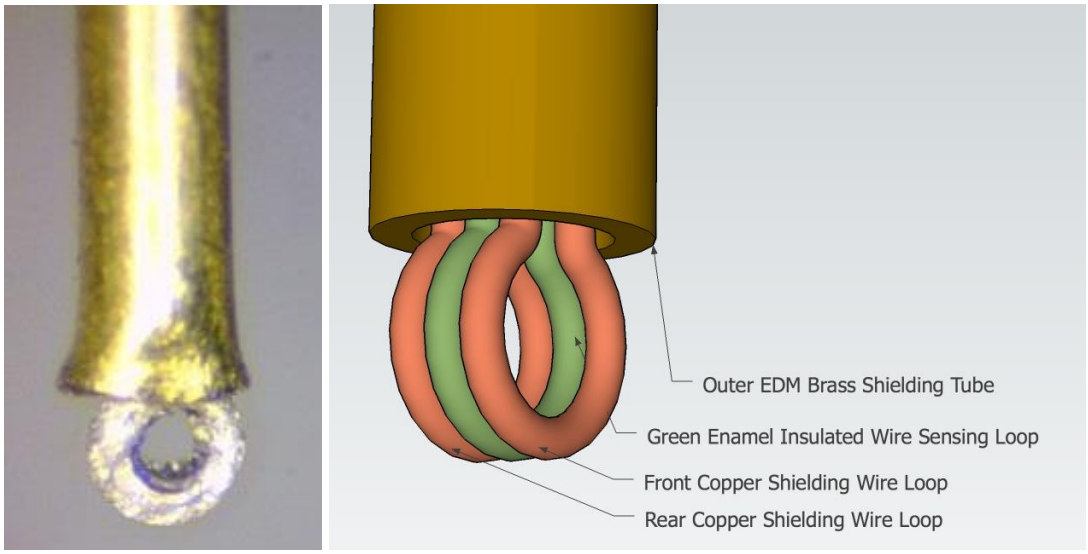

Figure 5-27 The parts of the input unit of the current probe: the brass tube and the shielded loop antenna emerging from the open end of the brass tube.

5.12 Evaluation of the Multiple Loop Shielding Technique

As stated in the previous chapters, the characteristics of the microstrip line are well known and thus it is useful to use it to examine the MLST and show its ability to respond to magnetic field. Four types of test can be performed with the microstrip line:

1. Standing wave distribution along the length of the microstrip line.
2. Current distribution across the width of the microstrip line.
3. Electric field rejection test
4. Frequency response (bandwidth).

5.12.1 Standing Wave Test

In this test, the same procedure given in section 5.8.2 is applied here to compare the locations of the maxima and minima of the voltage and current along the length of the microstrip line terminated with an open load.

Unlike the case of the unshielded loop shown in Figure 5-24, scanning the microstrip line with the new current probe demonstrate that the voltage peaks do indeed interlace with the current maxima. The result of this test is shown in Figure 5-28 and shows that this probe offers excellent electric-field rejection.

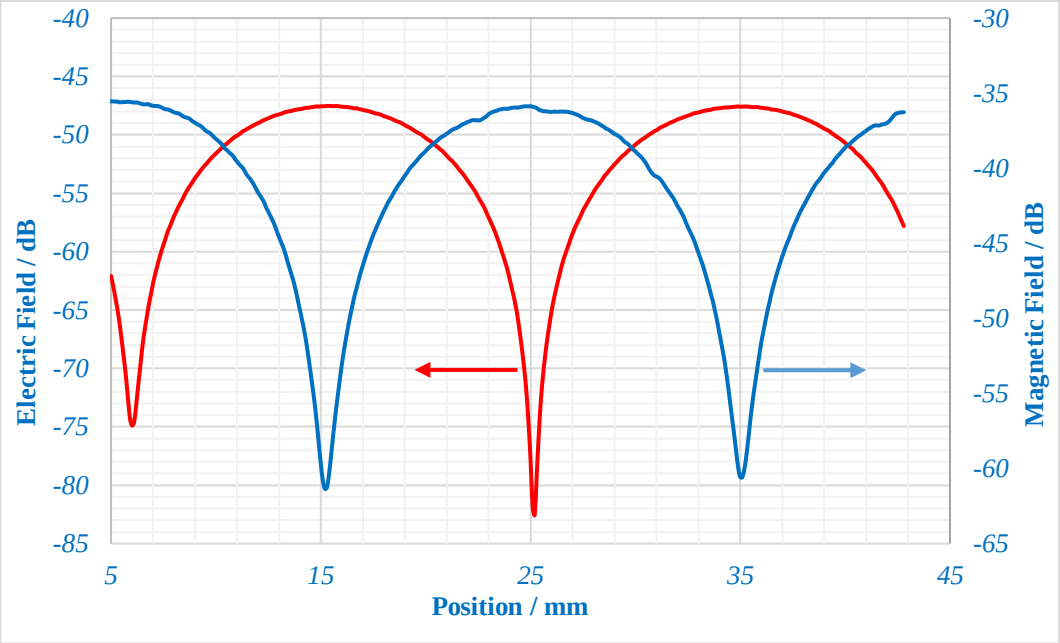

Figure 5-28 The results of the standing wave test along open end microstrip line.

5.12.2 Current Distribution (Inverted Umbrella) Test

Current distribution across the width of matched microstrip line has the shape of an inverted umbrella where the current density at the edges is higher than the middle area, see section 3.10.3.1. In this test, a 50 Ω microstrip line of 1.62 mm track width, fabricated from Rogers PCB matched with 50 Ω load at one end and 1 mW RF power supplied at the other end at 3 GHz. Scan results at different heights are shown in Figure 5-29 and the inverted umbrella current distribution is very clear at a 5 µm height where the spatial resolution is 1.53. As probe height increases, both the spatial resolution and the sensitivity decrease, see Figure 5-29(A) – (B).

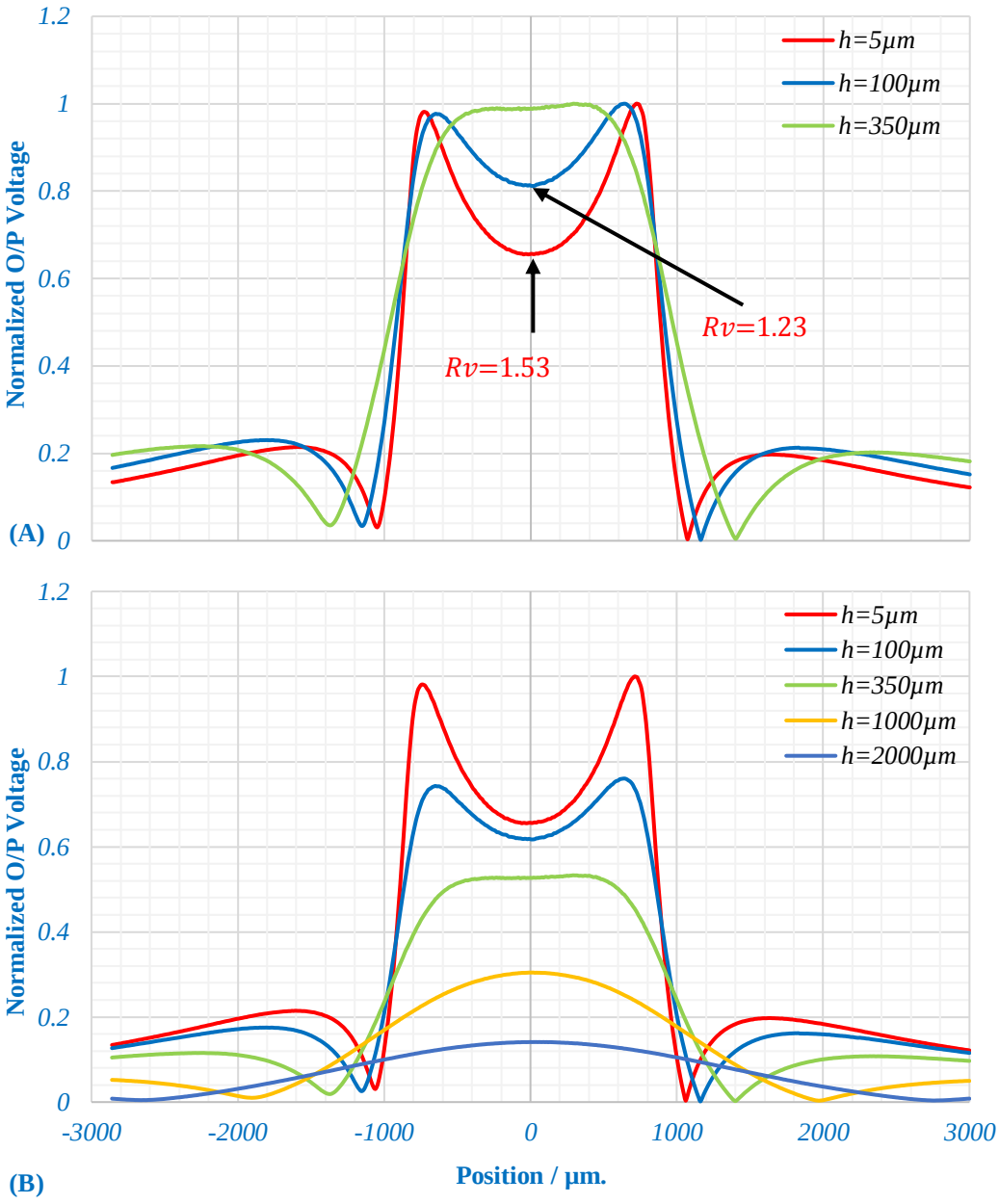

Figure 5-29 Current distribution across the width of the microstrip line at different heights. (A) In terms of spatial resolution. (B) In terms of sensitivity.

In this case, the minima location represents the magnitude of the current in the middle of the microstrip line and thus the value of R_v here describes how realistic this current measurement is. Figure 5-30 shows the output voltage at the edges and the middle area of the microstrip line.

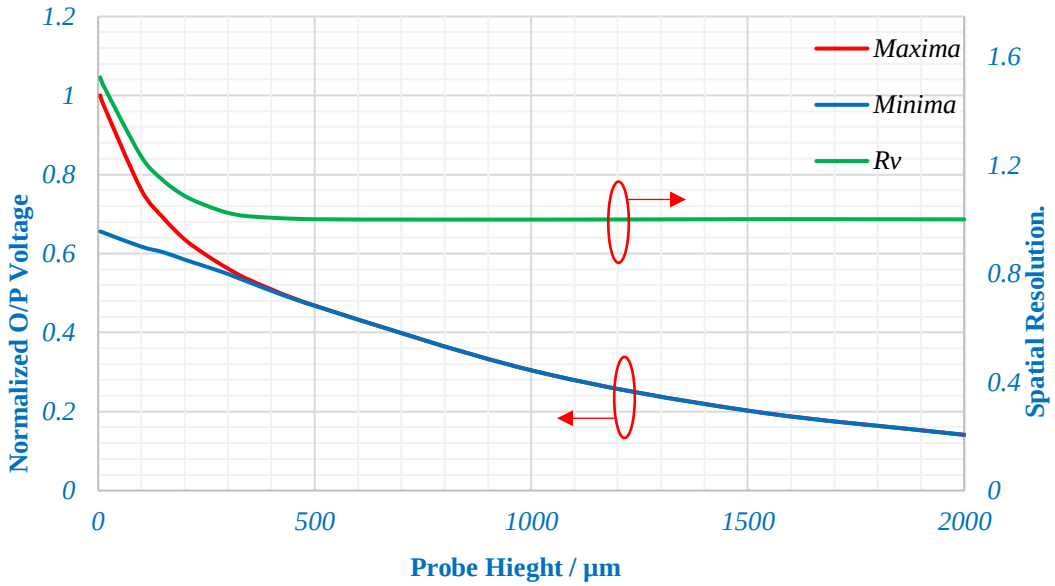

Figure 5-30 Current probe response as a function of probe height at the edges of the microstrip line, maxima, and its middle area, minima.

5.12.3 EFRR Test

The third method to verify the fidelity of this miniaturized contactless current probe is to compare the results of its response to magnetic and electric fields. This can be obtained by placing the probe at a fixed location above the microstrip line loaded with 50 Ω at one end and connected to the VNA at the other end. The frequency of the VNA is swept twice. In the first sweep, the plane containing the loop is set to be parallel to the length of the microstrip line so that the probe is mainly responding to the magnetic field, see Figure 5-31. In the second sweep, the probe is rotated ninety degrees, so it mainly responds to the electric field. The results of this test are shown in Figure 5-32 and the average of the EFRR = 22.7 dB and the maximum value is 39 dB at 5.25 GHz.

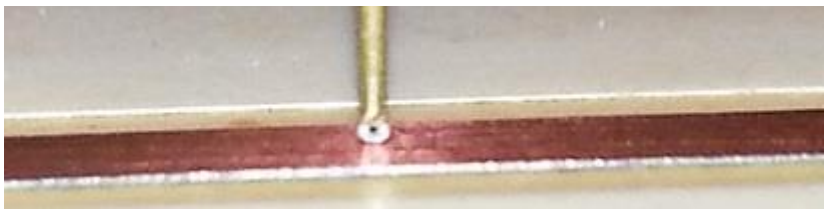

Figure 5-31 The plane containing the loop is parallel to the length of the microstrip line.

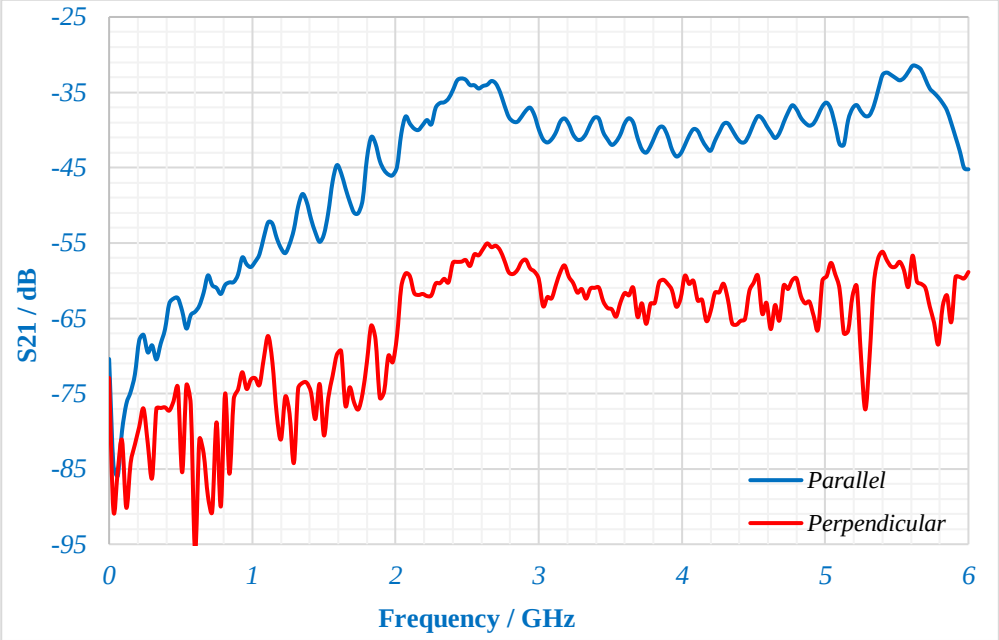

Figure 5-32 Results of the electric field rejection.

5.12.4 Bandwidth Test

The bandwidth of the probe was obtained by placing the probe at a fixed location above the microstrip line. Instead of moving the probe, a standing wave pattern is generated by terminating the microstrip line with short circuit load. The sweep of frequency at this fixed location shows the voltage nulls traversing the probe tip and suggests a probe bandwidth up to 9 GHz as shown in Figure 5-33. Comparing this response with that of the voltage probe (at the same location) demonstrates that the voltage peaks do interlace with the current maxima.

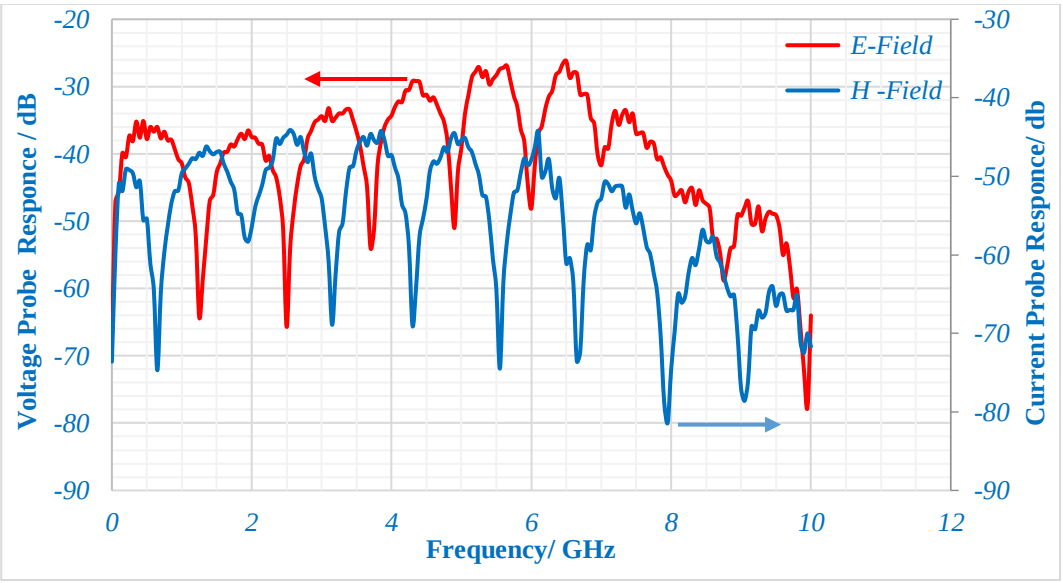

Figure 5-33 Frequency sweep with current and voltage probe in fixed position.

5.13 Spatial Resolution Test

To test and prove the spatial resolution of this miniaturized current probe, we used thin film circuits similar to that shown in Figure 5-19. It is implemented on a piece of alumina substrate of 250 µm thickness, 11.5 mm length and 4.5 mm width.

The bottom layer is the ground plane. The top layer is a 0.7 mm track width widened in the middle to two flat manifolds spaced by 1.5 mm. These manifolds are connected by a parallel array of fingers of 25 µm width. This array has 23 fingers and 100 µm spacing between adjacent fingers.

The power delivered through these test fixture was three watts and terminated with 50 Ω load at the other end. The spatial resolution scan for this test fixture clearly shows the inverted umbrella of the current distribution, see Figure 5-34. The spatial resolution of this probe is around 62.5 µm.

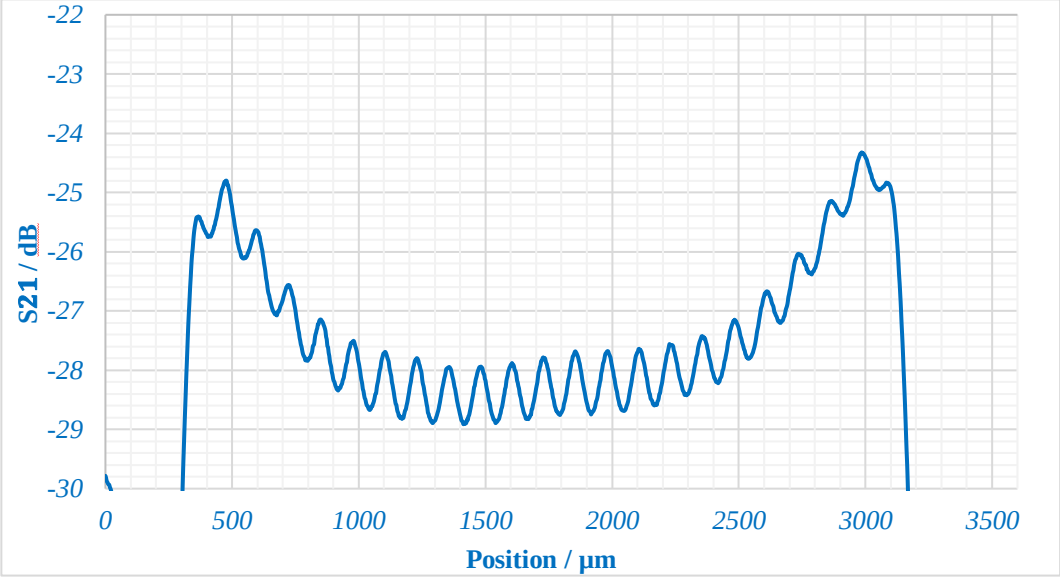

Figure 5-34 A 62.5 µm spatial resolution tests results of the voltage probe.

5.14 Conclusion

A broadband voltage probe with high spatial resolution has been developed and the design criteria presented in this chapter. This probe has demonstrated an ability to measure directly the current on adjacent tracks that are spaced at 100 µm, with a useful bandwidth up to 9 GHz. The developed current probe is thus claimed to have the capability to measure the magmatic field distribution at a spatial resolution equal to 62.5 µm.

6 Novel Measurements of Current Within A Microwave Transistors

6.1 Introduction

The main aim of the work presented in this thesis is to provide a tool that is capable of scanning within the periphery of high power microwave devices; this shows directly how the power and more specifically the current is distributed among the parts of the DUT. In the previous chapters, successful design, development and fabrication of the contactless voltage and current probes have been achieved and these probes are then tested against passive test fixtures. The next step is to perform in-situ active measurements inside microwave power transistors. As mentioned in chapter two, all the previous in-situ active measurements have been based on the voltage probe only. Two research groups reported these in-situ measurements one from Cardiff University [214] and the other from Delft University [215]. The main difference between the two groups is that the Cardiff group used the voltage probe to perform voltage measurements only while Delft group took this a step further by indirectly predicting the current from measurements of the voltage probe. Voltage measurement is important and can help in characterizing the DUT, but unfortunately, it cannot provide an insight into how the power and more specifically how the current is distributed. In this chapter, a new and a novel method of characterizing microwave power transistors is described. The current probe is the main tool for this

characterization, where the currents inside the microwave power transistors are directly quantified.

6.2 LDMOS Power Transistor and its Test Circuit

LDMOS transistors are widely used in mobile communications and specifically in base stations; therefore, one is used here to apply the technique of spatial current measurement. This type of transistor has been used by the Cardiff University research group and the Delft University research group and their voltage measurements can be reviewed in [214], [215] respectively.

An Ampleon (formerly NXP) LDMOS microwave power transistor BLF7G22L-130 is used as the device under test. It is a 130 W enhancement mode MOSFET operating over the frequency range from 2 GHz to 2.2 GHz [216]. The test circuit board used with this transistor is shown in Figure 6-1. The transistor is biased by two positive voltages: the drain voltage 31 V and the gate voltage 3.891 V.

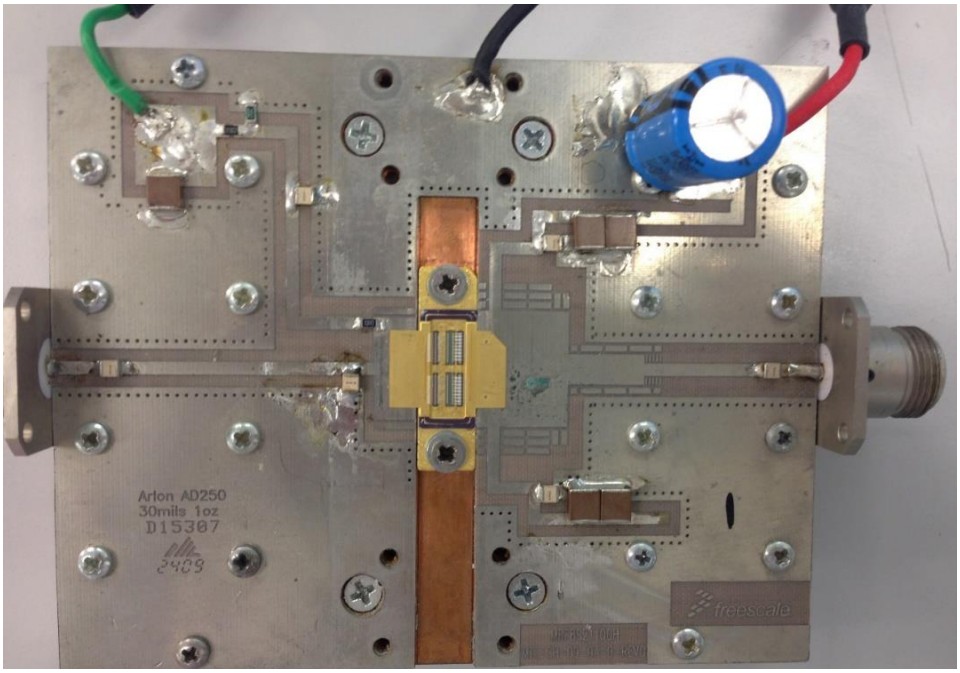

Figure 6-1 Circuit board used in testing the LDMOS microwave power transistor (BLF7G22L-130).

6.3 Preparing the LDMOS Transistor for the Measurement

The BLF7G22L-130 is packaged with a ceramic lid to protect the dies and the bond wires. This cover must be removed to allow the contactless probe to move inside the transistor. This process requires the use of a hot plate with controlled temperature set to 170^{o} C so

that the adhesive joining the lid to the body of the transistor melts and the lid is then easily removed, see Figure 6-2. The de-lidded transistor is then placed within its test circuit board.

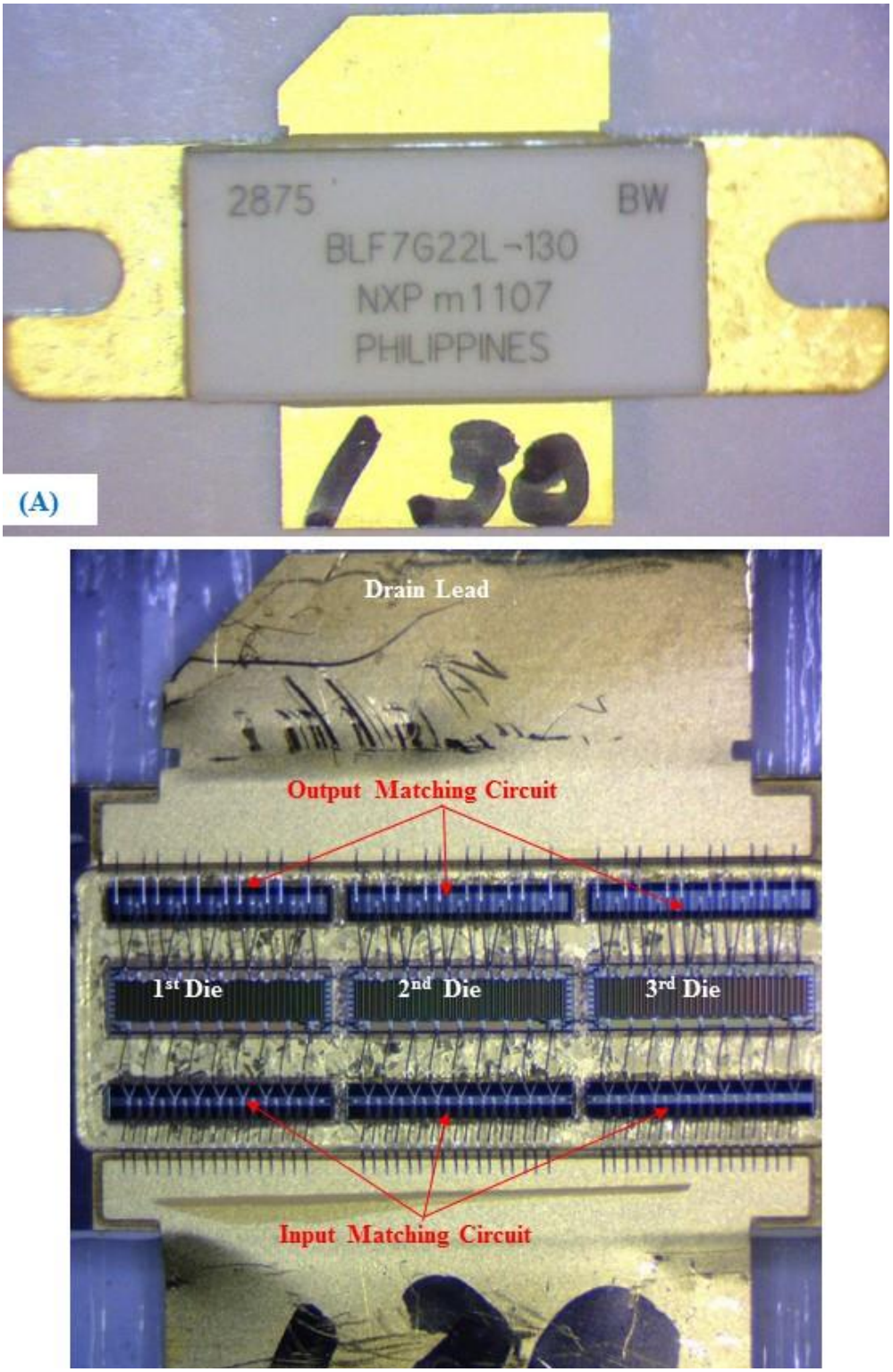

Figure 6-2 LDMOS microwave power transistor BLF7G22L-130 (A) With lid (B) Without Lid**.**

6.4 Controlling the Temperature of the LDMOS Transistor

As seen in chapter four and five the spatial resolution and the sensitivity of the contactless measurement is inversely proportional to the distance between the probe and the DUT and this distance is in the range 5 -30 μm.

Due to the low efficiency of the microwave power transistor, for example for the BLF7G22L-130 is thirty percent, the temperature of the power transistor increases quickly as the output power increase and thus a thermal expansion occurs to all dimensions of the transistor's internal parts. The most important of these dimensions is the heights of the bond wires and the dies, for example the rise in the temperature of the BLF7G22L-130 from 20° C to 65° C can introduce around 12 μm increase in the height of these parts. Therefore, it essential to control the transistor temperature and hold it constant within the scan time to enhance the accuracy of the measurement and to avoid damage if the probe tip touches the bond wires or the die. To overcome this problem a water-cooled heat sink is used to maintain a constant operating temperature.

6.5 Internal Structure of the BLF7G22L-130

This LDMOS transistor consists of three dies and two matching circuits one of them is connected to the gate of the transistor and the other one is connected to the drain, see Figure 6-2(B). Each of these dies consists of five cells and these cells are connected to the matching circuits and the transistor leads via bond wires.

There are four arrays of bond wires are used to connect between the various parts as follows:

1. This array connects the drain lead to the drain pads on the die and consist of ten wires per die, distributed in four pairs in the middle and a single wire at each of the ends of the array, see Figure 6-3.
2. This array connects the output matching circuit to the drain pads on the die and consists of five wires per die, see Figure 6-3.
3. This array connects the gate pads on the die to the input matching circuit and consists of nine wires per die. These nine wires are then extended to the gate lead as shown in Figure 6-3.
4. This array connects the gate lead to the input matching circuit and consists of seventeen wires per die, see Figure 6-3.

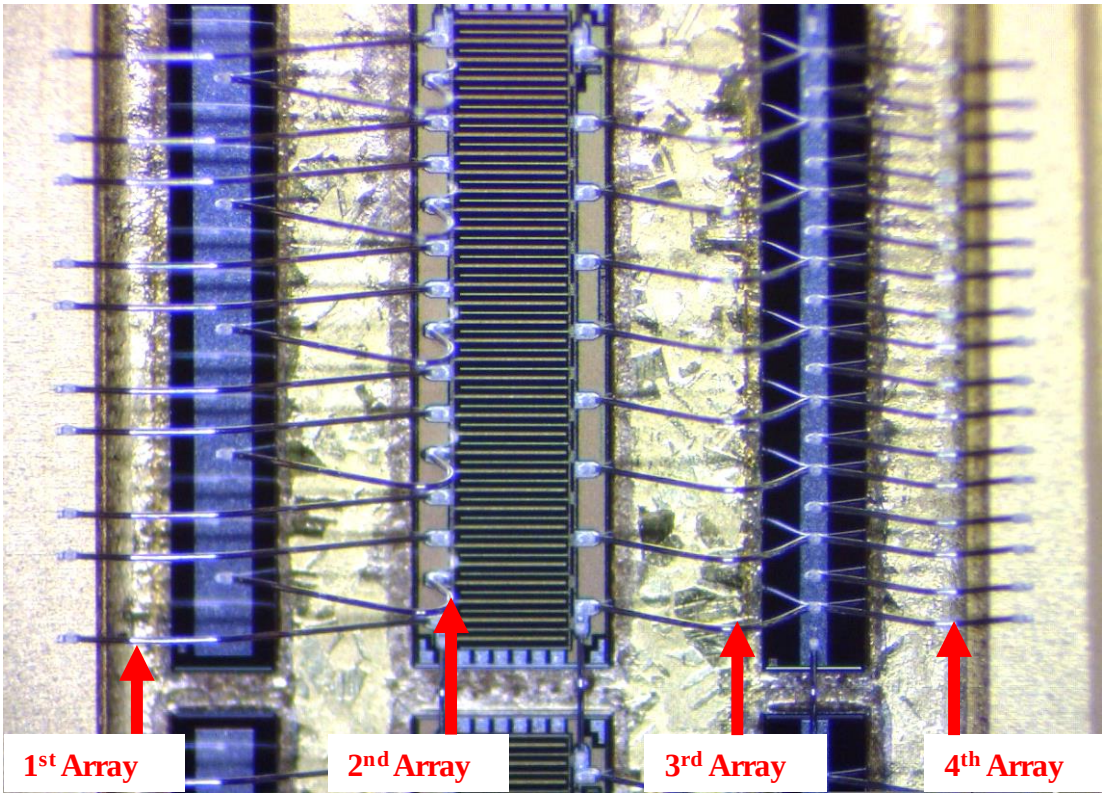

Figure 6-3 Four bond wires arrays inside BLF7G22L-130 : the 1st array connect the drain lead to the die, the 2nd array connects the die to the output matching circuit, the 3rd array connects the input matching circuit to the die and the 4th array connects the gate lead to the input matching circuit.

6.6 Multiple Scans of the Current Wave Planes

As shown in Figure 6-2(B) and Figure 6-3 the microwave power transistors consist of dies, matching circuits and the bond wires for the electrical connection. The challenge for the designers of these devices is how to guarantee a balanced share of the load between the dies in first place and between individual bond wires. The only available tool for real time measurements is thermal imaging which is clearly not enough to discern how the current is actually distributed among the transistors parts. With the successful design and fabrication of the miniaturized contactless current probe, this information is now available.

Using the contactless current probe to scan along the length of the transistor at a specific location can illustrate how the current is distributed. If this process is repeated at different locations across the width of the transistor then the result highlights the progression of the spatial current waveform as it passes through the DUT. Figure 6-4 shows the path of

seven scans along the length of the BLF7G22L-130 starting with lead of the drain and ending with lead of the gate; the next even sections illustrate each of these scans.

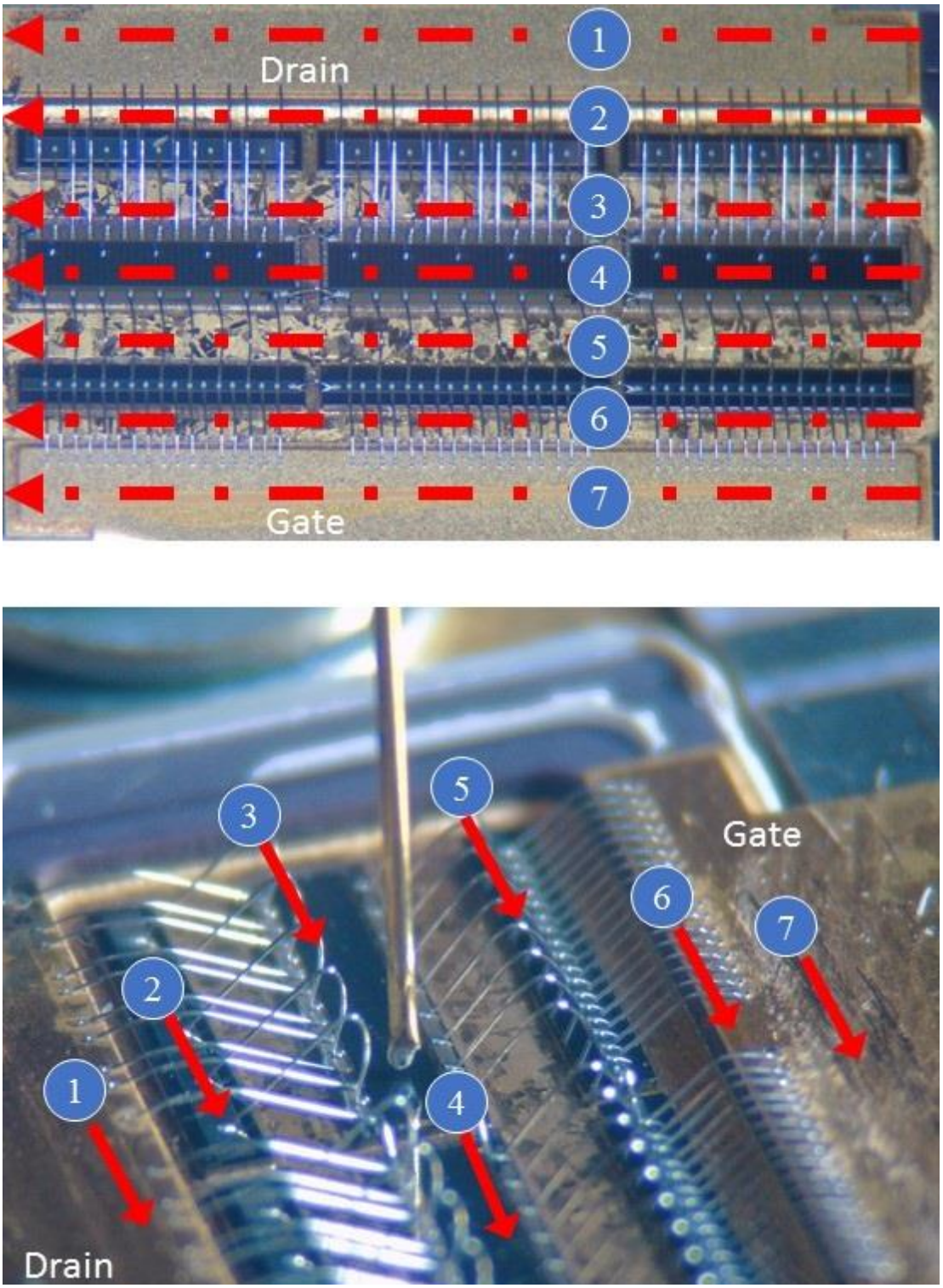

Figure 6-4 Multiple scans with contactless current probe along the length of the BLF7G22L-130: (1) the lead of the drain (2) the 1st array bond wires (3) the 2nd array of bond wires (4) the die (5) the 3rd array of bond wires (6) the 4th array of bond wires (7) the lead of the gate.

1. Scan along the lead of the drain: the trend of the variation in the magnitude is the usual inverted umbrella where the current peak values are shown near the edges of the lead and with a small increase around the middle of lead, see Figure 6-5(A). Figure 6-5(B) shows the phase variation edges and the middle of the lead is less than fifteen degrees.

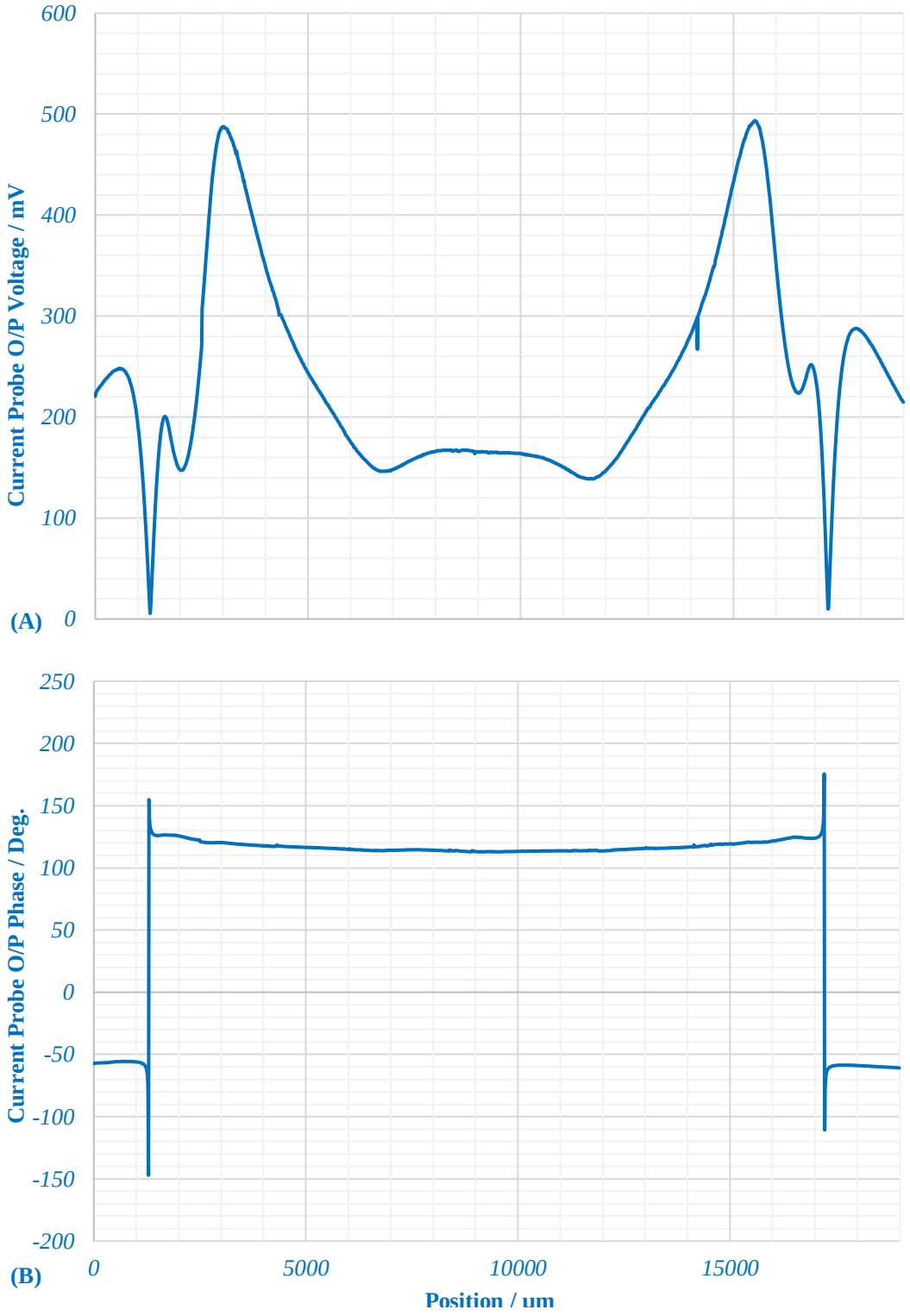

Figure 6-5 Scan results along the lead of the drain. (A)The magnitude. (B) The phase.

2. Scan along the 1st array of the bond wires: the ten bond wires connected to each die from the side of the drain are recognized in Figure 6-6(A) and the inverted umbrella represents the general trend of the current distribution. Regarding the phase variation, its value slightly increases as it moves away from the centre die toward the two side dies, see Figure 6-6(B).

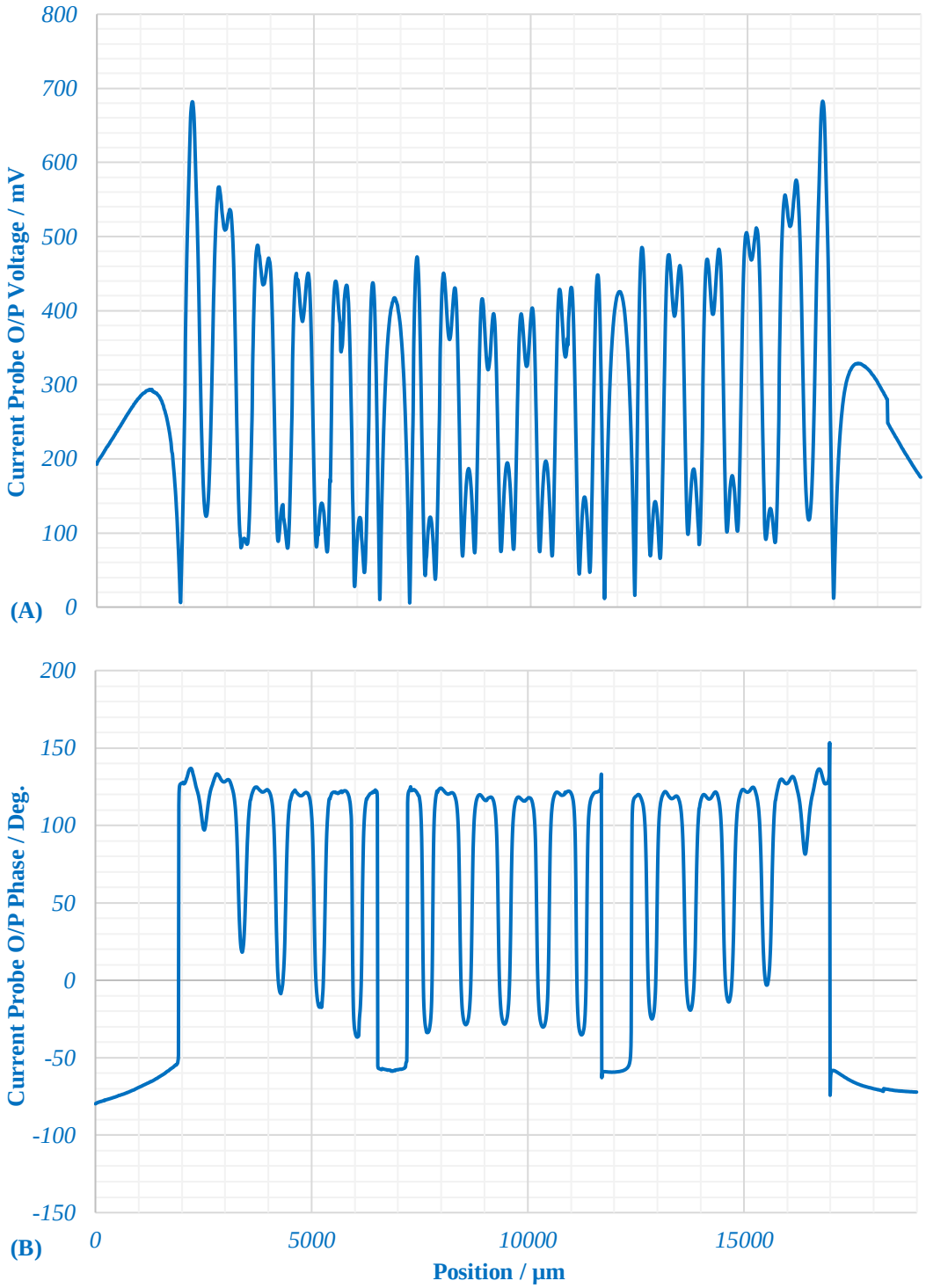

Figure 6-6 Scan results along the 1st array of the bond wires. (A) The magnitude. (B) The phase.

3. Scan along the 2nd array of the bond wires: the five bond wires connecting between each output matching circuit and the associated die are clearly shown in Figure 6-7(A)which indicates a large amount of current passing in them. The phase of these currents is around 50°, see Figure 6-7(B)**,** and in a comparison with previous scans is reduced by around 70°.

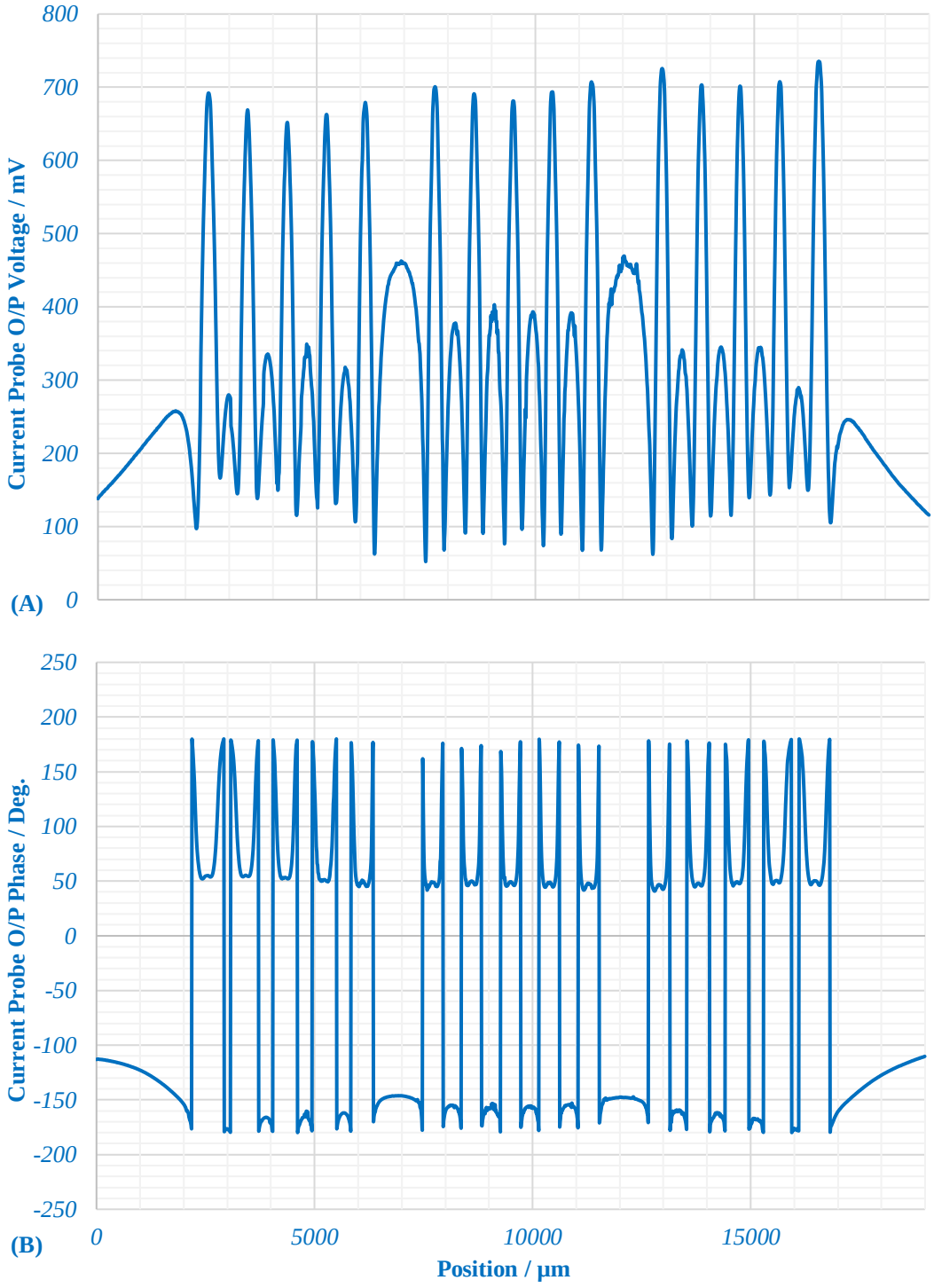

Figure 6-7 Scan results along the 2nd array of the bond wires. (A) The magnitude. (B) The phase.

4. Scan along the dies: the return currents are shown with relatively high values between dies and this is due to the small distance between probe tip and ground plate at the bottom of the transistor package. The overall trend of the current distribution is the inverted umbrella, see Figure 6-8(A), and the phase varies between 50° and 70° as shown in Figure 6-8(B).

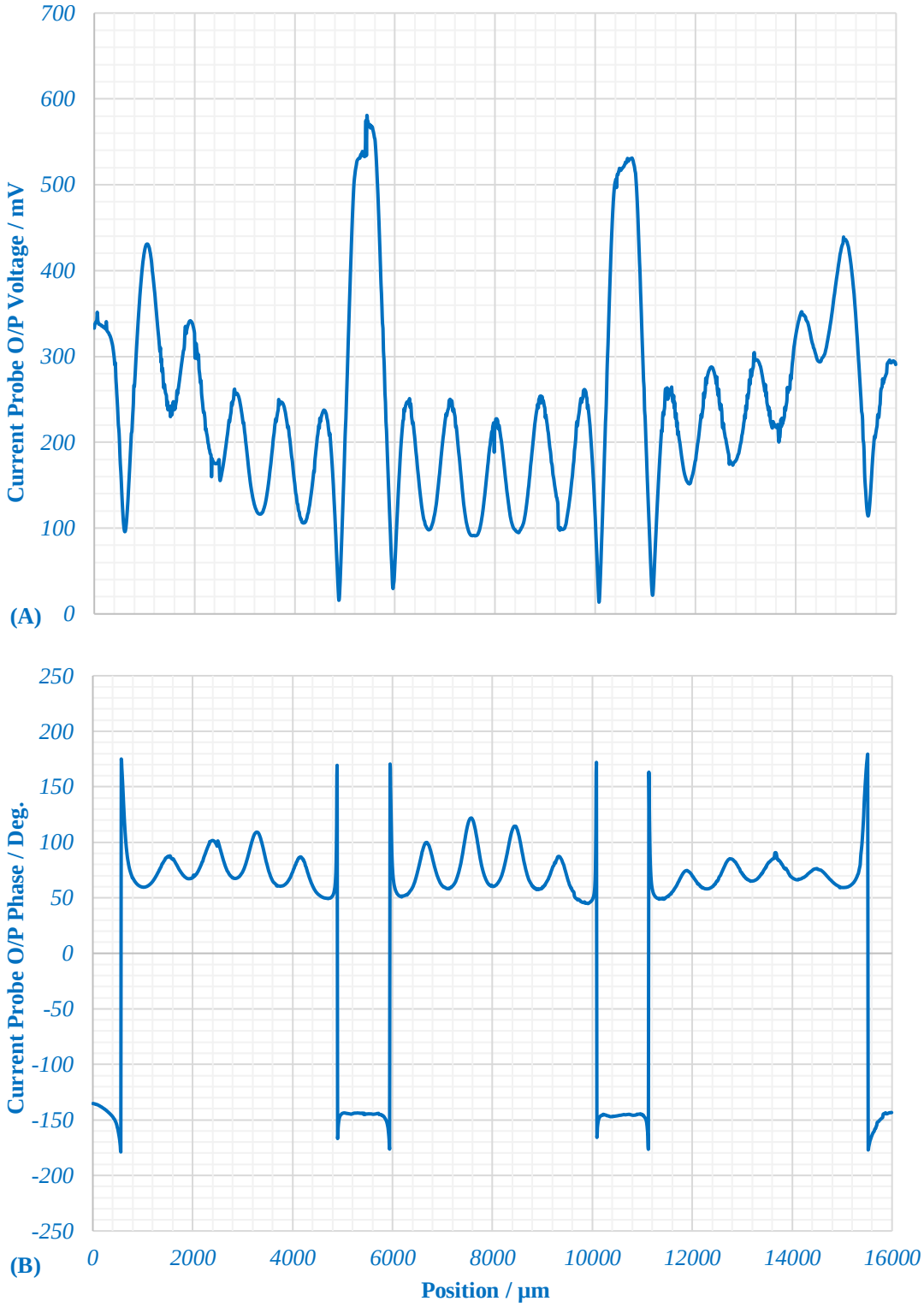

Figure 6-8 Scan results along the dies. (A) The magnitude. (B) The phase.

5. Scan along the 3rd array of the bond wires: this array is connecting the dies to their associated input matching circuit. The nine bond wires for each die are recognized clearly for both the magnitude, see Figure 6-9(A), and phase, see Figure 6-9(B).

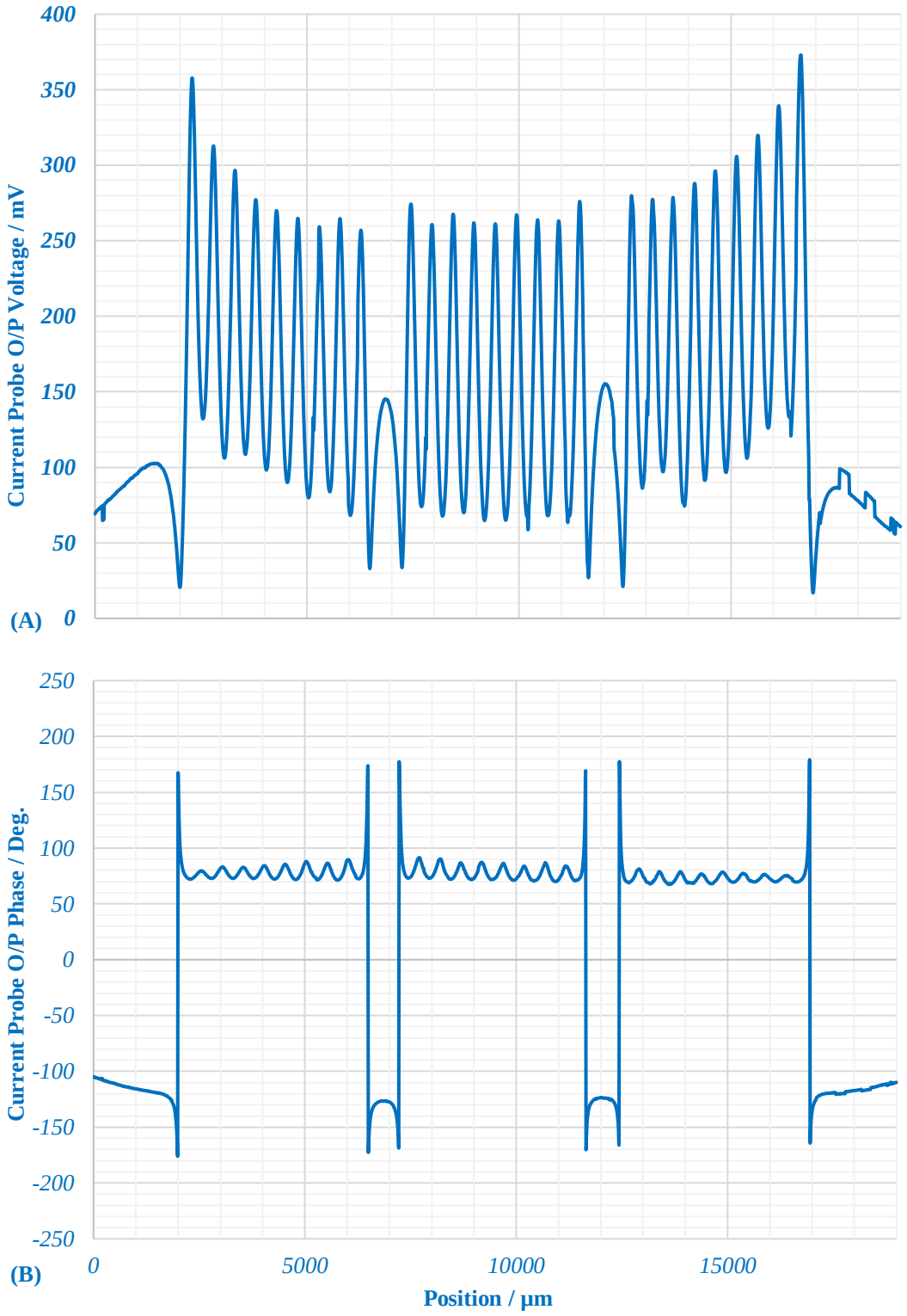

Figure 6-9 Scan results along the 3rd array of the bond wires. (A) The magnitude. (B) The phase.

6. Scan across the 4th array of the bond wires: the current distribution of the bond wires between the input matching circuit and the gate lead also has the inverted umbrella and the asymmetry between their sides, see Figure 6-10(A), is due to the crooked lead of the gate as shown in Figure 6-12. The phase variation is between 60° -75°, see Figure 6-10(B).

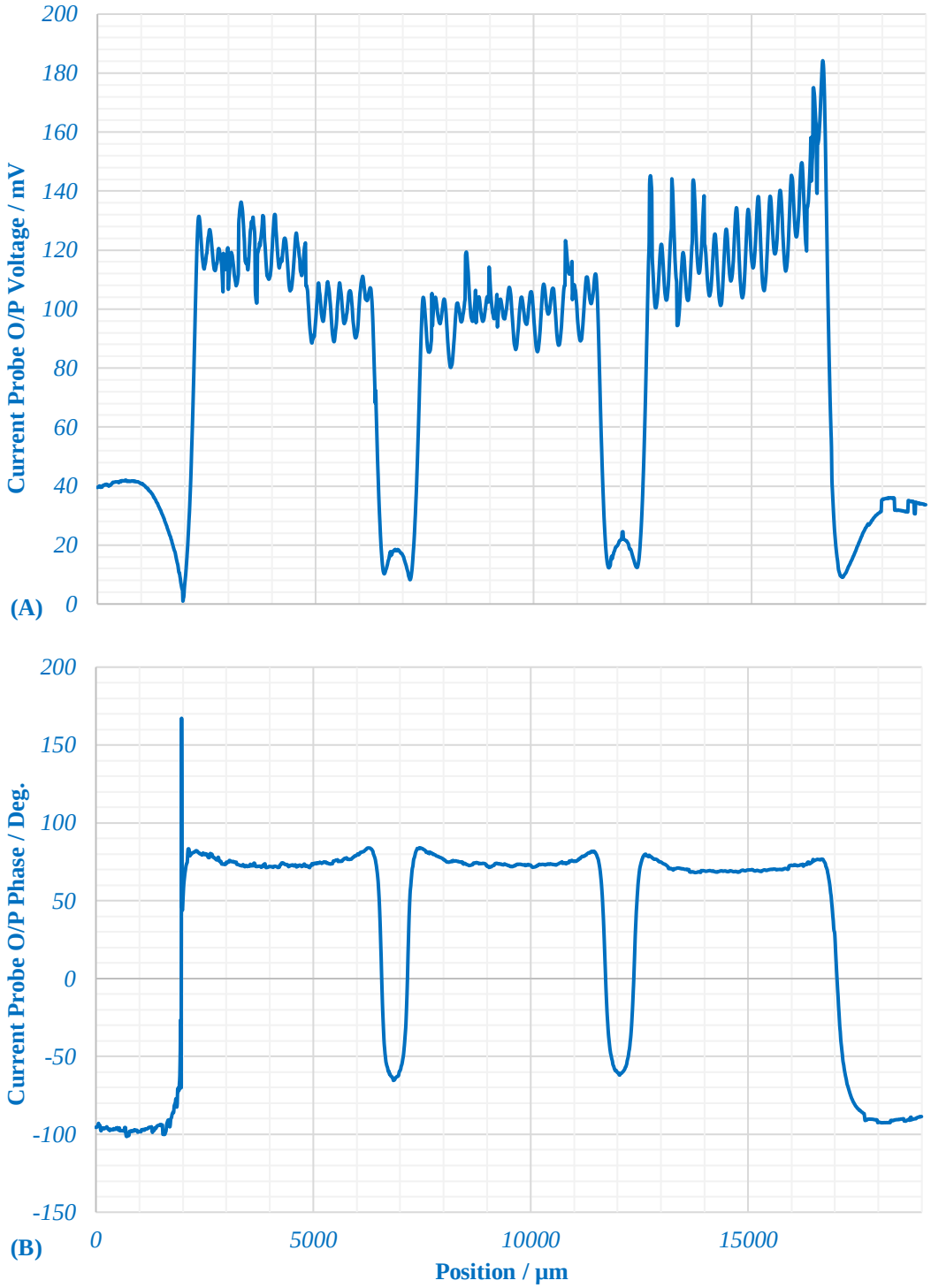

Figure 6-10 Scan results across the 4th array of the bond wires. (A) The magnitude. (B) The phase.

7. Scan along the lead of the gate: this lead was deformed while removing the ceramic lid, see Figure 6-12, and due to that, the current distributed along the lead becomes asymmetrical for both the magnitude, see Figure 6-11(A), and phase, see Figure 6-11(B).

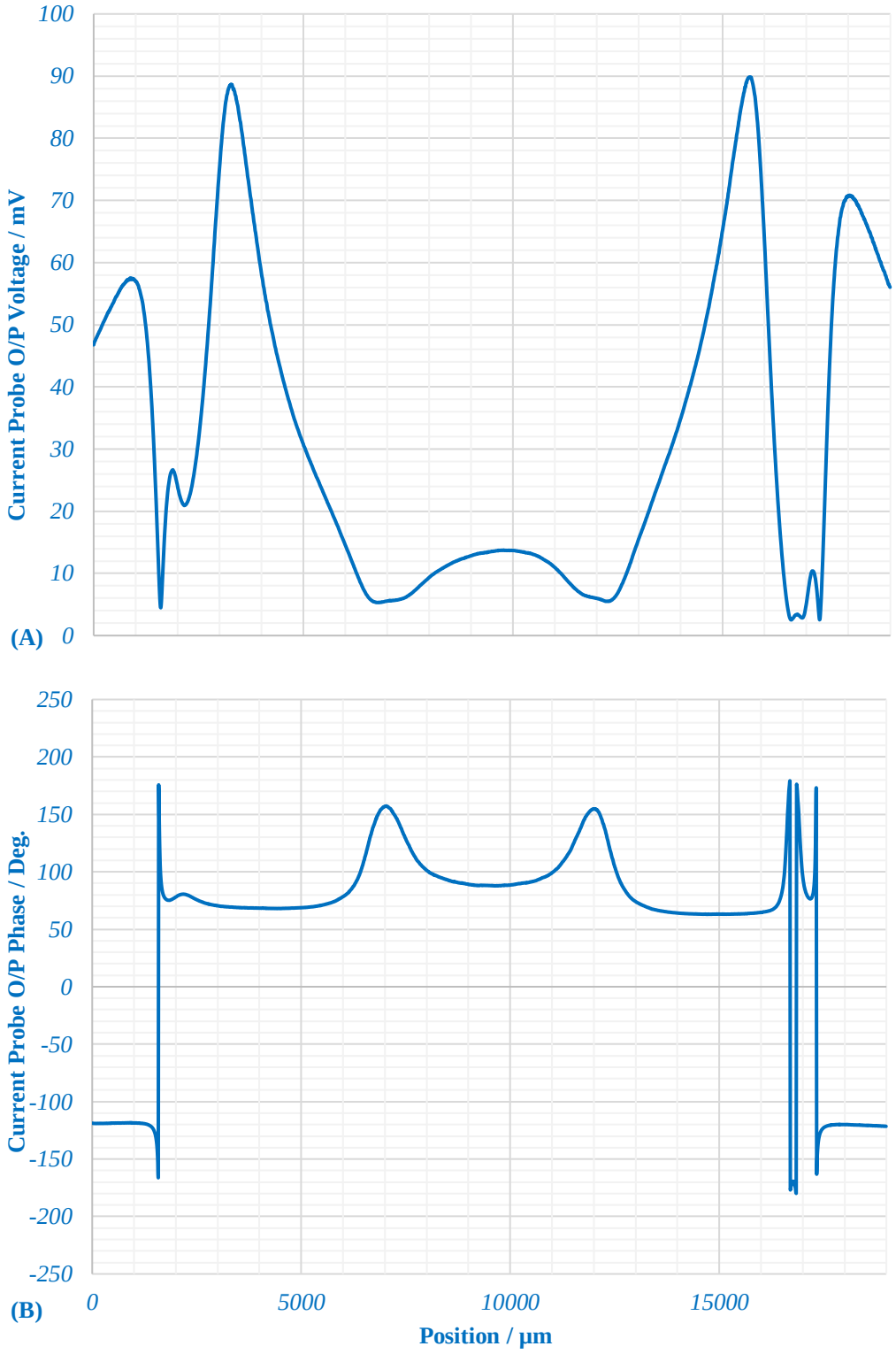

Figure 6-11 Scan results along the lead of the gate. (A) The magnitude. (B) The phase.

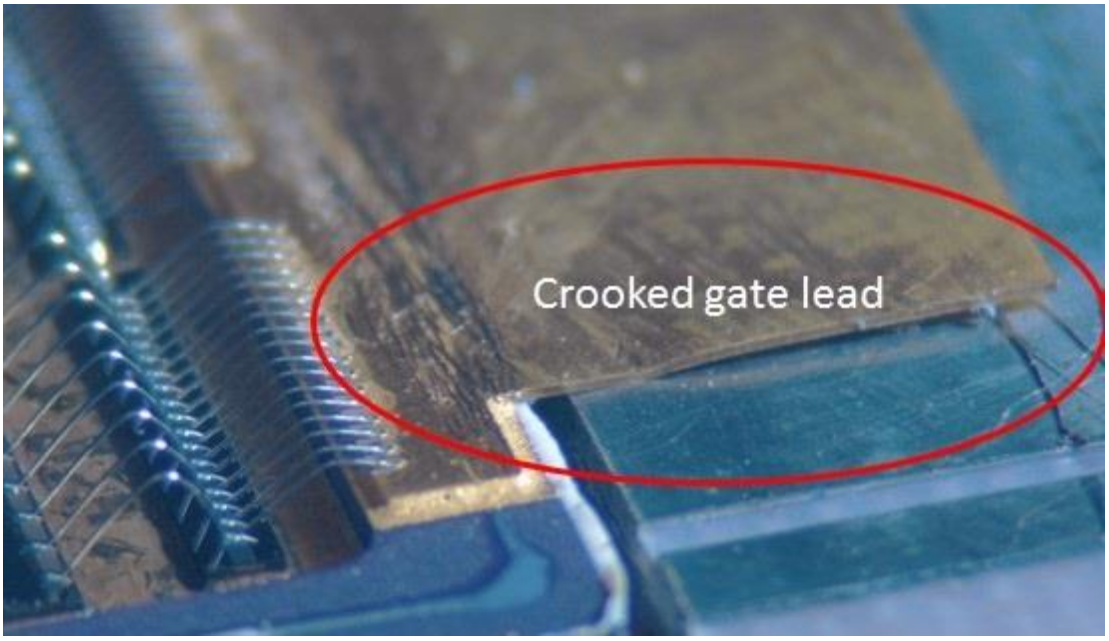

Figure 6-12 The crooked gate lead causes asymmetrical current distribution as shown in Figure 6-10 and Figure 6-11.

6.7 Current distribution in the Drain Bond Wires and in the Dies

The previous results showed that the current distribution among the adjacent dies and their associated bond wires is not even, those dies on the sides are carrying more current than the central die. Although this current probe provides relative measurement data, this type of information is very important for the microwave transistor designer. The aim for those designers is to ensure an even current and voltage distribution in order to enhance overall efficiency and reliability of the device. The proposed contactless current probe successfully shows the current differences between identical parts within the DUT. Reducing these differences to zero is the key for new generation of high efficiency and more reliable microwave power transistors.

As explained in chapter two, the contactless measurements have a strong dependency on the distance to the DUT and therefore they are generally classified as a relative measurement technique rather than an absolute technique. In addition to that, the output response of the current probe is also a function of the angle between the plane containing the loop antenna and the DUT.

One of two approaches can be used to find the absolute value of the current. In the first instance, the absolute value is found after calibrating the current probe. Unfortunately, the XYZ stage we have had three axes only; in order to conduct an accurate current probe

calibration, it should be upgraded to have at least four axes. The fourth axis is the rotation around the longitudinal axis of the loop antenna with a movement step that is a fraction of a degree.

The other approach can be applied whenever the total current passing in the parallel parts (for example the dies within the power transistor) is known. Fortunately, this current is related to the net current drawn from the DC power. For example, in a common source class-AB amplifier, the maximum AC drain current is equal to the maximum DC current. The next step is to normalise the spatial current measurements across the drain bond wires, see Figure 6-13, and then sum the magnitude of the normalised peaks (above the bond wires). The probe's scaling factor (SF) is then calculated by dividing the maximum AC current by the sum of the peaks. Finally, each of the normalized peaks is then multiplied by the scaling factor to find its absolute current, see Table 6-1, and hence the die current is equal to the sum of those bond wires attached to it.

Table 6-1 Current in each bond wire.

Die No.	**Bond Wires Currents / Amp.**									
	W_1	W_2	W_3	W_4	W_5	W_6	W_7	W_8	W_9	W_{10}
1	0.283	0.235	0.223	0.203	0.195	0.187	0.187	0.183	0.180	0.182
2	0.196	0.187	0.179	0.173	0.165	0.164	0.167	0.178	0.179	0.186
3	0.202	0.197	0.192	0.195	0.201	0.201	0.213	0.232	0.239	0.284

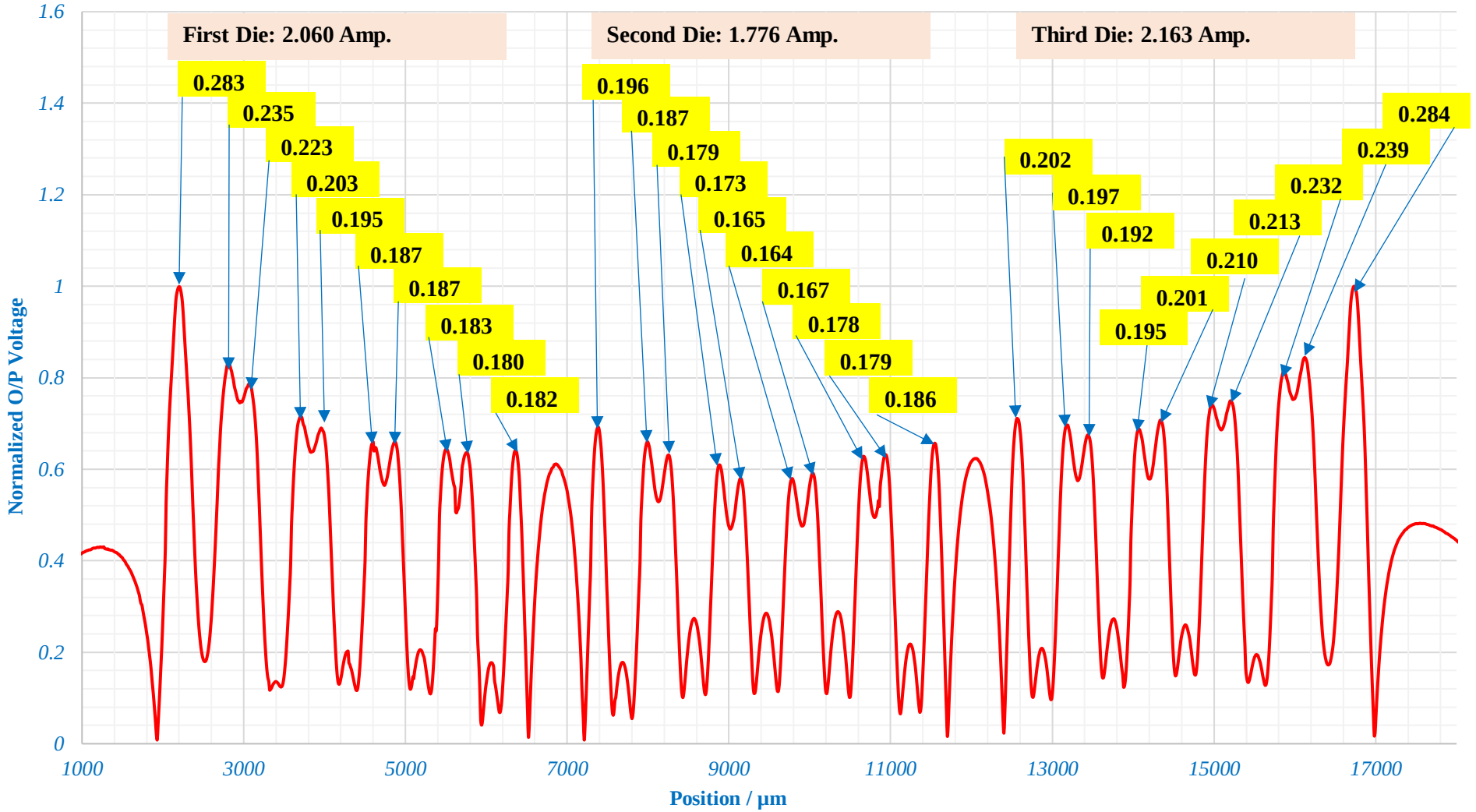

Figure 6-13 Current distribution among the drain bond wires and among the three dies.

7 Conclusions and Future Work

7.1 Conclusions

The work presented in this thesis dealt with a series of important topics related to the contactless probing of high power microwave devices; the main contributions were illustrated in chapters four, five and six.

In chapter one, we pointed to the problem of low efficiency in a microwave power transistor which in turn causes a large amount of power to be consumed by commercial base stations managed by the wireless network communications companies. The microwave circuit designers need a tool for real-time measurements of the voltage and the current distributed inside microwave circuit and more specifically inside microwave power transistors. The miniaturized contactless probes emerge as an excellent solution to directly quantify the voltage and the current with minimum intrusion to the DUT.

Next, in chapter two, we started with electromagnetic theory concepts and defining the region of electromagnetic radiation around the sources of the electromagnetic energy. We paid particular attention to the near-field region where the contactless measurements take place and provided clarification of the boundary limits of this region. Different types of electromagnetic sources were explored, and their characteristics were discussed in detail. Next, a comparison of the electric and magnetic sources with their mathematical analyses was given. Because real life sources are not only an electric source alone or magnetic source alone but a mixture of both, a mathematical expression was given to describe these practical electromagnetic sources. In addition to that, the properties of the monopole and

the loop antenna were presented where each of them is the sensing part of the contactless voltage and current probes respectively. The output signals of these antennas were then expressed in terms of their dimensions and those of the practical source.

In chapter three, we described the main parts of the contactless voltage and current measurement setup. These parts are divided into three essential levels: (1) measurement control and management level, (2) measurement instrument level and (3) measurement action level. Next, the structure of a generic contactless probe was presented with a detailed explanation of the materials used to fabricate each of its parts. Also, we focused on the environments of the real measurements. This included the mechanical and electrical characteristics of the bond wires, the semiconductor dies, and the microstrip line ...etc. the final part of this chapter was devoted to the set of tests used to inspect the characteristics of the newly fabricated probes. These tests are the non-intrusiveness test, the bandwidth test, the spatial resolution test and the measurement fidelity test. To verify these tests, we fabricated suitable test fixtures for both the miniaturised contactless probe and the scaled-up probe that was fabricated from standard coaxial cables.

In chapter four, we started with the geometrical parameters that are affecting the spatial resolution and the sensitivity of the contactless voltage probe. The first aim was to establish the design criteria for the voltage probes. For this purpose, we used different sizes of the scaled-up voltage probes, fabricated from standard coaxial cables and thus the design criteria were also verified experimentally. The results showed that the diameter of the internal conductor of the coaxial cable has a dominant influence on the voltage probe spatial resolution and sensitivity. Through these experiments, we identified a new definition for the spatial resolution which permits comparing spatial resolution of different probes in terms of their output signal rather than the spatial formula. Furthermore, different techniques applied here with the aid of the ADS software to enhance voltage probe sensitivity. A simple but effective inductive element included in the design of the voltage probe, provided a passive gain and thus enhanced the sensitivity by around 20dB. A miniaturized voltage probe fabricated from a miniaturised coaxial cable followed by a miniaturized chip scale amplifier were combined to deliver a novel probe with spatial resolution of 25 µm and a useful operating bandwidth up to 7 GHz. Furthermore, this gain enables time domain oscilloscope measurements to be made.

Chapter five was dedicated to the direct real-time current quantification by using the contactless current probes. In a similar approach to that applied in chapter four, chapter five began with establishing the design criteria of the contactless current probes to achieve

high spatial resolution. We used the standard coaxial cable to fabricate scaled-up current probes to examine the influence of the geometrical aspects on both the probe spatial resolution and the probe sensitivity. The experimental results showed that current probe spatial resolution is mainly controlled by the radius of the conductor that had been used to form the loop antenna while the sensitivity is mainly controlled by the radius of the loop antenna. We used the differential amplifier to enhance both the sensitivity and the probe's ability to reject the electric field. We found experimentally that relying on the differential amplifier alone to reject the electric field is not sufficient. The standing wave test was applied, and the results showed a considerable contribution from the electrical field with magnetic field component. To solve this issue, we created a novel technique to shield the miniaturised loop antenna. The advantages of this technique over the planar shielding technique is that its overall size (the shield and the miniaturized loop) are small which permits more freedom to move inside the power transistors. This new shielding technique consists of three adjacent copper loops two for said shielding and one in the middle of enamelled wire which forms the loop antenna. The outer circumference of these three loops was then painted with high conductivity silver epoxy to complete the shielding around the loop antenna. Next, to verify the immunity of the multiple loop shielding technique, we applied three tests to it: In the first one, the probe scanned the current distribution across the width of the microstrip line and the result was a very clear inverted umbrella. In the second test, we applied the standing wave test and the results showed that the maxima of the current waves were occurring at the locations of minima of the voltage wave. The last test is the electric field rejection ratio and the recorded values were 22.7 dB for the average and 39 dB for the maximum. Finally, the miniaturised contactless current probe was tested to show a spatial resolution of at least 62 μm and a usable bandwidth up to 9 GHz.

Finally, in chapter six, we demonstrated innovation with a novel spatial waveform characterization of a microwave power transistor under normal operating conditions. One of the fundamental requirements for the designer of these devices is to understand how the power, and more specifically how the currents, are distributed among their parts, i.e. bond wires and dies. Although the contactless probes are classified as relative measurement tools, they are still very useful in showing the differences between adjacent identical parts inside the DUT. The target for those designers is to ensure the adjacent and identical parts of the device share equally the total power and have a similar amount of current passing in each of them. Scanning these parts with the contactless current probe

at a specific height and specific orientation of the loop antenna can satisfy this essential need. To show the ability of the miniaturised current probe to do that, we performed seven spatial scans along the length of a 130W LDMOS power transistor and each of these scans was started at a specific location along its width. The first scan was along the lead of the drain and the last one was along the lead of the gate. The spatial waveforms resulting from these scans showed that the total current was not equally divided among the adjacent dies and associated bond wires. The general trend of those sub-currents is the inverted umbrella. Those dies on the sides were carrying higher current than the middle one. In addition to that we were able to estimate the absolute values of the currents in the drain bond wires and their associated dies as wall. To do that, we first found the probe scaling factor by normalizing the scan results and then dividing the total drain current by the total sum of all maxima. The absolute current in each bond wire was then calculated from the product of the probe factor and the respective current ratio.

7.2 Future Work

Our recommendations to improve the work presented in this thesis are:

1. Floating Measurements.

   The circuit of the contactless probes can be modified to work in the floating mode, which means eliminating the common ground with the DUT. This modification is important because it reduces the likelihood of accidental damage that might occur if the probe touches the DUT.

   To accomplish this there are two things that must be achieved: firstly, a floating power supply should be used to feed the power to the probe; secondly, transmitting the probe output signal over a non-conducting, non-metallic, channel. Both of these requirements can be achieved by using fibre optic cables. Two cables are used: one for power transfer and the other for data transfer.

   The ‘power over fibre’ technology might be applied here to supply the DC power needed by the probe. High-power laser diodes can be used to emit unmodulated light with high energy at the transmitter side (near the DC power supply). The fibre optic cable then is used to transfer this light to a miniaturized solar cell on the probe side. It is essential here to use high-efficiency solar cells to support the miniaturization requirements of the contactless probes. The multiple-junction solar cells are recommended for such applications due to their high efficiency achieved from a small cell size.

On the other hand, a Vertical Cavity Surface Emitting Laser (VCSEL) might be used as a light modulator in response to the probe output voltage. This modulated light is then propagated from the probe side through a fibre optic cable to the other side where it is then received and demodulated. The DO188_VCSEL is one industrial example of the miniaturized VCSEL (250 µm X 1000 µm X 150 µm) that offers a useful bandwidth up to 7.5 GHz with a low threshold current of 1mA.

2. Spatial Resolution Enhancement.

As shown in chapters four and five, the spatial resolution of both voltage and current probes depends on the diameter of the wire used to create the monopole antenna and the loop antenna respectively. Therefore, enhancing the spatial resolution of the contactless voltage and current probes can be performed by using a smaller size enamelled wire, such as AWG 56 (12 µm diameter).

Thus, the spatial resolution of the voltage probe can be improved to around 12 µm, and for the current probe it becomes 39 µm instead of 62.5µm.

3. Single Biasing Voltage.

The miniaturized current probe presented in this work offers 12 dB gain and 22.7 dB average rejection of the electric field. This current probe has a single stage differential amplifier and one current source: each biased with three DC voltages (see Figure 5-15): one for the current source and the others for the differential amplifier pairs. To get more gain and a higher rejection of the electric field, a multi-stage differential amplifier is recommended.

Adding more stages to the differential amplifier will require two additional DC biasing voltages for each stage. Thus, for three stages of the differential amplifier and their associated current sources, the total number of DC biasing connections is seven.

This will require a larger probe housing that permits seven SMA connectors to be attached, as well as six bias tees to be used. One solution to avoid this complexity is to implement these bias tees inside the current probe by replacing each with a surface mounted inductance and capacitor. One end of the inductance is connected to a single DC biasing voltage and the other end is connected to the associated differential pair.

One advantage of this solution is that it will require increasing the length of the probe housing without increasing its cross section.

The other advantage here is the possibility of designing a buffer stage after the last differential amplifier so that only a single output is needed. This will eliminate the need for the BALUN to do the subtraction between the outputs of the last differential amplifier.

It is also possible to apply this solution to the voltage probe to get more gain by cascading multiple stages of amplification with only one DC supply connection.

4. MMIC Amplifier.

A further step toward constructing an industrial version of the contactless probe, and also to reduce probe manufacturing steps, is to use MMIC amplifiers instead of an amplifier constructed from discrete components.

Multiple stages of the differential amplifier can be designed and implemented within an MMIC, and it can be used with both the voltage and the current probes. With the voltage probe, one of the differential amplifier inputs is connected to the ground and the other is connected to the monopole antenna, while for the current probe inputs are used as usual.

In addition to that, MMICs can offer wider bandwidth and consume less power than the discrete version of the amplifier.

5. Unshielded Loop Antenna.

The main problem with the unshielded loop antenna, presented in section 5.8, is a lot of asymmetrical electric field that is picked up by the loop and their leads. The reason behind this is the asymmetry of the structure used in the implementation of the probe. The PCB track that forms the loop is attached to one side of the alumina, which increases the intensity of the electric field from the other side.

In addition to that, the large cross-section area of the alumina substrate (250 µm X 250 µm) allows more of the electric field to emerge through it and be picked up by the leads of the loop.

Also, loop leads are parallel tracks which means that each of them receives a different amount of the electric field; thus, this introduces a larger differential signal.

One solution to this problem is the MLST presented in this thesis, see section 5.11.

The other possible solution is to use the enamelled thin wire alone to form an unshielded loop antenna and then carefully twist its leads. This approach can increase the symmetry of the antenna structure and thus reduce the differential signal resulting from the electric field, which means increasing the EFRR value.

The loop antenna might then be cascaded with the multiple differential amplifier stages solution proposed in 3 and 4 to gain further reduction of the common mode electric field signals.

This solution (if successful) can enhance the value of the spatial resolution of the current probe to be equal to the diameter of the enamelled wire, and also will simplify the probe construction

6. Simultaneous Measurements of the Voltage and the Current.

Having a probe able to measure both the voltage and the current simultaneously can halve measurement time, since time is needed for one scan only. Furthermore, it is possible to measure the wave impedance at each location more accurately. This means having both the loop antenna and the monopole antenna implemented in the same probe.

In terms of designing the amplifiers within the housing of this probe, we propose a pair: a differential amplifier connected to the loop antenna and a single end amplifier connected to the monopole antenna.

This will require four biasing voltages (alternatively applying the approaches described in 3 and 4 above). Fortunately, the design of the current probe housing presented in Figure 3-7(A) has enough space for up to five coaxial cables (the DC biasing voltages are passed through these coaxial cables). Therefore, it is possible to implement both the voltage and the current probes in this housing.

To apply this idea, the loop antenna is used to mechanically support the monopole antenna and the end of the monopole is attached to the centre of the loop with glue, see Figure 7-1.

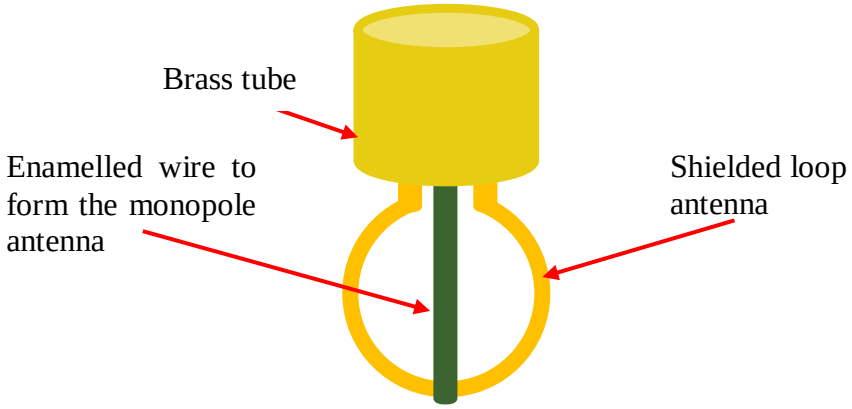

Figure 7-1 The loop and the monopole antenna mounted within the same brass tube.

7. Harmonic Measurement.

   Harmonic measurement vitally important to fully evaluate the performance of the amplifier under test. Fortunately, both the voltage and the current probes presented through this work have a sufficiently broad bandwidth, 7 GHz and 9 GHz respectively. Therefore, both of them may be used to measure the second harmonic and even the third harmonic, in addition to the fundamental component.

8. Five-axis Mechanical Movement Stage.

   The XYZ stage could be modified to deliver five-axis movement and, furthermore, to add stepper motors to each axis to ensure precise probe location. This, of course, will require updating the LabVIEW code to maintain full control of the stepper motors.

9. Absolute Measurement

   The miniaturised contactless probe presented in this work functioned very well for the relative measurement. However, if the absolute values are needed, and the approach presented in section 6.7 is not applicable, then the contactless probe should be calibrated over the range of the operating frequencies.

8 REFERENCES

[1] R. Gupta and E. C. Strinati, "Base-station duty-cycling and traffic buffering as a means to achieve green communications," *IEEE Veh. Technol. Conf.*, 2012.

[2] T. Sriram Prasanth, M. Saiujan Kumar, and T. Shankar, "A survey on techniques related to base station sleeping in Green communication and CoMP analysis," *Proc. 2nd IEEE Int. Conf. Eng. Technol. ICETECH 2016*, no. March, pp. 1059–1067, 2016.

[3] J. Joung, C. K. Ho, and S. Sun, "Green Wireless Communications : A Power Amplifier Perspective," *Signal Inf. Process. Assoc. Annu. Summit Conf. (APSIPA ASC), 2012 Asia-Pacific*, no. Cci, pp. 1–8, 2012.

[4] M. Kuball *et al.*, "Measurement of Temperature in Active High-Power AlGaN / GaN HFETs Using Raman Spectroscopy," *IEEE Electron Device Lett.*, vol. 23, no. 1, pp. 10–12, 2002.

[5] D. M. Risbud, K. Pedrotti, M. Power, J. W. Pomeroy, and M. Kuball, "Thermal characterization of high voltage GaN-on-Si Schottky Barrier Diodes (SBD) for designing an on-chip thermal shutdown circuit for a power HEMT," *Wide Bandgap Power Devices Appl. (WiPDA), 2015 IEEE 3rd Work.*, pp. 156–161, 2015.

[6] P. H. Aaen *et al.*, "Multi-Physics Modeling of High-Power Microwave Transistors," *IEEE MTT-S Int. Microw. Symp. Dig.*, pp. 3–5, 2012.

[7] P. H. Aaen, J. A. Plá, and C. A. Balanis, "Modeling Techniques Suitable for CAD Based Design of Internal Matching Networks of High-Power RF/Microwave Transistors."

[8] P. H. Aaen and S. Gillespie, “Distributed Multiphysics Modeling of Microwave Power Transistors,” *IEEE MTT-S Int. Conf. Numer. Electromagn. Multiphysics Model. Optim.*, 2015.

[9] C. A. Balanis, *ADVANCED ENGINEERING ELECTROMAGNETICS*, 2nd ed. John Wiley & Sons, Inc., 2012.

[10] “Alternate Forms of Maxwell’s Equations.” [Online]. Available: http://www.maxwells-equations.com/forms.php.

[11] M. N. O. Sadiku, *Elements of Electromagnetics*, 6th ed. Oxford University Press, 2015.

[12] C. A. Balanis, *Antenna Theory Analysis and Design*, 3rd ed. Wiley & Sons, Incorporated, John, 2005.

[13] “Physik Oberstufe/ Schwingungen und Wellen/ Elektromagnetische Wellen – Wikibooks, Sammlung freier Lehr-, Sach- und Fachbücher.” [Online]. Available: https://de.wikibooks.org/wiki/Physik_Oberstufe/_Schwingungen_und_Wellen/_Elektromagnetische_Wellen.

[14] D. H. Staelin, *Electromagnetics and Applications*. Department of Electrical Engineering and Computer Science Massachusetts Institute of Technology Cambridge, MA, 2011.

[15] C. R. Paul, *Introduction to Electromagnetic Compatibility*. JOHN WILEY & SONS, 2006.

[16] S. Silver, *Microwave Antenna Theory and Design*. 1949.

[17] P. V. Nikitin, K. V. S. Rao, and S. Lazar, “An Overview of Near Field UHF RFID,” *2007 IEEE Int. Conf. RFID*, pp. 167–174, 2007.

[18] R. Patton and N. Yang, “How to Measure All Types of Antennas Using Very-Near-Field.” [Online]. Available: http://www.electronicinstrument.com/emmat.pdf. [Accessed: 28-Dec-2016].

[19] S. Laybros, P. F. Combes, and H. J. Mametsa, “The ‘very-near-field’ region of equiphase radiating apertures,” *IEEE Antennas Propag. Mag.*, vol. 47, no. 4, pp. 50–66, 2005.

[20] C. Capps, “Near-field or far field?,” *Edn-bost. THEN DENVER*, vol. 46, no. 18, pp. 95–102, 2001.

[21] S. Laybros and P. F. Combes, “On Radiating-Zone Boundaries of Short, Lambda/2 and Lambda Dipoles,” *IEEE Antennas Propagat. Mag.*, vol. 46, no. 5, pp. 53–64, 2004.

[22] J. D. Kraus and R. J. Marhefka, *Antennas For All Applications*, 3rd ed. McGraw-Hill, 2002.

[23] V. Kraz, “Near-Field Methods of Locating EMI Sources,” *Compliance Engineering*, pp. 1–7, 1995.

[24] A. Committee, I. Antennas, and P. Society, *IEEE Standard Definitions of Terms for Antennas*, vol. 2013. 2014.

[25] C. Suriano, J. Suriano, T. Holmes, and Q. Yu, “Antenna Fundamentals.” [Online]. Available: https://interferencetechnology.com/antenna-fundamentals/.

[26] M. Mardiguian, *Controlling Radiated Emisions by design*, 3rd ed. Springer International Publishing, 2014.

[27] CHRISTIAN KUECK, “Layout Power Supply Boards to Minimize EMI - Part 3: EMI Basics,” *Linear Technology Corp*, 2013. [Online]. Available: www.powerelectronics.com.

[28] J. L. N. Violette, D. R. J. White, and M. F. Violette, *ELECTROMAGNETIC COMPATIBILITY HANDBOOK*. 1987.

[29] Ali M. Niknejad, *Electromagnetics for High-Speed Analog and Digital Communication Circuits*. CAMBRIDGE UNIVERSITY PRESS, 2007.

[30] N. N. Rao, *Elements of Engineering Electromagnetics*, 1st ed. Prentice-Hall, 1977.

[31] H. W. Ott, *Electromagnetic Compatibility Engineering*. JOHN WILEY & SONS, 2009.

[32] J. L. Volakis, C.-C. Chen, and K. Fujimoto, *Small Antennas*. McGraw-Hill, 2010.

[33] F. M. Greene, “The near-zone magnetic field of a small circular-loop antenna,” *J. Res. Natl. Bur. Stand. Sect. C Eng. Instrum.*, vol. 71C, no. 4, p. 319, 1967.

[34] H. W. Ott, *NOISE REDUCTION TECHNIQUES IN ELECTRONIC SYSTEMS*. JOHN WILEY & SONS, 1988.

[35] W. H. Hayt and J. J. A. Buck, *Engineering Electromagnetics*, 8th ed. McGraw-Hill, 2012.

[36] D. JOHN and L. VOLAKIS, *ANTENNA ENGINEERING HANDBOOK*. McGraw-Hill, 2007.

[37] C. R. Paul, *Inductance: Loop and Partial*. 2009.

[38] J. J. Carr, *Practical Antenna Handbook 4th Edition*, 4th ed. McGraw-Hill, 2001.

[39] W. Propagation, S. Committee, and P. Society, *IEEE Standard Methods for Measuring Electromagnetic Field Strength of Sinusoidal Continuous Waves, 30 Hz to 30 GHz*, vol. 1991. 1991.

[40] F. Greene, "A new near-zone electric field-strength meter," *J. Res. Natl. Bur. Stand. - Co Eng. Instrum.*, vol. 71C, no. 1, pp. 51–57, 1966.

[41] F. M. Greene, "NBS Field-Strength Standards and Measurement (30 Hz to 1000 MHz)," *Proc. IEEE*, vol. 55, no. 6, pp. 970–981, 1967.

[42] M. Kanda, "An Electromagnetic Near-Field Sensor for Simultaneous Electric and Magnetic-Field Measurements," *IEEE Trans. Electromagn. Compat.*, vol. EMC-26, no. 3, pp. 102–110, 1984.

[43] T. Babij and H. Bassen, "Broadband isotropic probe system for simultaneous measurement of complex E-and H-fields," 1986.

[44] L. D. Driver and M. Kanda, "An Optically Linked Electric and Magnetic Field Sensor for Poynting Vector Measurements in the Near Fields of Radiating Sources," *IEEE Trans. Electromagn. Compat.*, vol. 30, no. 4, pp. 495–503, 1988.

[45] F. Silva, F. Sanchez, P. J. Riu Costa, and R. Pallàs-Areny, "Low-cost near-field probe for simultaneous E and H measurement with analog optical link," in *IEEE International Symposium on Electromagnetic Compatibility*, 1997, pp. 533–536.

[46] M. E. G. Upton and A. C. Marvin, "Improvements to an Electromagnetic Near-Field Sensor for Simultaneous Electric and Magnetic Field Measurement," *IEEE Trans. Electromagn. Compat.*, vol. 35, no. 1, pp. 96–98, 1993.

[47] N. Uddin and A. Thiede, "Integrated active sensors for chip-level near-field scanning," in *German Microwave Conference, 2010*, 2010, vol. 8, no. c, pp. 28–31.

[48] K. Tajima, R. Kobayashi, N. Kuwabara, and M. Tokuda, "Development of Optical Isotropic E-Field Sensor Operating More than 10 GHz Using Mach-Zehnder Interferometers," *IEICE Trans. Electron.*, vol. 85, no. 4, pp. 961–968, 2002.

[49] P. Dijkstra and A. Van Peer, “Probe for measuring an electric field,” 2013.

[50] P. Bienkowski, “ELECTROMAGNETIC FIELDS MEASUREMENTS – METHODS AND ACCURACY ESTIMATION,” in *EHE’07 – 2nd I nternational Conference on Electromagnetic Fields, Health and Environment*, 2007, pp. 7–10.

[51] Y. Gao and I. Wolff, “Miniature electric near-field probes for measuring 3-d fields in planar microwave circuits,” *IEEE Trans. Microw. Theory Tech.*, vol. 46, no. 7, pp. 907–913, 1998.

[52] Y. Gao and I. Wolff, “A new miniature magnetic field probe for measuring three-dimensional fields in planar high-frequency circuits,” *IEEE Trans. Microw. Theory Tech.*, vol. 44, no. 6, pp. 911–918, 1996.

[53] N. Uddin, M. Spang, T. Mager, and A. Thiede, “Integrated Active Sensors for Near-Field Scanning,” in *VXV International Symposium on Theoretical Engineering*, 2009, vol. 1, no. 1, pp. 1–5.

[54] J. M. Dienot, “Applications of integrated near-field antennas for diagnosis of electromagnetic noises in hybrid electronic architectures,” in *2013 IEEE 11th International Workshop of Electronics, Control, Measurement, Signals and their application to Mechatronics*, 2013.

[55] A. Tankielun, H. Garbe, and J. Werner, “Calibration of electric probes for post-processing of near-field scanning data,” in *2006 IEEE International Symposium on Electromagnetic Compatibility, 2006. EMC 2006.*, 2006, vol. 1, no. 2, pp. 119–124.

[56] *IEEE Standard for Calibration of Electromagnetic Field Sensors and Probes, Excluding Antennas, From 9 kHz to 40 GHz*. Institute of Electrical and Electronics Engineers, Inc., 2013.

[57] D. Morgan, *A Handbook for EMC Testing and Measurement*. The Institution of Engineering and Technology, 2007.

[58] E. M. Montrose M. I. Nakauchi, *TESTING FOR EMC COMPLIANCE Approaches and Techniques*. A JOHN WILEY & SONS, INC., 2004.

[59] N. Uddin and M. Spang, “Integrated active near-field sensor in GaAs technology,” in *Proceedings of the 4th European Microwave Integrated Circuits Conference, Italy*, 2009, no. September, pp. 278–281.

[60] N. Uddin, M. Spang, and A. Thiede, “Miniature Loop Antenna for Active Near-Field Sensor,” in *Microwave Conference (GeMIC), ...*, 2008, pp. 348–351.

[61] A. Thiede, N. Uddin, and A. S. Awny, “Integrated active miniature sensors for electro-magnetic near field measurement,” in *cccc2012 Asia-Pacific Symposium on Electromagnetic Compatibility, APEMC 2012 - Proceedings*, 2012, pp. 197–200.

[62] S. Aoyama, S. Kawahito, and M. Yamaguchi, “Integrated active magnetic probe in silicon-on-insulator complementary metal-oxide-semiconductor technology,” *Japanese J. Appl. Physics, Part 1 Regul. Pap. Short Notes Rev. Pap.*, vol. 45, no. 9 A, pp. 6878–6883, 2006.

[63] S. Aoyama, S. Kawahito, and M. Yamaguchi, “Fully integrated active magnetic probe for high-definition near-field measurement,” in *2006 IEEE International Symposium on Electromagnetic Compatibility, 2006. EMC 2006.*, 2006, vol. 2, no. c, pp. 426–429.

[64] K. L. D. X. D. X. Dqg *et al.*, “Non-contacting signal transmission measurement and modeling by coupling theory,” in *2015 Asia-Pacific Microwave Conference (APMC)*, 2015, vol. 1, pp. 1–3.

[65] D. Chevallier, D. Baudry, and A. Louis, “Improvement of Electrical Near-Field Mea Surements Withanelectro-Optic Test Bench,” *Prog. Electromagn. Res.*, vol. 40, no. February, pp. 381–398, 2012.

[66] Robert E. Collin, *Foundations for Microwave Engineering*, 2nd ed. A JOHN WILEY & SONS, INC., 2001.

[67] M. Shinagawa, T. Nagatsuma, K. Ohno, and Y. Jin, “A real-time electro-optic handy probe using a continuous-wave laser,” *IEEE Trans. Instrum. Meas.*, vol. 50, no. 5, pp. 1076–1080, 2001.

[68] M. Spang, M. Albach, N. Uddin, and A. Thiede, “Miniature dipole antenna for active near-field sensor,” in *German Microwave Conference, GeMIC 2009*, 2009, no. 2.

[69] S. C. Cripps and A. Porch, “An active, non-intrusive, high resolution microwave field probe with applications in high power RF device and circuit design,” in *Wireless and Microwave Technology Conference (WAMICON), 2010 IEEE 11th Annual*, 2010, pp. 1–4.

[70] C. F. Campbell, “Probe Based Simulation Technique for Modeling Saturated Power Amplifiers,” in *Proceedings of the 6th European Microwave Integrated Circuits Conference*, 2011, no. October, pp. 176–179.

[71] N. Dehghan, A. Porch, S. C. Cripps, and P. H. Aaen, “A novel high resolution E-field microscope system with applications in HPA diagnostics,” in *Microwave Measurement Symposium (ARFTG), 2011 78th ARFTG*, 2011, pp. 1–3.

[72] W. Mann and A. Kortke, “Highly sensitive optoelectronic E-field probes for interference free near field antenna measurements,” in *ITG FACHBERICHT*, 2003, pp. 5–8.

[73] P. Neelakanta and D. DeGroff, “Light-emitting diode as radio-frequency detector: development of RFI-free electromagnetic field sensor,” *Electron. Lett.*, vol. 25, no. 23, pp. 1606–1608, 1989.

[74] R. Penze and J. Rosolem, “Fiber powered extender for XG-PON/G-PON applications,” *J. Opt. Commun. Netw.*, vol. 6, no. 3, pp. 250–258, 2014.

[75] S. Perhirin *et al.*, “A power-over-fiber system and its low consumption remote equipment for submarine applications,” in *2013 MTS/IEEE OCEANS - Bergen*, 2013, pp. 2–7.

[76] P. C. Choubey, A. Oudhia, R. Dewangan, and V. Y. T. P. G. Autonomous, “A review : Solar cell current scenario and future trends,” *Recent Res. Sci. Technol. 2012*, vol. 4, no. 8, pp. 99–101, 2012.

[77] M. N. Zervas and C. a. Codemard, “High Power Fiber Lasers: A Review,” *IEEE J. Sel. Top. Quantum Electron.*, vol. 20, no. 5, pp. 1–23, 2014.

[78] M. Communications and S. Republic, “Optically powered fiber optic sensors,” *Informatica*, vol. 5, no. 3, pp. 1–7, 2005.

[79] “Non-Invasive, Turn-Key Test and Measurement Systems.” [Online]. Available: http://www.fiber-sensors.com/products/. [Accessed: 29-Mar-2017].

[80] “Electroptic Field Sensors System : RF & Microwave Instrumentation : Products : Instruments : Commercial Services : National Physical Laboratory.” [Online]. Available: http://www.npl.co.uk/instruments/products/rf-microwave/electroptic-field-sensors-system/. [Accessed: 29-Mar-2017].

[81] “INTRODUCING NEOSCAN: A NON INVASIVE TURNKEY FIELD

MEASUREMENT SYSTEM." [Online]. Available: http://www.emagtech.com/content/neoscan-system. [Accessed: 29-Mar-2017].

[82] "ULTRA-WIDEBAND NON-INVASIVE FIELD MEASUREMENT SYSTEM." [Online]. Available: http://www.emagtech.com/content/neoscan-system-0. [Accessed: 29-Mar-2017].

[83] *IEEE Recommended Practice for the Measurement of Potentially Hazardous Electromagnetic Fields — RF and Microwave*. 1992.

[84] D.-J. Lee, J.-Y. Kwon, and N.-W. Kang, "Field analysis of electro-optic probes for minimally invasive microwave sampling.," *Opt. Express*, vol. 22, no. 3, pp. 2897–909, 2014.

[85] D.-J. Lee and J. F. Whitaker, "An optical-fiber-scale electro-optic probe for minimally invasive high-frequency field sensing.," *Opt. Express*, vol. 16, no. 26, pp. 21587–97, 2008.

[86] Q. Chen, K. Sawaya, and K. Ito, "Recent Research Activities on Antennas in Japan," in *7th European Conference on Antennas and Propagation (EUCAP 2013)* -, 2013, pp. 177–181.

[87] C. S. Andrews, "Next generation high sensitivity, broadband electrical field sensor," *Fiber Optic Sensors and Systems*, pp. 1–6, Jun-2007.

[88] J. R. Hwang, R. K. Lai, J. Nees, T. Norris, and J. F. Whitaker, "A field-sensitive photoconductive probe for sampling through passivation layers," *Appl. Phys. Lett.*, vol. 69, no. 15, pp. 2211–2213, 1996.

[89] H. Togo, "Fiber-mounted electro-optic probe for microwave electric-field measurement in plasma environment," *NTT Tech. Rev.*, vol. 11, no. 11, pp. 1–6, 2013.

[90] X. Wang, C.-Y. Lin, S. Chakravarty, J. Luo, A. K.-Y. Jen, and R. T. Chen, "Effective in-device r_33 of 735 pm/V on electro-optic polymer infiltrated silicon photonic crystal slot waveguides," *Opt. Lett.*, vol. 36, no. 6, p. 882, 2011.

[91] X. Zhang, A. Hosseini, C. Lin, J. Luo, A. K. Jen, and R. T. Chen, "Demonstration of Effective In-device r 33 over 1000 pm / V in Electro-optic Polymer Refilled Silicon Slot Photonic Crystal Waveguide Modulator," in *CLEO:2013 Technical Digest*, 2013, vol. 2, pp. 2–3.

[92] "LiNbO3 CRYSTAL, Lithium Niobate, Electro Optical Crystal." [Online]. Available: http://www.redoptronics.com/LiNbO3-crystal-electro-optical.html. [Accessed: 30-Mar-2017].

[93] X. Zhang *et al.*, "Integrated Photonic Electromagnetic Field Sensor Based on Broadband Bowtie Antenna Coupled Silicon Organic Hybrid Modulator," *J. Light. Technol.*, vol. 32, no. 20, pp. 3774–3784, 2014.

[94] X. Zhang *et al.*, "Wideband Electromagnetic Wave Sensing Using Electro-optic Polymer Infiltrated Silicon Slot Photonic Crystal Waveguide," *Adv. Photonics Commun.*, vol. 1, no. c, p. IW2A.3, 2014.

[95] M. Iwanami *et al.*, "Magnetic near-field measurements over LSI package pins by fiber-edge magnetooptic probe," *J. Light. Technol.*, vol. 21, no. 12, pp. 3273–3281, 2003.

[96] M. Tsuchiya *et al.*, "High-speed and high-spatial resolution fiber-optic measurement technique for RF magnetic field distribution," in *The 16th Annual Meeting of the IEEE Lasers and Electro-Optics Society, 2003. LEOS 2003.*, 2003, vol. 2, no. c, pp. 929–930.

[97] M. Iwanami, S. Hoshino, M. Kishi, and M. Tsuchiya, "Magnetic near-field distribution measurements over finite meander circuit patterns by fiber-optic magneto-optic probe," in *2003 IEEE Symposium on Electromagnetic Compatibility. Symposium Record (Cat. No.03CH37446)*, 2003, vol. 1, pp. 347–352 vol.1.

[98] T. S. M. Iwanami *et al.*, "Current profiling for μm-class planar circuit patterns by fiber-edge magneto-optic probe," in *MWP 2003 Proceedings. International Topical Meeting on Microwave Photonics, 2003.*, 2003, pp. 341–344.

[99] S. Wakana, E. Yamazaki, M. Iwanami, S. Hoshino, M. Kishi, and M. Tsuchiya, "Study of the Crystal Size Effect on Spatial Resolution in Three-Dimensional Measurement of Fine Electromagnetic Field Distribution by Optical Probing," *Jpn. J. Appl. Phys.*, vol. 42, no. Part 1, No. 10, pp. 6637–6640, 2003.

[100] M. Takahashi *et al.*, "Optical scanning probe system for electromagnetic near field measurements," in *2009 IEEE International Symposium on Electromagnetic Compatibility*, 2009, pp. 6–11.

[101] S. Nakamatsu, R. Yamaguchi, and S. Uebayashi, "Highly-accurate Measurement

of Current Distribution Using Polarization-stabilized MO Probe," *Collab. Proj. DoCoMo R&D Tech. J.*, vol. Vol.8, pp. 50–54, 2006.

[102] S. Nakamatsu, R. Yamaguchi, S. Uebayashi, M. Kishi, and M. Tsuchiya, "Measurement of current phase distribution for wireless devices using polarization stabilized MO probe," in *2006 IEEE Antennas and Propagation Society International Symposium*, 2006, pp. 445–448.

[103] R. Kantor and I. V. Shvets, "Measurement of electric-field intensities using scanning near-field microwave microscopy," *IEEE Trans. Microw. Theory Tech.*, vol. 51, no. 11, pp. 2228–2234, 2003.

[104] M. Kanda, "Standard Probes for Electromagnetic Field Measurements," *IEEE Trans. Antennas Propag.*, vol. 41, no. 10, pp. 1349–1364, 1993.

[105] "Active near field probes." [Online]. Available: http://www.laplace.co.uk/product/18/. [Accessed: 30-Mar-2017].

[106] "RF Near Field Probe Set DC to 9GHz EMF & RF close field sniffer-set for use with any Spectrum Analyzer or Measurement Receiver." [Online]. Available: http://www.aetjapan.com/catalog/PDF_hard/ProbeSystem_en.pdf. [Accessed: 30-Mar-2017].

[107] "Magnetic Field Measurement System." [Online]. Available: http://www.aaronia.com/Datasheets/Antennas/RF-Near-Field-Probe-Set.pdf. [Accessed: 30-Mar-2017].

[108] "Test equipment - Probes - Small near field probes - Electromagnetic Compatibility - Wavecontrol." [Online]. Available: http://www.wavecontrol-emc.com/en/53559/-/Small-near-field-probes.htm. [Accessed: 30-Mar-2017].

[109] "Magnetic Field Probe :: | AET.Inc,." [Online]. Available: http://www.aetjapan.com/english/hardware_detail.php?magnetic_field_prob#field81. [Accessed: 30-Mar-2017].

[110] R. Kantor and I. V. Shvets, "Method of increasing spatial resolution of the scanning near-field microwave microscopy," *J. Appl. Phys.*, vol. 93, no. 9, pp. 4979–4985, 2003.

[111] R. Kantor and I. V. Shvets, "High-resolution near-field measurements of microwave circuits," in *Microwave and Optical Technology*, 2004, vol. 5445, pp.

318–323.

[112] A. Stöhr, R. Heinzelmann, and T. Alder, “Electroabsorption modulators for broadband fiber electro-optic field sensors,” *Appl. Photonic Technol. 2. Springer US*, pp. 871–876, 1997.

[113] “TDS components | TDS E-field probes | TDS H-field probes | remote unit standalone | remote unit PXI » SPEAG, Schmid & Partner Engineering AG.” [Online]. Available: https://www.speag.com/products/tds/time-domain-probes/. [Accessed: 30-Mar-2017].

[114] J. P. Everett *et al.*, “Optimization of LDMOS Power Transistors for High Power Microwave Amplifiers using Highly Efficient Physics-Based Model,” in *Proceedings of the 6th European Microwave Integrated Circuits Conference*, 2011, no. October, pp. 41–44.

[115] P. H. Aaen, J. A. Plá, and J. Wood, *Modeling and characterization of RF and Microwave Power FETs*. CAMBRIDGE UNIVERSITY PRESS, 2007.

[116] N. Ando *et al.*, “Development of Miniaturized Thin-Film Magnetic Field Probes for On-Chip Measurement,” *J. Magn. Soc. Japan*, vol. 30, no. 4, pp. 429–434, 2006.

[117] S. K. Dutta *et al.*, “Imaging microwave electric fields using a near-field scanning microwave microscope,” *Appl. Phys. Lett.*, vol. 74, no. 1, pp. 156–158, 1999.

[118] T. Dubois *et al.*, “Near-field electromagnetic characterization and perturbation of logic circuits,” *IEEE Trans. Instrum. Meas.*, vol. 57, no. 11, pp. 2398–2404, 2008.

[119] H. Funato, T. Suga, and M. Suhara, “Double Position-Signal-Difference Method for Electric Near-Field Measurements,” in *2013 IEEE International Symposium on Electromagnetic Compatibility (EMC)*, 2013, pp. 621–625.

[120] N. Yu *et al.*, “Measurement of Electric Field Distributions using Small Coaxial Probe in Microstrip-Line Circuits and Comparison with FD-TD method,” *Microw. Conf. 2003 33rd Eur.*, vol. 56, no. 3, pp. 543–546, 2003.

[121] T. Hiraoka, C. P. Chen, T. Anada, J. P. Hsu, Z. W. Ma, and C. C. Christopoulos, “Electric field distributions in microwave planar circuits by small coaxial probe and comparison with FDTD method,” in *2005 European Microwave Conference*, 2005, vol. 2, pp. 1071–1074.

[122] H. S. U. Hiraoka, T., Neishi, Y., Anada, T., & Jui-Pang, "Two dimensional electric field measurement in microstrip-line circuits by coaxial-type probe," *IEICE Trans. Electron.*, vol. 88, no. 1, pp. 77–82, 2005.

[123] Z. Yan, J. Wang, W. Zhang, Y. Wang, S. Member, and J. Fan, "A Miniature Ultrawideband Electric Field Probe Based on Coax-Thru-Hole via Array for Near-Field Measurement," *IEEE Trans. Instrum. Meas.*, vol. PP, no. 99, pp. 1–9, 2017.

[124] Z. Yan, J. Wang, W. Zhang, Y. Wang, and J. Fan, "A Simple Miniature Ultra-Wide Band Magnetic Field Probe Design for Magnetic Near-Field Measurements," *IEEE Trans. Antennas Propag.*, vol. 1, no. c, pp. 1–1, 2016.

[125] G. Yingjie and I. Wolff, "Measurements of field distributions and scattering parameters in multiconductor structures using an electric field probe," in *1997 IEEE MTT-S International Microwave Symposium Digest*, 1997, vol. 3, pp. 1741–1744.

[126] Y. Gao, A. Lauer, Q. Ren, and I. Wolff, "Calibration of electric coaxial near-field probes and applications," *IEEE Trans. Microw. Theory Tech.*, vol. 46, no. 11 PART 1, pp. 1694–1703, 1998.

[127] Y. Gao and I. Wolff, "A simple electric near field probe for microwave circuit diagnostics," in *Microwave Symposium Digest, 1996., IEEE MTT-S International*, 1996, vol. 3, pp. 1537–1540 vol.3.

[128] L. Nativel *et al.*, "MMIC's characterization by very near-field technique," *Microw. Opt. Technol. Lett.*, vol. 41, no. 3, pp. 209–213, 2004.

[129] D. Uchida, T. Nagai, Y. Oshima, and S. Wakana, "Novel high-spatial resolution probe for electric near-field measurement," in *2011 IEEE Radio and Wireless Symposium*, 2011, pp. 299–302.

[130] N. Dehghan, S. Cripps, A. Porch, and J. Lees, "An improved electric field probe with applications in high efficiency PA design and diagnostics," in *Microwave Measurement Conference (ARFTG), 2013 81st ARFTG*, 2013, pp. 1–4.

[131] K.-S. S. Chen, Y.-H. H. Liu, and T. S. Horng, "Spatially-Resolved Near-Field Diagnosis of Differential Signaling Performance for Wireless Device RFI / EMC Applications," in *Electromagnetic Compatibility (APEMC), 2015 Asia-Pacific Symposium on*, 2015, vol. 1, no. 3, pp. 3–5.

[132] Y. Gao and I. Wolff, "Electric field investigations on active microwave circuits,"

in *Microwave Conference, 1996. 26th European*, 1996, vol. 2, pp. 662–664.

[133] R. Hou, M. Spirito, B. J. Kooij, F. Van Rijs, and L. C. N. De Vreede, "Contactless measurement of in-circuit reflection coefficients," in *IEEE MTT-S International Microwave Symposium Digest*, 2012, no. 2, pp. 2–4.

[134] R. Hou, M. Spirito, F. Van Rijs, L. C. N. De Vreede, and S. Member, "Contactless Measurement of Absolute Voltage Waveforms by a Passive Electric-Field Probe," *IEEE Microw. Wirel. Components Lett.*, pp. 1–3, 2016.

[135] N. Dehghan and S. C. Cripps, "A novel in-situ calibration technique for a high resolution E-Field probe," in *2015 IEEE MTT-S International Microwave Symposium (IMS)*, 2015, pp. 1–3.

[136] R. Hou, M. Spirito, J. Gajadharsing, L. C. N. De Vreede, and L. C. N. de Vreede, "Non-intrusive characterization of active device interactions in high-efficiency power amplifiers," in *Microwave Symposium Digest (IMS), 2013 IEEE MTT-S International*, 2013, pp. 1–3.

[137] R. Hou, M. Spirito, R. Heeres, F. Van Rijs, and L. C. N. De Vreede, "Non-intrusive near-field characterization of distributed effects in large-periphery LDMOS RF power transistors," in *2015 IEEE MTT-S International Microwave Symposium, IMS 2015*, 2015, pp. 2–4.

[138] R. Hou, M. Lorenzini, M. Spirito, T. Roedle, F. Rijs, and L. C. N. de Vreede, "Nonintrusive Near-Field Characterization of Spatially Distributed Effects in Large-Periphery High-Power GaN HEMTs," *IEEE Trans. Microw. Theory Tech.*, vol. 64, no. 11, pp. 4048–4062, 2016.

[139] Y. T. Chou and H. C. Lu, "Magnetic near-field probes with high-pass and notch filters for electric field suppression," *IEEE Trans. Microw. Theory Tech.*, vol. 61, no. 6, pp. 2460–2470, 2013.

[140] T. Adorno, M. Horkheimer, S. S. Osofsky, and S. E. Schwarz, "A non-contacting probe for measurements on high-frequency planar circuits," *Microw. Symp. Dig. 1989., IEEE MTT-S Int.*, vol. 40, no. 8, pp. 823–825 vol.2, 1989.

[141] R. R. Grzybowski and D. Umamchandani, "Magnetic field probe for measuring surface current distributions on millimetre wave microstrip antennas," *Electron. Lett.*, vol. 27, no. 1, pp. 71–73, 1991.

[142] Y. Gao and I. Wolff, "A miniature magnetic field probe for measuring fields in

planar high-frequency circuits," *Microw. Symp. Dig. 1995., IEEE MTT-S Int.*, vol. 3, pp. 1159–1162, 1995.

[143] R. Wang and M. Tabib-azar, "Noncotact Evanescent Miccrowave Mgnetic Dipole Probe Imaging of Ferromagnets," *IEEE Trans. Magn.*, vol. 43, no. 7, pp. 3165–3170, 2007.

[144] N. Masunaga, K. Ishida, M. Takamiya, and T. Sakurai, "EMI camera LSI (EMcam) with 12 × 4 on-chip loop antenna matrix in 65-nm CMOS to measure EMI noise distribution with 60-μm spatial precision," in *Proceedings of the Custom Integrated Circuits Conference*, 2010, pp. 4–6.

[145] N. Masunaga, K. Ishida, T. Sakurai, and M. Takamiya, "EMI Camera LSI (EMcam) with On-Chip Loop Antenna Matrix to Measure EMI Noise Spectrum and Distribution," *IEICE Trans. Electron.*, vol. E95.C, no. 6, pp. 1059–1066, 2012.

[146] S. Aoyama, S. Kawahito, and M. Yamaguchi, "An Active Magnetic Probe Array for the Multiple-Point Concurrent Measurement of Electromagnetic Emissions," *IEEE Trans. Magn.*, vol. 42, no. 10, pp. 3303–3305, 2006.

[147] N. N. Mai-Khanh, T. Iizuka, M. Yamada, O. Morita, and K. Asada, "An integrated high-precision probe system for near-field magnetic measurements on cryptographic LSIs," *Sensors, 2012 IEEE*, vol. 13, no. 7, pp. 1–4, 2012.

[148] N. N. Mai-Khanh, T. Iizuka, M. Yamada, O. Morita, and K. Asada, "An integrated high-precision probe system in 0.18-μm CMOs for near-field magnetic measurements on cryptographic LSIs," *IEEE Sens. J.*, vol. 13, no. 7, pp. 2675–2682, 2013.

[149] Y. Shigeta, N. Sato, K. Arai, and M. Ya, "High Spatial Resolution On-chip Active Magnetic Field Probe for IC Chip-L Level Near Field Measu urements," in *EMC'14/Tokyo*, 2014, pp. 569–572.

[150] N. N. Mai-Khanh, T. Iizuka, A. Sasaki, M. Yamada, O. Morita, and K. Asada, "A Near-Field Magnetic Sensing System With High-Spatial Resolution and Application for Security of Cryptographic LSIs," *Instrum. Meas. IEEE Trans.*, vol. 64, no. 4, pp. 840–848, 2015.

[151] N. N. Mai-Khanh, T. Iizuka, S. Nakajima, and K. Asada, "Spacial Resolution Enhancement for Integrated Magnetic Probe by Two-Step Removal of Si-Substrate Beneath the Coil," *Magn. IEEE Trans.*, vol. 51, no. 1, pp. 1–4, 2015.

[152] M. Yamaguchi, S. Yabukami, and K. I. Arai, "A new permeance meter based on both lumped elements / transmission line theories," *IEEE Trans. Magn.*, vol. 32, no. 5 PART 2, pp. 4941–4943, 1996.

[153] M. Yamaguchi *et al.*, "Two dimensional electromagnetic noise imaging system using planar shielded-loop coil array," *1999 Int. Symp. Electromagn. Compat. (IEEE Cat. No.99EX147)*, pp. 51–54, 1999.

[154] ECMA International, "Measuring Emissions from Modules," ECMA International, 2007.

[155] U. Frqwuh, O. D. Irxguh, and U. D. Oljkwqlqj, *Integrated circuits -Measurement of electromagnetic emissions 150 kHz to 1 GHz – Part 6: Measurement of conducted emissions – Magnetic probe method*. IEC, 2008.

[156] M. Yamaguchi, S. Koya, H. Torizuka, S. Aoyama, and S. Kawahito, "Shielded-loop-type onchip magnetic-field probe to evaluate radiated emission from thin-film noise suppressor," *IEEE Trans. Magn.*, vol. 43, no. 6, pp. 2370–2372, 2007.

[157] M. Yamaguchi *et al.*, "Development of an on-chip micro shielded-loop probe to evaluate performance of magnetic film to protect a cryptographic LSI from electromagnetic analysis," in *IEEE International Symposium on Electromagnetic Compatibility*, 2010, pp. 103–108.

[158] S. Muroga, K. Arai, S. Dhungana, R. Okuta, Y. Endo, and M. Yamaguchi, "3-D Magnetic-Near-Field Scanner for IC Chip-Level Noise Coupling Measurements," *IEEE Trans. Magn.*, vol. 49, no. 7, pp. 3886–3889, Jul. 2013.

[159] M. Yamaguchi, S. Muroga, S. Nanba, K. Arai, K. Yanagi, and Y. Endo, "A 60 × 60 μ m 2 Size Planar Shielded Loop Probe for Low Lift-Off On-Chip Magnetic Near Field Measurements," in *Proc. of the 2013 International Symposium on Electromagnetic Compatibility (EMC Europe 2013)*, 2013, pp. 977–980.

[160] N. Masuda, N. Tamaki, T. Kuriyama, J. C. B. J. C. Bu, M. Yamaguchi, and K. Arai, "High frequency magnetic near field measurement on LSI chip using planar multi-layer shielded loop coil," *2003 IEEE Symp. Electromagn. Compat. Symp. Rec. (Cat. No.03CH37446)*, vol. 1, pp. 80–85, 2003.

[161] N. Ando *et al.*, "Miniaturized thin-film magnetic field probe with high spatial resolution for LSI chip measurement," in *2004 International Symposium on Electromagnetic Compatibility (IEEE Cat. No.04CH37559)*, 2004, vol. 2.

[162] N. Tamaki, N. Masuda, T. Kuriyama, J. C. Bu, M. Yamaguchi, and K. I. Arai, "A miniature thin-film shielded-loop probe with a flip-chip bonding for magnetic near field measurements," *Electron. Commun. Japan, Part II Electron. (English Transl. Denshi Tsushin Gakkai Ronbunshi)*, vol. 88, no. 4, pp. 37–45, 2005.

[163] S. Li *et al.*, "Development and application of a high-resolution thin-film probe," in *IEEE International Symposium on Electromagnetic Compatibility*, 2007, pp. 7–11.

[164] Y. T. Chou and H. C. Lu, "Electric field coupling suppression using via fences for magnetic near-field shielded-loop coil probes in low temperature co-fired ceramics," in *IEEE International Symposium on Electromagnetic Compatibility*, 2011, pp. 6–10.

[165] Y. Chou and H. Lu, "Space Difference Magnetic Near-Field Probe With Spatial Resolution Improvement," *IEEE Transacitions Microw. Theory Tech. Vol. 61, No.12, December 2013*, vol. 61, no. 12, pp. 4233–4244, 2013.

[166] S. S. Osofsky and S. E. Schwarz, "Design and performance of a noncontacting probe for measurements on high-frequency planar circuits," *IEEE Trans. Microw. Theory Tech.*, vol. 40, no. 8, pp. 1701–1708, 1992.

[167] T. Zelder and H. Eul, "Contactless network analysis with improved dynamic range using diversity calibration," *2006 Eur. Microw. Conf.*, no. September, pp. 478–481, 2006.

[168] T. Zelder, H. Rabe, and H. Eul, "Contactless electromagnetic measuring system using conventional calibration algorithms to determine scattering parameters," *Adv. Radio Sci.*, vol. 5, pp. 427–434, 2007.

[169] T. Zelder, B. Geck, M. Wollitzer, I. Rolfes, and H. Eul, "Contactless network analysis system for the calibrated measurement of the scattering parameters of planar two-port devices," *Proc. 37th Eur. Microw. Conf. EUMC*, no. October, pp. 246–249, 2007.

[170] K. Yhland, J. Stenarson, and C. Wingqvist, "Noncontacting measurement of reflection coefficient and power in planar circuits up to 40 GHz," *69th ARFTG Microw. Meas. Conf. - Addressing Metrol. Needs Futur. High-Speed Inf. Commun. Syst.*, 2007.

[171] K. Yhland and J. Stenarson, "Noncontacting measurement of power in microstrip circuits," *2006 67th ARFTG Microw. Meas. Conf. - Meas. Des. High Power*

Devices Syst., pp. 201–205, 2007.

[172] T. Zelder, B. Geck, M. Wollitzer, I. Rolfes, and H. Eul, "Contactless vector network analysis with printed loop couplers," *IEEE Trans. Microw. Theory Tech.*, vol. 56, no. 11, pp. 2628–2634, 2008.

[173] T. Zelder and B. Geck, "Contactless scattering parameter measurements," *IEEE Microw. Wirel. Components Lett.*, vol. 21, no. 9, pp. 504–506, 2011.

[174] J. Stenarson, K. Yhland, and C. Wingqvist, "An in-circuit noncontacting measurement method for S-parameters and power in planar circuits," *IEEE Trans. Microw. Theory Tech.*, vol. 49, no. 12, pp. 2567–2572, 2001.

[175] K. Sugawara, C. P. Chen, Z. Ma, T. Anada, and D. W. P. Thomas, "Non-contacting electric and magnetic field probe for measuring EM fields on microwave planar circuits," in *Asia-Pacific Microwave Conference Proceedings, APMC*, 2007.

[176] Hewlett-Packard Company, "Using a Network Analyzer to Characterize High-Power Components. Application Note 1287-6.," 1998. [Online]. Available: http://www.av.it.pt/medidas/data/Manuais & Tutoriais/11- PNA NetWork Analyser/CD1/high_power.pdf. [Accessed: 11-Feb-2017].

[177] A. C. Fischer, J. G. Korvink, N. Roxhed, G. Stemme, U. Wallrabe, and F. Niklaus, "Unconventional applications of wire bonding create opportunities for microsystem integration," *J. Micromech. Microeng*, vol. 23, no. 8, pp. 83001–18, Aug. 2013.

[178] M. Schneider-Ramelow, "Drahtbonden - Fraunhofer IZM," *Fraunhofer-Institut für Zuverlässigkeit und Mikrointegration IZM*. [Online]. Available: http://www.izm.fraunhofer.de/de/abteilungen/system_integrationinterconnectiontechnologies/leistungsangebot/prozess-_und_produktentwicklung/drahtbonden.html. [Accessed: 11-Feb-2017].

[179] M. Schneider-Ramelow, "Wire Bonding Quality Assurance and Testing Methods," *Fraunhofer-Institut für Zuverlässigkeit und Mikrointegration (IZM)*. [Online]. Available: https://ssd-rd.web.cern.ch/ssd-rd/bond/talks/2-04_Schneider-Ramelow.pdf. [Accessed: 11-Feb-2017].

[180] R. Gilardoni, "Ribbon Bonding for High Frequency Applications Advantages of Ribbon and the Impact on the Microwave Market." [Online]. Available: http://www.circuitnet.com/news/uploads/1/Hesse-Knipps_ribbonbonding.pdf.

[Accessed: 11-Feb-2017].

[181] D. Nicholson and H. Lee, "Characterization and Modeling of Bond Wires for High-Frequency Applications," in *Microwave Engineering Europe.*, 2006, pp. 40–46.

[182] "Wire Bonding Services - MicroTek," *Microtek, Inc.* [Online]. Available: http://www.utekinc.com/wire-bonding-services/. [Accessed: 12-Feb-2017].

[183] L. Cupido, "Wire Bonding (For Microwave and Millimeter-Wave, on a low budget)," 2005. [Online]. Available: http://www.qsl.net/ct1dmk/wire_bonding.pdf. [Accessed: 11-Feb-2017].

[184] I. J. Bahl, *Fundamentals of RF and Microwave Transistor Amplifiers*, 1st ed. Wiley-Blackwell, 2009.

[185] R. Lang, J. Gill, D. GOTCH, and R. Hilton, "Improved matching techniques for wide-bandgap power transistors," U.S. Patent Application 15/108,937, filed December 31, 2014., 2016.

[186] "Copper (Cu) Wire Bonding Technical Benefits," *anysilicon*, 2012. [Online]. Available: http://anysilicon.com/copper-cu-wire-bonding-technical-benefits-overview/. [Accessed: 11-Feb-2017].

[187] "Bonding Wires for Semiconductor Technology," *Heraeus*. [Online]. Available: http://www.scanditron.com/sites/default/files/material/heraeus_bondingwire_brochure.pdf. [Accessed: 11-Feb-2017].

[188] "3D Bondwire Electrical Modeling Results Gold Bondwire Partial Self and Mutual Inductance (nH) 1 mil Diameter," *Amkor Technology, Inc.* .

[189] "Microwaves101 | Microwave FET Tutorial." [Online]. Available: https://www.microwaves101.com/encyclopedias/microwave-fet-tutorial. [Accessed: 14-May-2017].

[190] F. Maloberti, "Layout of Analog CMOS Integrated Circuit Transistors and Basic Cells Layout." [Online]. Available: http://ims.unipv.it/Courses/download/AIC/Layout02.pdf. [Accessed: 12-Oct-2017].

[191] F. T. Ulaby, E. Michielssen, and U. Ravaioli, *Fundamentals of Applied Electromagnetics*. Prentice Hall, 2010.

[192] L. G. Maloratsky, *RF and Microwave Integrated Circuits*. Elsevier India, 1999.

[193] "Microstrip Line Calculator | em: talk." [Online]. Available: http://www.emtalk.com/mscalc.php. [Accessed: 17-Feb-2017].

[194] T. Edwards and M. Steer, *Foundations for Microstrip Circuit Design*, 4th ed. Wiley-Blackwell, 2016.

[195] Robert Kollman, "Power Tip 26: Current distribution in high-frequency conductors," *EETimes*, 2010. [Online]. Available: http://www.eetimes.com/document.asp?doc_id=1278215. [Accessed: 16-Feb-2017].

[196] R. Faraji-Dana and Y. L. Chow, "The current distribution and AC resistance of a microstrip structure," *IEEE Trans. Microw. Theory Tech.*, vol. 38, no. 9, pp. 1268–1277, 1990.

[197] A. M. L. Al-Ziayree, S. C. Cripps, and R. M. Perks, "A novel microwave non contact current probe with high spatial resolution," in *2016 IEEE MTT-S International Microwave Symposium (IMS)*, 2016, pp. 1–3.

[198] D. K. Cheng, *Field and wave electromagnetics*, 2nd ed. Addison-Wesley, 1989.

[199] R. H. Caverly, "Characteristic Impedance of Integrated Circuit Bond Wires," *IEEE Trans. Microw. Theory Tech.*, vol. 34, no. 9, pp. 982–984, 1986.

[200] "Wire Microstrip Impedance | Electronics and Electrical Engineering Tools | EEWeb Community." [Online]. Available: https://www.eeweb.com/toolbox/wire-microstrip-impedance. [Accessed: 11-Mar-2017].

[201] S. Fikar, R. Bogenberger, and A. L. Scholtz, "A 100GHz bandwidth matched chip to PCB transition using bond wires for broadband matching," *12th IEEE Work. Signal Propag. Interconnects, SPI*, pp. 2–5, 2008.

[202] P. H. Aaen, J. A. Plá, and C. A. Balanis, "On the Development of CAD Techniques Suitable for the Design of High-Power RF Transistors."

[203] S. A. P. Rizvi and R. A. A. Khan, "Klopfenstein tapered 2-18 GHz microstrip Balun," *Proc. 2012 9th Int. Bhurban Conf. Appl. Sci. Technol. IBCAST 2012*, pp. 359–362, 2012.

[204] L. Song and Y. Zhang, "Internal matching circuit design of RF LDMOS power transistor," in *2016 International Conference on Integrated Circuits and*

Microsystems (ICICM), 2016, pp. 11–14.

[205] S. Ramo, J. R. Whinnery, and T. Van Duzer, *FIELDS AND WAVES IN COMMUNICATION ELECTRONICS*. John Wiley & Sons, Inc., 1994.

[206] Avago Technologies, "VMMK-1218 0.5 to 18 GHz Low Noise E-PHEMT in a Wafer Scale Package," *AVAGO*. [Online]. Available: http://www.mouser.com/ds/2/678/V02-1081EN-DS-VMMK-1218-02Feb20120-908954.pdf. [Accessed: 19-Jul-2017].

[207] Avago Technologies, "VMMK-1225 0.5 to 26 GHz Low Noise E-PHEMT in a Wafer Scale Package," *AVAGO*. [Online]. Available: http://www.mouser.com/ds/2/678/V02-1082EN_DS_VMMK-1225_2014-01-090-909543.pdf. [Accessed: 19-Jul-2017].

[208] Avago Technologies, "VMMK-3603 1 -6 GHz Positive Gain Slope Low Noise Amplifier in SMT Package." [Online]. Available: http://www.mouser.com/ds/2/38/V02-2919EN+DS+VMMK-3603+26Dec2012-211565.pdf. [Accessed: 19-Jul-2017].

[209] "Twin_Wire.jpg (4000×3200)." [Online]. Available: http://www.drjamesnagel.com/images/Twin_Wire.jpg. [Accessed: 31-Jul-2017].

[210] O. a Garcia-perez, V. Gonzalez-posadas, J. L. Jimenez-martin, J. M. Serna-puente, and D. Segovia-vargas, "Design of Differential Low Noise Amplifiers for UWB Antennas in the Low Band of the SKA Project," *29th Gen. Assem. Int. Union Radio Sci.*, pp. 3–6, 2008.

[211] AVAGO, "Characteristics of E-pHEMT vs . HBTs for PA Applications White Paper," 2010.

[212] S. A. Burney and C. Qunsheng, "Design of an LNA with Ultra Low Noise and Model Noise," in *Progress In Electromagnetics Research Symposium Proceedings*, 2011, pp. 679–683.

[213] AVAGO, "Avago introduces 18 GHz and 26.5 GHz low-noise E-pHEMT in 0402 Compatible Packages Produced by Advanced Wafer-scale Packaging Technology," *AVAGO*, 2012.

[214] N. Dehghan, "High Resolution Electric Field Probes with Applications in High Efficiency RF Power Amplifier Design," Ph.D. dissertation, Cardiff University, 2014.

[215] R. Hou, “Non-intrusive Near-field Characterization of Microwave Circuits and Devices,” Ph.D. dissertation, Delft University, 2015.

[216] Ampleon, “BLF7G22L-130 | Power LDMOS transistor | AMPLEON,” *Ampleon*, 2015. [Online]. Available: http://www.ampleon.com/products/mobile-broadband/2.0-2.2-ghz-transistors/BLF7G22L-130.html. [Accessed: 15-Nov-2017].

[217] C. F. M. Carobbi, L. M. Millanta, and L. Chiosi, “The high-frequency behavior of the shield in the magnetic-field probes,” in *IEEE International Symposium on Electromagnetic Compatibility. Symposium Record (Cat. No.00CH37016)*, 2000, vol. 1, pp. 35–40.

9 APPENDICES

APPENDIX ONE

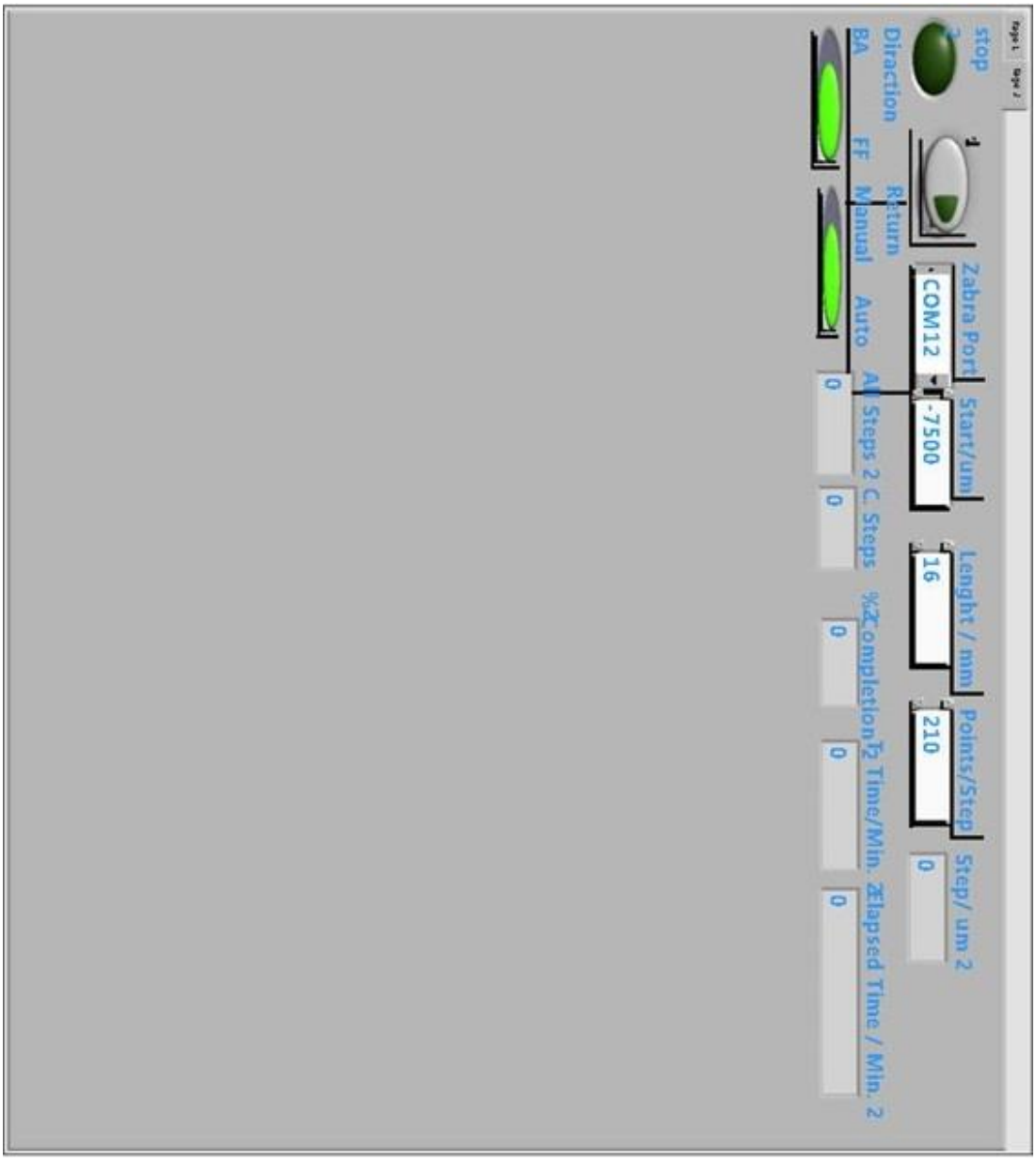

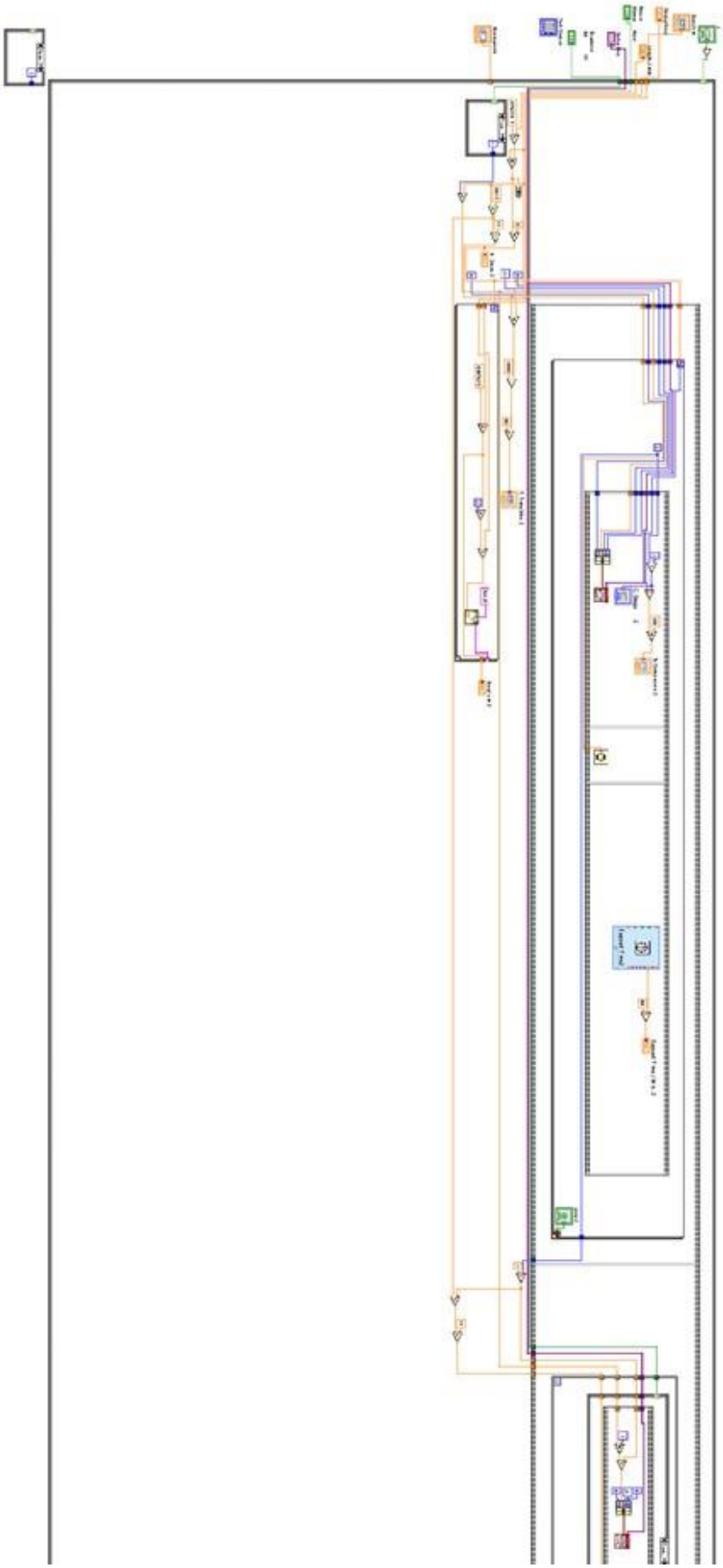

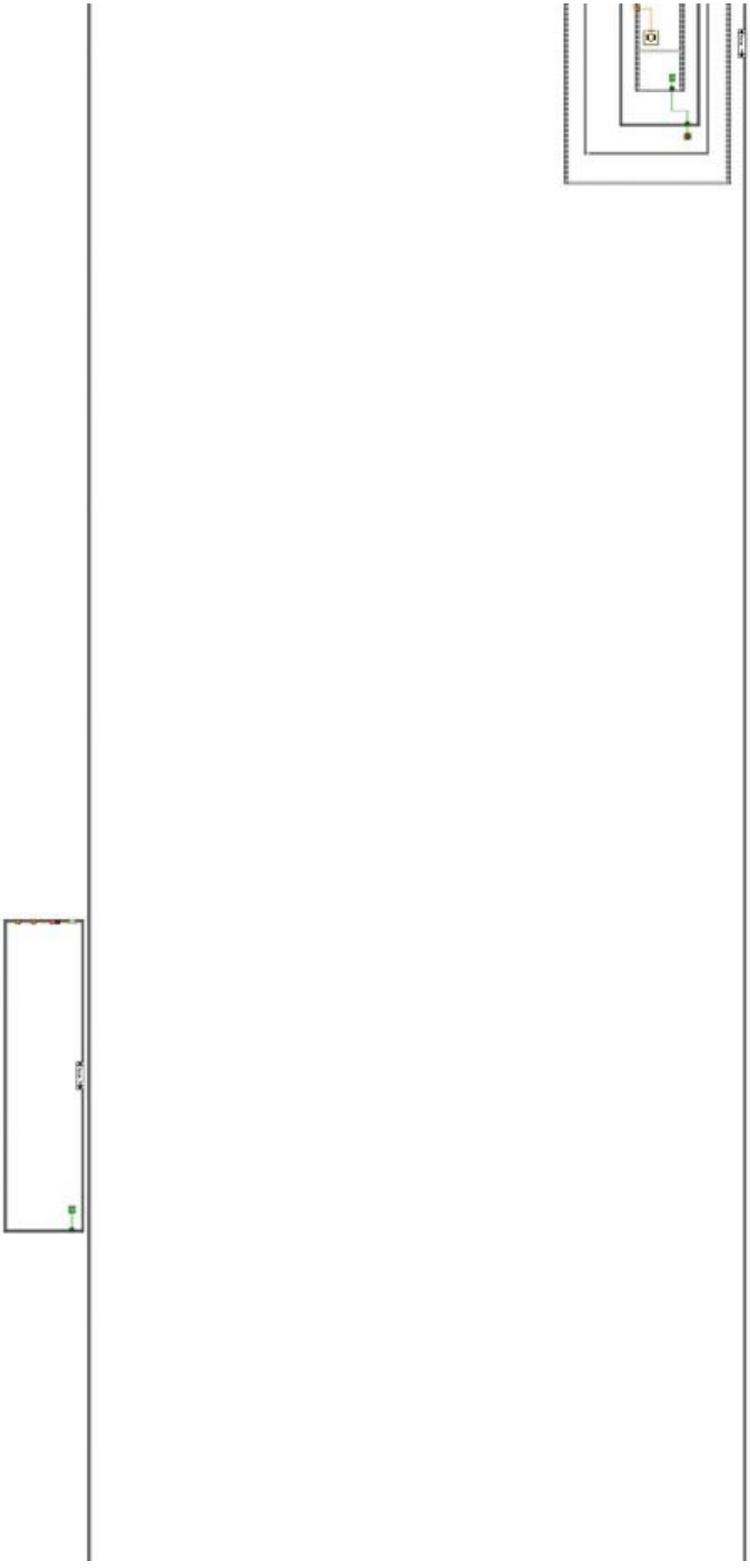

APPENDIX TWO

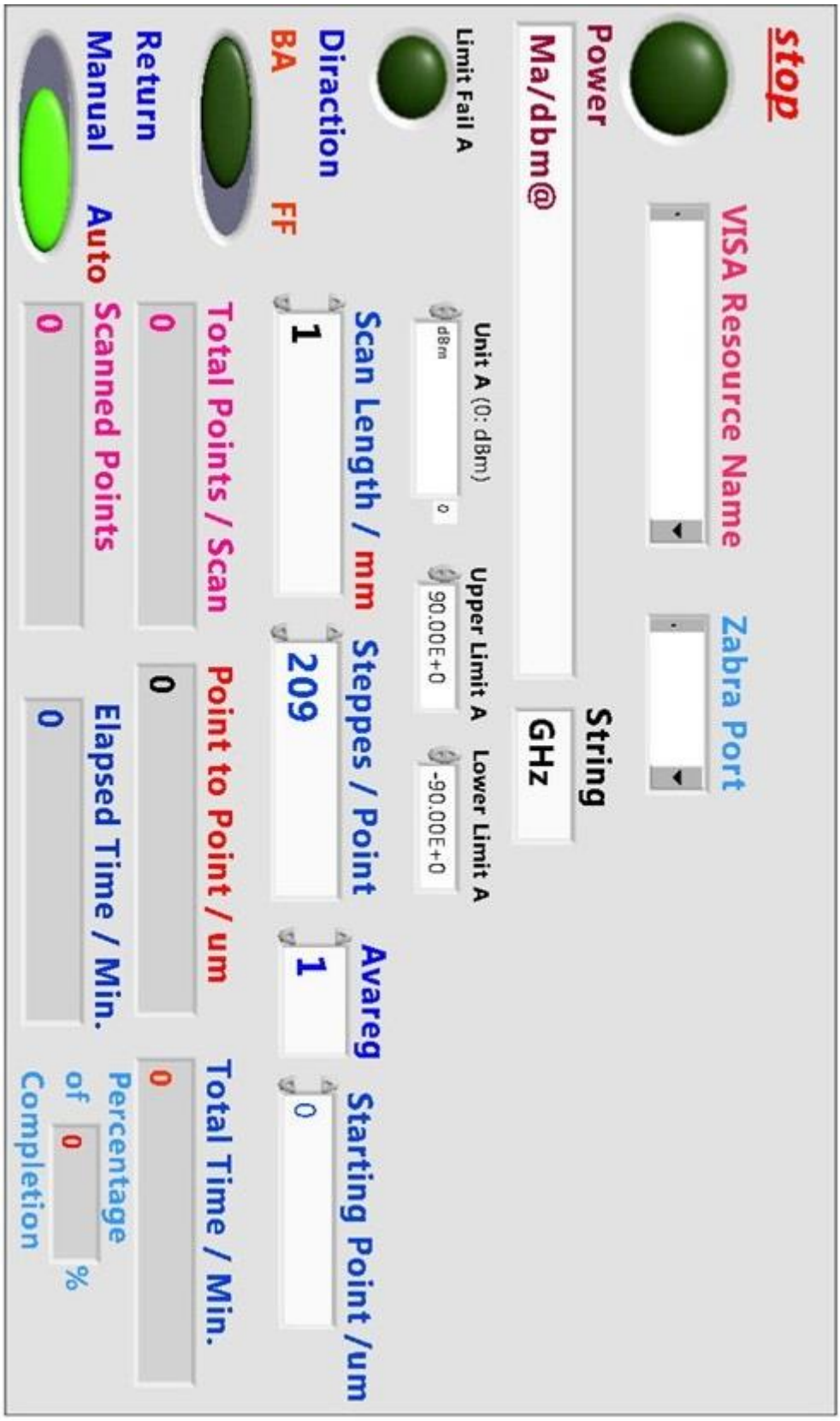

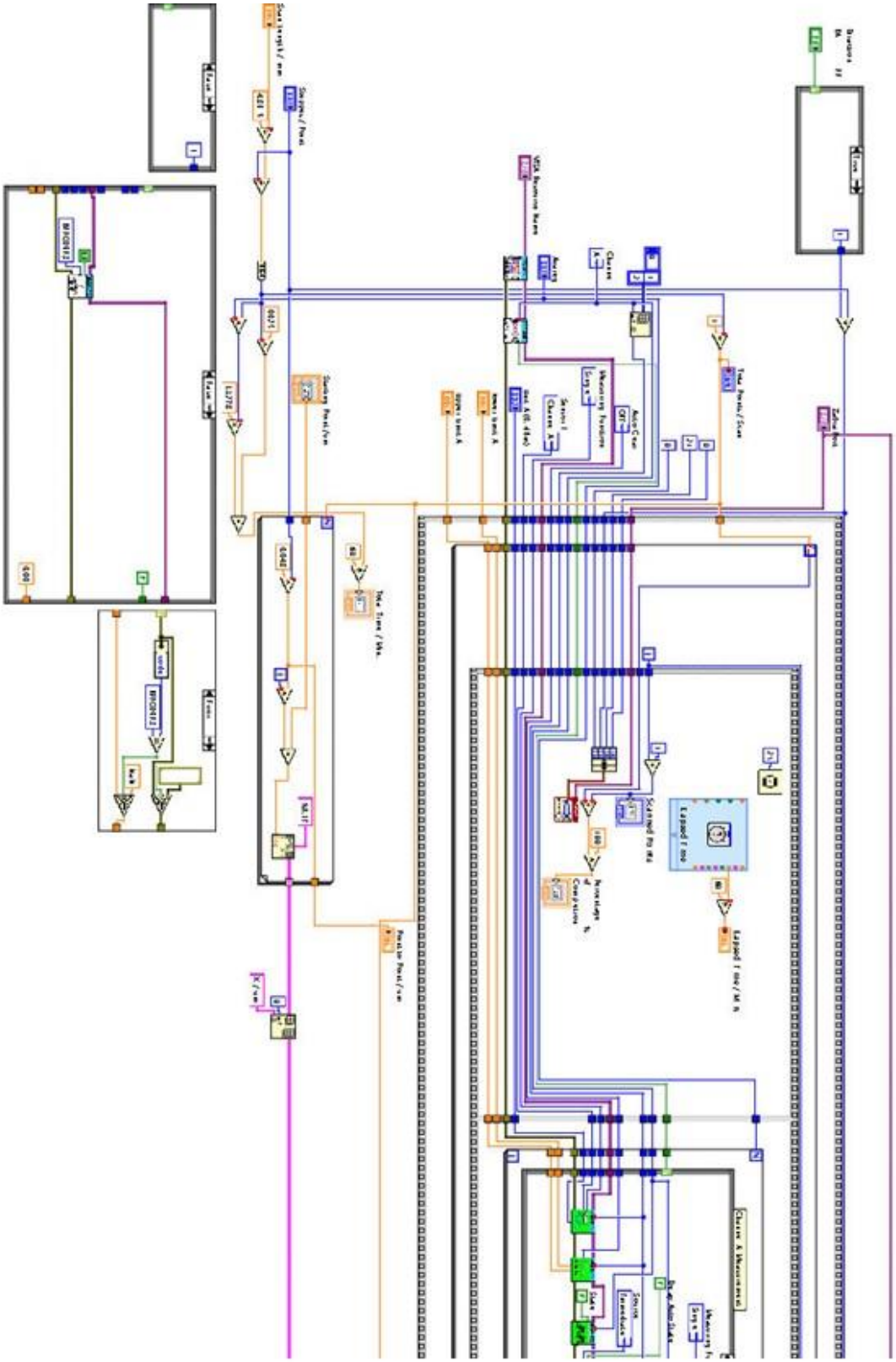

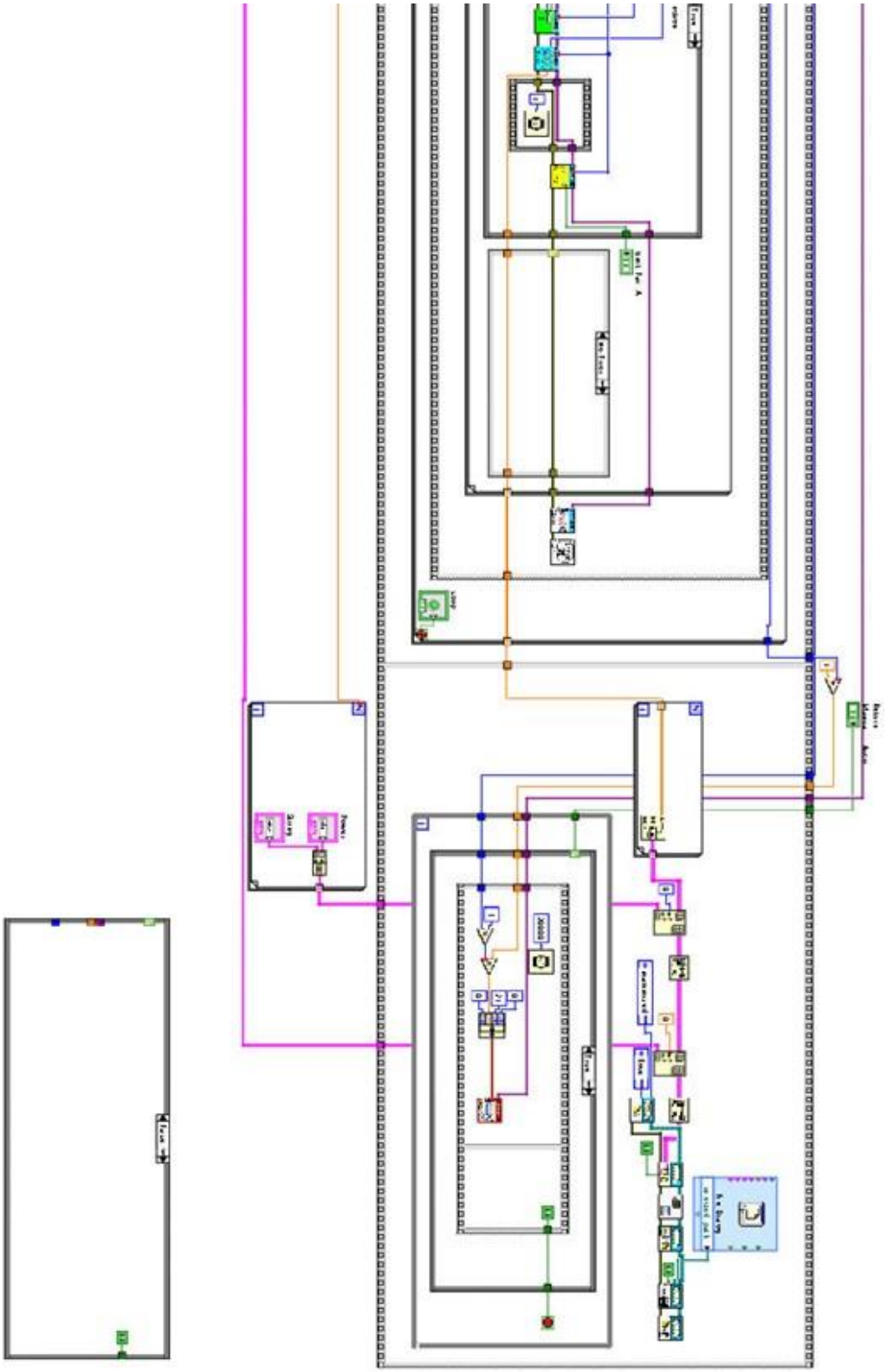

APPENDIX THREE

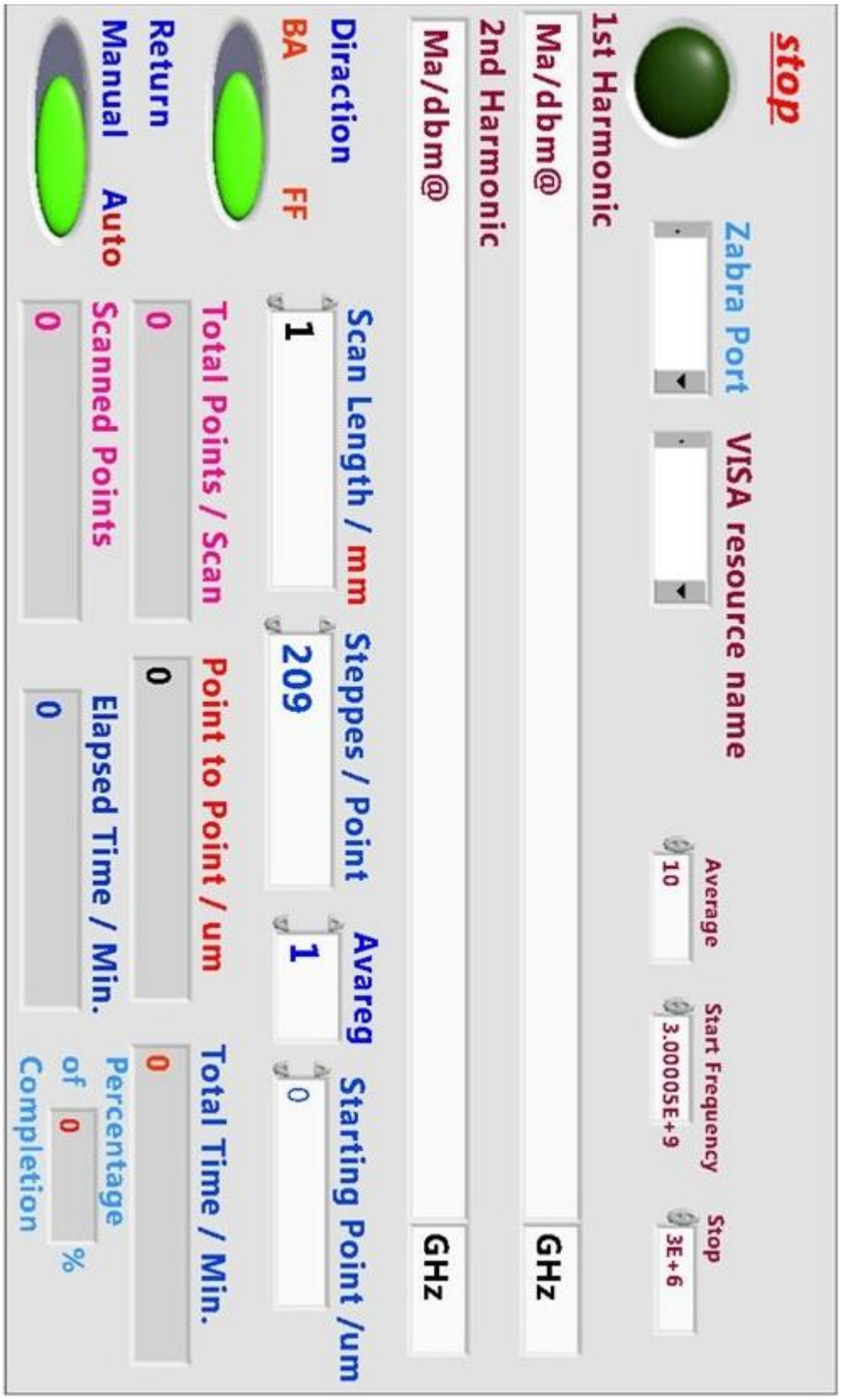

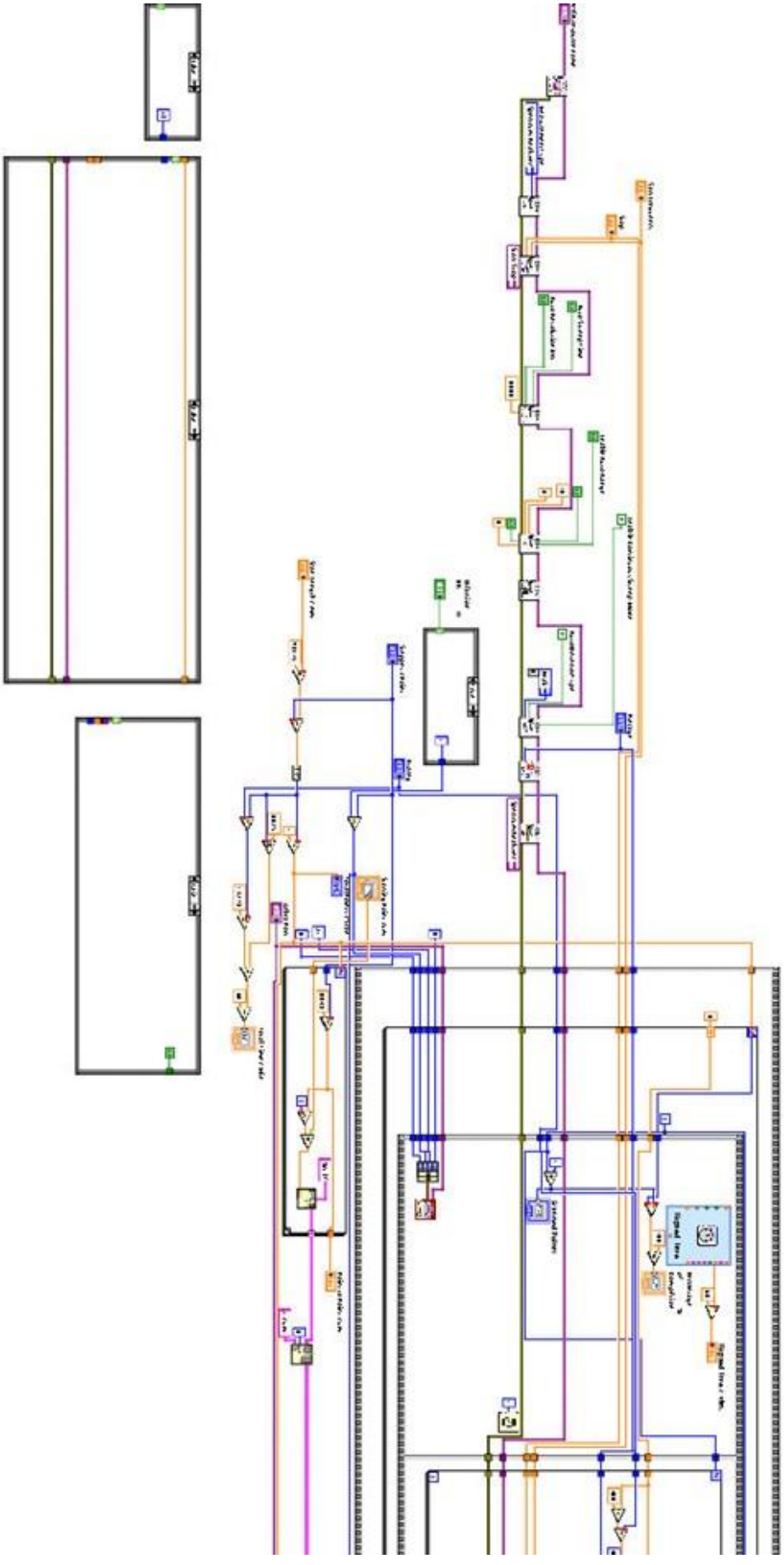

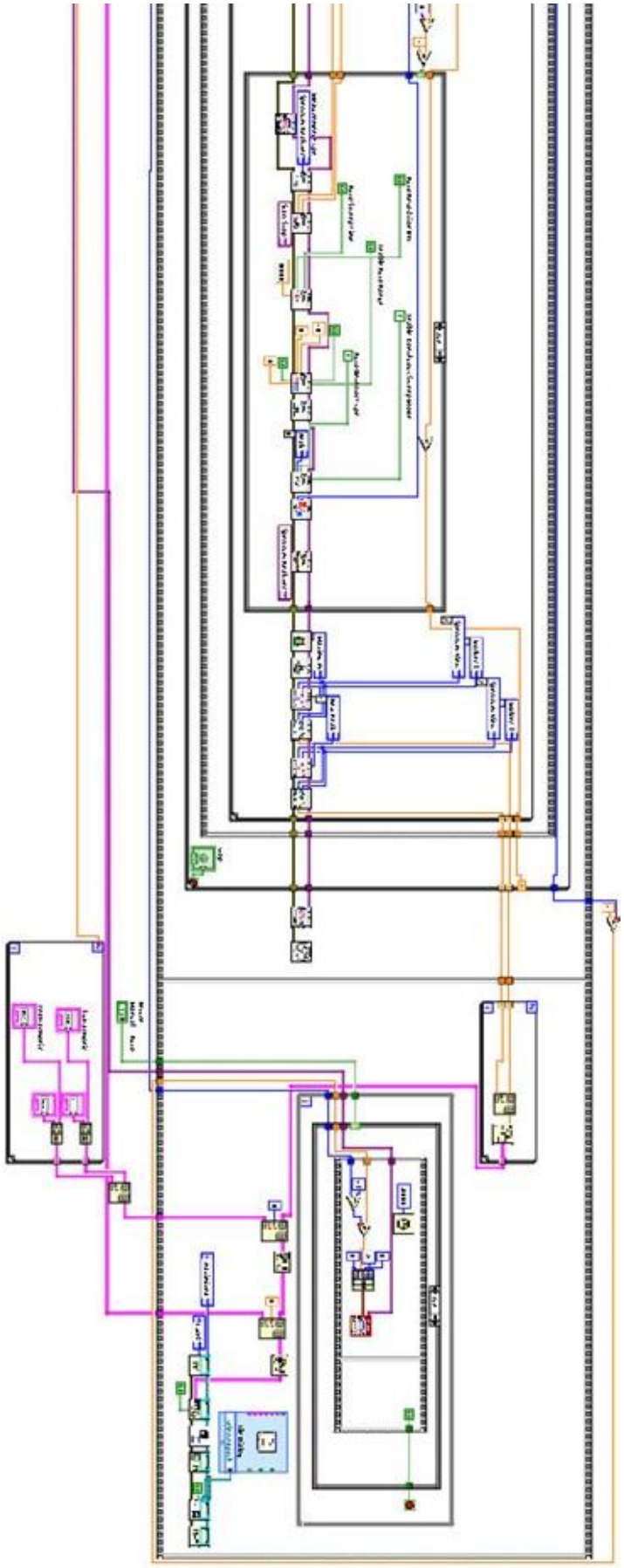

APPENDIX FOUR

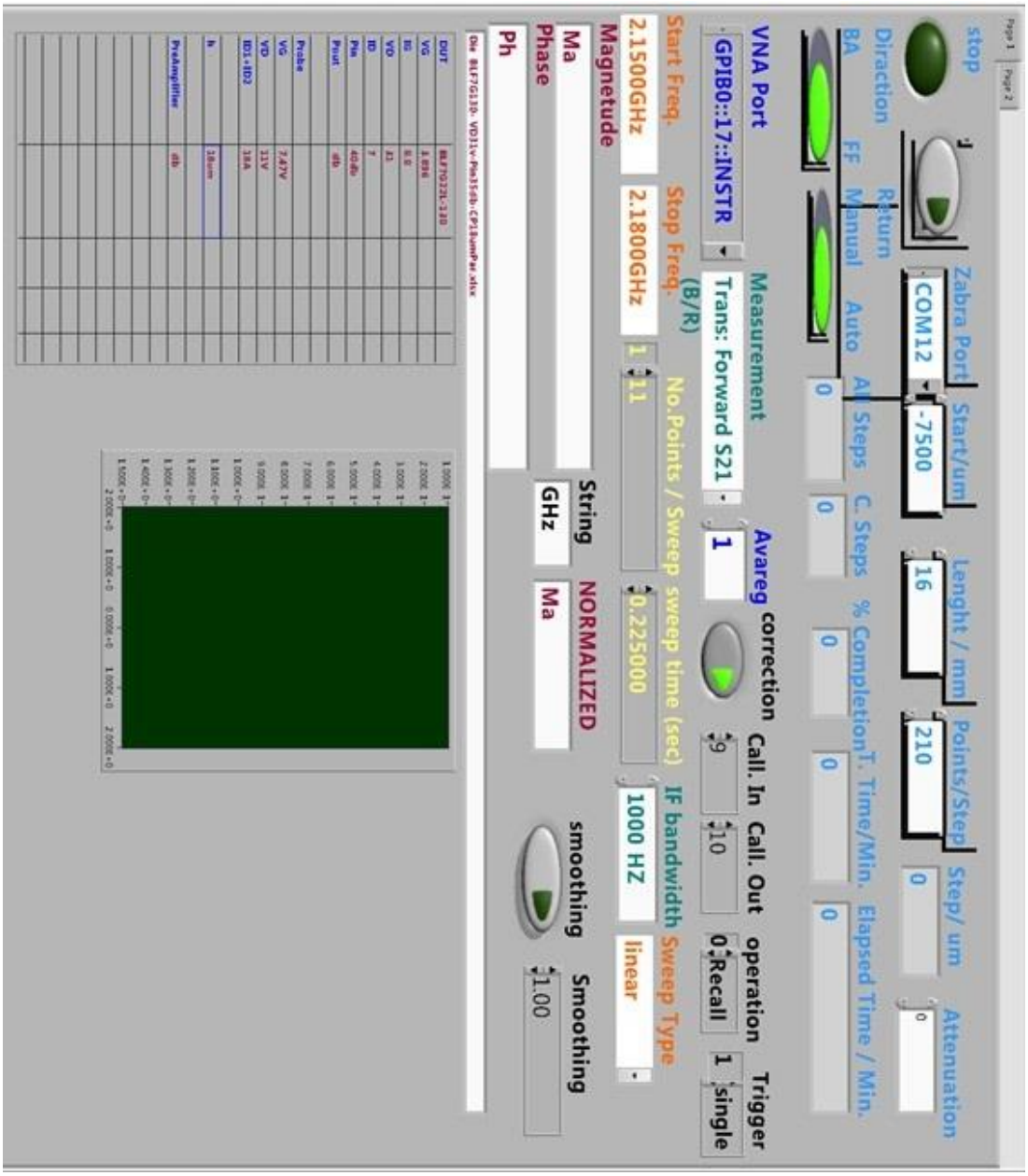

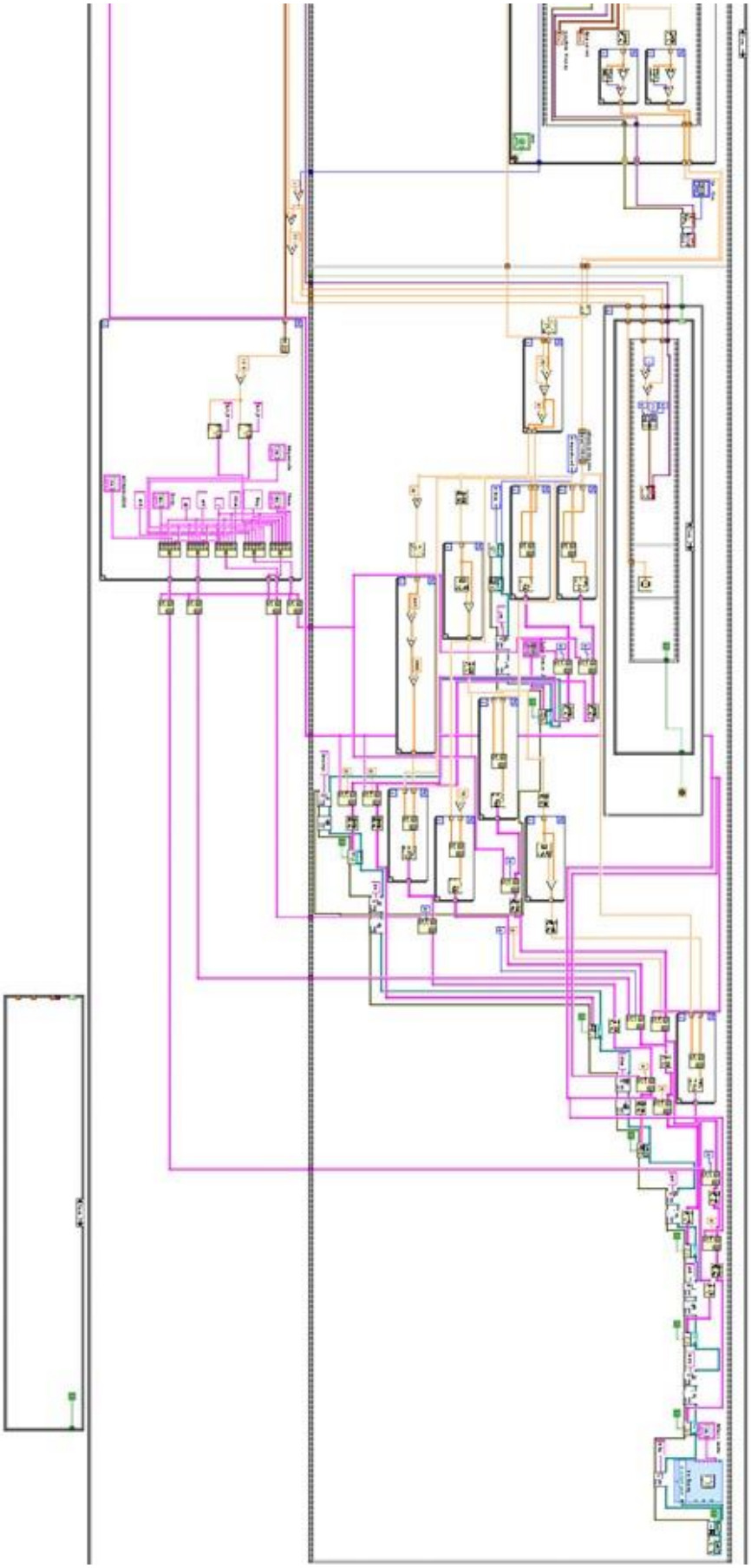

APPENDIX FIVE